# Ion optical calibration of
# the PLASTIC sensor on STEREO

Inauguraldissertation
der Philosophisch-naturwissenschaftlichen Fakultät
der Universität Bern

vorgelegt von

**Reto Karrer**

von Zürich

Leiter der Arbeit:

Prof. Dr. P. Bochsler

Physikalisches Institut der Universität Bern

# Ion optical calibration of
# the PLASTIC sensor on STEREO

Inauguraldissertation
der Philosophisch-naturwissenschaftlichen Fakultät
der Universität Bern

vorgelegt von

**Reto Karrer**

von Zürich

Leiter der Arbeit:

Prof. Dr. P. Bochsler

Physikalisches Institut der Universität Bern

Von der Philosophisch-naturwissenschaftlichen Fakultät angenommen.

Der Dekan:

Bern, 12. April 2007        Prof. Dr. P. Messerli

**Abstract**

On the 26th of October 2006, the two spacecraft of the STEREO mission were successfully launched onboard a Delta II rocket. STEREO (Solar-Terrestrial Relation Observatory) is the third of five NASA Solar Terrestrial Probes (STP) missions of the international Sun-Earth connections program. STEREO will study coronal mass ejections (CME) and further the 3D understanding of the inner heliosphere. The PLASTIC (Plasma and Suprathermal Ion Composition) instrument measures *in situ* the velocity distribution, mass and charge states of solar wind ions and suprathermal ions distributions. PLASTIC consists of a top-hat energy per charge analyzer, a time-of-flight (TOF) section, and an electronic box supplying the voltages for the deflection electrodes and the particle detectors and for signal processing. With PLASTIC three functions are realized in one instrument: (1) the determination of the mass and charge state distribution of suprathermal ions in a in-ecliptic range up to $360°$, (2) energy, mass and charge states measurements of solar wind heavy ions ($Z > 2$) in a field of view of $45°$ in-ecliptic centered on solar wind direction and $\pm 20°$ out-of-ecliptic and (3) measurements of the distribution functions of solar wind protons and alpha particles in the same field of view. To accomplish this, the PLASTIC entrance system/energy analyzer (ESEA) consists of three apertures with different geometric factors: the Wide-Angle Partition (WAP), the Solar Wind Sector (SWS) main channel and the SWS S-channel with a smaller geometric factor. The ion selection is realized with a complex system of electrostatic deflection electrodes. The main part of the work reported in this dissertation covers the ion optical calibration of the PLASTIC sensor. Since there are two spacecraft, two flight models and a flight spare had to be fully characterized for instrument response. Necessary for the understanding of in-flight instrument response, all ion measurement functions and ion optical parameters were determined prior to launch. To enhance the characterization a newly developed floatable detector was used to test the influence of a post-acceleration voltage path after the ESEA. These parameters were then compared with the integrated system (entrance system/energy analyzer, TOF and electronic box). To prepare for the data reduction phase, I evaluated measurements from SOHO/CELIAS/MTOF. Studying the nickel/iron ratio in the solar wind, it can be concluded that nickel undergoes the same enrichment processes as other elements with low first ionization potential. With the recent launch of STEREO and PLASTIC commissioning, I present the first preliminary results of in-flight data.

# Contents

# Chapter 1

# Introduction

## 1.1 Solar physics

In this section a brief overview over solar physics is presented. For a deeper look at this topic I refer to the introductory book by M. Stix on the sun, [57] and to the book *Introduction to Space Physics*, edited by M.G. Kivelson and C.T. Russell, [40].

### 1.1.1 The Sun

Compared to other stars, the sun is a quite ordinary star, only about $5 \cdot 10^9$ years old. But nevertheless the sun with its mass $M_\odot$ of about $2 \cdot 10^{30}$ kg is important for us. Additionally, it is the most accessible for studies. Its radius is $r_\odot = 696000$ km and thus the mean density is $1.4 \cdot 10^3$ kg/m$^3$ (compared to $5.5 \cdot 10^3$kg/m$^3$ for the earth). The mean distance sun earth (1 astronomical unit, AU) is $1.5 \cdot 10^8$ km or 215 solar radii.

The sun is a massive ball of gas held together and compressed by its own gravitational attraction. The solar composition consists mainly of hydrogen (90 % of all atoms) and helium (10 %), other elements like carbon, nitrogen and oxygen compose only about 0.1 % of the solar mass and their abundance ratios are very roughly the same as on the earth. Our current knowledge of the composition of the sun and of the solar system bases on remote sensing measurements of the photosphere (see [4]), *in situ* measurements of the solar wind (various references, e.g. see [8]) and meteorite measurements (see [42]).

The sun consists of three layers below the atmosphere, the *core* (about $0.25 \cdot r_\odot$), the *radiative zone* (above the core to $0.75 \cdot r_\odot$) and the *convection zone*. The sun's atmosphere consists of three layers, too. The lowest is the *photosphere* which emits most of the solar light. The *chromosphere* is above the photosphere and on top of it lies the *corona*, extending out into the heliosphere (beyond the earth's orbit). For more details, see [57].

Observations show that the convective zone rotation depends on the latitudinal position, the equator rotates with a period of 26 days, whereas regions near the poles take 37 days to rotate. Contrary the core seems to rotate rigidly. Due to the different rotation periods, the convection zone changes its shape. Additionally, large temperature gradients cause convective instabilities, which result in the granulation covering the solar surface at the photosphere.

In the last decades the picture of the sun got several new facets. The influence of the solar magnetic field was investigated. Considering the number of sun spots, darker regions on the solar surface, a 11-years cycle can be found. Coinciding with this cycle is also the activity of the sun. This indicates a close relation between the number of sun spots and the solar activity, namely coronal mass ejections. Often the sun spots occur in pairs, a bipolar configuration with opposite magnetic fields. The magnetic orientation in these bipolar groups remains the same on each hemisphere. This magnetic orientation reverses from one solar cycle to the next. So in fact, considering the global solar magnetic field, the solar cycle would rather last 22 years.

On the surface of the sun a lot of structures can be distinguished, see Figure 1.1, a first picture of the STEREO/SECCHI imager instrument. There one sees coronal loops where plasma flows along magnetic
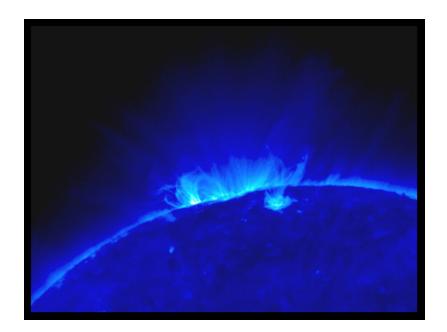
Figure 1.1: *A close up of loops in a magnetic active region. These loops, observed by STEREO's SECCHI/EUVI telescope, are at a million degrees K. This powerful active region, AR903, observed here on Dec. 4, 2006, produced a series of intense flares, particle storms, and coronal mass ejections over the next few days.*

field lines, dark filament regions, prominences, which actually belong to the chromosphere. They are colder than the surrounding corona and much denser. When they become unstable they can erupt revealing their true geometry as flux tubes with their bases in the chromosphere. Solar flares occur when flux tubes rise and their magnetic field lines reconnect below them. The reconnection releases a large amount of energy which accelerates the eruption. Large temporal disturbances of the corona are called Coronal Mass Ejections, see below.

### 1.1.2 Solar wind

The solar wind is a constant flow of ionized solar plasma resulting from the huge difference in gas pressure between the solar corona and the interstellar space. This pressure differences drives the plasma outwards despite the restraining influence of solar gravity. The idea of a solar wind occurred early in the 20th century when Chapman proposed a singly ionized particle beam from the sun. Later it was stated that the solar wind must be neutral, a plasma stream with the same amount of positively and negatively charged particles (see [10]). In the 1950s the existence of a solar wind was presumed on the basis of the evidence that small variations in the earth's magnetic field were produced by observed solar activity and also from theoretical models for the equilibrium state of the solar corona. In the mid 1960s it was first observed directly by space probes. The solar wind is significantly influenced by solar activity and transmits it to planets, comets, dust particles and cosmic rays, which are immersed in the solar wind. The influence on comets was pointed out by Biermann in 1951 [5].
The most extensive and detailed observations of the solar wind were made from spacecraft near the orbit of the earth. The solar wind is a hot and tenuous plasma gas, consisting mostly of ionized hydrogen (or of protons and electrons in nearly the same number), 96 %, and a small admixture of ionized helium, 3.9 % and still fewer ions of heavier elements. The density of ambient solar wind with a nearly radial flow speed of 440 km/s is about 6.6 $cm^{-3}$ at one astronomical unit, resulting in a flux density of approximately $3.0 \cdot 10^8$ $cm^{-2} \cdot s^{-1}$. Embedded in this plasma is a weak magnetic field ($7 \cdot 10^{-9}$ Tesla) oriented in a direction nearly parallel to the ecliptic plane (the plane of the earth's orbit around the sun) and approximately 45° to a line from the sun to the observer at 1 AU.
From the mentioned pressure difference between the solar corona an the interplanetary space it follows with mass and momentum conservation for a model solar wind speed regarding the restraining gravitational
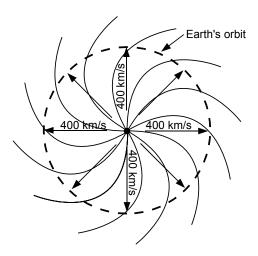
Figure 1.2: *Spiral interplanetary magnetic-field lines frozen into a radial solar wind expansion at 400 km/s. (Adapted from [52]).*

force:

$$u^2 - \frac{2kT}{m} - \frac{2kT}{m} \log\left(\frac{mu^2}{2kT}\right) = 8\frac{kT}{m} \log\left(\frac{r}{r_c}\right) + 2GM_\odot\left(\frac{1}{r} - \frac{1}{r_c}\right) \tag{1.1}$$

where $r_c = \frac{GM_\odot m}{4kT}$, $M_\odot$ is the solar mass, $T$ the coronal temperature and $m$ the sum of proton and electron mass, see [51] and [33]. Assuming a coronal temperature of $1 \cdot 10^6$ K the solar wind speed reaches 480 km/s at 1 AU. Magnetic field lines are frozen in the plasma flowing out. These field lines and the radial stream define a flux tube reaching out in the interplanetary space.

The sun rotates about an axis nearly perpendicular to the ecliptic plane, with a rotation rate varying with location and with latitude on a heliographic coordinate system. Successive parcels of plasma fluid move outwards from a fixed solar source at the base of such a flux tube. The source moves beneath it due to the solar rotation. So the actual trace of fluid parcels emitted from that source takes the shape of a spiral. Magnetic field lines frozen into the expanding plasma and their fixed source at the base of the corona are drawn into the same spiral configuration, see Figure 1.2.

The solar wind is a continuous flow from the sun and has to merge with an interstellar background that has a pressure of $\sim 10^{-13}$ Pa. Since the solar wind is supersonic[1] the influence of the (slower) interstellar matter cannot be felt within the supersonic region of the solar wind. In many supersonic flows it occurs the formation of a shock wave which abruptly slows the solar wind to a subsonic speed. After this shock the solar wind matter can gradually adjust to dynamic and pressure equilibrium. The spacecraft Voyager I passed on 16 December 2004 this *Termination Shock* which lies at about 100 AU, see [18].

The solar wind originating from the coronal holes, where open magnetic field lines propagate into the heliosphere, is faster than the ambient solar wind ($\sim 440$ km/s), usually above 600 km/s. The slow solar wind emerges from equatorial regions. The fast solar wind is usually very steady, the slow solar wind shows velocity variations and the origin is less well known than for the fast solar wind.

### 1.1.3 The Heliosphere

The heliosphere is the region where the sun and the solar wind dominates. Its size is still not known, but as mentioned above, the Termination Shock lies at about 100 AU. The Termination Shock is the boundary of the heliosphere, at which the solar wind is abruptly slowed down to 20 km/s. The sun and the heliosphere move with about 23 km/s in the interstellar space.

---

[1]The solar wind speed is larger than the speed of sound $c_s = \sqrt{\gamma p/\rho}$, where $\gamma$ is the ratio of the specific heat at constant pressure to the specific heat at constant volume, $p$ the pressure and $\rho$ the density. The speed of sound is the velocity at which information can be transmitted.
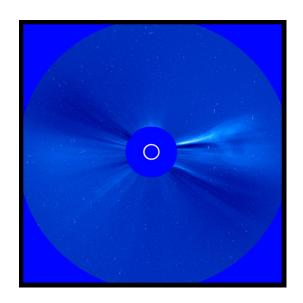
Figure 1.3: *The first coronal mass ejection (CME) observed by STEREO. This image was taken on Dec. 9, 2006 with STEREO's SECCHI/Cor2 coronagraph. The white circle shows the location of the solar disk. The mass ejection can be seen on the right hand side of the image as outward directed streak ending in a faint ring.*

### 1.1.4   Coronal Mass Ejections

A coronal mass ejections (CME) is an ejection of material from the corona. CMEs have a propagation speed between less than 100 km/s and up to 2000 km/s. Ejection masses are typically in the range of $10^{12}$ to $10^{13}$ kg. Near solar minimum activity they occur at a rate of $\sim 0.2$ events per day, near solar activity maximum the rate is $\sim 3.5$ events per day over the whole sun. Since not all CMEs can be detected by the coronagraphs, the rate might even be higher. CMEs often originate from prominences which explosively erupt from the chromosphere when the enclosing magnetic field lines reconnect. They represent the opening up to interplanetary space of previously closed coronal magnetic field lines.

 In [26] a overview over CMEs is presented. And in [12] a theoretical view on CMEs is given. Still CMEs are not yet well understood. That's where the STEREO mission with its 3D look on the sun, can bring new insight.

### 1.1.5   The FIP-effect

Comparing the distribution of chemical elements in the solar wind with the distribution in the photosphere, a notable deviation was found. Elements with a first ionization potential (FIP)[2] below 10 eV are enriched, relative to the elements with a higher FIP, compared to their photospheric abundance ratio, see Figure 1.4. Additionally, *in situ* measurements of the solar wind indicate that the low-FIP elements are enriched relative to hydrogen, too. The first observation of the relative enhancement of the low-FIP elements was made in the solar energetic particles (see review article by Meyer [46]). Later several observations supported the FIP-effect. Latest measurements are presented in Chapter 8 for nickel as a low-FIP element. The differentiation of the elements should take place in the chromosphere, since major chemical elements occur as neutrals in the photosphere, while those with lower FIP are partially ionized (see [19]). Between the photosphere, where the elements are mostly neutral, and the corona, where there is a fully ionized plasma, several recombination and ionization processes can occur. Many models were developed describing or explaining the fractionation processes in the chromosphere, see review article by P. Bochsler [8].

---

[2]First ionization potential: The amount of energy needed to remove completely the first electron from a neutral atom.
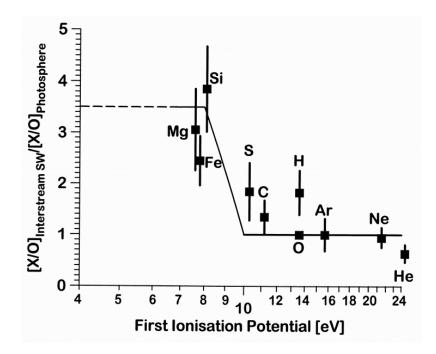
Figure 1.4: *Figure from [8]. Interstream solar wind abundances normalized with oxygen relative to photospheric abundances as given by [28]. The elements with a first ionization potential below 10 eV are enriched in the solar wind relative to those with a higher FIP.*

## 1.2 The STEREO Mission

### 1.2.1 Overview

The Solar-TErrestrial RElation Observatory is the third of five NASA Solar Terrestrial Probe (STP) missions of the international Sun-Earth connections program. The STEREO mission will offer a new perspective on solar eruptions by imaging coronal mass ejections (CME) and background events simultaneously from two nearly identical observatories on heliocentric orbits at 1 AU. The two STEREO spacecraft will continuously drift away from the Earth by $\sim 22°$/year, one ahead of the Earth (STEREO A), one behind (STEREO B). The primary scientific objective of the mission is to advance our understanding of the three-dimensional structure of the solar corona and of origin and the consequences of CMEs. The other scientific goals of the STEREO mission are:

- Characterization of CMEs through the heliosphere

- Discovering the mechanisms and sites of energetic particle acceleration in the low corona and the interplanetary medium

- Developing a 3-D-time-dependant model of the magnetic topology, temperature, density and velocity structure of ambient solar wind

### 1.2.2 Instruments on STEREO

There are four instrument packages on STEREO: SECCHI, IMPACT, S/WAVES and PLASTIC. Following they are summarized.

**SECCHI (Sun-Earth Connection Coronal and Heliospheric Investigation)**

Suite of remote-sensing instruments consisting of an extreme ultraviolet imager, two white-light coronagraphs, and a heliospheric imager. These instruments will study the 3-D evolution of CMEs from their origin at the Sun's surface through the corona and interplanetary medium to their eventual impact at Earth and beyond.

**IMPACT (*In situ* Measurements of PArticles and CME Transients)**

IMPACT provides measurements of solar wind electrons, interplanetary magnetic fields and solar energetic particles. It consists of seven instruments: a solar wind electron analyzer, a magnetometer and an array of particle detectors measuring the energetic ions and electrons accelerated in CME shocks and in solar flares.

**S/WAVES (STEREO/WAVES)**

S/WAVES is an interplanetary radio burst tracker which will trace the generation and evolution of traveling plasma disturbances from the Sun to Earths orbit. As a radio and plasma wave receiver, S/WAVES is both a remote-sensing and an *in situ* instrument.

**PLASTIC (PLAsma and SupraThermal Ion Composition Instrument)**

PLASTIC is described in the following section.

## 1.3 PLASTIC

The PLasma and SupraThermal Ion Composition (PLASTIC) sensor will measure *in situ* kinetic properties and charge states of solar wind ions and suprathermal ions in an energy range between 0.2 keV/e and 86 keV/e. It is a primary instrument on STEREO to investigate physical processes low in the corona and in the inner heliosphere.

### 1.3.1 Scientific objectives

The primary scientific goal of the STEREO mission is to study the origin, evolution and propagation of CMEs through the heliosphere. The contribution of CMEs to the heliospheric mass flux is modest. Nevertheless CMEs play an important role in heliospheric structure and processes.

Because for most of the particle populations ion acceleration takes place in low-density regions where interactions are rare, not enough photons are produced to allow measurements. To get information on the properties of energetic ion populations, they have to be studied *in situ*. Their element or charge state abundances often provide a unique signature of their own origin or reveal plasma properties (e.g., bulk velocity, kinetic temperature), which are not accessible otherwise. The elemental and charge state composition of minor ions in CME-related solar wind provides important signatures related to the coronal conditions at the solar wind acceleration site. The possibility to study *in situ* the individual charge states provides a diagnostic tool for the plasma parameters in the source region. These measurements give us in addition accurate information about ambient solar wind and energetic particles ahead of CMEs as well as plasma, magnetic field and energetic particles characteristics of interplanetary disturbances as they pass the spacecraft.

Information on the acceleration site can be deduced from elemental and charge state composition measured *in situ*.

To get all the relevant information we need to expand our knowledge of CMEs and acceleration processes we have to know the state of ambient solar wind before, during and after these disturbances.

### 1.3.2 Instrument overview

The PLASTIC instrument consists of three main components (see Figure 1.5):

- **Entrance System/Energy Analyzer (ESEA)**
  The ESEA consists of three different apertures, main channel (MC), S-channel (SC) and Wide-Angle Partition (WAP). They are followed by an electrostatic energy analyzer (ESA) which is the same for all apertures. In the entrance system the distinction of the different solar wind particles occurs (S-channel for protons and alpha particles, main channel for heavy, less abundant particles). This separation is realized with a collection of electrodes (SCO-L, SCO-U, SCI-L and SCI-U), that deflect the incident ions towards the ESA, whereas negative voltage is applied to SCO-L and SCI-U, the other two S-channel electrodes are grounded. See Figure 1.7 and Table 1.1 for an overview over the electrodes of the ESEA.

- **Time of Flight section (TOF)**
  The TOF is the part below the ESEA where the particles exiting the ESA first are accelerated towards a carbon foil producing secondary electrons when they pass the carbon foil. The ESEA is mounted on the structure which holds the carbon foils. At the bottom of the TOF section there is the detector board on which the particle detectors (micro-channel plates (MCP) and solid-state detectors (SSD)) are placed.

- **Electronic Box**
  The Electronic Box contains the operation and command electronics of the instrument. The power supplies provide the requested voltage to the instrument components (ESEA deflection electrode bias, post-acceleration (PAC) bias, and the voltage for all detector systems, e.g., MCP). Additionally, the electronic box contains all the commanding sub-systems and the electronics for data transfers to

and from the the processing units. A logic board performs the analog-to-digital conversion of the measured signals and ensures the data communication between the sub-systems and the classifier board. The classifier board processes the data further. The data is then communicated to and from the instrument data procession unit (IDPU), which is outside PLASTIC and is shared with the STEREO/IMPACT instruments.
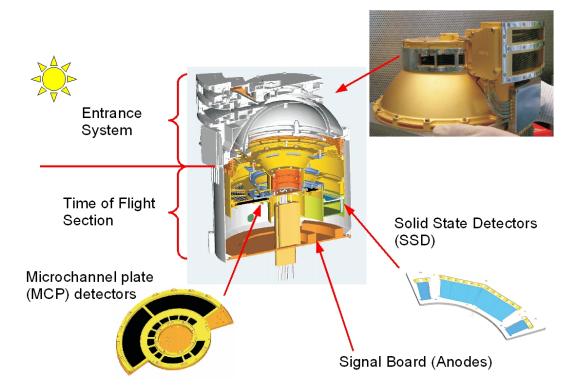
Figure 1.5: *The PLASTIC sensor with Entrance System/Energy Analyzer (ESEA) and the Time of Flight section (TOF). The electronic box is below the TOF. See text for details.*

**Entrance system/energy analyzer (ESEA)**

The ESEA has three different apertures:

**Solar Wind Sector S-channel (SC)** With the S-channel the distribution functions of solar wind protons and alpha particles are measured, providing density, velocity, kinetic temperature and its anisotropy. The geometric factor of the S-channel is small to prevent the detectors to saturate.

**Solar Wind Sector main channel (MC)** With the main channel the elemental composition, charge state distribution, kinetic temperature and velocity of some less abundant major solar wind ions (e.g., C, N, O, Ne, Mg, Si and Fe) are measured.

**Wide Angle Partition (WAP)** With the WAP the distribution functions of suprathermal ions and solar energetic particles from H through Fe are measured. The comparatively large geometric factor allows the study of relatively rare particles.

The measurement of the ion populations mentioned above represent a dynamic range of the order of $\sim 10^{10}$ (solar wind protons to suprathermal particles, see [45]). The solar wind composition is dominated by protons ($\sim 96\%$) and helium ($\sim 3.9\%$). The most abundant of the heavy ions ($Z > 2$) is oxygen. The ratio between hydrogen and oxygen is [O/H] $\sim 1/2000$, [63]. To prevent the detectors of fast aging the flux of hydrogen and helium on to the detectors must be reduced. This is achieved with two apertures with different geometric factors (S-channel for H and He with a smaller geometric factor, main channel for

heavy elements with a larger geometric factor). All particles in the solar wind flow at the same bulk speed (with differences less than the Alfvén speed, see [61]) so the particles with different $m/q$ can be identified by their different $E/q$ ratios, since $E/q = m/q \cdot \frac{v^2}{2}$. This selection takes place in the electrostatic analyzer (ESA) of PLASTIC. In most solar wind conditions the most abundant solar wind elements have different m/q than the less abundant ones (e.g. m/q = 1 for $H^+$ and m/q=2.67 for $O^{6+}$).

The real advantage of PLASTIC with its three different apertures and hence its large dynamic range is that it will be possible to measure the abundant particles (protons and alpha particles with 99.9 % abundance in the solar wind) and the heavy elements with the same detector. This is not the case in older missions (cf. SOHO/CELIAS [32], ACE/SWICS [22], ULYSSES/SWICS [23]). From other mission it is known that the detection efficiency changes during operation. Because in PLASTIC all solar wind particles are counted with the same set of detectors the detection efficiency degradation will be comparable for all particles counted with the Solar Wind Section (SWS) or can more easily compensated. So the elemental abundance ratios in the solar wind can be quoted related to hydrogen instead of oxygen or silicon.
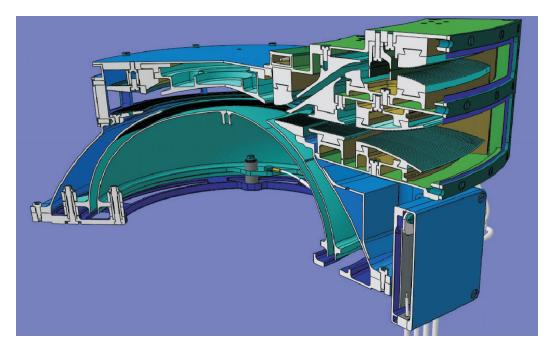


Figure 1.6: *Isometric view of the entrance system/energy analyzer of PLASTIC. On the right hand side is the solar wind section (SWS) with the two apertures S-channel (above) and main channel. Drawing J. Fischer.*
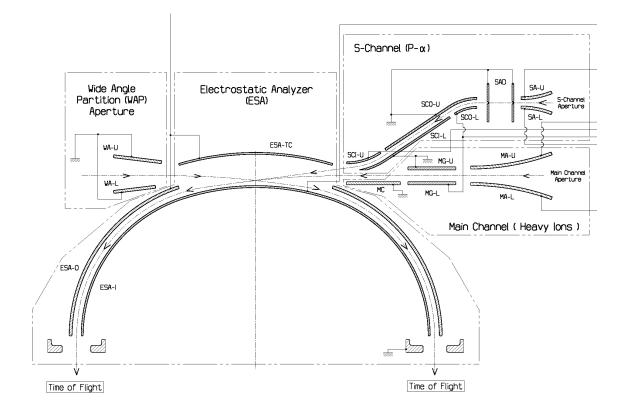
Figure 1.7: *PLASTIC ESEA electrodes. The abbreviations are explained in Table 1.1.*

| | | |
|---|---|---|
| SAD | : | S-channel Aperture Diaphragm |
| SA-L | : | S-channel Aperture Lower duckbill electrode |
| SA-U | : | S-channel Aperture Upper duckbill electrode |
| SCI-U | : | S-Channel Inner Upper electrode |
| SCI-L | : | S-Channel Inner Lower electrode |
| SCO-U | : | S-Channel Outer Upper electrode |
| SCO-L | : | S-Channel Outer Lower electrode |
| MA-L | : | Main channel Aperture Lower duckbill electrode |
| MA-U | : | Main channel Aperture Upper duckbill electrode |
| MG-L | : | Main channel Gate Lower electrode |
| MG-U | : | Main channel Gate Upper electrode |
| MC | : | Main Channel electrode |
| ESA-TC | : | ElectroStatic Analyzer Top-Cap electrode |
| ESA-I | : | ElectroStatic Analyzer Inner electrode |
| ESA-O | : | ElectroStatic Analyzer Outer electrode |
| WA-L | : | Wide Angle partition Lower electrode |
| WA-U | : | Wide Angle partition Upper electrode |

Table 1.1: *PLASTIC ESEA electrodes*

### 1.3.3 Functional design

In Figure 1.10 the measurement principle of PLASTIC is schematically shown. The entrance system/energy analyzer (ESEA) is on top of the figure. Below there is the post-acceleration region and the Time-of-Flight (TOF) section. At the bottom there are the particle detectors (Microchannel plates (MCP) and solid state detectors (SSD)). The ion trajectories are drawn in red, the start and stop electron trajectories in blue. Measured values and parameters are in green. A solar wind ion is fully characterized by its velocity, mass and charge. The scientific goals of PLASTIC require the separation of the dominant solar wind particles in $\mathbf{v}$, $m$ and $q$. This can be achieved with three measurements:

**(1) Energy per charge** The PLASTIC ESA steps through the $E/q$ range between 0.2 and 86 keV/e in 132 logarithmic steps ($\Delta V_{ESA} \approx 0.05 \cdot V_{ESA}$) The ESA has a fine $E/q$ resolution $\frac{\Delta E/q}{E/q} \approx 6\%$. This $E/q$ selection is the first measurement.

**(2) Time of flight** The ions with $E/q$ are accelerated by the post-acceleration voltage $V_{\mathrm{acc}}$ after the ESA. Their energy before entering the carbon foil is $E_{\mathrm{acc}} = q(E/q + V_{\mathrm{acc}})$. When passing through the carbon foil they loose part of their energy and leave the carbon foil with $E_{\mathrm{res}}$. Secondary electrons are produced on both sides of the carbon foil by the passing ions. The secondary electrons emitted on the exit side of the carbon foil are deflected and pulled towards the MCP at the bottom of the TOF section. They give the start signal of the time of flight measurement. When the ions hit the SSD at the end of the TOF section they produce secondary electrons, which trigger the stop signal. The length of the flight path is known and together with the time of flight $\tau$ of the ion the velocity can be calculated which is the second measurement.

**(3) Residual energy** The SSD at the end of the TOF section measures the residual energy of the ions. This gives the third measurement.

For each ion PLASTIC performs three measurements, $E/q$, $v$ and $E$ which allows to determine v, $m$ and $q$. The energy measurement is influenced by two processes: (1) The energy loss $E_{\mathrm{loss}} = E_{\mathrm{acc}} - E_{\mathrm{res}}$ is statistically distributed and (2) the SSD measures only part of the energy $E_{\mathrm{res}}$. From SSD calibration measurements the relation between measured energy $E_{\mathrm{SSD}}$ and $E_{\mathrm{res}}$ is known: $E_{\mathrm{SSD}} = \alpha_{\mathrm{SSD}}(E, m)E$

With the measured parameters ($E/q = k_{\mathrm{ESA}} \cdot V_{\mathrm{ESA}}$, $v$ and $E_{\mathrm{SSD}}$) the mass $m$ and mass per charge $m/q$ of each ion can be determined:

$$m = \frac{2E_{\mathrm{SSD}}}{\alpha_{\mathrm{SSD}}(E,m)}\left(\frac{\tau}{d}\right)^2 \tag{1.2}$$

$$m/q = 2(k_{\mathrm{ESA}}V_{\mathrm{ESA}} + V_{\mathrm{acc}} - E_{\mathrm{loss}}/q)\left(\frac{\tau}{d}\right)^2 \tag{1.3}$$

with $k_{ESA}$ Analyzer constant of the electrostatic energy analyzer (ESA) and $V_{\mathrm{ESA}}$ voltage of the energy analyzer (see Chapter 3), $V_{\mathrm{acc}}$ the acceleration voltage after the exit slit of the entrance system, $d$ distance carbon foil SSD detector and $\tau$ time of flight.

Solar wind particles enter PLASTIC through the Solar Wind Sector (SWS), see Figure 1.8. All three measurements are performed for these particles. The 45° SWS is centered on the Sun spacecraft line. All other sections, which are part of the WAP, are for suprathermal particles. Suprathermal particles entering the WAP in the two neighboring 12° sectors of the SWS and in one eight of the whole instrument are characterized like solar wind particles, $E/q$, $v$ and $E_{\mathrm{SSD}}$. In the other half of the sensor (the non-SSD sector of WAP) only $E/q$ and $v$ of the particles are measured giving $m/q$ of the suprathermal ions. One eighth of the WAP is blocked since particles cannot enter the ESA there due to spacecraft structures.

The PLASTIC instrument scans the energy per charge from 0.2 to 86.5 keV/e for the main channel and the WAP and up to 12 keV/e for the S-Channel allowing to measure alpha particles up to 1100 km/s and protons up to 1500 km/s. This allows to measure even high speed CMEs without saturating the SSD and MCP detectors of the TOF section.

In addition to the parameters named above, $v$, $E$, $m$ and $q$, for particles entering the Solar Wind Sector (SWS) also the out-of-ecliptic (elevation) and in-ecliptic (azimuthal) angles can be determined using either
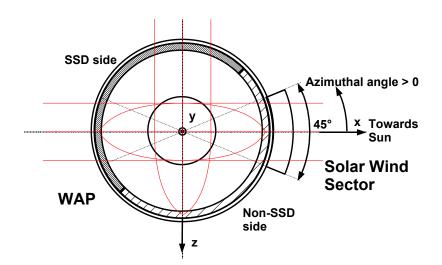
Figure 1.8: *Schematic top view of PLASTIC. The used coordinate system is oriented as follows: x-axis towards the sun, z-axis in earth orbit direction and y-axis parallel to the ecliptic north. x- and z-axis lie in the ecliptic plane. Trajectories (red lines) that enter the ESEA parallel, are focused on the same focus point. The azimuthal angle is anticlockwise in the x-z-plane, the y-axis is its turning axis. Ions entering PLASTIC through the Solar Wind Sector (SWS), are focused on the SSD side of the detector plane, allowing a triple coincidence measurement (Start signal, stop signal and energy measurement).*

the deflection plates (*Duck Bills, DB*) at the entrance of SC and MC (deflection plate voltage, out-of-ecliptic angle) or the position where the particle hits the detector (position measurement, in-ecliptic angle). During operation the deflection voltages are scanned so that the DB deflect particles entering from an out-of-ecliptic angle between -20 and +20 degree, accepting either 2 degree (main channel) or 0.2 degree (S-channel) for each of the 32 sweeping steps. Thus, we measure the full three-dimensional distribution of solar wind particles. All these measurements request that PLASTIC fulfills certain requirements which are summarized in Table 1.2.

| | Solar Wind Sector | | Wide Angle |
| | S-Channel | Main Channel | Partition |
|---|---|---|---|
| Measured Species | H, He | He - Fe | H - Fe |
| Energy Range [keV/e] | 0.2 - 15 | 0.2 - 100 | 0.2 - 100 |
| $\Delta E/E$ | 0.06 | 0.06 | 0.13 |
| Geometrical Factor per 22.5° sector [cm$^2$ · sr · keV/keV] | $3 \cdot 10^{-6}$ | $2.5 \cdot 10^{-4}$ | $2.2 \cdot 10^{-3}$ |
| Active Area [cm$^2$] | $\sim 10^{-3}$ | $\sim 1$ | – |
| Instantaneous Field-of-View | $45° \times 1.5°$ | $45° \times 2°$ | $315° \times \pm7°$ |
| Angular Resolution | $5° \times 1.5°$ | $5° \times 2°$ | $22.5° \times \pm7°$ |
| Total Field-of-View | $45° \times \pm20°$ | $45° \times \pm20°$ | $270° \times \pm7°$ |
| Time Resolution | $\sim 1$ min | $\sim 1$ min | $\sim 5$ min |

Table 1.2: *Goals for PLASTIC instrument.*
Instantaneous Field-of-View: *Accepted angular range for each sweeping step;* Total Field-of-View: *Total angular ranges in- and out-of-ecliptic when sweeping. See text for explanations.*

**Measurement procedure**

In operation the ESA voltage is changed to accept particles with $E/q$ from 86.5 keV/e towards 0.2 keV/e in 132 sweep steps (ESA sweep), every step with a 4.67% lower ESA voltage. In addition, for every energy step the voltage of the deflection plates is changed in 32 linear sweep steps (DB sweep) to deflect particles from $+20°$ to $-20°$. There are 4096 sweep steps in one minute, each step 12.8 milliseconds.

The main channel and the S-channel are never used simultaneously. When the flux in the TOF section exceeds a certain threshold (approximately 1000 counts/sec) the Instrument Data Processing Unit (IDPU) will switch in the next ESA step to the S-channel. Negative voltage is applied to the two S-channel electrodes SCO-L and SCI-U that the positive ions entering the S-channel aperture are deflected towards the ESA. To prevent particles from entering the main channel the the same voltage is applied to the MG-L electrode of the main channel as to the SCO-L electrode, see Figure 1.9. All particles entering the main channel aperture are then deflected. The suppression factor of the main channel gate is sufficient to ensure no influence on the count rates through the S-channel aperture. (See Section 3.7 for the gate functionality measurements.)

Meanwhile particles can enter through the WAP, whose acceptance is 270° in-ecliptic and up to $\pm7°$ out of ecliptic. The WAP sector has no deflection plates but a wider acceptance range out-of-ecliptic than the main and the S-channel.
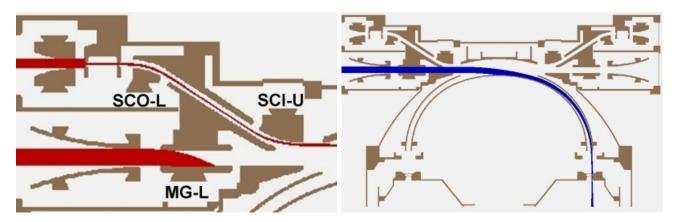


Figure 1.9: *3D SIMION simulations of the beam trajectories through the S-channel (left side) and main channel and ESA (right side). The positive ions passing through the S-channel are deflected by the two S-channel electrodes SCO-L and SCI-U towards the ESA. The ions simultaneously entering the main channel are deflected by the electrode MG-L. The same voltage is applied to SCO-L and MG-L.*

ESEA

WAP
suprathermals

Post-acceleration

TOF

Electronics

$E_{acc}$
$E_{res}$

$E_{acc}$
$E_{res}$

SSD
Energy

Start, Stop

Ions

Electrons

Post-acceleration $V_{acc}$

MCP

Position
Mapping

$E_{res}$
$E_{acc}$

$E_{acc}/q = E/q + V_{acc}$

$E_{res}/m$

Start Stop

$\tau$

$m/q$

$E, q, m$

Carbon foil

Time
of
flight
$\tau$

WA-U
WA-L

ESA-I
ESA-TC
Z
Main axis

Energy
analyzer
$E/q$

MC
ESA-O
MG-L
MG-U
SCI-U
SCI-L
SCO-U
SCO-L
MA-L
MA-U
SAD
SA-L
SA-U

$y$

S-channel
protons, alphas

Main channel
heavy ions

$x$
Towards Sun

Elevation
angle
$\pm 20°$

Figure 1.10: *Schematic view of PLASTIC. Figure adapted from [2]. The entrance system/energy analyzer (ESEA) is followed by a post-acceleration region and a time-of-flight section (TOF). The aperture on the right side is the Solar Wind Sector (SWS) consisting of the S-channel (SC) (for protons and alpha particles) and the main channel (MC) (for ions with Z > 2). The SWS covers only 45° the rest is covered by the Wide Angel Partition (WAP) which is designed for suprathermal and pick-up ions. The x − z plane lies in the ecliptic (azimuthal angle), the x−axis pointing towards the Sun, the y−axis towards north and z is perpendicular to x and y pointing towards east. The out-of-ecliptic angle (elevation angle) is positive above the ecliptic, the azimuthal angle is positive towards west.*

### 1.3.4 Calibration of PLASTIC

Like the PLASTIC instruments (Laboratory prototype, Engineering Qualified Model (EQM), Flight Models 1, 2 and Flight Spare (FM1, FM2 and FS)) consists of different parts also the calibration process was divided:

**Design of the entrance system/energy analyzer (ESEA)** The ESEA was designed at University of Bern (UBe). The laboratory prototype was produced at the workshop of the University of Bern, see [2]. The EQM and the flight models (FM1,FM2 and FS) were produced by Contraves Space AG, Zürich.

**Ion optical calibration of ESEA** The ion optical calibration of the ESEA models was done in Bern (For LP, EQM see [2] and [7]; for FM1, FM2 and FS see Chapter 3.

**Thermal tests of ESEA** Performed at University of Bern by Martin Sigrist and Beat Zahnd.

**Partial discharge test of ESEA** Performed at University of Bern by Jürg Jost.

**UV suppression measurements of ESEA** The UV suppression tests were performed in the MEFISTO ion optical facility at the University of Bern [43]. For the measurements see [49].

**MCP detectors** The MCP detector boards were tested in Bern, [6].

**SSD detectors** The SSD detector were calibrated in MEFISTO, [15] and [6].

**Carbon foils** The carbon foils were calibrated in Bern, [2] and [3].

**Time of flight section** The TOF section was designed and built at the University of New Hampshire (UNH).

**Electronic box** The electronic box was built at the University of New Hampshire.

**Integrated instrument** The instruments were integrated at the University of New Hampshire. Calibration measurements with integrated FM1, IFM1, and integrated FM2, IFM2, were performed at UNH and at UBe, see Chapter 6.

### 1.3.5 Integrated PLASTIC onboard STEREO

The two flight models FM1 and FM2 were selected for flight. The integrated FM1 is onboard the ahead spacecraft STEREO A, called PLASTIC FMA. The integrated FM2 is onboard the behind spacecraft STEREO B, called PLASTIC FMB.

## 1.4   Overview over this work

The main topic of this work is the ion optical calibration of the PLASTIC sensor on STEREO, since the knowledge of all ion optical parameters and ion measurement functions is important for later data reduction of the in-flight data. Before I discuss the ion optical calibration, I present a first-order numerical simulation of trajectories in electrostatic analyzers. The following chapters cover the ion optical calibration of PLASTIC in three steps. In the first chapter I look at the entrance system/energy analyzer that was designed at the University of Bern. In the following chapter I discuss a novel floatable detection system, which was used during ion optical calibrations with post-acceleration, discussed in the fifth chapter. There the time of flight section is added, proceeding towards the integrated instrument. And finally calibration measurements with the integrated instruments are presented. To conclude the part about PLASTIC, first flight data from the STEREO mission are shown. To prepare for the data phase of STEREO, I evaluated data from SOHO/CELIAS/MTOF to determine the nickel/iron ratio in the solar wind. This is reported in Chapter 8.

This work is embedded in the complete calibration process of all PLASTIC subsystems, which is described above. Similar processes were necessary for previous space mission instruments like SOHO/CELIAS [32] or ACE/SWICS [22], which were also partly performed at the University of Bern.

# Chapter 2

# Instrument simulations

## 2.1  Electrostatic Analyzers

As seen in the previous chapter about the PLASTIC instrument, the energy per charge selection is performed in an electrostatic analyzer (ESA), that is part of the entrance system/energy analyzer (ESEA). Electrostatic analyzers (ESA) are widely used to select particles by their energy per charge $E/q$, e.g., the electrostatic analyzer described by Carlson, [9]. They used an ESA similar to the ESA in PLASTIC. In this chapter a first-order numerical simulation of a spherical electrostatic analyzer is described.

In [59] Vasyliunas also analyzed the characteristics of electrostatic analyzers, and how to describe their geometric capabilities. Another study is presented in [27]. All studies looked at ESAs where the particle trajectories is in the equatorial plane, where the electric field does not have an azimuthal component. Whereas the electric field in the S-channel of PLASTIC has an azimuthal component and therefore, it is not easy to calculate, [2]. Since the energy analyzer of PLASTIC is a toroidal electrostatic analyzer, the next paragraph gives a brief overview over the main characteristics of such an ESA.

### 2.1.1  Toroidal electrostatic analyzers

H. Wollnik described the electric potential in a toroidal ESA with a power series expansion, see [65], [64], [66]. In 1967 Theodoridis and Paolini presented an analytic expression of the electrostatic potential and the geometric parameters of an ESA, see [50], [58]. But they did not show measurements. Measurements and simulations are shown in [70] and [71], where an ESA similar to PLASTIC is presented. As mentioned above, the AMPTE energy analyzer, discussed in [9], is a predecessor of the PLASTIC entrance system/energy analyzer.

In Figure 2.1, trajectories through a spherical symmetric ESA are shown. Parallel incident particles of same energy are focused in one point after 90 degree. ESAs have a $E/q$ acceptance bandwidth where parallel incident particles can pass through the ESA hemisphere. This bandwidth defines in addition the transmission.

## 2.2  Two dimensional model of a spherical Electrostatic Energy Analyzer

### 2.2.1  Motivation

The aim of this section is to give a simple model of a spherical energy analyzer which can be compared with the actual design of the PLASTIC entrance system/energy analyzer (ESEA). At the beginning a first order approximation of the ion trajectories is presented and thereafter the potential and the electric field in a spherical and a cylindrical energy analyzer, derived from the first calculations. As F. Allegrini showed in his PhD thesis [2], the S-channel geometry cannot easily be represented mathematically since the trajectories through the S-channel are not in the equatorial plane as they are for a toroidal electrostatic
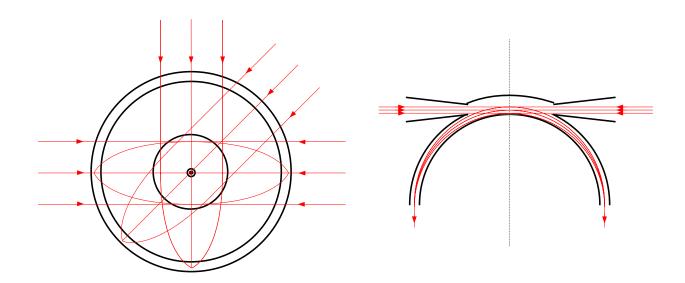
Figure 2.1: *Toroidal electrostatic energy analyzer.* Left: *Top view of the trajectories through an spherical ESA.* Right: *Side view of the trajectories. Parallel incident particles of same energy per charge are focused in one point after 90 deg.*
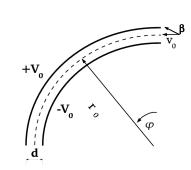
energy analyzer, like in PLASTIC. Therefore, I do not write about trajectories in the S-channel, but refer to F. Allegrini's Ph.D. thesis.

## 2.2.2  First order approximation of ion trajectories

The derivation of a first order approximation for ion trajectories in an spherical electrostatic analyzer (ESA) is presented in this section. Only small variations of a trajectory on a circle are considered. In the calculations made here only first order terms are considered, allowing to replace $\sin \beta$ with $\beta$ for small $\beta$ and neglecting quadratic terms. The basic idea of the following calculation is similar to the calculation made by Wollnik in [65]. From the Lagrange equation, Equation (2.5), the deviation from the paraxial way through a spherical ESA is calculated.

**Variables:**

| | | |
|---|---|---|
| radius of the sphere: | $r_0$ | |
| radial coordinate: | $r = r(t) = r_0(1 + \epsilon(t))$ | |
| angle: | $\varphi = \varphi(t)$ | |
| voltage: | $V = V(r)$ | |
| electric field: | $E(r) = -\frac{dV}{dr}$ | |
| nominal velocity: | $v_0$ | |
| nominal kinetic energy: | $T_0 = \frac{1}{2}mv_0^2$ | |
| nominal angular velocity : | $\omega_0 = \frac{v_0}{r_0}$ | |
| initial velocity: | $v_s$ | |
| initial kinetic energy for $r = r_0$: | $T = T_0(1 + \delta)$ | |
| elevation angle at $t = 0$: | $\beta$ | |
| azimuthal angle at $t = 0$: | $\alpha$ | |
| width of capacitor: | $d$ | |

**The Lagrange function for ions in an ESA:**

Electric field on position $r$:

$$E(r) = -E_0 \frac{r_0^2}{r^2} \tag{2.1}$$

Force on a charged particle with $r_0$ and $v_0$:

$$F = qE_0 = m\frac{v_0^2}{r_0} \tag{2.2}$$

From (2.1) and (2.2) it follows for the Potential $U$ and the kinetic energy $T$:

$$U(r) = -mv_0^2\left(\frac{r_0}{r} - 1\right) \tag{2.3}$$

$$T(\dot{r}, \dot{\varphi}) = \frac{1}{2}m(\dot{r}^2 + r^2\dot{\varphi}^2) \tag{2.4}$$

where $r \cdot \varphi$ is the azimuthal component of the velocity.
The Lagrange function:

$$L = T - U = \frac{1}{2}m(\dot{r}^2 + r^2\dot{\varphi}^2) + mv_0^2\left(\frac{r_0}{r} - 1\right) \tag{2.5}$$

**Solution of the Lagrange equation:**

The Lagrange Equation $\frac{\partial L}{\partial q} = \frac{\mathrm{d}}{\mathrm{d}t}\frac{\partial L}{\partial \dot{q}}$ for each coordinate:

$$mr\dot{\varphi}^2 - mv_0^2\frac{r_0}{r^2} = \frac{\mathrm{d}}{\mathrm{d}t}m\dot{r} = m\ddot{r} \tag{2.6}$$

$$0 = \frac{\mathrm{d}}{\mathrm{d}t}(mr^2\dot{\varphi}) \tag{2.7}$$

$$\Rightarrow mr^2\dot{\varphi} = \text{constant} = mr^2\dot{\varphi}|_{t=0}$$

And with $v_s \cos\beta \cos\alpha = r(0)\dot{\varphi}(0)$ it follows for $\dot{\varphi}$:

$$\dot{\varphi} = \frac{r(0)v_s \cos\beta \cos\alpha}{r(t)^2} = \frac{r_0(1+\varepsilon_0)v_s \cos\beta \cos\alpha}{r_0^2(1+\varepsilon)^2} \tag{2.8}$$

Outside the ESA there are fringe fields. But in this calculation the electric field is 0 outside the ESA, inside the electric field is not 0. So there is a potential jump at the boundary. For the kinetic energy of a particle with $T$ it follows ($T \to T - U(0)$):

$$
\begin{aligned}
T = T_0(1+\delta) &= \frac{1}{2}mv_0^2(1+\delta) \\
&= \frac{1}{2}mv_s^2 - mv_0^2\left(\frac{r_0}{r(0)} - 1\right)
\end{aligned}
\tag{2.9}
$$

$$
\begin{aligned}
\Rightarrow v_s^2 = 2v_0^2\left(\frac{1}{1+\varepsilon_0} - 1\right) + v_0^2(1+\delta) &\simeq 2v_0^2(1-\varepsilon_0 - 1) + v_0^2(1+\delta) \\
&= v_0^2(1 + \delta - 2\varepsilon_0) \\
\Rightarrow v_s \simeq v_0(1 + \delta - 2\varepsilon_0)^{1/2} &= v_0\left(1 + \frac{1}{2}\delta - \varepsilon_0\right)
\end{aligned}
\tag{2.10}
$$

With (2.8) and (2.10):

$$
\begin{aligned}
\dot{\varphi}(t) &\simeq = \frac{r_0(1+\varepsilon_0)v_0(1 + \frac{1}{2}\delta - \varepsilon_0)\cos\alpha \cos\beta}{r_0^2(1+\varepsilon)^2} \\
&\simeq \frac{v_0}{r_0(1+\varepsilon)^2}\left(1 + \frac{1}{2}\delta\right)\cos\alpha \cos\beta
\end{aligned}
\tag{2.11}
$$

Now with (2.6) and(2.11):

$$
\begin{aligned}
\ddot{r} &= r\dot{\varphi}^2 - \frac{v_0^2}{r_0(1+\varepsilon)^2} \\
&\simeq r_0(1+\varepsilon)\frac{v_0^2(1+\frac{1}{2}\delta)^2}{r_0^2(1+\varepsilon)^4}\cos^2\alpha\cos^2\beta - \frac{v_0^2}{r_0}(1+\varepsilon)^{-2} \\
&= \frac{v_0^2(1+\frac{1}{2}\delta)^2}{r_0(1+\varepsilon)^3}\cos^2\alpha\cos^2\beta - \frac{v_0^2}{r_0}(1+\varepsilon)^{-2} \qquad (2.12) \\
\Rightarrow \ddot{\varepsilon} &= \frac{v_0^2}{r_0^2}(1+\frac{1}{2}\delta)^2(1+\varepsilon)^{-3}\cos^2\alpha\cos^2\beta - \frac{v_0^2}{r_0}(1+\varepsilon)^{-2} \\
&\simeq \omega_0^2(1+\delta)(1-3\varepsilon) - \omega_0^2(1-2\varepsilon) \simeq \omega_0^2(\delta-\varepsilon) \\
\Rightarrow \ddot{\varepsilon}+\omega_0^2\varepsilon-\omega_0^2\delta &= 0 \qquad\qquad\qquad\qquad\qquad\qquad\qquad\qquad\qquad\qquad (2.13)
\end{aligned}
$$

The solution and initial conditions for (2.13) are:

$$
\begin{aligned}
\varepsilon(t) &= A\cos(\omega_0 t)+B\sin(\omega_0 t)+C \\
&= A\cos(\omega_0 t)+B\sin(\omega_0 t)+\delta \qquad\qquad\qquad\qquad\qquad (2.14) \\
\text{with } \varepsilon(0) &= \varepsilon_0 = A+\delta \qquad\qquad\qquad\qquad\qquad\qquad\qquad\qquad\qquad (2.15) \\
\text{and } r_0\dot{\varepsilon}(0) &= r_0\omega_0 B = v_s\sin\beta \simeq v_0(1+\frac{1}{2}\delta-\varepsilon_0)\beta \simeq v_0\beta \qquad (2.16) \\
\Rightarrow \varepsilon(t) &= (\varepsilon_0-\delta)\cos(\omega_0 t)+\beta\sin(\omega_0 t)+\delta \qquad\qquad\qquad (2.17)
\end{aligned}
$$

And with $\varphi \simeq \omega_0 t$:

$$
\varepsilon(\varphi) = (\varepsilon_0-\delta)\cos(\varphi)+\beta\sin(\varphi)+\delta \qquad\qquad\qquad\qquad (2.18)
$$

### 2.2.3 Instrument simulations using first order approximation

From Equation 2.18 conditions can be derived for which the ions with $\varepsilon_0$, the initial position, with a given elevation angle $\beta_0$ and with a given energy $U = U_0(1+\delta)$ can pass the ESA. Now the transmission dependent on the energy/charge and on the initial angle is discussed.

**Energy and angle acceptance**

From Equation (2.18) the condition follows for which the ions can pass the ESA: $|\varepsilon(\varphi)| \leq d/2r_0$ for all $\varphi \in [0°, 90°]$. The maximum $\varepsilon$ is given by $\frac{d\varepsilon}{d\varphi} = 0$: $\varphi_{\max} = tan^{-1}(\frac{\beta_0}{\varepsilon_0-\delta})$. This gives:

$$
|(\varepsilon_0-\delta)\ \cos(\varphi_{\max})+\beta\sin(\varphi_{\max})+\delta| \leq d/2r_0, \qquad\qquad (2.19)
$$

where $\varphi_{\max} = tan^{-1}(\frac{\beta_0}{\varepsilon_0-\delta})$.

Using Eq. (2.19) the energy acceptance for a given angular distribution or the angle acceptance for a given energy distribution can be simulated, see Fig. 2.2. In this simulation the angle or the energy respectively are normally distributed with a variance of 0.1 deg (angular distribution) or $0.001 \times E/q_{\text{nominal}}$ (energy distribution) which is similar to the beam used in the CASYMS ion beam facility. The dimensions of the analyzer are $r_0 = 61$ mm and $d = 4$ mm.

From the simulations presented in Fig. 2.2 the full width half maximum (FWHM) of the angle scan is $\approx 3$ deg and the FWHM of the energy scan is $\approx 6\%$ of the nominal energy.

When plotting the transmission depending on the energy and the angle with the beam conditions discussed above we get Fig. 2.3.
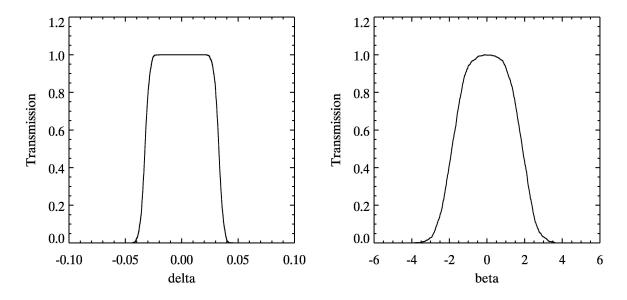
Figure 2.2: *Simulated energy and elevation angle (degrees) scans for particles with energy $U = U_0(1 + \delta)$. The incident angle $\beta$ was normally distributed in this simulation.*
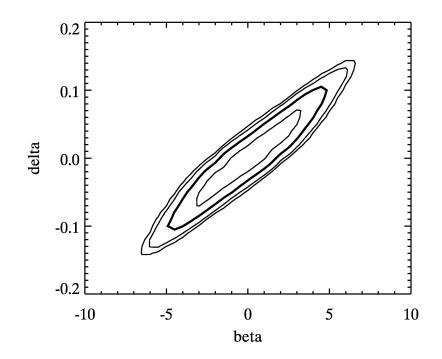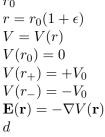


Figure 2.3: *Simulated transmission dependent on energy delta and elevation angle beta (deg). The simulated beam is a delta distribution beam in angle and energy, like the ion beam provided in CASYMS ion beam facility. The contour lines are 10%, 20%, **50%** and 90% from maximum transmission.*
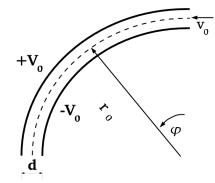
### 2.2.4 Potential and electric field in a spherical electrostatic energy analyzer

In this paragraph the potential and the electric field in a spherical energy analyzer are derived from conditions as for the PLASTIC energy analyzer. Since the PLASTIC ESA is not a spherical ESA but rather a compound system of two spherical ESAs, the potential and the electric field calculated here is only a estimation.

**Variables:**

| | |
|---|---|
| radius of the sphere: | $r_0$ |
| radial coordinate: | $r = r_0(1 + \epsilon)$ |
| voltage: | $V = V(r)$ |
| voltage for $r = r_0$: | $V(r_0) = 0$ |
| voltage for $r = r_+$: | $V(r_+) = +V_0$ |
| voltage for $r = r_-$: | $V(r_-) = -V_0$ |
| electric field: | $\mathbf{E}(\mathbf{r}) = -\nabla V(\mathbf{r})$ |
| width of capacitor: | $d$ |
| angle: | $\varphi$ |

**Conditions for potential $V$:**

| | |
|---|---|
| **Laplace equation:** | $\nabla^2 V = \triangle V = \frac{1}{r^2}\frac{\partial}{\partial r}\left(r^2\frac{\partial V}{\partial r}\right) = 0$ |
| Voltage for $r = r_0$: | $V(r_0) = 0$ |
| Voltage for $r = r_+$: | $V(r_+) = +V_0$ |
| Voltage for $r = r_-$: | $V(r_-) = -V_0$ |
| Distance $d$: | $d = r_+ - r_-$ |

| | |
|---|---|
| **Ansatz:** | $V(r) = -V_m\left(\frac{r_0}{r} - 1\right)$ with $V_m = \lim_{r\to\infty} V(r)$ and |
| | $\nabla^2 V = \frac{1}{r^2}\frac{\partial}{\partial r}\left(r^2 V_m\frac{r_0}{r^2}\right) = 0$ |

**Expressions for $V$ and $E$:**

$$V(r_+) = V_0 = -V_m\left(\frac{r_0}{r_+} - 1\right) \tag{2.20}$$

$$\Rightarrow r_+ = \frac{r_0}{1 - V_0/V_m} \tag{2.21}$$

$$\text{similar}: \quad r_- = \frac{r_0}{1 + V_0/V_m} \tag{2.22}$$

$$r_+ - r_- = r_0\left(\frac{1}{1 - V_0/V_m} - \frac{1}{1 + V_0/V_m}\right) = r_0\left(\frac{2V_0/V_m}{1 - (V_0/V_m)^2}\right) = d \tag{2.23}$$

$$\Rightarrow V_m = V_0\left(\frac{r_0}{d} + \sqrt{(\frac{r_0}{d})^2 + 1}\right) = V_0\frac{r_0}{d}\left(1 + \sqrt{1 + (\frac{d}{r_0})^2}\right) \tag{2.24}$$

$$\Rightarrow r_+ = \frac{r_0}{1 - V_0/V_m} = r_0\frac{1 + \sqrt{1 + (\frac{d}{r_0})^2}}{1 + \sqrt{1 + (\frac{d}{r_0})^2} - \frac{d}{r_0}} \tag{2.25}$$

$$r_- = \frac{r_0}{1 + V_0/V_m} = r_0\frac{1 + \sqrt{1 + (\frac{d}{r_0})^2}}{1 + \sqrt{1 + (\frac{d}{r_0})^2} + \frac{d}{r_0}} \tag{2.26}$$

For V and E follows :

$$V(r) = -V_m\left(\frac{r_0}{r} - 1\right) = -V_0\frac{r_0}{d}\left(1 + \sqrt{1 + (\frac{d}{r_0})^2}\right)\left(\frac{r_0}{r} - 1\right) \tag{2.27}$$

$$E(r) \;=\; -\nabla V(r) = -\frac{\partial V}{\partial r} = -V_0 \frac{r_0}{d}\left(1 + \sqrt{1 + (\tfrac{d}{r_0})^2}\right)\left(\frac{r_0}{r^2}\right) \tag{2.28}$$

### 2.2.5  Derivation of analyzer constant $k_{ESA}$ of a spherical ESA

**Analyzer constant $k_{ESA}$:**  $k_{ESA} = \frac{E/q}{\Delta V} = \frac{E/q}{2V_0}$

$$V(r) \;=\; -V_0 \frac{r_0}{d}\left(1 + \sqrt{1 + (\tfrac{d}{r_0})^2}\right)\left(\frac{r_0}{r} - 1\right) \tag{2.29}$$

$$E(r) \;=\; -V_0 \frac{r_0}{d}\left(1 + \sqrt{1 + (\tfrac{d}{r_0})^2}\right)\left(\frac{r_0}{r^2}\right) \tag{2.30}$$

$$\frac{m v_0^2}{r_0} \;=\; F(r_0) = qE(r_0) \tag{2.31}$$

$$v_0^2 \;=\; \frac{2E/q}{m/q} \tag{2.32}$$

$$\Rightarrow 2E/q \;=\; E(r_0)r_0 = V_0\frac{r_0}{d}\left(1 + \sqrt{1 + (\tfrac{d}{r_0})^2}\right)\left(\frac{r_0^2}{r_0^2}\right) \tag{2.33}$$

$$\Rightarrow \frac{E/q}{2V_0} \;=\; k_{ESA} = \frac{r_0}{4d}\left(1 + \sqrt{1 + (\tfrac{d}{r_0})^2}\right) \tag{2.34}$$

And with $d = 4.0$ mm and $r_0 = 61.0$ mm follows:

$$k_{ESA} = 7.63$$

and for $r_0 = 67$ mm:
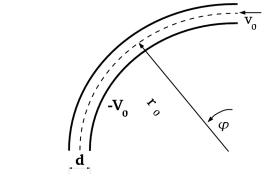
$$k_{ESA} = 8.38$$

### 2.2.6  Potential and E-field in a cylindrical capacitor

I present here the potential and the electric field of a cylindrically shaped energy analyzer. It must be mentioned that the S-channel electrodes are not cylindrically shaped. But this approximation is sufficient for a first estimation of the S-channel electrode constants.

**Variables:**

| | |
|---|---|
| radius of the sphere: | $r_0$ |
| radial coordinate: | $r = r_0(1 + \epsilon)$ |
| voltage: | $V = V(r)$ |
| Voltage for $r = r_+$: | $V(r_+) = 0$ |
| Voltage for $r = r_-$: | $V(r_-) = -V_0$ |
| electric field: | $\mathbf{E}(\mathbf{r}) = -\nabla V(\mathbf{r})$ |
| width of capacitor: | $d$ |
| angle: | $\varphi$ |



**Conditions for potential $V$:**

| | |
|---|---|
| **Laplace equation:** | $\nabla^2 V = \triangle V = \frac{1}{r}\frac{\partial}{\partial r}\left(r\frac{\partial V}{\partial r}\right) = 0$ |
| Voltage for $r = r_0$: | $V(r_0) = -\frac{1}{2}V_0$ |
| Voltage for $r = r_+$: | $V(r_+) = 0$ |
| Voltage for $r = r_-$: | $V(r_-) = -V_0$ |
| Distance $d$: | $d = r_+ - r_-$ |

| | |
|---|---|
| **Ansatz:** | $V(r) = A\log r + B$, (private communication P. Bochsler, 2007) |
| | $\nabla^2 V = \frac{1}{r}\frac{\partial}{\partial r}\left(r V_m \frac{1}{r}\right) = 0$ |

**Expressions for $V$ and $E$:**

$$V(r_0) = -\frac{V_0}{2} = A \log r_0 + B \tag{2.35}$$

$$V(r_+) = 0 = A \log r_+ + B \tag{2.36}$$

$$V(r_-) = -V_0 = A \log r_- + B \tag{2.37}$$

$$\Rightarrow \frac{V_0}{2} = V(r_+) - V(r_0) = A \log\left(\frac{r_+}{r_0}\right) \tag{2.38}$$

$$\Rightarrow A = \frac{V_0}{2 \log\left(\frac{r_\pm}{r_0}\right)} \text{ and} \tag{2.39}$$

$$B = -\frac{V_0}{2} \frac{\log r_+}{\log\left(\frac{r_\pm}{r_0}\right)} \tag{2.40}$$

For V and E follows :

$$V(r) = \frac{V_0}{2 \log\left(\frac{r_\pm}{r_0}\right)} \log\left(\frac{r}{r_+}\right) \tag{2.41}$$

$$E(r) = -\nabla V(r) = -\frac{\partial V}{\partial r} = -\frac{V_0}{2 \log\left(\frac{r_\pm}{r_0}\right)} \frac{1}{r} \tag{2.42}$$

Replacing $r_+$ :

$$V(r_-) = -V_0 = \frac{V_0}{2 \log\left(\frac{r_\pm}{r_0}\right)} \log\left(\frac{r_-}{r_+}\right) \text{ and } r_+ = r_- + d \tag{2.43}$$

$$\log\left(\frac{d + r_-}{r_0}\right) = -\frac{1}{2} \log\left(\frac{r_-}{d + r_-}\right) = \frac{1}{2} \log\left(\frac{d + r_-}{r_-}\right) \tag{2.44}$$

$$\Rightarrow r_-^2 + dr_- - r_0^2 = 0 \tag{2.45}$$

$$\Rightarrow r_- = -\frac{d}{2} \pm \sqrt{\frac{d^2}{4} + r_0^2} \tag{2.46}$$

$$\Rightarrow r_- = \sqrt{\frac{d^2}{4} + r_0^2} - \frac{d}{2} \text{ and} \tag{2.47}$$

$$r_+ = \sqrt{\frac{d^2}{4} + r_0^2} + \frac{d}{2} \tag{2.48}$$

### 2.2.7 Derivation of analyzer constant $k_{ESA}$ of a cylindrical electrostatic energy analyzer (ESA)

**Analyzer constant $k_{ESA}$:** $k_{ESA} = \frac{E/q}{\Delta V} = \frac{E/q}{V_0}$

$$E(r) = \frac{V_0}{2 \log\left(\frac{r_\pm}{r_0}\right)} \frac{1}{r} = \frac{V_0}{2 \log\left(\frac{\sqrt{\frac{d^2}{4} + r_0^2} + \frac{d}{2}}{r_0}\right)} \frac{1}{r} \tag{2.49}$$

$$\frac{mv_0^2}{r_0} = F(r_0) = qE(r_0) \tag{2.50}$$

$$v_0^2 = \frac{2E/q}{m/q} \tag{2.51}$$

$$\Rightarrow 2E/q = E(r_0)r_0 = \frac{V_0}{2 \log\left(\frac{\sqrt{\frac{d^2}{4} + r_0^2} + \frac{d}{2}}{r_0}\right)} \frac{r_0}{r_0} \tag{2.52}$$

$$\Rightarrow \frac{E/q}{V_0} = k_{ESA} = \frac{1}{2} \frac{1}{2 \log\left(\frac{\sqrt{\frac{d^2}{4} + r_0^2} + \frac{d}{2}}{r_0}\right)} = \frac{1}{4} \frac{1}{\log\left(\frac{\sqrt{\frac{d^2}{4} + r_0^2} + \frac{d}{2}}{r_0}\right)} \tag{2.53}$$

For the two S-Channel Electrodes SCO-L and SCI-U follows:

- SCO-L, $d = 3.0$ mm and $r_0 = 18.5$ mm:

$$k_{SCO-L} = 3.09$$

- SCI-U, $d = 4.0$ mm and $r_0 = 27.5$ mm:

$$k_{SCO-L} = 3.44$$

### 2.2.8 Conclusions

The numerical simulations discussed above give a simplified picture of the instrument parameters of PLASTIC as a first estimation. In Table 2.1 the instrument parameters calculated above are summarized. For a more precise simulation of the PLASTIC ESEA the numerical analysis mentioned in this section is not sufficient. Rather a numerical simulations has to be performed. For PLASTIC, a thorough simulation with the ion optics simulation program SIMION, see [14], was done, which is extensively discussed by F. Allegrini in [2]. SIMION allows to model problems with 2D symmetrical or 3D asymmetrical electrostatic potential arrays. The geometry can either be programmed directly in SIMION or alternatively defined in text files with commands that are read by SIMION. In SIMION the geometry of the electrodes are defined by potential arrays. The electrostatic potential outside of electrodes are determined solving the Laplace equation by finite difference methods.

Together with this simulations we have a theoretical prediction for the parameters measured during the calibration campaign discussed later in Chapter 3.

| | |
|---|---|
| Angular acceptance (deg) | $\approx 3$ |
| Energy/charge acceptance (relative) | $\approx 0.06$ |
| Analyzer constant ESA $k_{\text{ESA}}$ (eV/e V) | $\approx 8.2$ |
| Analyzer constant SCO-L $k_{\text{SCO−L}}$ (eV/e V) | 3.09 |
| Analyzer constant SCI-U $k_{\text{SCI−U}}$ (eV/e V) | 3.44 |

Table 2.1: *Instrument functions from simulations. For the S-channel electrodes SCO-L and SCI-U the calculated analyzer constants are only a rough estimation due to the reasons named above about the shape of their electrodes.*

# Chapter 3

# Calibration of the PLASTIC entrance system/energy analyzer

## 3.1 Introduction

In this chapter the ion optical calibration of the entrance system/ energy analyzer (ESEA) of PLASTIC is outlined and discussed in detail. The information gathered during calibration is crucial for later data analysis to get back real counts from raw counts.

In the succeeding chapters, Chapters 5 and 6, similar calibration measurements are explained. Those are then compared to the results written in this chapter. All measurements outlined in these three chapters are performed in the same ion optical facilities at the University of Bern, CASYMS ion beam facility and MEFISTO ion beam facility, see Appendix B.2.

After prototype testing the final version of the ESEA was designed and simulated with SIMION ion optical simulation software, [14], at the University of Bern, see [2]. After ion beam and other functional tests with the engineering model (EQM, see [7]) three flight instruments were built, Flight Model 1 (FM1), Flight Model 2 (FM2) and Flight Spare (FS)[1]. All four were calibrated at the ion beam facilities at University of Bern ( They are briefly described in Appendix B.2). The calibration campaign of the two flight models lasted from January 2004 to June 2004 whereafter the ESEAs were shipped to the University of New Hampshire, USA, for integration with time of flight section and electronics to the integrated PLASTIC instruments IFM1 and IFM2.

The aim of the calibration of ESEA was to test whether the flight models fulfill the design goals and show agreement with the simulations. In addition, as mentioned above, a good understanding of the instrument function is crucial for the data reduction. Therefore, the main part of the calibration was to characterize all instrument parameters as well as possible.

## 3.2 Calibration specifications

### 3.2.1 General

All models (FM1, FM2 and FS) were calibrated to assess functionality and find the ion optical constants. These constants were compared with earlier simulations ([2]) and measurements with the EQM ([7]). The following calibration parameters were determined:

- Analyzer constants

- Deflection constants and elevation angle acceptance

- $E/q$ resolution

---

[1]When building space-borne instruments, it is favorable to build a spare model in case the flight instrument is damaged or not suitable for flight.

- Azimuthal angle acceptance

- Active area

- Geometric factor

In addition, the functionality of the main channel gate and S-channel switching electrode collection were tested. In the following subsection each ion optical parameter is explained.

### 3.2.2 Ion optical parameters

**Analyzer constants**

The analyzer constant $k_{\text{ESA}}$ is defined as the ratio of the $E/q$ of the ions passing through the ESEA and the ESA voltage $V_{\text{ESA}}$, where the transmission is the highest. Specifically, the constant is the ratio of the kinetic energy per charge, $E_{\text{kin}}/q$, and the potential difference, $\Delta V_{\text{ESA}}$, between the two hemisphere electrodes ESA-O and ESA-I, see Figure 3.1:

$$k_{\text{ESA}} = \frac{E_{\text{kin}}/q}{\Delta V_{\text{ESA}}} \tag{3.1}$$

As shown in Section 3.3 the ratio is equal for all beam energies and their respective ESA voltages.

The S-channel additionally consists of a set of electrodes. To two electrodes (SCO-L and SCI-U, see Figure 3.1) are potentials applied when the S-channel is activated. There is a constant relation between $E/q$ and the applied voltage, $V_{\text{electrode}}$, as well:

$$k_{\text{electrode}} = \frac{E_{\text{kin}}/q}{V_{\text{electrode}}} \tag{3.2}$$

The analyzer constants are used for in-flight tuning of the instrument electrodes according to the desired beam energy acceptance. Hence a full instrument calibration is important, as discussed previously.

**Angular deflection constants**

In addition to the $E/q$ selection, an elevation angle selection will be executed in flight whereby particles are deflected into the entrance system by the deflection plates (*Duckbills*, MA-L, MA-U, SA-L, SA-U). This operation only occurs in the Solar Wind Sector (SWS). Particles entering from $-20°$ to $+20°$ are deflected into the instrument. The ratio of the accepted angle, $\beta$, and the particle energy per charge, $E_{\text{kin}}/q$, to the deflection plate voltage, $V_{\text{deflection}}$, is the deflection plate constant:

$$k_{\text{deflection}} = \frac{\beta \cdot E_{\text{kin}}/q}{V_{\text{deflection}}} \tag{3.3}$$

**Energy per charge resolution**

The energy per charge ($E/q$) resolution of all three apertures (main channel (MC), S-channel (SC) and WAP) was measured. The $E/q$ resolution varies between the three channels due to different aperture sizes and geometry. For a given setting of ESEA electrodes (ESA voltage for MC and WAP; SCO-L and SCI-U voltage for SC, before ions pass into the same cylindrically symmetric ESA as shown in Figure 3.1) the $E/q$ resolution, ($\frac{FWHM\ E/q}{E/q}$), must be known[2]. For practical reasons the beam energy was fix and the ESA voltage was tuned during calibration. Thus, the ESA voltage resolution for a given $E/q$ was quantified. However, since $E/q$ and $V_{\text{ESA}}$ are directly proportional, the resolutions $\frac{\Delta E/q}{E/q}$ and $\frac{\Delta V}{V_{\text{ESA}}}$ are equivalent. See Section 3.3 for details of the measurements.

Both ESA electrodes (ESA-I and ESA-O) were tuned to the same absolute voltage but opposite polarity, as it is done in flight.

---

[2]FWHM: full width at half maximum of the measured energy distribution
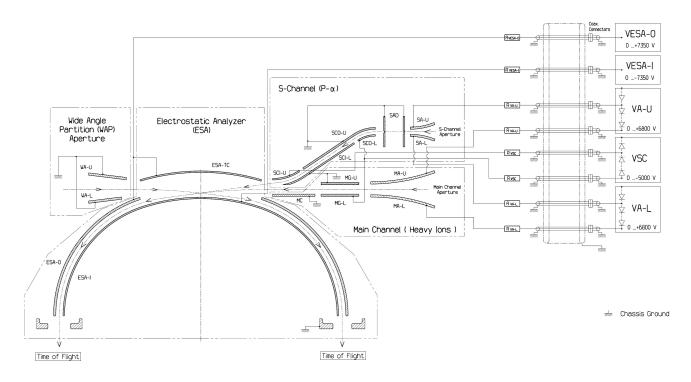
Figure 3.1: *Electrodes of the PLASTIC ESEA. The highest allowed voltage is written on the right side for each potential. Drawing by M. Sigrist, University of Bern.*

### Elevation angle acceptance

Additionally, all apertures have a finite elevation angle acceptance. It was measured for each channel and the full width half maximum (FWHM) of its distribution was quantified, giving the angular acceptance of the respective channel.

Together with the $E/q$ resolution, the angular acceptance defines the total transmission of the instrument for a given energy and angular step.

### Active area

The effective area is the differential transmission coefficient of the transmitted ion counts per unit time through an instrument aperture and the incident ion flux at given instrument settings. The active area, $A_{\text{act}}$, determined during calibration is defined as the ratio of the number of particles which pass through the ESEA at a given $E/q$ and the number of incident particles of a parallel beam.

$$A_{\text{act}} = \frac{n}{\Phi\,t} = \frac{n_{\text{ssl}}}{\Phi\,t\,\eta_{\text{ssl}}} \tag{3.4}$$

where $n$ is the number of counts during accumulation time $t$, $\Phi$ the ion beam flux; $n_{\text{ssl}}$ is the number of counts detected by a particle detector with detection efficiency $\eta_{\text{ssl}}$. See Appendix C for the calibration of the used particle detector.

### Geometric factor

The geometric factor of an instrument characterizes the angular and energy acceptance of an instrument. There are several explicit definitions of geometric factors, see Appendix A. I used the geometric factor applied by F. Allegrini during laboratory prototype calibration and EQM simulations, [2]. It is defined as follows:

$$G = \iiint T \cos\theta \, \mathrm{d}A_{\text{act}} \, \frac{\mathrm{d}E}{E} \, \mathrm{d}\Omega \tag{3.5}$$

where $T$ is the transmission, $\mathrm{d}A_{\mathrm{act}}$ the differential active area and $E$ the beam energy.
For our measurements I use the discrete form of (3.5):

$$G = \alpha_{\mathrm{SWS}} \sum_i^N \sum_j^M \Delta\theta_i \, \frac{\Delta E_j}{E_j} \, (A_{\mathrm{act}})_{ij} \tag{3.6}$$

The derivation of the geometric factor can be found in Appendix A.1.

### 3.2.3 Test sequence

The same calibration test sequence was performed for all models:

- The instrument was mounted into the instrument chamber of CASYMS or MEFISTO ion beam facility.

- When the pressure in the instrument chamber was low enough (below $1 \cdot 10^{-6}$ mbar), the basic functionality of the instrument electrodes was tested.

- $E/q$ selection capability was verified.

- Angular acceptance and deflection constants were measured.

- Analyzer constants of all channels and their electrodes were determined.

- Geometric factor of all channels were measured.

- Azimuthal scans for all channels were performed.

- Functionality of the main channel gate (MG-L electrode) was tested.

### 3.2.4 Calibration Facilities

The measurements with the Flight Models and the Flight Spare were carried out in the CASYMS ion beam facility [21] and in the MEFISTO ion beam facility ([43] and [31]). Figure 3.4 shows the setup in the CASYMS ion beam facility and Figure 3.5 in MEFISTO.

In CASYMS the turntable allowed rotation around two axes ($\alpha_{\mathrm{CASYMS}}$ and $\beta_{\mathrm{CASYMS}}$) and translation in one direction ($z_{\mathrm{CASYMS}}$-Axis). In addition, a turning plate mounted on the turntable allowed a third turn axis ($\theta_{\mathrm{CASYMS}}$), see Figures 3.2 and 3.3.

It was possible to turn the instrument 180° in both directions as well as changing the lateral position allowing to calibrate all channels and azimuthal positions without breaking the vacuum. The instrument was mounted in CASYMS in a aluminium shielding box preventing ions from affecting the pre-amplifier electronics.

The ion beam facility CASYMS provides a broad parallel beam of an area of $12 \cdot 12$ cm$^2$. The ions are at low charge states in an energy range between 5 eV/e and 60 keV/e with an energy spread of about 0.1 percent. The beam divergence is about 0.3°. Therefore, the energy and the angular distribution of the ion beam can generally be assumed to be a delta distribution relative to the instrument acceptance. For PLASTIC ESEA calibration Ar$^+$ and He$^+$ beams were used in an energy range between 100 eV/e and 60 keV/e. Almost all calibration experiments were performed in CASYMS, only some high flux gate tests and high beam energy scans were performed in the MEFISTO instrument chamber, since the beam flux in MEFISTO is much higher and the beam more collimated than in CASYMS. The MEFISTO ion source delivers a pencil beam of a flux up to 2 MHz/0.1 cm$^2$ for Ar$^{4+}$ compared to 0.1 MHz/0.1 cm$^2$ for Ar$^+$ provided by the CASYMS ion source. In the MEFISTO chamber there is a two-axes turntable ($\alpha_{\mathrm{MEFISTO}}$ and $\beta_{\mathrm{MEFISTO}}$). The instrument is mounted differently, see Figure 3.5. The axes are comparable:

- $\alpha_{\mathrm{MEFISTO}}$ corresponds to $\beta_{\mathrm{CASYMS}}$
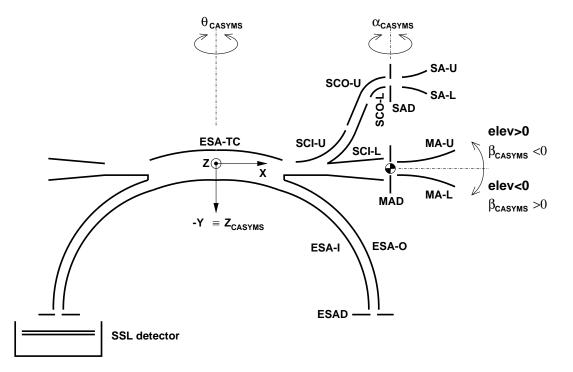
Figure 3.2: *Experimental setup in CASYMS instrument chamber and turn axes. Shown are all axes and their notation in CASYMS. The out-of-ecliptic angle (elevation angle, **elev**) is called $\beta_{\mathrm{CASYMS}}$. The in-ecliptic angle corresponds to $\theta_{\mathrm{CASYMS}}$, respectively. Figure adapted from [2].*
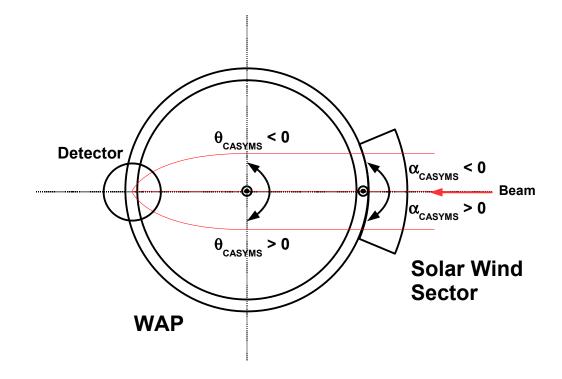


Figure 3.3: *Turn Axes in CASYMS, top view. PLASTIC ESEA is mounted upside down. The beam entering from the right hand side (red trajectories) is guided through the ESEA onto the detector. The in-ecliptic or azimuthal angle corresponds to $\theta_{\mathrm{CASYMS}}$.*

Figure 3.4: *Mounting of PLASTIC ESEA in CASYMS facility. The instrument was mounted upside down, the TOF-section would be above. The ion beam comes from the left hand side. On the right picture the theta table can be seen which allows turning around the $\theta_{\mathrm{CASYMS}}$-axis in figure 3.2*
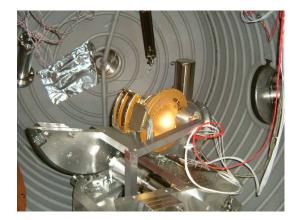


Figure 3.5: *Mounting of PLASTIC ESEA in MEFISTO facility. The table allowed only restricted turns. The ion beam comes from the left hand side. See text for turning axes comparison between CASYMS and MEFISTO.*

- $\beta_{\mathrm{MEFISTO}}$ corresponds to $\theta_{\mathrm{CASYMS}}$

The turning range in the MEFISTO chamber was limited due to mechanical constraints. Additionally, changing between S-channel and main channel could only be done manually after breaking the vacuum. The ECR ion source[3] allows high ion current and high charge states (i.e. Argon up to 8+). The beam is a pencil beam with a diameter of $\sim 2$ cm at instrument position.

### 3.2.5 Experimental techniques

**Signal detection**

All ions passing through the ESEA were counted by a position sensitive microchannel plate detector in chevron plate configuration, whose diameter was 4 cm [53]. Before and after the ion optical calibration of the PLASTIC instruments the detection efficiency $\eta_{\mathrm{SSL}}$ of the so called SSL detector[4] had to be determined for different ions and beam energies. The beam flux from the CASYMS ion source was measured

---

[3]Electron Cyclotron Resonance Ion Source (ECRIS), see [20]
[4]*Space Science Laboratory*, [41]

Figure 3.6: *Images recorded by the SSL detector for a parallel Ar$^+$ beam, beam energy 3 keV. From top left to bottom: main channel, S-channel and WAP.*

by a channeltron detector[5]. The detection efficiency was determined relatively to the beam scanner in CASYMS.[6] The detector calibration is discussed in Appendix C.
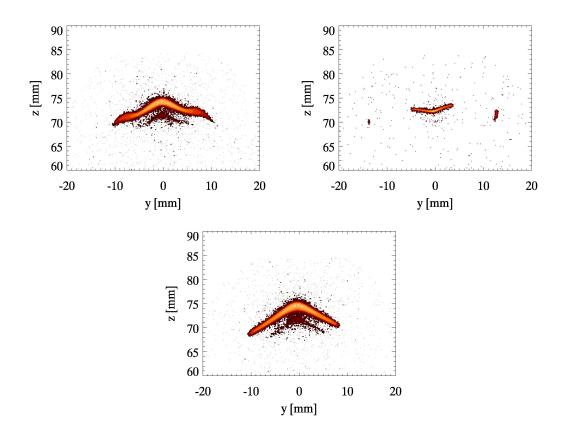
For an Ar$^+$ beam, $E/q$ = 3 keV/e, the SSL efficiency is 0.65 with an error of 0.02. For an ion beam with $E/q$ = 5 keV/e the efficiency is slightly higher, 0.67. For lower energies the efficiency of the detector decreases rapidly, due to secondary electron emission of the MCP. The efficiency is given by $\eta_{SSL} = A_0(1 - \exp(-0.6E))$, where $A_0 \simeq 0.75$ and $E$ is the energy in keV. (This relation is discussed in [35]).

The SSL detector was mounted above the exit slit of the ESEA. In CASYMS the instrument could be turned independently from the detector when turning around the theta-axis (see Figures 3.2 and 3.4).

The position information signal of the SSL detector was amplified inside the chamber. The amplified signal was read out with the position analyzer belonging to the detector, [54]. A PC can be connected to the position analyzer to save the accumulated position information and the total counts. Alternatively, the signal from the position analyzer can be read out with the computer controlling the table movements of the instrument chamber (MicroVAX). More details on the used MCP detector can be found in Appendix C or in [41].

The total counts measured with the SSL detector were used as transmission signal. The total counts are the integrated counts over the azimuthal angle range that is covered by the detector (diameter 40 mm), see in Figure 3.3. Since only Additionally, the position information was stored in quadratic arrays for all measurements. The resolution of the detector is 256 × 256 pixel, see Figure 3.6 for beam images of all three channels.

---

[5]Channeltron detectors (CEM), purchased from *Dr. Sjuts GmbH*, [24], see [21] and [56].

[6]The channeltron detector used in CASYMS has an efficiency of almost 1 for beam energies higher than 2 keV/e. Therefore, an efficiency of 1 was assumed for all measurements.

**SSL data files:**

The parameters for each measurement (e.g., accumulation time, total counts, user defined parameters) and the position information are stored either in a binary format file, when the Quantar software is used, or in an ascii file, when the detector signal is read out by the MicroVAX. Both types of these files are called SSL-files here. Images can be produced from these data files showing the shape of the measured beam spot.

**Ion optical calibration**

After achieving the necessary pressure conditions first functional tests were performed with the ESEA to ensure all electrodes were connected correctly and that the instrument works properly. The instrument voltage settings for a given beam $E/q$ are compared with the known values from earlier measurements or simulations (Laboratory prototype measurements and SIMION simulations see [2], EQM measurements see [7]).

At the beginning the analyzer constants were determined and the respective angular and energy acceptance of all analyzer electrodes. Thereafter the deflection constants for the deflection plates (Duckbills, DB) were obtained. For the S-channel the SCO-L and the SCI-U electrodes had to be calibrated in addition to the ESA electrodes ESA-I and ESA-O, see Figure 3.1. All results are discussed in Sections 3.3 and 3.4. To complete the picture of the ion optical parameters, the geometric factor, Equation (3.5), the active area, Equation (3.4), and the azimuthal response of each aperture and model were characterized, see Sections 3.6 and 3.5. The geometric factor and the azimuthal response measurements give an overall picture of the ion optical response of the three apertures.

All electrodes were either connected to a power supply or grounded. The voltages for the two ESA electrodes (ESA-O/ESA-TC and ESA-I) were provided by one power supply with two outputs of the same voltage but opposite polarity. The S-channel electrodes and the deflection plates had their own power supply.

## 3.3 Energy acceptance, analyzer constants

### 3.3.1 General

The approach to characterize the energy acceptance and the analyzer constants was the same for all apertures and models:

1. An elevation angle scan to find the optimal incident angle for the beam. The electrode voltages were tuned as expected from earlier measurements.

2. At the given elevation angle an ESA voltage scan was performed, in steps of 0.5 to 1.0 percent of the nominal voltage.

3. When testing the S-channel tuning, the SCO-L followed by the SCI-U voltages were scanned to find the maximum transmission.

4. Finally a second elevation angle scan was performed.

5. If the nominal position varies significantly (more than 2 percent), the same procedure is repeated from the beginning.

The ion beam in CASYMS or MEFISTO was set to a specific energy per charge value, e.g., $E/q = 3$ keV/e.[7] The voltage expected from measurements with the EQM or simulations was applied to the instrument electrodes. Then a first elevation scan was performed, in elevation angle steps of about (MC and WAP) or 0.1° (SC). After the elevation angle was set for maximum measured intensity, the applied

---

[7]The extraction voltage used in the CASYMS ion source is 3 keV/e, hence the beam energy without any post acceleration is always 3 keV/e. For the first tests the energy used was always 3 keV/e, for convenience.

voltage of the two ESA hemisphere was changed in steps of 1 percent of the expected nominal value (e.g., the ESA voltage was $\pm 180$ V at $E/q = 3$ keV/e). The applied voltages of the two ESA hemispheres have the same absolute value but different sign (ESA-I negative, ESA-O positive voltage). The voltage was supplied by a power supply with two outputs of opposite polarity. The measured intensity is plotted versus positive ESA voltage. (See Figure 3.7 for ESA voltage scans of all channels.) To find the nominal voltage value for a given beam energy per charge, $E/q$, a special fit function and a Gaussian is applied to the voltage distribution. The fit function, a convolution of a Gaussian with a trapezoid function, is explained in Appendix A. The function was developed by F. Allegrini, [2]. The median of the measured distribution is used to calculate the analyzer constants (Equations 3.2 and 3.1). The full width at half maximum divided by the nominal voltage is the respective energy acceptance, see Figure 3.7. The median of each distribution function is plotted against the corresponding beam energy, e.g., in Figure 3.11. The analyzer constant for each channel is then calculated using a regression curve through all data points.
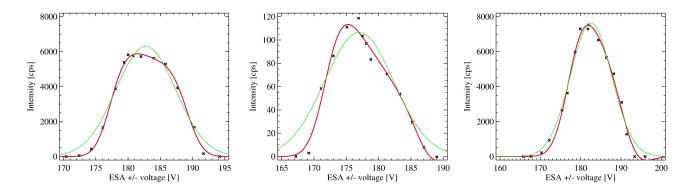


Figure 3.7: *ESA voltage scan for FM1. Measured intensity of an $Ar^+$ beam with $E/q=3$ keV/e by SSL detector as a function of the ESA voltage on each ESA hemisphere.*
*From left to to right: main channel, S-channel and WAP.*
*Red line: fit using Equation (A.13); green line: Gauss fit for comparison.*

### 3.3.2 Main channel

First the main channel was characterized. With its wider aperture than the S-channel it is easier to find the right elevation angle. Through the main channel ions with an energy per charge up to 100 keV/e can be transmitted. The restriction is due to the highest allowed potential difference between the two ESA hemispheres ($\pm 7350$ V, tested in partial discharge tests at the University of Bern). For FM1 the beam energy was set to 3, 5, 10 and 20 keV/e, for FM2 and FS 0.5, 1, 2, 3, 5, 10 and 20 keV/e. The measurement was performed as described above. In the Figure 3.11 the calculated median and the FWHM for different beam energies is plotted against beam energy per charge. To prevent saturation of the used MCP detectors, the number of transmitted ions had to be kept below $10^5$ per second over the whole detection area and below $10^2$ per second on one channel. Since the ion transmission is high for the main channel, see later in Section 3.6, the ion beam intensity was low, usually below 1 kHz/0.1 cm$^2$.

### 3.3.3 S-channel

The S-channel has a much smaller aperture than the main channel, thus it needs a much higher beam intensity to obtain count rates with reasonable statistics (sufficient signal above the background noise level of the detector). The beam intensities were usually around 20 kHz/0.1 cm$^2$. The narrow angular acceptance of the S-channel, resulting from the series of entrance slits (SAD, see Figure 3.1), requires precise entry angle tuning, such that the beam can pass into the S-channel. Hence at the beginning of an ESA voltage scan always an elevation angle scan was performed to find the optimal elevation angle.
To deflect the beam through the S-channel into the ESA hemisphere, two additional guiding electrodes are necessary, SCO-L and SCI-U, see Figure 3.2. These electrodes allow to deflect ions with $E/q$ up to 12
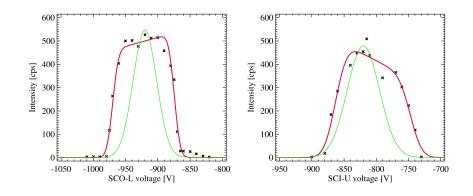
Figure 3.8: *SCO-L and SCI-U voltage scan for FM1 S-Channel. $E/q=3$ keV/e, $Ar^+$ beam. Red line: fit using Equation (A.13); green line: Gaussian fit for comparison.*
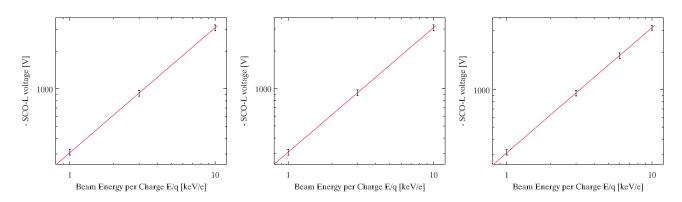


Figure 3.9: *S-Channel SCO-L voltage versus Beam Energy. Red line: Linear fit through data points. From left to right: FM1, FM2 and FS*

keV/e. $E/q = 12$ keV/e corresponds to a solar wind velocity of 1500 km/s (protons) or 760 km/s (helium ions). Most of the time the proton and alpha particle distributions will be measured by the SC. The energy of ambient solar wind protons is about 1 keV/e.[8] The beam energy used during calibration was between 0.5 and 10 keV/e (For an ESA scan, see Figure 3.7). In the Figure 3.12 the median of the ESA voltage distribution is plotted versus the beam energy. The error bars are the FWHM of the corresponding distribution.

Additionally, the deflection characteristics of the two guiding S-channel electrodes (SCO-L and SCI-U) had to be determined. Typical voltage scans are shown in Figure 3.8 for FM1 and $E/q = 3$ keV/e. To ensure the best transmission for both electrodes the median of the distribution function was selected instead of the voltage for maximum intensity. In Figures 3.9 and 3.10 the measured nominal electrode voltages are plotted against beam energy, error bars represent the FWHM of the distribution.

### 3.3.4   Wide-Angle Partition

For the WAP the measurement principle was the same as for the main channel. The results are similar except that the transmission is higher for the WAP than for the MC due to the larger aperture and the more open geometry. The energy acceptance is also slightly higher than for the main channel, see Figure 3.7 for an ESA voltage scan for FM1 and $E/q = 3$ keV/e. Since the WAP azimuthal range is much larger than that of the solar wind sector channels, different azimuthal positions were crosschecked. The different azimuthal positions showed neither an effect on the energy acceptance nor on the nominal ESA voltage. In Figure 3.13 the median of the ESA voltage distributions is plotted against the corresponding beam energy.

---

[8]$v_{\mathrm{SW}} \approx 440$ km/s
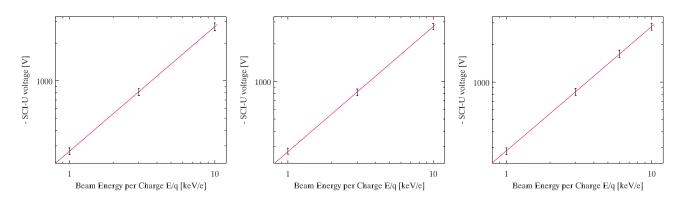
Figure 3.10: *S-Channel SCI-U voltage versus Beam Energy. Red line: Linear fit through data points. From left to right: FM1, FM2 and FS*



Figure 3.11: *Main channel ESA voltage difference versus beam energy. Red line: linear fit through the data points. The error bars correspond to the FWHM of the voltage distribution at the given energy per charge, see Figure 3.7. From left to right: FM1, FM2 and FS*
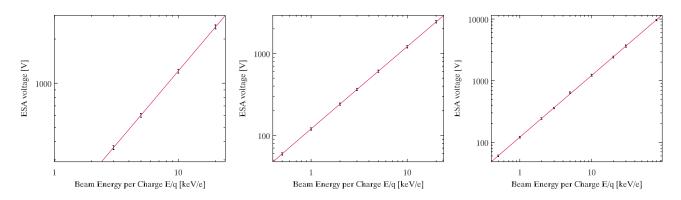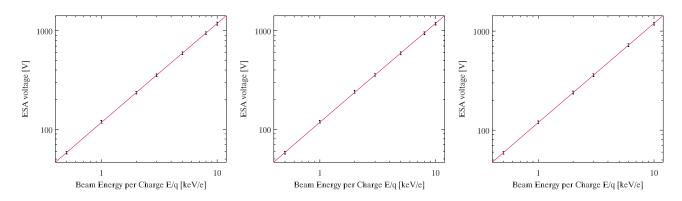


Figure 3.12: *S-channel ESA voltage difference versus beam energy. Red line: linear fit through data points. From left to right: FM1, FM2 and FS*
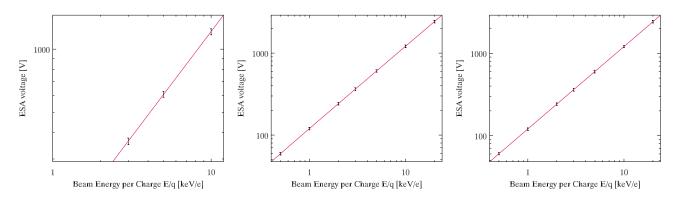
Figure 3.13: *WAP ESA voltage difference versus beam energy. Red line: linear fit through data points. From left to right: FM1, FM2 and FS*

### 3.3.5  Summary analyzer constants and energy acceptance

In flight, the analyzer constants calculated during the calibration campaign are used to convert solar wind $E/q$ into ESA voltage. When the S-channel is enabled the voltages applied to the two S-channel electrodes (SCO-L and SCI-U) have a fixed ratio during the ESA sweeps, related to the ESA voltage. For a given ESA step, all voltages are defined. Therefore the analyzer constants must be known as exact as possible. In Table 3.1 all measured analyzer constants are listed. The analyzer constants are calculated using the slope $a$ of the linear regression curve $y = a \cdot x + b$ through all data points in the Figures 3.11, 3.12 and 3.13, weighted by their error. For each beam energy the median of the positive ESA voltage distribution was calculated and plotted.[9] The ESA analyzer constants is then given by $k_{\mathrm{ESA}} = \frac{E/q}{\Delta V_{\mathrm{ESA}}} = 1/a_{\mathrm{ESA}}$. For the two S-channel electrodes SCO-L and SCI-U the analyzer constant is $k_{\mathrm{SC}} = \frac{E/q}{V_{\mathrm{SC}}} = 1/a_{\mathrm{SC}}$. The error of the analyzer constants is the error of the linear regression through all data points. The error of each data point is the error of the median determination.

It was more difficult to measure the ESA voltage distribution for lower beam energies (below 2 keV/e) because the measured count rate was lower. In addition, the ESA voltage tuning was more delicate at low voltages. The lower count rate was due to the lower detection efficiency of the SSL detector we used (see Appendix C). Additionally, the beam profile was less homogeneous than for higher beam energies. It showed a divergent profile, the beam intensity was lower in the center than at the flanges. This had an influence on the measured transmission for low beam energies. Thus, the active area measured for lower beam energies seems to be lower than for higher beam energies.

When comparing the analyzer constants of the ESA electrodes, WAP and MC are similar, but the SC has a larger $k_{\mathrm{ESA}}$, implying that the positive applied voltage on the ESA hemisphere is smaller for ions passing through the S-channel than for ions passing through the main channel. In Figure 3.14 one can see that the ion trajectories through the S-channel have a different incident angle to the midplane of the ESA than ions passing through the main channel, i.e., the elevation angle is larger (about $0.2°$)[10].

---

[9]The median of the ESA voltage distribution was chosen instead of the maximum or the mean of the distribution, because in flight the voltages applied to the electrodes are not scanned as fine as during calibration. The median ensures the most likely transmission since the voltage distributions showed a slight asymmetry.

[10]To deflect ions entering the ESA with a positive incident angle, a lower ESA voltage is necessary, see geometric factor measurements in Section 3.6 for comparison.

| Channel | Electrode | FM1 | | FM2 | | FS | |
|---|---|---|---|---|---|---|---|
| | | Analyzer constant | FWHM | Analyzer constant | FWHM | Analyzer constant | FWHM |
| S-channel | SCO-L | 3.23(1) | 10.40% | 3.25(1) | 10.64% | 3.19(1) | 10.40% |
| | SCI-U | 3.68(1) | 13.20% | 3.64(1) | 10.75% | 3.59(2) | 13.80% |
| | ESA | 8.46(1) | 6.35% | 8.46(2) | 6.26% | 8.38(3) | 6.12% |
| Main channel | ESA | 8.26(1) | 6.12% | 8.26(2) | 6.48% | 8.25(2) | 6.30% |
| WAP | ESA | 8.25(4) | 6.77% | 8.26(1) | 7.30% | 8.28(1) | 6.67% |

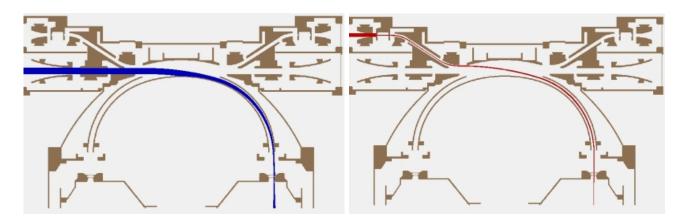Table 3.1: *Overview of all analyzer constants (eV/eV) of FM1, FM2 and FS.*



Figure 3.14: *3D SIMION simulations of the beam trajectories through the main channel (left side) and the S-channel (right side). The ions passing through the S-channel enter the ESA with a larger incident angle than ions passing through the main channel.*
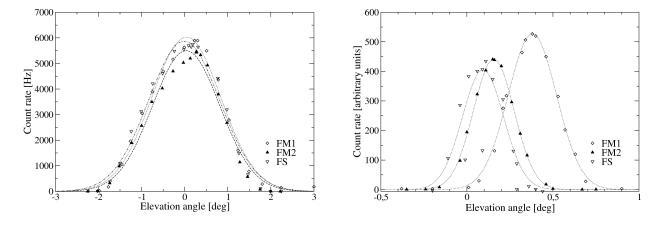
Figure 3.15: *Elevation angle scan for main channel (left plot) and S-channel (right plot), all flight models. $E/q=3$ keV/e, $Ar^+$. A Gauss fit to the data is plotted for comparison.*

## 3.4   Angular acceptance, deflection constants

### 3.4.1   General

The deflection plates of main and S-channel of PLASTIC are used to deflect ions into the aperture. In flight the deflection plate voltage is changed in 32 steps to accept particles from $-20°$ to $+20°$.

The deflection constant, Equation 3.3, characterizes the relation between deflection plate voltage and accepted angle for a given $E/q$. So for each set of deflection plates (MA-L and MA-U, SA-L and SA-U respectively), the deflection constant had to be measured. At the same time the angular acceptance ranges of all channels could be determined. This acceptance range is necessary to deconvolve the angular distribution of the solar wind.

To derive the deflection constant the instrument was turned around the CASYMS beta angle axis (see Figure 3.2), corresponding to the elevation angle axis of PLASTIC, but with opposite sign. In our case the deflection voltage was applied to one of the two deflection plates and then the corresponding elevation angle distribution was measured. The median of the distribution is the deflected angle for this given deflection voltage. The fit function to calculate the median is the same as used for the ESA voltage scans, see Appendix A. The deflected angles are plotted versus the deflection voltage, Figure 3.16 shows the main channel measurements for $E/q = 3$ keV/e. Positive deflection voltage means always positive voltage on the lower deflection plate. If the upper deflection plate is used, the voltage must have negative polarity.

### 3.4.2   Main channel and S-channel

For several beam energies the angular acceptance was measured when scanning the elevation angle, see Figure 3.15, where an elevation angle scan for each model is plotted. The measured distributions for the S-channel do not have the same median. There are two reasons for this shift. First the elevation angle of the turntable cannot be determined better than to $0.1°$. And in addition, the shape and vertical position (z-axis in Figure 3.2) can differ between the three models due to complicated fabrication of the slits. This has to be considered during data analysis. See also later in Section 3.5 about the azimuthal angle response. To get the deflection constant, the deflection angle for a given deflection plate voltages was measured, performing an elevation angle scan. In Figure 3.16 the measured medians of the elevation angle distributions are plotted as a function of the deflection plate voltage. For the S-channel measurements see Figure 3.17. Both measurements were performed for beam energy $E/q = 3$ keV/e. The error bars shown on the plots are the measured FWHM of the corresponding elevation angle scan. For the measurements presented here, usually the lower deflection plate (MA-L and SA-L) was enabled, the upper one grounded.

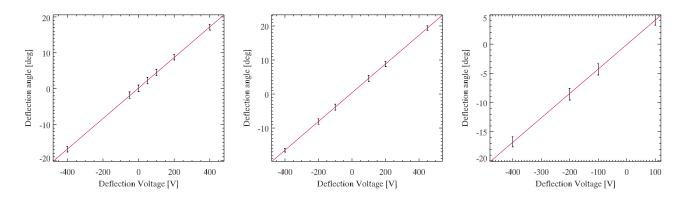Figure 3.16: *Main channel deflection angle versus deflection voltage of the lower deflection plate, MA-L. Deflection measured for 3 keV/e beam. Red line: linear fit through data points.*
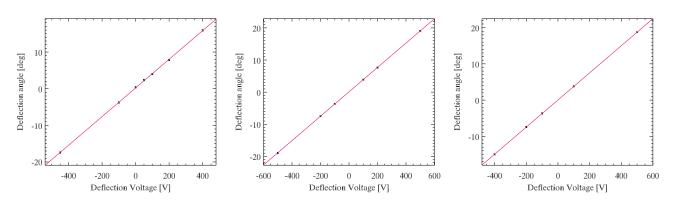*From left to right: FM1, FM2 and FS*



Figure 3.17: *S-channel deflection angle versus deflection voltage. Deflection measured for 3 keV/e beam. Red line: linear fit through data points.*
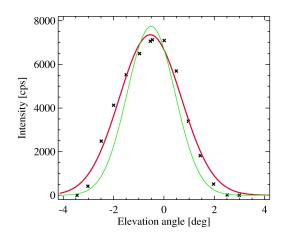*From left to right: FM1, FM2 and FS*

Figure 3.18: *Elevation angle scan for WAP. E/q=3 keV/e, Ar$^+$*
*green line: Gauss fit; red line: fit using Equation (A.13)*

| Channel | FM1 | | FM2 | | FS | |
|---|---|---|---|---|---|---|
| | Deflection Constant | angular FWHM | Deflection Constant | angular FWHM | Deflection Constant | angular FWHM |
| S-Channel | 0.117(1) | 0.37 | 0.114(1) | 0.27 | 0.112(1) | 0.27 |
| Main Channel | 0.128(3) | 1.9 | 0.127(3) | 1.8 | 0.126(7) | 1.9 |
| WAP | – | 3.2 | – | 3.1 | – | 3.2 |

Table 3.2: *Overview of all deflection constants and angular acceptance ranges of FM1, FM2 and FS (deflection constant ° keV/e V$^{-1}$, angular acceptance in degrees)*

### 3.4.3 Wide-Angle Partition

Since the WAP does not have deflection plates only the angular acceptance was determined. In Figure 3.18 the angular acceptance range is about 3°, the whole acceptance range is more than 7°, allowing to cover a large part of the suprathermal ion angle distribution.

### 3.4.4 Summary angular acceptance and deflection constants

Like the analyzer constants, the deflection constants have to be well known. During flight, the deflection voltage is applied related to the actual voltage of the ESA since the deflection angle depends on the deflection plate voltage and the ion energy, i.e. for higher beam energy the deflection plate voltage must be higher as well to deflect ions by the same angle. The deflection angle $\beta$ is given by $\beta = k_{\text{deflection}} \frac{V_{\text{deflection}}}{E_{\text{kin}}/q}$, cf. Equation (3.3). The geometry of the deflection plates allows to deflect particles from $-20°$ to $20°$ for energies up to 43.2 keV/e, since the highest allowed DB voltage is 6800 V ($0.127 \cdot \frac{6800}{43.2} = 20°$).

The deflection constant is calculated using the slope of the linear regression curve $y = a \cdot x + b$ through all measured deflected angles, weighted with their errors. Neglecting the intercept $b$, we find for the deflection constant $k_{\text{deflection}} = a \cdot E/q$, with Equation (3.3) and $a \cdot V_{\text{deflection}} = \beta_{\text{deflection}}$. The error of the deflection constants is the error given by the linear regression. The relative error of the measured angles is calculated as the square root of the sum of all relative errors squared of the factors of Equation (3.3). See Table 3.2 for all deflection constants and angular acceptance widths.

The deflection constants for all three models are in very good agreement, the difference between main and S-channel is due to a slightly different geometry of the deflection plate. The angular acceptance is the FWHM of the elevation angle distribution.

## 3.5    Azimuthal response

### 3.5.1    General

For a complete characterization of the ion optical capabilities of the ESEA not only energy and angle acceptance is crucial but also the azimuthal angle response. Since the instrument can be turned in the CASYMS instrument chamber without moving the detector (theta axis in Figure 3.2) the ion optical transmission as a function of the azimuth angle can be measured. For the measurements discussed in this section the instrument is always turned around the theta axis. The center of the Solar Wind Sector is at 60°.

For all measurements one has to keep in mind that the ion beam of the CASYMS facility is almost a delta beam with very small energy and angular dispersion. When measuring the solar wind the energy and angular distribution is much larger smearing out the clearly visible features in the measurements discussed below.

### 3.5.2    Main channel and Wide-Angle Partition

A complete azimuthal scan was performed for the WAP and the main channel[11], by measuring the ion optical transmission through the ESEA as a function of the azimuthal angle. For FM1 and FS the measurements were automated whereas for the FM2 the measurement was done manually. See Figure 3.19 for complete scans with constant elevation angle. In Figure 3.20 the intensity measurements are shown compared to the mechanical structures of the ESEA. Below the polar plot of the transmission is a bottom view of the ESEA, where the exit slit of the ESA can be seen. One can clearly see the dependence of the transmission on the spokes and blockages of the ESEA. The lower transmission through the main channel are due to a narrower aperture of the main channel.

For the FS the transmission measurement was expanded, an elevation angle scan was performed for each azimuthal step, 171 azimuthal steps with step size 2° and 7 elevation angle steps with 0.5° step size, see Figure 3.21. The transmission matrix reflects the broad angular acceptance of the WAP. In addition, one can see that the maximum angle for WAP and MC are different.

### 3.5.3    S-channel

At the entrance of the S-channel, behind the two deflection plates, there are two small slits, SAD on Figure 3.1, which reduce the ion transmission through the SC. They are not completely uniform, having a slit width between 20 and 40 micrometers. A complete azimuthal and elevation angle scan was performed for all three models, revealing the shape of the slits, see Figure 3.22. For FM1 and FS the azimuthal response measurement was automated. An elevation angle scan was done between 35° and 85° azimuth, every 2°. For FM2 at seven different azimuth positions (43, 48, 54, 60, 66, 72, 77 degrees) an elevation scan was done. The measurement for FM2 was performed on different days, therefore the intensity had to be normalized to the beam intensity. The measurements for FM1 and FS were performed on one day, the beam intensity was monitored but did not change more than statistically during the measurements.

The transmission response plot for FM1 shows a large dependence on the azimuthal angle. Since the solar wind has a wider energy and angle distribution than CASYMS, where we have an almost parallel ion beam, the transmission response matrix would be smeared out in flight. Nevertheless, an influence might be seen. Also FS showed in the center of the Solar Wind Sector a lower transmission than on its flanges. When comparing the SC of the three models, one would tend to select FM2 and FS for flight instead of FM1 and FM2.

---

[11]Since the main channel and the WAP are on the same lateral position, both channels could be measured at the same time.
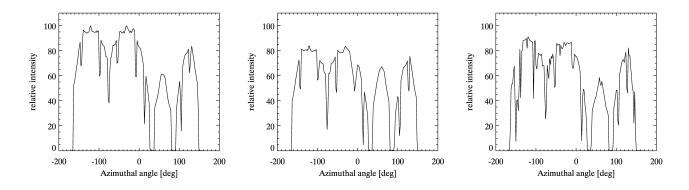
Figure 3.19: *Azimuthal response of WAP and main channel. The center of the Solar Wind Sector is at 60°. Elevation angle for whole scans 0° (FM2 and FS) and 0.5° (FM1). The intensity difference is due to different active areas of the three models.*
*From left to right: FM1, FM2 and FS*
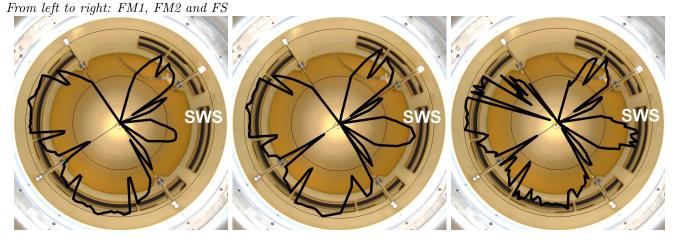


Figure 3.20: *Azimuthal response of WAP and main channel. Elevation angle for whole scans 0° (FM2 and FS) and -0.5° (FM1).*
*For comparison the exit slits of the ESEA are visible below the polar plot of the intensity. The intensity was normalized for each model to its maximum value. All measurements were performed with a 3 keV/e Ar+ beam in CASYMS chamber. SWS Solar Wind Sector.*
*From left to right: FM1, FM2 and FS*
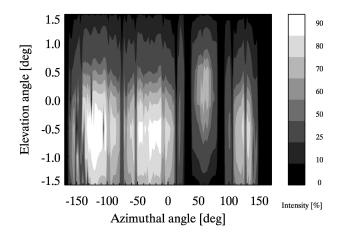


Figure 3.21: *Azimuthal response of FS. The center of the Solar Wind Sector is at 60°. 171 azimuthal steps, step size 2°, 7 elevation angle steps, step size 0.5°.*

Figure 3.22: *Azimuthal response of S-channel. The center of the Solar Wind Sector (SWS) is at* $60°$*. The inner contour lines are at 60, 70, 80 and 90 %.*
*From left to right: FM1, FM2 and FS*

## 3.6 Geometric factor, active area

The geometric factor and the active area are important to derive fluxes from the measured counts. In addition, the geometric factor is an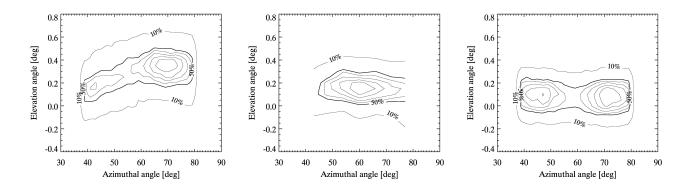 effective number to compare different plasma instruments like STEREO/PLASTIC or SOHO/CELIAS/CTOF [32]. The geometric factor, in the definition used here (Equation (3.5), for details see Appendix A), characterizes the angular and energy acceptance of PLASTIC. In discrete form, the geometric factor is $G = \alpha_{\mathrm{SWS}} \sum_i^N \sum_j^M \Delta\theta_i \, \frac{\Delta E_j}{E_j} \, (A_{\mathrm{act}})_{ij}$ (Eq. (3.6)), where the beam energy $E_j$ is stepped in M steps of step size $\Delta E_j$, the elevation angle $\theta_i$ is stepped in N steps of step size $\Delta\theta_i$. For each of the pairs $(E_j, \theta_i)$ the active area $(A_{\mathrm{act}})_{ij}$ is measured[12]. In the measurements presented here, the step sizes $\Delta E_j$ and $\Delta\theta_i$ were constant. The energy and elevation angle ranges were selected to cover the whole acceptance range of the instrument at a certain tuning (for FM1 and FS 5 keV/e, FM2 3 keV/e). All measurements were performed in CASYMS, where we have a broad and parallel beam, irradiating entirely the apertures of PLASTIC. While the geometric factor measurements for FM1 and FS were automated, the measurements for FM2 were done manually. The automated measurement was always performed equally: The beam energy was stepped over a range where we completely cover the energy acceptance of the the corresponding channel. For each energy a beam profile was measured to get the beam flux.[13] Then a complete elevation angle scan was performed. At each step the transmitted signal was measured during an accumulation time $T$ and the position information stored in $128 \times 128$ pixel or $64 \times 64$ pixel arrays.

The automated measurements were controlled by a PASCAL/FORTRAN program running on the MicroVAX computer, steering the turntable and the beam energy, as well as reading out the data from the SSL detector, see [56] for details on the CASYMS automatization.

### 3.6.1 Main channel

For FM1 and FS the geometric factor measurement was automated. The ESA electrodes were tuned to accept 5 keV/e ions ($V_{\mathrm{ESA}} = \pm 300$ V), beam intensity below $1$ kHz/0.1 cm$^2$. Then the beam energy was stepped from 4 keV/e up to 6 keV/e in increments of 50 keV/e. For each energy step, an elevation angle scan was performed, from $-6.0°$ to $+6.0°$ with step size $0.5°$. The data accumulation time for each angle and energy step was 20 seconds. In Figure 3.23 all stored beam images are plotted for FS, for each energy and angle step one image.

The FM2 measurements were performed manually. Unlike FM1 and FS, the beam energy was fix and the ESA voltage was changed. Beam energy 3 keV/e, the ESA voltage was scanned from 140 V up to 215 V,

---

[12] $A_{\mathrm{act}} = \frac{n}{\Phi t} = \frac{n_{\mathrm{ssl}}}{\Phi t \, \eta_{\mathrm{ssl}}}$, where $n$ number of counts during time $t$, $\Phi$ is the ion beam flux; $n_{\mathrm{ssl}}$ is the total number of counts detected by a particle detector with detection efficiency $\eta_{\mathrm{ssl}}$, Equation (3.4).

[13] The profile was measured in two directions, y- and z-axis of the beam scanner in CASYMS instrument chamber, at 13 positions between y=-60 mm and y=+60 mm for z=0 mm and 13 positions between z=-60 mm and z=+60mm for y=0 mm.

and an elevation angle scan in steps of 0.5° was performed at each ESA step. To get the same elevation angle versus beam energy per charge contour plot, the data for the ESA voltage had to be converted into energy per charge.[14] See Figure 3.26 for contour plots of the transmission for all models. All measurements were performed in CASYMS with an $Ar^+$ beam.

### 3.6.2   S-channel

For all models the guiding electrodes (both ESA, SCO-L and SCI-U) were tuned for 5 keV/e ion acceptance ($V_{ESA} \simeq 300$ V, $V_{SCO-L} \simeq -920$ V and $V_{SCI-U} \simeq -835$ V). The beam intensity was much higher than for the main channel, about 20 kHz/0.1 cm². As for the main channel of FM1 and FS, the energy was changed in steps of 40 eV/e from 4400 eV/e up to 5600 eV/e. For each energy step an elevation angle scan was performed from -0.6° up to +0.6° for FM2 and FS, from -1.0° up to +0.4° for FM1, with a step size of 0.05° for all models. The data accumulation time for each angle and energy step was 30 seconds. In Figure 3.24 all stored beam images are plotted for FS, for each energy and angle step one image. The measurements for FM1 and FS were automated (see main channel), the FM2 measurement was performed manually, but the procedure was the same. See Figure 3.27 for all models. All measurements were performed in CASYMS using an $Ar^+$ beam.

The ion beam of the CASYMS beam facility is almost monochromatic and parallel, with a very small angular dispersion of about 0.2°. The angular acceptance of main channel and WAP is much larger than this dispersion, unlike the S-channel, where the angular acceptance measured in CASYMS is about 0.3°. Assuming a Gaussian angle distribution, the deconvolved distributions of ion beam and instrument, i.e. the FWHM of the beam and the instrument acceptance, are similar. This means that we might exaggerate the instrumental angular acceptance, since we mainly map the beam distribution. This affects the calculation of the geometric factor. But the calculation of the active area of the S-channel is correct, considering the high beam flux and the entire irradiation of the S-channel aperture. The angular and energy acceptance contour plot could have a smaller elevation angle acceptance, reducing also the geometric factor. But the uncertainty due to beam flux fluctuation and low count rates on the SSL detector is comparable to the influence of the too wide angular acceptance, assuming a instrumental acceptance of 0.2°. Additionally, the geometric factor measurements are performed at a certain azimuthal angle. One has to keep in mind that the transmission depends on the azimuthal position, see Figure 3.22. The transmission varies for a given elevation angle and energy significantly over the whole azimuthal acceptance range.

### 3.6.3   Wide-Angle Partition

As for the two other channels, for FM1 and FS the geometric factor measurement was automated. For FM2 the measurement was done manually.

For FM1 and FS the ESA electrodes (ESA-I/ESA-O) were tuned for a beam energy of 5 keV/e. The beam intensity was below 1 kHz/0.1 cm² to prevent saturation of the SSL detector. The beam energy was changed from 3.8 keV/e to 6.2 keV/e in steps of 70 eV/e. The step size of the elevation angle scan was 0.7°. For each step data was accumulated during 20 seconds. In Figure 3.25 all signal images for FS are plotted.

For FM2 the procedure was similar to the one explained above for the main channel. The ESA voltage was changed between 135 V and 216 V in 2 V steps, the elevation angle between -7.0° and 9.5° in 0.5° steps.

See 3.28 for contour plots of all models. All measurements were performed in CASYMS, for FM1 and FM2 an $Ar^+$ beam was used, for FS a $He^+$ beam.

---

[14]Increasing the ESA voltage at a defined beam energy has the same effect as decreasing the beam energy for a given ESA voltage. So, to convert the ESA voltage into beam energy, the difference of the tuned ESA voltage to the nominal ESA voltage (i.e. for $E/q = 3.0$ keV/e $V_{ESA} = \pm 180$ V) times the analyzer constant $k_{ESA}$ times 2 must be added to the beam energy per charge (when the ESA voltage is lower than the nominal ESA voltage) or subtracted from the beam energy per charge (when the ESA voltage is higher than the nominal ESA voltage). E.g., (180 V$-$160 V) $\times k_{ESA} \times 2 + 3000$ eV/e$= 3330$ eV/e.
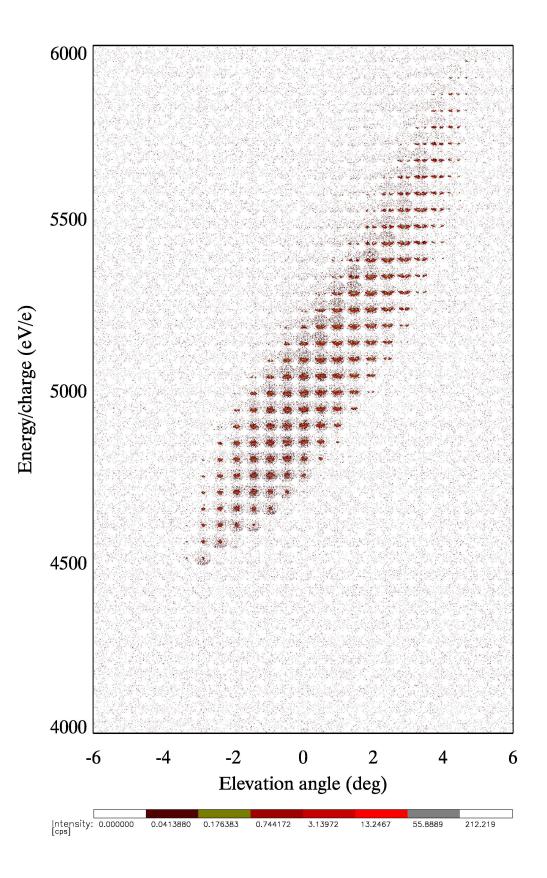
Figure 3.23: *FS main channel SSL images of the geometric factor measurement. The instrument was tuned for E/q = 5 keV/e and the beam energy was increased in steps of 50 keV/e from 4000 keV/e up to 6000 keV/e. For each beam energy the elevation angle was changed in steps of 0.5° from -6° to +6°. Accumulation time was 20 seconds.*
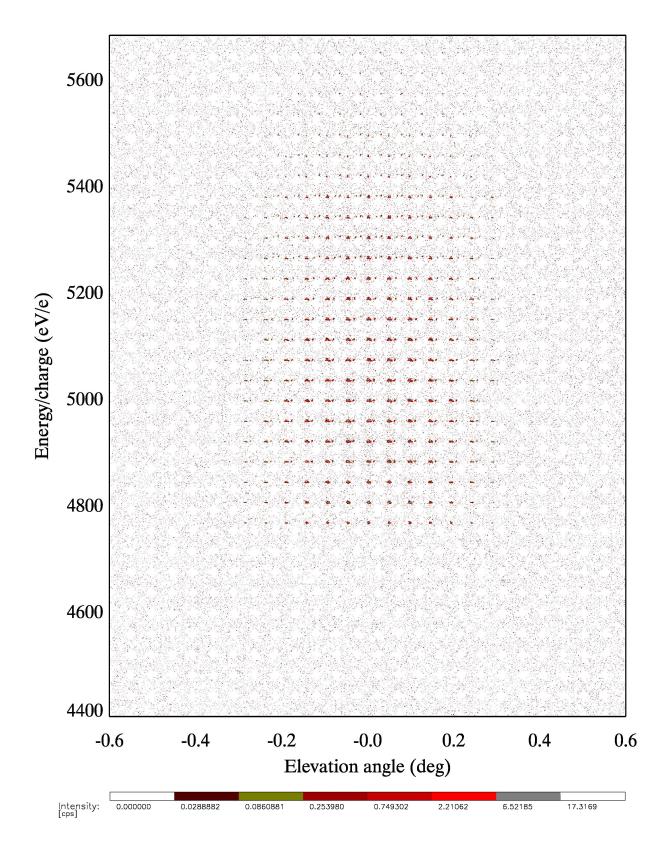
Figure 3.24: *FS S-channel SSL images of geometric factor measurement. The instrument was tuned for E/q=5 keV/e. The beam energy was increased in steps of 40 keV/e from 4400 keV/e up to 5680 keV/e. For each beam energy the elevation angle was turned in steps of 0.05° from -0.6° to +0.6°. Accumulation time was 30 seconds.*
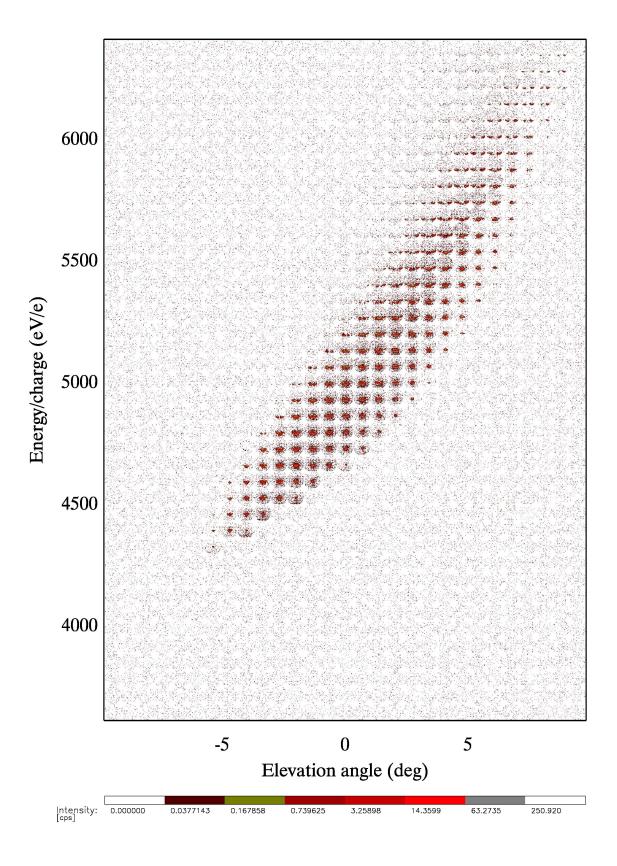
Figure 3.25: *FS WAP SSL images of the geometric factor measurement. The instrument was tuned for E/q=5 keV/e. The beam energy was increased in steps of 70 keV/e from 3600 keV/e up to 6400 keV/e. For each beam energy the elevation angle was turned in steps of 0.7° from -9.8° to +9.8°. Accumulation time was 20 seconds.*

| Channel | Azimuthal Position | FM1 | FM2 | FS |
|---|---|---|---|---|
| S-Channel | 0 | $1.41(4) \cdot 10^{-3}$ | $1.50(4) \cdot 10^{-3}$ | $0.91(3) \cdot 10^{-3}$ |
| Main Channel | 0 | $8.9(7) \cdot 10^{-1}$ | $7.5(5) \cdot 10^{-1}$ | $7.8(3) \cdot 10^{-1}$ |
| WAP | -90 | $8.2(3) \cdot 10^{-1}$ | – | – |
|  | -180 | $1.12(8)$ | $9.4(4) \cdot 10^{-1}$ | $1.02(5)$ |
|  | -38.5 | $4.7(2) \cdot 10^{-1}$ | – | – |

Table 3.3: *Active area of each channel (in cm$^2$).*
*FM1 and FS measured at E/q=5 keV/e, MC and WAP FM2 at E/q=3 keV/e. SC FM2 at E/q=5 keV/e*

### 3.6.4   Summary active area

For each channel and model, the highest value of the transmission matrix is taken as the active area. In Table 3.3 all active area values are listed. Comparing the three apertures, it is obvious that the main channel has a much larger transmission than the S-channel. This fulfills the design goal of the S-channel as being suitable for protons and alpha particles. The WAP has a slightly larger active area, what can be explained by the larger aperture, see the elevation angle scan in Figure 3.18. Since the two models which finally fly, should be as similar as possible, the comparison between the three models is interesting. Main channel and WAP show no larger discrepancies, but for the S-channel, the flight spare has a much smaller active area than the two other models. The reason is that the two slits of the FS S-channel are smaller than the slits of the two older models. This can also be seen when comparing the azimuthal response plots, Figure 3.22, where the FS has the smallest elevation angle acceptance range. Depending on the azimuthal position the active area for a given ESA voltage and deflection step can vary by a factor of 1.5. Summarizing, it can be concluded that the S-channel is the most difficult channel to describe. Due to the very small elevation acceptance a small deviation has a rather big impact on the transmission. However, the solar wind is neither perfectly parallel nor monochromatic, smearing out the expected count rate distribution over the deflection and ESA voltage steps.

The large calculated error for WAP and MC is mostly due to the large error of the measured beam intensity (relative error about 10 %) and for the S-channel also the smaller measured signal contributes. For all measured data the absolute error was taken as $\sqrt{\text{measured value}}$. The beam intensity is the weighted average of the seven innermost measured points during the beam scan. As error for each of this data points the Poisson error was taken.

The total relative error of the active area is the square root of the sum of the relative errors of each factor squared (see Equation (3.4)).

### 3.6.5   Summary geometric factor

For all channels and instruments the geometric factor is listed in Table 3.4. The geometric factor is always calculated for a 45° sector, allowing to compare all channels. The WAP has a wide elevation angle acceptance, whereas the S-channel has a very narrow angular acceptance due to the two very small slits (SAD, see Figure 3.1) at the entrance of the S-channel. The energy acceptance is comparable for all three channels, thus it has only a small influence on the geometric factor. The relation between energy and elevation angle acceptance is clearly visible from the transmission plots of main channel and WAP, e.g., the accepted elevation angle depends on the $E/q$ acceptance tuning and vice versa. The S-channel does not show such a relationship. The S-channel accepts only incident ions parallel to the line of sight through the two slits. This restricts the ion transmission through the S-channel very effectively.

Comparing the instruments, one sees that the WAP and the main channel geometric factors do not differ much for all three models. However, the S-channel geometric factor for the flight spare is significantly smaller than for FM1 and FM2. The reason for this is the same as for the active area. The S-channel slits of FS are smaller than for the two flight models. This is also visible in Figure 3.22 where the angular acceptance of the SC is shown. (The width of the FS slits is about half of the width of FM1 and FM2.) The geometric factor plots, Figure 3.27, support this observation. The energy acceptance is similar for all
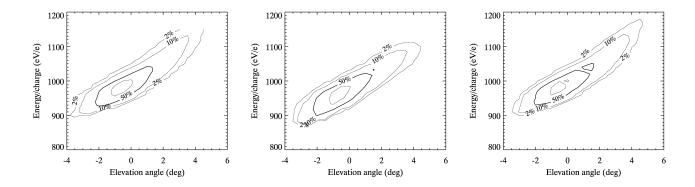
**Figure 3.26:** *Main channel geometric factor , beam energy $E/q = 5$ keV/e for FM1 and FS, beam energy 3 keV/e for FM2, $Ar^+$ beam for all models, energy normalized to 1000 keV/e. The contour line without label is at 90 % of maximum intensity.*
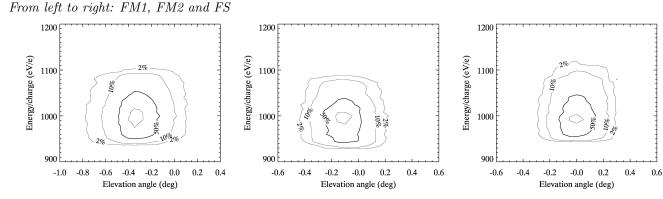*From left to right: FM1, FM2 and FS*



**Figure 3.27:** *S-channel geometric factor, beam energy $E/q=5$ keV/e for FM1, FM2 and FS, $He^+$ beam for FM1, $Ar^+$ beam for FM2 and FS, energy normalized to 1000 keV/e. The contour line without label is at 90 %.*
*From left to right: FM1, FM2 and FS*
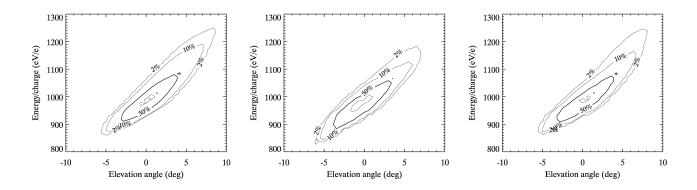


**Figure 3.28:** *WAP geometric factor, beam energy $E/q=5$ keV/e for FM1 and FS, beam energy 3 keV/e for FM2, $Ar^+$ beam, energy normalized to 1000 keV/e. The contour line without label is at 90 %.*
*From left to right: FM1, FM2 and FS*

|              |                     | **FM1**                | **FM2**                | **FS**                 |
|--------------|---------------------|------------------------|------------------------|------------------------|
| Channel      | Azimuthal Position  |                        |                        |                        |
| S-Channel    | 0                   | $6.0(5) \cdot 10^{-7}$ | $6.3(4) \cdot 10^{-7}$ | $3.2(3) \cdot 10^{-7}$ |
| Main Channel | 0                   | $3.15(4) \cdot 10^{-3}$ | $2.52(4) \cdot 10^{-3}$ | $2.41(3) \cdot 10^{-3}$ |
| WAP          | -90                 | $8.35(6) \cdot 10^{-3}$ | –                      | –                      |
|              | -180                | $6.82(7) \cdot 10^{-3}$ | $6.44(6) \cdot 10^{-3}$ | $6.39(6) \cdot 10^{-3}$ |
|              | -38.5               | $3.19(3) \cdot 10^{-3}$ | –                      |                        |

Table 3.4: *Geometric factor of each channel (in $cm^2$ eV/eV sr per 45° sector)*
*FM1 and FS were measured at $E/q = 5$ keV/e. FM2 for $E/q = 3$ keV/e except for SC, there $E/q = 5$ keV/e. For FM1 S-channel and WAP at -38.5° a $He^+$ beam was used, for all other an $Ar^+$ beam.*

|              |                          | **FM1** | **FM2** | **FS** |
|--------------|--------------------------|---------|---------|--------|
| Channel      | FWHM                     |         |         |        |
| S-Channel    | Energy acceptance (eV/eV)| 0.07    | 0.07    | 0.07   |
|              | Angular acceptance (°)   | 0.35    | 0.32    | 0.25   |
| Main Channel | Energy acceptance        | 0.12    | 0.12    | 0.12   |
|              | Angular acceptance       | 4.0     | 4.0     | 4.0    |
| WAP          | Energy acceptance        | 0.18    | 0.18    | 0.18   |
|              | Angular acceptance       | 7.0     | 7.2     | 7.0    |

Table 3.5: *Acceptance range for energy and angular acceptance plot. Full width half maximum of the transmission matrix (active area). $\Delta E/E_0$ and $\Delta\theta$ for the elevation angle $\theta$.*

three models, the energy acceptance of the S-channel is even comparable to the energy acceptance of the main channel at a given elevation angle, whereas the elevation angle acceptance is smaller for FS than for FM1 and FM2. The overall angular and energy acceptance ranges (FWHM of the contours, projected on the respective axis) are in Table 3.5, giving an impression of the total acceptance of the various channels. The calculated error is mostly due to the beam variations, especially at low energies ($\frac{\Delta I_{beam}}{I_{beam}} = 0.1$). The error of the geometric factor is calculated as the square root of the sum of all absolute errors squared of the terms in the sum (see Equation (3.6)). For more details see active area.
Looking at the S-channel energy and angular acceptance plots of the three models (Figure 3.27 and Figure 3.22), I would choose FM2 and FS as flight instruments, since they have similar energy and angular acceptance ranges. Looking at the values for the geometric factor or active area, one should chose FM1 and FM2. But since it is easier to deal with two different factors than with different geometry I would favor FM2 and FS.

## 3.7  Gate functionality

### 3.7.1  General

To prevent the more abundant particles in the solar wind like hydrogen and helium to enter the main channel and possibly saturate the detectors the particles must be deflected that these particles pass through the S-channel. When the S-channel is activated (negative voltage applied to SCI-U and SCO-L electrodes), all particles entering the main channel must be deflected by the *Gate Electrode* MG-L, which is connected to the SCO-L electrode. In flight the IDPU switches to the S-channel as soon as the count rate is higher than a predefined threshold value, see Section 1.3.

### 3.7.2  Measurements

**General**

Particles can influence the measurements in two ways:

1. When the S-channel is activated no particles should pass through the main channel. Therefore, it must be measured, how many particles enter the main channel and are counted at the exit slit of the ESEA, when negative voltage is applied to the gate electrode.

2. When the S-channel is switched off, no particles should pass through the S-channel. Therefore, it must be measured, how many particles pass through the S-channel by reflection.

To give a good approximation of the gate suppression, two kinds of experiments were performed:
(1) Measuring the flux through the main channel, when a finite potential is applied to the gate electrode and (2) measuring the flux through the disabled S-channel. These count rates were then compared to the count rates in regular measurement mode. To ensure best statistics the apertures were irradiated with a very high beam flux, up to 200 kHz/0.1 cm$^2$ for high beam energies.

**Particles entering main channel when S-channel enabled**

This measurement was performed as follows:

- Finite potential is applied to the gate electrode (MG-L), all other electrodes except for the ESA electrodes (ESA-I and ESA-O) are grounded.

- Intensive particle beam of various energies enters the main channel aperture.

- Long time measurements were done counting particles, which exit the ESA hemisphere. This was done for different elevation angles.

- Reference measurements through S- and main channel were performed.

For FM2 and FS both the angle dependence and the energy dependence were tested. First the elevation angle was scanned at a given beam energy. After that measurements with different beam energies were performed for the angle with highest gate signal. See Figures 3.29 and 3.30 for the measurements. The elevation angle for maximum gate signal of about 18° was also found by simulations.
Only a range of the detector image was used as *gate signal* (ROI1) for the calculation. For the same measurement also a reference range (ROI2) was selected. Then the ratio of the gate signal to the S-channel signal at 3 keV/e was calculated. All measurements were normalized by the beam intensity.

$$\frac{N_{Gate}}{N_{SC}} \quad < \quad 1.5 \cdot 10^{-3} \tag{3.7}$$

$$\frac{N_{Gate}}{N_{MC}} \quad < \quad 3.0 \cdot 10^{-6} \tag{3.8}$$

This shows that even a very weak signal through the S-channel should not be disturbed by particles entering the gated main channel. In addition, the number of counts is not larger than the noise level of the used MCP detector.
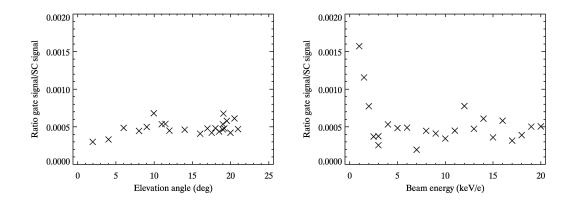
Figure 3.29: *FM2 gate test angle and energy scan. The angle scan was done at a beam energy of 3 keV/e. The beam energy scan was performed at an angle of 19°. For the energy scan the ratios are normalized by the beam energy. For low energies the beam intensity is underestimated.*
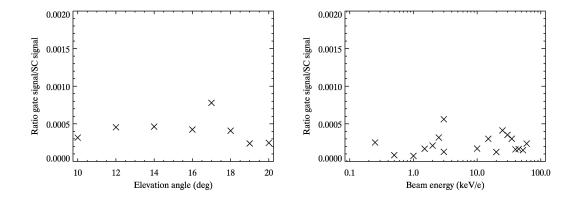


Figure 3.30: *FS gate test angle and energy scan. The angle scan was done at a beam energy of 5 keV/e. The beam energy scan was performed at an angle of 17°. For the energy scan the ratios are normalized by the beam energy. For low energies the beam intensity is underestimated.*
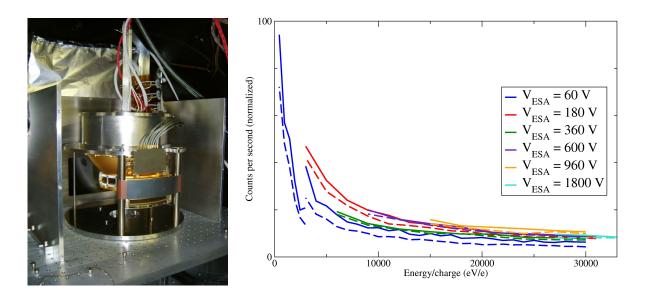
Figure 3.31: *To measure the flux of particles through the disabled S-Channel the Main Channel was blocked by a plate. This experiment was performed in CASYMS with a very intense beam.*
*For several ESA voltage tunings the beam energy was varied. The gate (solid line) and background (dashed line) signal was normalized by the beam intensity. Even at the maximum signal ($V_{ESA} = 60$ V and $E/q = 0.5$ keV/e. The signal is not larger than for other beam energies, but the beam intensity was much lower. The beam intensity measurements at these low beam energies have a large uncertainty because the beam profiles are not flat.) the ratio $\frac{N_{SC,refl}}{N_{SC}}$ is smaller than 0.005. The normalized SC signal is 4100 cps.*

### Particles entering the disabled S-channel

To measure the particle flux through the disabled S-channel the main channel was physically blocked to prevent particles from entering the main channel, see Figure 3.31. Another measurement was performed in the MEFISTO instrument chamber, where a very intense pencil beam was directed onto the S-channel. The spot size of the pencil beam in MEFISTO is about 2 cm in diameter, so no particles enter the main channel at the same time.

To measure the ratio of particles that still enter the S-channel to the number of particles expected passing through the main channel, the flux through the S-channel was counted and extrapolated to the main channel flux ($N_{MC} \simeq N_{SC} \cdot \frac{A_{Act,MC}}{A_{Act,SC}}$).

Measurements in MEFISTO gave the following suppression ratio:

$$\frac{N_{SC,refl}}{N_{MC}} \leq 10^{-7} \tag{3.9}$$

The measurement in CASYMS was performed for several beam energies and ESA voltage tunings (see Figure 3.31). The measurements gave the following minimum suppression ratio:

$$\frac{N_{SC,refl}}{N_{SC}} \quad < \quad 5 \cdot 10^{-3} \tag{3.10}$$

$$\frac{N_{SC,refl}}{N_{MC}} \quad < \quad 1 \cdot 10^{-5} \tag{3.11}$$

This value is an upper limit because the measurement depends strongly on the beam intensity measurement. Due to a not flat beam profile (minimum in the center), the beam intensity for low energies tends to be underestimated. This results in a higher normalization factor.

In addition, the measurement was always in the same order of magnitude as the noise level of the used MCP detector.

### 3.7.3 Summary and Conclusions

It could be shown that the measured signal was always smaller than the noise level of the used MCP detector. Neglecting the noise, the calculated ratios were below the statistical relevant values. So it can be stated:

- The gate electrode MG-L deflects effectively the particles entering the main channel when the S-channel is enabled.

- The signal of particles passing through the main channel is not influenced by particles entering the disabled S-channel.

## 3.8 Instrument function for PLASTIC entrance system/energy analyzer

The determined numbers and instrument response measurements allow to calculate the incoming solar wind flux from the measured count rate. It has to be noticed that all calibration measurements were performed with a parallel, almost monochromatic beam ($\Delta\phi < 0.2°$ and $\frac{\Delta E}{E} \leq 0.01$). But the solar wind has a kinetic temperature, which has to be considered. So the measured acceptance of the entrance system (active area $A_{act}$, see Section 3.6) from calibration data has to be convolved with the actual solar wind distribution:

$$A_{act,SW}(v, \alpha, \beta) = A_{act,CAL} * F_{SW}^* (v, \alpha, \beta) \tag{3.12}$$

where $F_{SW}^* = F_{SW}/n$ is the normalized solar wind distribution. The solar wind distribution $F_{SW}$ is assumed to be a three-dimensional Maxwellian distribution characterized by the kinetic temperature $T$ and the bulk velocity $\mathbf{v_b}$. The solar wind distribution is then given by:

$$F_{SW}^i(\mathbf{v}) = n_i\Big(\frac{m_i}{2\pi k_B T_i}\Big)^{\frac{3}{2}} \exp\Big( - \frac{m_i(\mathbf{v} - \mathbf{v_{b,i}})^2}{2k_B T_i}\Big) \tag{3.13}$$

with $n_i$ the density, $T_i$ the temperature and $\mathbf{v_{b,i}}$ the bulk velocity of an ion species $i$. According to investigations and data analysis of previous mission, the thermal velocity $v_{therm} = \sqrt{\frac{2k_B T_i}{m_i}}$ of the solar wind does not depend on the mass, meaning the temperature is proportional to the mass of the ion [61]: $v_{therm,i} = v_{therm}$.

The active area expected for a given solar wind distribution is then given by Equations (3.12) and (3.13):

$$A_{act,SW}(\mathbf{v}) = \int_{\mathbb{R}^3} A_{act,CAL}(\mathbf{w}) F_{SW}^*(\mathbf{v} - \mathbf{w}) \mathrm{d}^3 w \tag{3.14}$$

For spherical coordinates it follows:

$$A_{act,SW}(v, \alpha_0, \beta_0) = \int_{\mathbb{R}} \int_0^{2\pi} \int_0^{\pi} A_{act,CAL}(w, \alpha, \beta) F_{SW}^*(v - w, \alpha_0 - \alpha, \beta_0 - \beta) w^2 \cos\beta \mathrm{d}w \mathrm{d}\alpha \mathrm{d}\beta$$

In Figure 3.32 angular and energy acceptance contour plots are shown for different solar wind conditions.
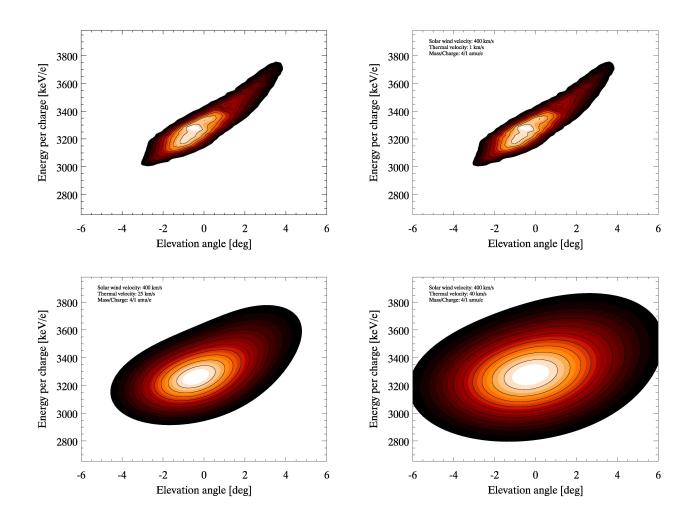
Figure 3.32: *Active area of main channel convoluted with different solar wind types, $He^+$ ions at 400 km/s. From top left to bottom right:*
*Active area measurement in CASYMS.*
*Active area convoluted with cold solar wind, $v_{SW} = 400$ km/s, $v_{th} = 1$ km/s.*
*Active area convoluted with normal solar wind, $v_{SW} = 400$ km/s, $v_{th} = 25$ km/s.*
*Active area convoluted with warm solar wind, $v_{SW} = 400$ km/s, $v_{th} = 40$ km/s.*

## 3.9    Summary and conclusions

### 3.9.1    Results

In the following tables all measured instrument parameters are summarized.

| Channel | Electrode | FM1 | | FM2 | | FS | |
|---|---|---|---|---|---|---|---|
| | | Analyzer constant | FWHM | Analyzer constant | FWHM | Analyzer constant | FWHM |
| S-channel | SCO-L | 3.23(1) | 10.40% | 3.25(1) | 10.64% | 3.19(1) | 10.40% |
| | SCI-U | 3.68(1) | 13.20% | 3.64(1) | 10.75% | 3.59(2) | 13.80% |
| | ESA | 8.46(1) | 6.35% | 8.46(2) | 6.26% | 8.38(3) | 6.12% |
| Main channel | ESA | 8.26(1) | 6.12% | 8.26(2) | 6.48% | 8.25(2) | 6.30% |
| WAP | ESA | 8.25(4) | 6.77% | 8.26(1) | 7.30% | 8.28(1) | 6.67% |

Table 3.6: *Analyzer constants (eV/eV)*

| Channel | FM1 | | FM2 | | FS | |
|---|---|---|---|---|---|---|
| | Deflection Constant | angular FWHM | Deflection Constant | angular FWHM | Deflection Constant | angular FWHM |
| S-Channel | 0.117(1) | 0.37 | 0.114(1) | 0.27 | 0.112(1) | 0.27 |
| Main Channel | 0.128(3) | 1.9 | 0.127(3) | 1.8 | 0.126(7) | 1.9 |
| WAP | – | 3.2 | – | 3.1 | – | 3.2 |

Table 3.7: *Deflection constants and angular acceptance ranges (deflection constant ° keV/e V$^{-1}$, angular acceptance in degrees)*

| Channel | Azimuthal Position | FM1 | FM2 | FS |
|---|---|---|---|---|
| S-Channel | 0 | $1.41(4) \cdot 10^{-3}$ | $1.50(4) \cdot 10^{-3}$ | $0.91(3) \cdot 10^{-3}$ |
| Main Channel | 0 | $8.9(7) \cdot 10^{-1}$ | $7.5(5) \cdot 10^{-1}$ | $7.8(3) \cdot 10^{-1}$ |
| WAP | -90 | $8.2(3) \cdot 10^{-1}$ | – | – |
| | -180 | 1.12(8) | $9.4(4) \cdot 10^{-1}$ | 1.02(5) |
| | -38.5 | $4.7(2) \cdot 10^{-1}$ | – | – |

Table 3.8: *Active area of each channel (in cm$^2$).*

| Channel | Azimuthal Position | FM1 | FM2 | FS |
|---|---|---|---|---|
| S-Channel | 0 | $6.0(5) \cdot 10^{-7}$ | $6.3(4) \cdot 10^{-7}$ | $3.2(3) \cdot 10^{-7}$ |
| Main Channel | 0 | $3.15(4) \cdot 10^{-3}$ | $2.52(4) \cdot 10^{-3}$ | $2.41(3) \cdot 10^{-3}$ |
| WAP | -90 | $8.35(6) \cdot 10^{-3}$ | – | – |
| | -180 | $6.82(7) \cdot 10^{-3}$ | $6.44(6) \cdot 10^{-3}$ | $6.39(6) \cdot 10^{-3}$ |
| | -38.5 | $3.19(3) \cdot 10^{-3}$ | – | – |

Table 3.9: *Geometric factor of each channel (in cm$^2$ eV/eV sr per 45° sector)*

### 3.9.2 Conclusions

I have discussed the ion optical calibration of the entrance system/energy analyzer of the PLASTIC sensor on STEREO. There are two flight models (FM1 and FM2) and a flight spare (FS) which had to be calibrated. Each of the three was carefully tested and calibrated and showed perfect functionality. Comparing the three models, the following can be concluded:

- All three models fulfilled the design goals as it is shown in Table 3.10.

- The analyzer constants are all similar for all three apertures. This has the advantage that the setting are similar for all models in flight. Particles passing through the S-channel enter the energy analyzer at a higher position (y coordinate in Figure 3.2) and under a different angle than those coming from the main channel. This explains the difference between the two corresponding analyzer constants.

- The angular deflection constants are similar, too, for all models. The geometry of the deflection plate allows full covering of $\pm 20°$ for ion energies up to $E/q = 43.2$ keV/e.

- All three models have similar active areas and geometric factors for the main channel and the WAP. When comparing the angular and energy acceptance (Figures 3.26 and 3.28) and the azimuthal angle response (Figure 3.19) the acceptance ranges are similar and the transmission matrices have comparable shapes. This ensures that the models have the same transmission in flight. Although the value for the active area and the geometric factor may differ, the overall acceptance is the same. The measured counts can more easily compared between the two instruments in space.

- The azimuthal acceptance of the WAP shows all mechanical features. All blockages are mapped, see in Figure 3.20. Nevertheless, in solar wind the beam has a spread in energy and angle, thus the features will be smeared out.

- The S-channel active areas and geometric factors differ more for all three models. Looking only at the measured values, FM1 and FM2 are very like, the transmission of FS is much smaller. The slits of FS are much narrower than the slits of FM1 and FM2. But comparing the angular and energy acceptance (Figure 3.27) and the complete angular transmission matrices of the S-channel (Figure 3.22) FM2 and FS show stronger similarity. However, the active area of the S-channel and the geometric factor are much smaller than requested (design goal) or expected from simulations. This reduces the transmission through the S-channel significantly. The reason is that the manufacturer achieved the design specifications very well (20 $\mu$m slit width).

- Generally, all three channels for all three calibrated instruments show a very good agreement. Contraves Space AG in Zürich did a very good job in manufacturing all three instruments.

The calibration process was a very long and repetitive process. But since we now know the instrument response very well, this will help during the data analysis from flight data. Anyway, the ESEA is only a part in the complicated transmission process. But because the part below the ESEA is the same for main and S-channel the understanding of the ESEA transmission is crucial for the deconvolution of the solar wind measurements. It is important to keep in mind that the beam used for calibration measurements in the CASYMS ion beam facility is an almost parallel monochromatic beam, allowing to map all the instrument features.

All information gathered during the calibration process is collected in plots or tables in this chapter or available in ascii format on the STEREO server, see Appendix E.

|  | Solar Wind Sector | | Wide Angle |
| --- | --- | --- | --- |
|  | S-Channel | Main Channel | Partition |
| Measured Species | H, He | He - Fe | H - Fe |
| Energy Range [keV/e] | 0.2 - 15 | 0.2 - 100 | 0.2 - 100 |
| $\Delta E/E$ |  |  |  |
| **Goal** | 0.06 | 0.06 | 0.13 |
| Simulation | 0.06 | 0.06 | 0.06 |
| EQM | 0.06 | 0.06 | 0.07 |
| FM1 | 0.06 | 0.06 | 0.07 |
| FM2 | 0.06 | 0.06 | 0.07 |
| FS | 0.06 | 0.06 | 0.07 |
| Geometrical Factor per 22.5° sector $[\text{cm}^2 \cdot \text{sr} \cdot \text{keV}/\text{keV}]$ |  |  |  |
| **Goal** | $3 \cdot 10^{-6}$ | $2.5 \cdot 10^{-4}$ | $2.2 \cdot 10^{-3}$ |
| Simulation | $5 \cdot 10^{-6}$ | $2.4 \cdot 10^{-3}$ | $3.5 \cdot 10^{-3}$ |
| EQM |  |  |  |
| FM1 | $3 \cdot 10^{-7}$ | $1.5 \cdot 10^{-3}$ | $3 \cdot 10^{-3}$ |
| FM2 | $3 \cdot 10^{-7}$ | $1.2 \cdot 10^{-3}$ | $3 \cdot 10^{-3}$ |
| FS | $1.5 \cdot 10^{-7}$ | $1.2 \cdot 10^{-3}$ | $3 \cdot 10^{-3}$ |
| Active Area $[\text{cm}^2]$ |  |  |  |
| **Goal** | $\sim 10^{-3}$ | $\sim 1$ | $-$ |
| Simulation | $1.2 \cdot 10^{-2}$ | 1.4 | 1.68 |
| EQM | $4.53 \cdot 10^{-3}$ | 0.99 | 1.31 |
| FM1 | $1.4 \cdot 10^{-3}$ | 0.9 | 1.12 |
| FM2 | $1.5 \cdot 10^{-3}$ | 0.8 | 0.94 |
| FS | $0.9 \cdot 10^{-3}$ | 0.8 | 1.02 |
| Instantaneous Field-of-View |  |  |  |
| **Goal** | $45° \times 1.5°$ | $45° \times 2°$ | $315° \times \pm7°$ |
| all FM | $45° \times 0.3°$ | $45° \times 2°$ | $315° \times 3°$ |
| Analyzer Constant [eV/eV] |  |  |  |
| Simulation | 8.334 | 8.127 | 8.127 |
| EQM | 8.47 | 8.35 | 8.23 |
| FM1 | 8.46 | 8.26 | 8.25 |
| FM2 | 8.46 | 8.26 | 8.26 |
| FS | 8.38 | 8.25 | 8.28 |
| Deflection Constant $[° \ (\text{keV/e}) \cdot \text{V}^{-1}]$ |  |  |  |
| Simulation | 0.0981 | 0.125 | $-$ |
| EQM | 0.114 | 0.129 | $-$ |
| FM1 | 0.117 | 0.128 | $-$ |
| FM2 | 0.114 | 0.127 | $-$ |
| FS | 0.112 | 0.126 | $-$ |

Table 3.10: *Goals for PLASTIC instrument compared with measurements. Simulation data from [2], EQM from [7].*
Instantaneous Field-of-View: *Accepted angular range for each sweeping step*

# Chapter 4

# Novel floatable detection system: *LaserCEM*

## 4.1 Introduction

The now existing detector systems like micro channel plate (MCP) detector or channeltron (CEM) detectors, that are widely used in space science, are difficult to operate at high voltage bias. The difficulty arises from bringing a small electrical signal in the mV range across a potential drop of several kV or even tens of kV. Flight instruments, e.g., PLASTIC, very often have a post-acceleration path after the energy analyzer that results in the MCP or CEM being operated at the post-acceleration potential. To be able to test the ion optical characteristics of such an energy analyzer either the complete flight instrument must be tested or a floatable particle detector on the post acceleration voltage must be used.

The largest difficulty is to transmit the detection signal to ground. In the detection system described here an optical fibre was used to transmit the signal from post-acceleration potential to ground potential. On the detector side we convert the signal into an optical signal using a VCSEL laser diode, and feed it into an optical fibre leading down to ground potential. On the ground side the optical signal is converted back to an electrical signal that can be used as a digital signal or an analog signal. The challenge of such a system is that a laser diode, that produces the light pulse, has a certain current threshold. Thus, the electrical signal from the particles must overcome this threshold to trigger the laser diode.

Before the now existing detector *LaserCEM II* has been developed, several detector types had been designed and constructed at the University of Bern. In [69] a detector is described where three microchannel plates are stacked to produce a current that is high enough to overcome the threshold of the used laser diode. Other setups were designed with batteries to provide a DC bias current a little bit below the threshold, so that the signal pulse from the detector exceeds the threshold of the laser diode much more easily.

In the present application a CEM was chosen because it is simpler to use and more robust than a MCP stack. Also for the CEM there is the problem that the delivered current pulse is too low to overcome the laser diode threshold. To amplify the current pulse several concepts were developed. In the last design coils were used as a transformer to amplify the pulse.

The novel instrument is a joint development of Martin Wieser, Peter Wurz, Jürg Jost, Martin Sigrist, Kurt Bratschi and Reto Karrer, all at that time working at the University of Bern.

### 4.1.1 Instrumentation

The main idea of the LaserCEM is to use a Channel Electron Multiplier (CEM)[1] for particle detection. A CEM delivers a charge pulse of about $10^7$ e per registered particle (i.e., a current pulse). Unfortunately,

---

[1]The Channel Electron Multiplier (CEM) used in the setup discussed here is from the company *Dr. Sjuts Optotechnik GmbH*, Germany. The type is KBL 25 RS, see Figure 4.2.

the amplitude of the current pulse is not enough to trigger a laser diode[2] and a suitable amplification is needed. The laser pulse from the laser diode is then transmitted to a counter on ground potential. The whole assembly with CEM and laser diode can be floated up to 30 kV. Additionally, a grid is mounted in front of the CEM aperture to minimize field effects at the CEM aperture. For a schematic of the LaserCEM setup see Figure 4.1.

Particles entering the CEM (see Figure 4.2) produce secondary electrons that are accelerated towards
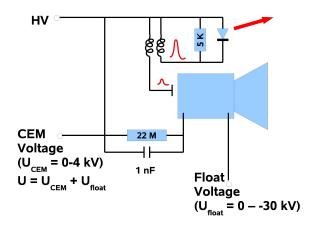


Figure 4.1: *Electrical schematic representing the measuring setup. The particles enter the CEM on the right side, the signal current amplitude is amplified by a 2:1 transformer and fed to the laser diode. The laser pulse is transmitted through a fibre to the counter on ground potential. The whole setup can be floated up to $\pm 30$ kV, the CEM voltage can be controlled separately.*
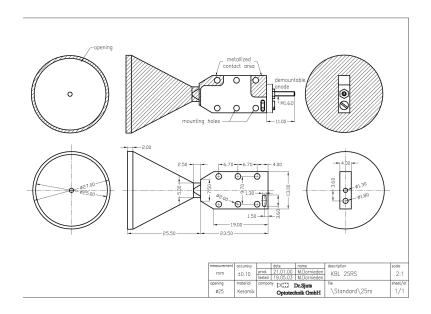


Figure 4.2: *The CEM KBL 25 RS from Dr. Sjuts Optotechnik GmbH*

the end of the biased cone initiating an electron avalanche. Depending on the CEM operation voltage the electron avalanche consists of $10^6$ to . For a pulse width of about 3 ns we get a current pulse of $I = \frac{10^6 \cdot 1.6 \cdot 10^{-19} \mathrm{e}}{3 \cdot 10^{-9} \mathrm{s}} \approx 5 \cdot 10^{-5}$ A or $5 \cdot 10^{-3}$ A for $10^8$ electrons. Since we want to operate the CEM at

---

[2]Laser diode for LaserCEM I: Type 2.5 Gbps Pigtailed 850 nm MM VCSEL 50/125 $\mu$m from *Avalon Photonics Ltd., Zrich, Switzerland*. Current threshold $\sim 2$ mA.
Laser diode for LaserCEM II: L2H-P790-LD-SM-L-3 from *Laser2000 GmbH, Germany*. Current threshold $\sim 1$ mA.
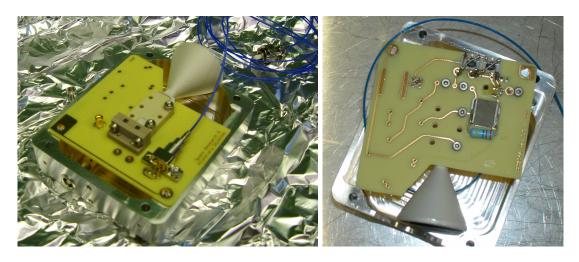
Figure 4.3: *LaserCEM I: The laser diode is visible on the left image, with the optical fibre (blue) directly attached. Right image:    The edges of the box containing the printed circuit board are rounded to optimize for high voltage operation.*

the lowest possible operation voltage (to preserve life time) a typical useful current pulse amplitude is about 1 mA. The current pulse arriving at the exit of the CEM is guided to the transformer were the current pulse is amplified by a factor two. The pulse current reaches the laser diode. The laser pulse from the laser diode is transmitted through an optical fibre out of the instrument chamber. In our setup, the optical signal is converted into an analog signal, which can be counted with a counter or registered with an oscilloscope.

The power supply used for both versions of the LaserCEM has one high voltage input (for the HV bias) and two high voltage outputs. One for the bias voltage (*Float voltage*) and a second output (*CEM voltage*) for the CEM bias voltage, where the provided CEM voltage is the sum of the CEM bias voltage and the float voltage, $U = U_{\mathrm{CEMbias}} + U_{\mathrm{Floatvoltage}}$.

### 4.1.2   Overview: Test and calibration experiments

At the beginning a prototype instrument was build, which is not discussed here. The first instrument used for calibration measurements was the *LaserCEM I*. The following instrument, *LaserCEM II*, has a new design and additional high voltage protection shield of the sensitive laser diode. But the concept described in the section above is the same for both LaserCEM.

## 4.2   LaserCEM I

LaserCEM I, see Figure 4.3, is the first detector of this kind that was used in STEREO/PLASTIC calibrations. The first measurements were performed for the IBEX_Lo prototype (see [62]). After that the LaserCEM was used for ion optical calibration measurements with post-acceleration voltage for PLASTIC ESEA, see Chapter 5. It allowed a high voltage bias up to 15 kV. The mechanical design is simpler than the design of the successor LaserCEM II where the laser diode is better protected against high voltage discharge. During measurements for IBEX, the laser diode of LaserCEM I was destroyed during a high voltage discharge. To prevent such damage the novel design of the LaserCEM II detector included a faraday cage protecting the laser diode, see Figure 4.7.

### 4.2.1   Detection efficiency

While the LaserCEM I was used, the detection efficiency decreased dramatically with time. The reason is that the surface of the CEM is cleaned when pumping the instrument chamber. The secondary electron yield depends on the cleanliness of the impinged surface, since the work function of the surface is lower for a dirty surface. Moreover, the CEM had to be operated at large operation voltage what led to fast

degradation of the CEM gain.

When using the LaserCEM I for PLASTIC ESEA measurements, it was also used for beam spot mapping after the post-acceleration path, see Section 5.3.7. To map the focused beam spot after the PLASTIC entrance system, the detector must be moved but neither the beam spot nor the ion optical path through the instrument must be changed. To achieve this, the detector and the instrument have to be turned in opposite directions, see Figure 4.4 for explanation.

Mapping the beam spot with the entire CEM aperture gave surprising results (see Figure 4.5). In the
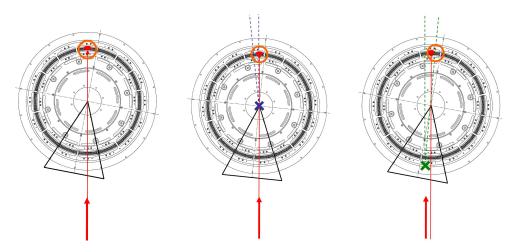


Figure 4.4: *Turning procedure with open aperture:*
Left: *Alpha = 0°, theta = −11° (At this theta position the focused beam passes through the center of a TOF structure aperture which is 22° wide. There is a spoke at theta = 0° .)*
Middle: *Alpha = 0°, theta is turned by +5°, theta = −6°; the focused particles hit the detector at the same location as on the left picture.*
Right: *Turning alpha by −5°, Alpha = −5°, theta = −6°*
*The particles pass now through the same TOF structure position as on the left picture, but they hit another position on the detector. The instrument and the detector are shifted to the right by approximately 5 mm.*
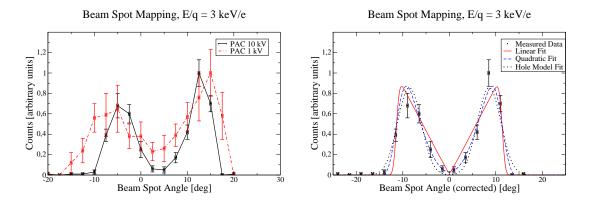


Figure 4.5: *Mapping of beam profile with open aperture. Measured data with fitted lines (see text for explanations)*

center where the signal was expected to be highest a drop in intensity was observed. The reason for this inhomogeneity seems to be the different detection efficiency of the CEM. In the middle the detection efficiency is very low, possibly due to the hole in the center of the CEM or due to different aging of the CEM surface. Three mathematical functions to model this effect were applied to the data:

1. *Linear Efficiency Model:*
   linear efficiency drop from the sides to the center, $L(x) = \left((a|x| + b)\chi_{[-x_0,x_0]}(x)\right)$, where $a$ and $b$

are parameters of the linear function, $x_0$ is the radial distance from CEM center and $\chi_{[-x_0,-x_0]}$ is 1 for $x \in [-x_0, -x_0]$ and 0 else. (See eq. (A.14) in Appendix A)

2. *Quadratic Efficiency Model:*
   quadratic efficiency drop from the sides to the center, $Q(x) = \left((ax^2 + b)\chi_{[-x_0,x_0]}(x)\right)$, where $a$ and $b$ are the parameters of the quadratic function and $\chi_{[-x_0,-x_0]}$ as defined above. (See eq. (A.15) in Appendix A)

3. *Hole Efficiency Model:*
   homogeneous efficiency over the whole surface except the center part (1 to 2 mm in diameter). In the center the detection efficiency was considered at least ten times smaller than on the sides, the hole is described with two characteristic functions: $H(x) = \left(\chi_{[-a,-b]}(x) + \chi_{[b,a]}(x)\right)$, where $a$ and $b$ are the radial positions of the hole and $\chi_{[-x_0,-x_0]}$ as defined above. (See eq. (A.16) in Appendix A)

All three models gave reasonable good agreement with the measurements and we cannot favor one. So the conclusion was that the efficiency difference could be due to a mixture of different detection efficiency and aging of the surface. To prove this and also to minimize the influence of different efficiency, a slit was mounted in front of the CEM aperture, see Figure 4.6. With a slit aperture in front of the CEM the influence of the detection position could be minimized at the prize of detection area, see Section 5.3.7.
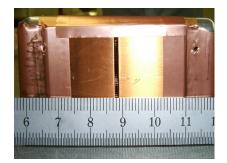


Figure 4.6: *LaserCEM I with two copper plates establishing a slit aperture.*

## 4.3   LaserCEM II

The most important improvement to older versions of the LaserCEM detector, is the faraday cage protecting the very sensitive laser diode against discharge from the detector box. Also a new laser diode type is used with a lower current threshold. Additionally, the detector has got a longer and less wide housing than its predecessor. This has the further advantage that it is easier to mount when space is restricted. Figure 4.7 shows an isometric drawing and Figure 4.8 shows two pictures of LaserCEM II. The electronic setup is shown in Figure 4.9.
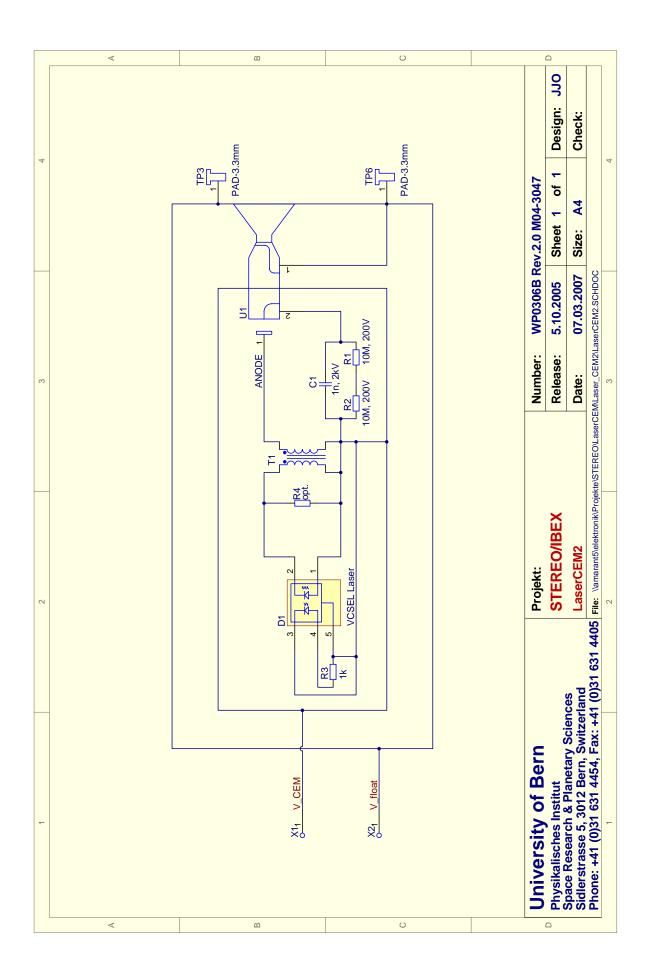
Figure 4.7: *Drawing of LaserCEM II. Well visible the faraday cage protecting the laser diode and proximity electronics from discharges. Drawings courtesy of K. Bratschi, UBe.*



Figure 4.8: *Pictures of LaserCEM II* Left: *Faraday cage of laser diode and electronics removed .* Right: *Assembled LaserCEM II without cover and grids in front of the CEM aperture. Courtesy Jürg Jost, UBe.*

Figure 4.9: *Drawing of LaserCEM II. Curtesy of Jürg Jost, UBe.*

### 4.3.1 Experimental setup

The first functionality tests before assembly were performed in the electronic workshop by J. Jost. After completing the tests for the channeltron and the laser diode, the detector was assembled. Before testing the detection capabilities, the detector had to go through a partial discharge test up to 30 kV. The partial discharge tests took place in the MEFISTO facility vacuum chamber, see Figure 4.10, the detection tests in CASYMS facility vacuum chamber, see Figure 4.11.

A pinhole was mounted on the beam scanner in the instrument chamber of CASYMS. This allowed on one side to irradiate the detector with lower particle flux and on the other side, it permitted to irradiate the CEM surface locally. The pinhole diameter is 3.61 mm. Assuming a parallel ion beam the irradiating spot size is $\sim$ 4 mm in diameter. The distance pinhole CEM aperture is 25 cm. When the pinhole was not in the beam, the whole CEM aperture was uniformly irradiated.

All measurements were performed with a counter[3]. The trigger level was about 40 mV. The counting mode was *Integration Mode.* Usually an integration time of 5 seconds was chosen.



Figure 4.10: *The LaserCEM II mounted in MEFISTO instrument chamber for partial discharge tests. The LaserCEM is placed inside an aluminium box. The distance test box to the LaserCEM is at least 2 cm.*



Figure 4.11: *The LaserCEM II mounted in CASYMS instrument chamber. The aperture points towards ion beam. On the left side the beam scanner can be seen. A plate with a 3.61 mm diameter pinhole is mounted on the beam scanner allowing position mapping. See text for explanations.*

### 4.3.2 High voltage testing

The high voltage tests took place in the MEFISTO chamber, see Figure 4.10. During these tests the bias voltage was slowly increased to 30 kV. To monitor the partial discharges or possible high voltage discharges the special partial discharge equipment of the electronic workshop of the physics institute of UBe was used, with which the applied voltage and partial discharge current can be measured. A partial discharge at the high voltage feedthrough caused a discharge current in the interior of the LaserCEM, which destroyed the laser diode. After replacing the high voltage feedthrough the tests were continued and showed no major partial discharges up to 30 kV. After long term periods (10 hours) on a bias voltage of 30 kV it can be guaranteed that the LaserCEM II is suitable to float on a high voltage bias up to 25 kV.

### 4.3.3 Laser pulse analysis

The laser pulse signal is converted to an analog signal by a opto-electonic converter. For the LaserCEM II a special converter was constructed allowing also to amplify the signal. The analog output signal can be fed into a counter or an oscilloscope. Since the laser diode has a current threshold, electronic noise from

---

[3]Universal counter, model HP 53132A, 225 MHz

the detector is suppressed. Each pulse is caused by a particle entering the CEM. To exclude noise from the amplifier the trigger level of the oscilloscope or the counter has to be set accordingly. A typical pulse from the opto-elecronic converter is shown on Figure 4.12. The average pulse width of the pulses is about 5 ns FWHM, the pulse height is about 200 to 500 mV, depending on the amplification.
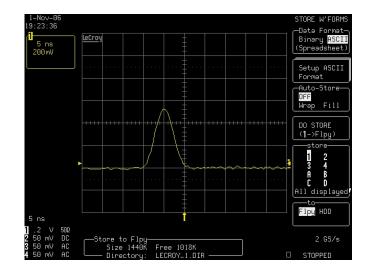


Figure 4.12: *Screen shot of a typical pulse from the laser diode. Pulse is 5 ns FWHM , pulse height 500 mV, trigger level 40 mV. The pulse is positive.*

### 4.3.4 Functionality tests

First functionality tests were performed after mounting the LaserCEM II in CASYMS and pumping the instrument chamber. Before the CEM was irradiated by an ion beam, it was tested if the residual ions or electrons can be detected by the LaserCEM. After these first tests all unnecessary ion or electron sources (e.g., cold cathode pressure gauge) were switched off to minimize the background.

**Efficiency versus CEM voltage $V_{\mathrm{CEM}}$**

The nominal CEM voltage is about 2.8 kV. A higher CEM bias would increase the detection efficiency but it would also accelerate the aging process. During measurements with the LaserCEM I the detection efficiency decreased rapidly with time, since the CEM surface was cleaned due to outgassing. To define the nominal voltage a CEM voltage scan was performed. The count rate increased with increasing CEM voltage.

**Efficiency versus ion beam energy**

The count rate was measured for different beam energies. Since the beam intensity increased for higher beam energies, the counts $N_{\mathrm{LaserCEM}}$ during a time $t$ must be divided by the beam flux $\Phi_{\mathrm{CASYMS}}$ to get the active area of the detector:

$$A_{\mathrm{act}} = \frac{N_{\mathrm{LaserCEM}}}{\Phi_{\mathrm{CASYMS}}\, t}$$

All measurements were performed with the reduced beam (pinhole), because irradiating the entire aperture caused saturation of the CEM. Figure 4.13 shows a measurement for a CEM voltage 2.9 kV, Figure 4.14 one for a CEM voltage 3.4 kV. For high CEM bias voltage, there was no longer a significant energy dependence indicating a good operation voltage. And at higher CEM voltage the count rate no longer depends on the beam energy. This indicates that with a CEM voltage above 3 kV, the signal pulse from the CEM is high enough to exceed the laser diode threshold.
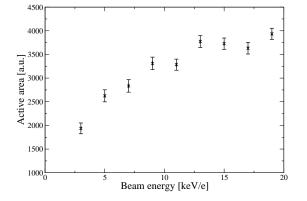
Figure 4.13: *Active area versus beam energy. The active area is the count rate divided by the beam flux per $cm^2$. The pinhole was in the beam, the irradiated position was the same for all energy steps. The CEM voltage was $V_{CEM} = 2900$ V. With increasing energy the active area increased.*
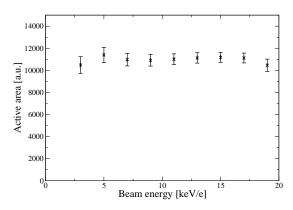
Figure 4.14: *Active area versus beam energy. The active area is the count rate divided by the beam flux per $cm^2$. The pinhole was in the beam, the irradiated position was the same for all energy steps. The CEM voltage was $V_{CEM} = 3400$ V. The active area shows no dependence on the energy.*

### Conclusions of functionality tests

The functionality tests demonstrated that the concept of the LaserCEM works. The effects of beam energy or intensity on the count rate must be an effect of the amplitude of the current pulse coming from the CEM, since standard CEM work without saturation for irradiation frequencies up to $MHz/cm^2$. No such high beam intensities were used during these measurements. So the solution must be either to use a laser diode with a lower threshold, to increase the pulse voltage from the CEM or a transformer with higher current amplification.

### 4.3.5   Position response measurements
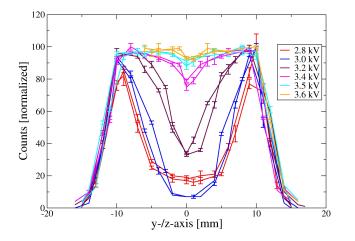
Since LaserCEM I showed a large position dependance of the detection efficiency, a thorough position response measurement was performed with LaserCEM II as well. Unlike LaserCEM I, where the beam was focused by the PLASTIC ESEA, see Section 4.2, the pinhole in front of the detector was used to measure the position response of LaserCEM II. The CEM surface could be irradiated moving the CASYMS beam scanner in y- and z-direction, see Figure 4.11. Positive z is upwards, positive y is to the right in beam direction.

The beam intensity was very low, preventing to saturate the CEM detector. For all CEM voltages a y- and a z-axis scan was performed, see Figure 4.15. The detector was on $-0.1$ kV bias voltage to repel residual electrons. The measurement revealed a large CEM voltage dependence, the dip in the center of the CEM even disappears when the CEM voltage $V_{CEM}$ is high enough. For $V_{CEM} = 3000$ V a complete 2D response mapping was done, covering the whole CEM aperture. The plot on Figure 4.16 supports the assumption that the detection efficiency is highest at the boundaries of the CEM and smallest in the center of the CEM.

### Conclusion from position mapping

Figure 4.15 shows that all particles are counted, when the CEM voltage is high enough. If a particle hits the CEM surface in the center, it produces less secondary electrons than when it hits the surface at the boundaries. The reason must be that secondary electrons from particles that hit the boundaries, are accelerated and produce additional secondary electrons. The electron avalanche is thus higher than from particles impinging in the center.

A possible remedy is that a thin carbon foil is mounted in front of the CEM aperture. The passing particles are spread in angle and thus in area and secondary electrons from the carbon foil enhance the
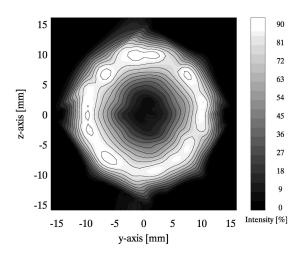
Figure 4.15: *y- and z-axis scans over the whole aperture of the LaserCEM. Always the same post acceleration voltage $V_{PAC} = 0.1$ kV. With increasing CEM voltage $V_{CEM}$ the dip in the center of the CEM disappears.*



Figure 4.16: *Contour plot of the measured signal. CEM voltage $V_{CEM} = 3000$ V and post acceleration voltage $V_{PAC} = 0.1$ kV preventing electrons to enter the detector.*

electron avalanche in the CEM. This would limit the use of the detector to energies of $\sim 1$ keV/nuc. Another solution would be to increase the amplitude of the voltage pulse from the CEM externally, see conclusions of this chapter.

## 4.4 Calibration measurements with LaserCEM

With LaserCEM I calibration measurements with PLASTIC ESEA were performed, see Chapter 5. The detector was used with bias voltage of 10 to 15 kV, allowing to test the ion optical capabilities of the PLASTIC ESEA.

With the new design, LaserCEM II, no measurements were performed yet. But the novel system will be used with future space missions.

## 4.5 Conclusions

The detector presented here is a working detector with the advantage, that it can be used on high voltage bias. The signal is converted into a laser pulse that is transmitted optically to ground potential. Thorough high voltage tests showed that the detector is stable using float potential up to 25 kV, allowing ion optical calibration measurements with post acceleration. At nominal CEM voltage the LaserCEM II showed a strongly position dependent detection efficiency, since the current from particles impinging at the center of the CEM is too weak to trigger the laser diode. This effect can be minimized by mounting a carbon foil in front of the CEM aperture, which would reduce the position dependence.

Additionally, another idea is pursued. A second fibre is fed into the LaserCEM II, allowing to provide a bias current for the laser diode. The principle is the same as for the signal processing from the detector, a laser pulse is converted back into a current. The next tests with the LaserCEM II should already use this principle.

# Chapter 5

# Calibration of the PLASTIC entrance system/energy analyzer with post-acceleration

## 5.1 Introduction

### 5.1.1 General remarks

The calibration of the PLASTIC Entrance System/Energy Analyzer (ESEA) was performed with a position sensitive microchannel plate detector (SSL [41]), which was on ground potential. In the integrated instrument the particle detectors of the Time-of-Flight section are on a high negative bias voltage (e.g., 20 kV). By this post-acceleration voltage the particles leaving the ESEA are focused towards the carbon foil. Different bias levels of the detector may affect the ion optical properties in the region of the ESEA exit. Thus for more rigorous comparisons of the ESEA calibration measurement (without post acceleration) with the calibration measurements of the integrated instrument, a floatable detector is needed.

Because the detector used here only provide restricted spatial information about the beam spot, simulations with the SIMION ion optical simulation software, see [14], are used to visualize the detailed focusing effects of the applied post-acceleration. See Figure 5.1 for simulated trajectories for beam energy 3 keV/e with and without post-acceleration voltage and in Figure 5.2 the corresponding beam images at the entrance of the LaserCEM detector are shown. For simulations for 5 keV/e, see Figures 5.3 and 5.4. The simulations show the large influence of the post-acceleration voltage on the ion trajectories.

Since the detection system used for these measurements has a very low detection efficiency, only the main channel and WAP could be tested. The count rate of ions passing through the S-channel was too low to be measured by the detector.

### 5.1.2 LaserCEM detector

Because of technical difficulties associated with electrically floating a detector, a new particle detection system was designed. The detection system used here, the LaserCEM, is described in detail in Chapter 4. The CEM bias voltage can be tuned separately from the high voltage bias. During the presented measurements the CEM voltage was between 2800 V and 3000 V. Because the detection efficiency decreased during the measurements the CEM voltage had to be increased to get enough signal counts. This enhanced the detection efficiency but also accelerated the degradation of the CEM surface.

With this newly designed detection system it is now possible to perform calibration measurements with applied post-acceleration voltage, but still a quite simple experimental setup. However, the detector (LaserCEM I) has still two issues to be improved:

- The signal is not absolutely calibrated, so only relative intensity has been considered in this study.

- The efficiency steadily decreases with time. The measurements have been corrected for this effect.

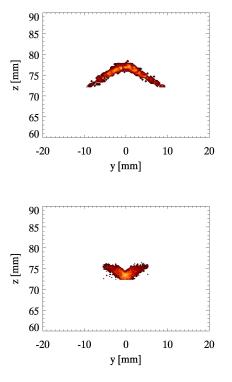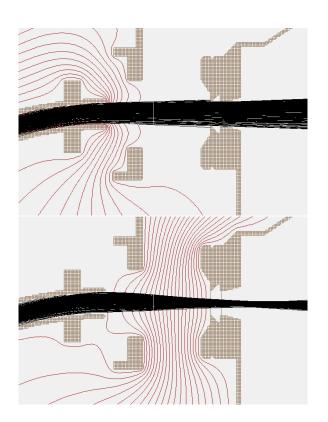Figure 5.1: *Beam trajectories for $E/q = 3$ keV/e and $V_{PAC} = 0$ kV (*top*) or $V_{PAC} = 15$ kV (*bottom*).*



Figure 5.2: *Beam image at CEM entrance position for $E/q = 3$ keV/e and $V_{PAC} = 0$ kV (*top*) or $V_{PAC} = 15$ kV (*bottom*).*
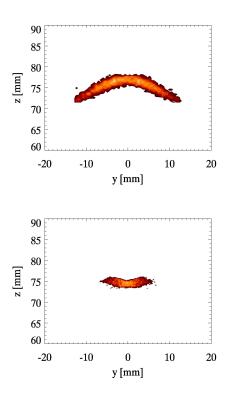


Figure 5.3: *Beam trajectories for $E/q = 5$ keV/e and $V_{PAC} = 0$ kV (top) or $V_{PAC} = 15$ kV (bottom).*



Figure 5.4: *Beam image at CEM entrance position for $E/q = 5$ keV/e and $V_{PAC} = 0$ kV (top) or $V_{PAC} = 15$ kV (bottom).*

The longer the instrument chamber is pumped the smaller is the detection efficiency of the CEM due to outgassing, what decreases the secondary electron yield.

After some days the efficiency does not drop as rapidly but becomes relatively constant. However, the detection efficiency is very low, about five times smaller than just after pumping.

When the chamber is vented the detection efficiency after pumping down is higher again. The same effect can be achieved when air is introduced through the leak valve of the vacuum chamber. The moist air on the CEM surface increase the detection efficiency again.

### Measurement principles with LaserCEM detector

- Before taking measurements one should wait about 24 h after closing and pumping. This ensures that the detection efficiency does not change too rapidly over the course of the measurements.

- When doing a complete scan (e.g., an ESA voltage scan) one should take two measurements of each scan value, starting at one end of the series and repeating it from the other end of the series. Adding these measurements together minimizes the effect of the decreasing detection efficiency.[1]

- The signal from the optical receiver should be monitored with an oscilloscope to select the right threshold value and to check the signal shape (one or two peaks). The width of the peaks on the oscilloscope is about 10 ns. The pulses are negative pulses.[2]

- The threshold of the counter[3] must be selected so only a real particle signal is counted. (Threshold levels of -30 to -35 mV have been used.)[4]

### 5.1.3 Overview over the Measurements

First experiments were performed in September and October 2005 in the CASYMS ion beam facility at the University of Bern. A second series of experiment was completed in January and February 2006.

### First experiments:

1. First Measurements with the LaserCEM detector:

   - High voltage tests of the PAC section up to 15 kV
   - Detection acceptance tests with a direct beam onto the detector

2. Intensity dependence on the applied post-acceleration voltage to the PLASTIC ESEA and upper TOF mockup.

3. Elevation and azimuthal angle measurements with the Main Channel (MC) aperture of PLASTIC FS

4. ESA voltage measurements with MC of PLASTIC FS

5. Combined azimuthal scans to map the beam spot after PAC path.

Because the detection efficiency of the CEM can vary significantly across the CEM surface, see Section 4.2.1, an approximately one millimeter wide slit was mounted in front of the CEM aperture to minimize spatial effects of the detection efficiency for the second series of measurements. Additionally, the slit provides high resolution when mapping the focused beam spot. See Figure 5.5.

---

[1] Assuming even a constant decreasing factor with time, the decreasing efficiency can be neglected.

[2] The laser diode used has its own threshold so no detector noise should be collected. Any noise signal is electronic noise from the opto-electronic converter, no background noise of the measurements. The observed signal on the oscilloscope are real particles detected by the CEM. The current threshold of the laser diode is about 1 mA.

[3] Universal counter, model HP 53132A, 225 MHz

[4] The *Integration* counter mode was used, triggered on negative slope, 50 $\Omega$ resistivity.
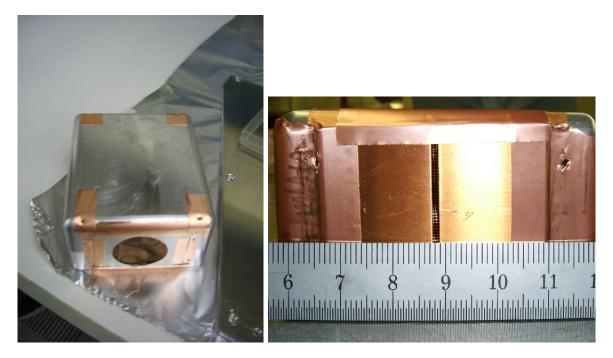
Figure 5.5: *The LaserCEM detector. On the left image the full CEM aperture is exposed to the beam. A grid reduces field effects. On the right image the slit is visible, which reduces the influence of the locally different detection efficiency of the CEM.*

**Second experiments:**

1. Functionality tests

2. PAC voltage scans

3. Energy and elevation angle acceptance measurements (geometric factor measurements)

4. ESA voltage scans with different PAC voltages of the suprathermal sector of WAP

5. Azimuthal angle measurements of main channel and WAP

All measurements of the second series were performed with the slit aperture in front of the LaserCEM.

## 5.2    Experimental Setup

### 5.2.1    Experimental Setup in CASYMS

#### Mounting of PLASTIC FS in CASYMS

The PLASTIC ESEA Instrument is mounted upsidedown on a 3-axes table, two turning axes (alpha and beta) and a translation axis (z) for up and down movements. In addition the instrument is fixed on a turning plate (theta axis) which can be turned by $\pm 180°$. See Figures 5.6 and 5.7 for details.

#### Mounting of LaserCEM detector

The LaserCEM detector is mounted above the structure where the carbon foils are mounted in PLASTIC (*TOF structure*). The distance between the exit slit of the ESEA and the location of PLASTIC carbon foil is 1.2 cm, the distance between the last grid of the TOF structure and the grid in front of the LaserCEM is 2.4 cm. See Figure 5.8.

The detector is mounted on the alpha-beta-turntable in the CASYMS instrument chamber but not on the theta turning plate. Thus it does not move when the theta axis is turned.
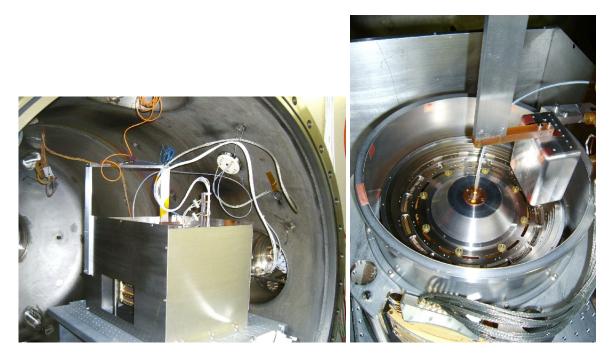
Figure 5.6: *Mounting of PLASTIC FS and the LaserCEM detector in CASYMS. The LaserCEM detector is mounted 2.4 cm away from the last grid of the TOF structure.*
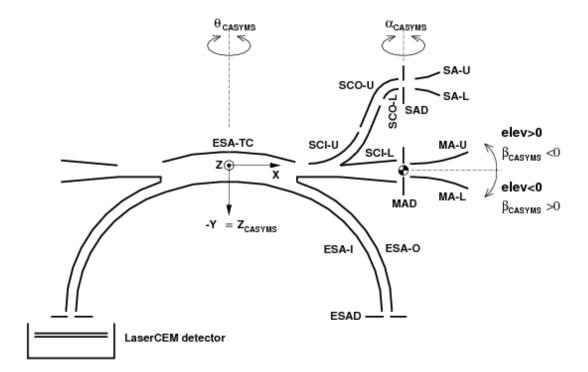


Figure 5.7: *Turning Axis in CASYMS (figure adapted from [2])*
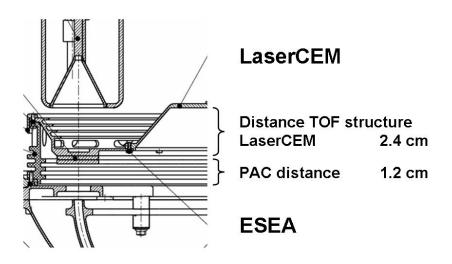
Figure 5.8: *Mounting of LaserCEM above the TOF structure.*

### 5.2.2   Turning procedure in CASYMS for beam spot shape measurements

**Overview**

In CASYMS there are two azimuthal turning axes, alpha and theta (see Figure 5.7). When the instrument is turned around the theta axis the detector is not moved. The beam is focused on the same location of the LaserCEM, only having a different trajectory through ESEA and TOF section, entering at a different azimuthal angle. The LaserCEM must be moved as well to measure the profile of the focused beam. During the first beam spot mapping measurements it was observed that the detection efficiency varies across the CEM surface. So instead of measuring the beam spot the spatial dependence of the CEM detector was measured. As mentioned above in a second setup a slit was mounted in front of the CEM aperture. The beam spot mapping procedure is described in the following two paragraphs.

**CEM full aperture**

The detection in the CEM the signal strongly depends on the position where the particles hit the CEM. This happens because the focused beam irradiates the CEM surface differently. This effect will be shown in Section 5.3.7. In Figure 5.9 the turning procedure for assessing the CEM efficiency position dependence is explained.

**CEM slit**

With a slit aperture the beam spot can be more effectively mapped and the influence of the detection efficiency variation with position can be minimized. The turning procedure is similar to the one described above. See Figure 5.10 for details and explanation.

## 5.3   Measurements

### 5.3.1   Overview

The measurement procedure was already outlined above (Section 5.1). In addition one has to consider the very low count rate (about 20 counts per second or less), thus the integration time must be increased. The measurements were performed as follows:

- Start at one end of the series (e.g., 160 V for an ESA voltage scan)
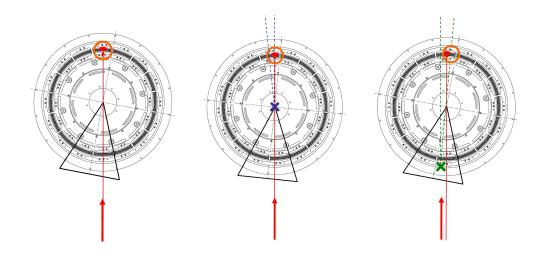
Figure 5.9: *Turning procedure with open aperture:*
*Red arrow indicates the direction of the beam, the red spot is the focus of the beam at the exit of the ESEA, the orange circle is the CEM. The triangle symbolizes the SWS.*
Left: *alpha = 0°, theta = −11° (At this theta position the focused beam passes through the center of a TOF structure aperture which is 22° wide. There is a spoke at theta = 0° .)*
Middle: *alpha = 0°, theta is turned by +5° (blue dashed line), theta = −6°; the focused particles hit the detector at the same location as on the left picture.*
Right: *turning alpha by −5° (green dashed line), Alpha = −5°, theta = −6°*
*The particles pass now through the same position as on the left picture, but they hit another position on the detector. The instrument and the detector are shifted to the right by approximately 5 mm.*
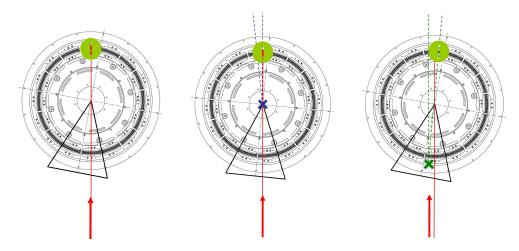


Figure 5.10: *Turning procedure with slit aperture:*
*Red arrow indicates the direction of the beam, the red spot is the focus of the beam at the exit of the ESEA, the green circle represents the CEM with the slit. The triangle symbolizes the SWS.*
Left: *alpha = 0°, theta = −11° (At this theta position the focused beam passes through the center of a TOF structure aperture which is 22° wide. There is a spoke at theta = 0° .)*
Middle: *alpha = 0°, theta is turned by +5° (blue dashed line), theta = −6°; the focused particles hit the detector at the same location as on the left picture.*
Right: *turning alpha by −5° (green dashed line), Alpha = −5°, theta = −6°*
*The particles pass now through the same TOF structure position as on the left picture, but they hit another position on the detector. The instrument and the detector are shifted to the right by approximately 5 mm.*
*With the slit only a small part of the beam spot is detected. The beam shape can be mapped with this procedure.*

- Integrate signal during 5 second intervals

- Take at least five such intervals (at least 25 seconds total)
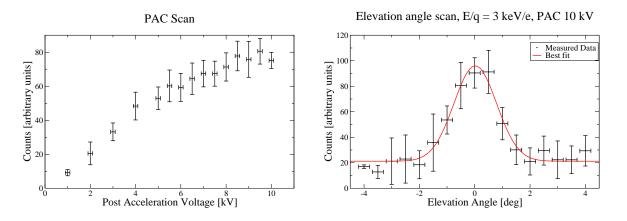
Figure 5.11: Left: *post-acceleration voltage scan*
Right: *elevation angle scan with E/q = 3 keV/e and $V_{PAC}$ = 10 kV.*
*(Both measurements performed with full aperture of LaserCEM, for the elevation angle scan the counter threshold was set high such that background signal was collected (∼ 20 counts).)*

- Repeat the last two steps for each measurement step

- When the end of the series is reached, the same procedure is used in repeating the measurement in reverse order.

A counter was used to count the particles. The threshold of the counter is set to suppress the electronic noise occurring after the optical converter. It was set between -35 and -30 mV, depending on the noise level of the electronics.

### 5.3.2   ESEA with post-acceleration measurements with full area LaserCEM detector

#### Post-acceleration voltage scan

As seen in Figure 5.11, the collection efficiency through the ESEA did not increase beyond an applied PAC voltage of 8 kV. As the PAC voltage is increased, the beam passing the ESEA becomes more focused. For PAC voltages higher than 8 kV the beam spot size on the CEM position is smaller than the aperture of the CEM (2.5 cm) and thus the beam is not cut by the TOF structure.

#### Elevation angle scan

During functionality tests also an elevation angle scan was performed, see in Figure 5.11. The angular acceptance range is similar to the angular acceptance of the ESEA without PAC, indicating that all particles exiting the ESEA pass through the TOF mockup aperture. On the flanks of the elevation angle plot, the signal is not zero as it is expected. This is due to an unsuitable counter setting in which the trigger level was set too low. In later tests the signal on the flanks was zero as expected.

### 5.3.3   Main channel azimuthal angle scans

For azimuthal scans only the rotating plate on which the instrument is mounted is turned (theta axis, see Figure 5.7). The alpha angle was fixed during the azimuthal angle scan.
The intensity varies due to the shape of the TOF structure and the grids over the carbon foil aperture (see figure 5.12).

#### Measurements with full aperture

Two azimuthal scans were performed at two different alpha angles, -5° and 0°. Since the focused beam hit the sides of the CEM surface at -5°, the count rate was much higher than for the measurement at
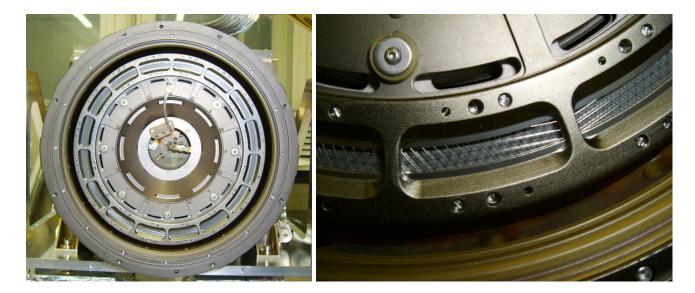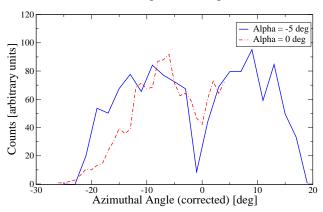
Figure 5.12: *Left:* TOF structure of the integrated instrument. For the PAC measurements a similar TOF structure is used.
*Right:* Picture of one aperture in the TOF structure. The grids can be seen.



Figure 5.13: *Azimuthal angle scan with full aperture. PAC 10 kV, two different alpha angle positions.*

alpha=$0°$. Turning around the alpha axis also changed the exit position of the beam at the exit slits of the ESEA. To be able to compare the two measurements, one has to shift the azimuthal position of the -$5°$ measurement by +$5°$, see Figure 5.13. The spoke in the middle of the solar wind sector (at $0°$) is well visible. The focused beam hits the spoke and thus the transmission is reduced. Additionally the grids mounted on the aperture reduce the transmission, too.

**Measurements with slit aperture**

With the slit aperture the detection efficiency dependence was reduced. With this configuration a more thorough measurement was done, step size one degree, see Figure 5.14. Like the measurements with the full aperture, the spoke in the middle of the Solar Wind Sector and the grids can be seen. For comparison an azimuthal angle scan with the integrated FM1 is shown. To minimize the influence of the grids on the transmission another azimuthal scan was done by wobbling the energy.[5] The azimuthal scan with the wobbling beam energy shows less strong visible spokes than the measurement without wobbling, as

---

[5]In CASYMS the beam energy can be set to oscillate within a defined range, in this measurement $\pm 3\%$ of $E_0/q$. This causes a wobbling shift of the focused beam perpendicular to the azimuthal direction.

Azimuthal Angle Scan, E/q = 3 keV/e
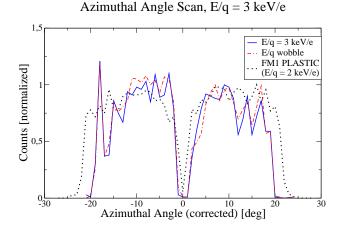


Figure 5.14: *Azimuthal angle scan with slit aperture, PAC voltage for LaserCEM measurements 10 kV. A comparison plot is shown with an azimuthal angle scan for the integrated FM1. The PAC voltage for the integrated FM1 was 20 kV.*

expected.

### 5.3.4   Main channel ESA voltage scans

After optimizing the elevation angle for highest signal, the ESA voltage scans were performed for different beam energies. The elevation angle was optimized for all measurements. All measurements were performed with the full aperture. Because only relative measurements were made the influence of different detection efficiency was neclected. Therefore, the intensity in the plots in Figure 5.15 is given with arbitrary units. The fit function for the ESA voltage Scans is described in Appendix A. To determine the Analyzer constant $k_{ESA}$[6] the median of the ESA voltage distribution for different beam energies is plotted against the beam energy, see Figure 5.16.[7] From the regression curve the analyzer constant was calculated $k_{ESA} = 8.31(5)$ keV/e kV. The error is the weighted error of the mean of the four calculated analyzer constants for each energy. The average FWHM of the ESA voltage scans is 5.75 % of the central value of the ESA voltage scans.

The ESA scan discussed above were performed with PAC voltage 10 kV. For several beam energies (5 keV/e, 10 keV/e and 15 keV/e He$^+$ ions) ESA scans were performed for PAC voltage $V_{PAC} = 15$ kV, too. See Figure 5.17 for $E/q = 5$ keV/e and PAC voltage 15 kV. From PAC voltage scans (see Figure 5.11 we know that the transmission does not increase longer for $E/q = 3$ keV/e above 10 kV PAC voltage. See Figure 5.1 for the simulation of the trajectories of 3 keV/e ions (without PAC voltage and with 15 kV PAC voltage) and Figure 5.3 for 5 keV/e ions. For 3 keV/e and 5 keV/e ions PAC 15 kV is high enough that all particles pass through the TOF structure aperture.

### 5.3.5   Main channel angular and energy acceptance measurement (geometric factor)

With the LaserCEM a very sparse angular and energy acceptance measurement of the main channel was done. Due to the efficiency effects mentioned above in section 5.1 it was not possible to do a measurement with a fine resolution. The instrument was tuned to 5000 keV/e acceptance ($V_{ESA} = \pm300$ V), elevation angle 0 deg. For each beam energy (4500, 4750, 5000, 5100, 5250 and 5500 keV/e) an elevation angle scan was performed. The same procedure was followed as for the other scan measurements. See Figure 5.18 for the contour plot of the measurement. This measurement is only qualitative, not giving a geometric factor value.

---

[6]The analyzer constant is the relation between beam energy per charge and the potential difference of the applied ESA voltage $k_{ESA} = \frac{E/q}{\Delta V_{ESA}}$

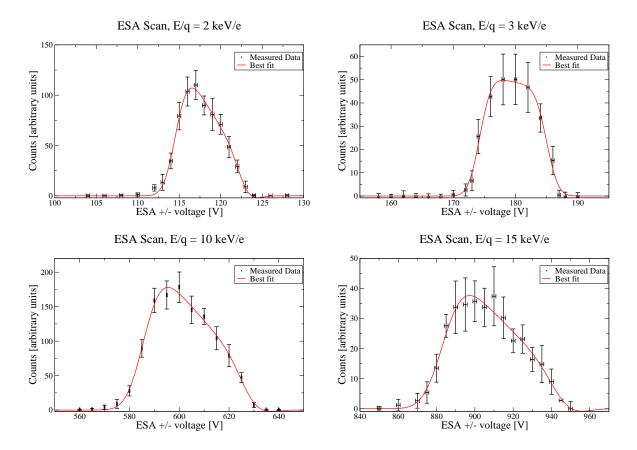[7]For the discussion about using the median, see Section 3.3.5

Figure 5.15: *ESA voltage scan with entire Aperture, different beam energies. PAC voltage 10 kV. The used fit function for all plots is described in Appendix C in [2].*
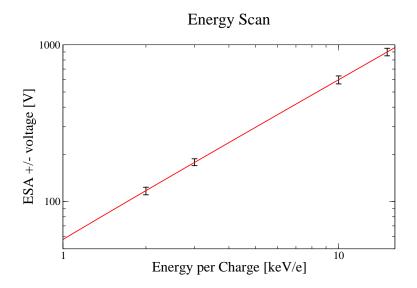


Figure 5.16: *ESA voltage versus Beam Energy, Analyzer Constant $k_{ESA} = 8.31(5)$ keV/e /kV, PAC always 10 kV*
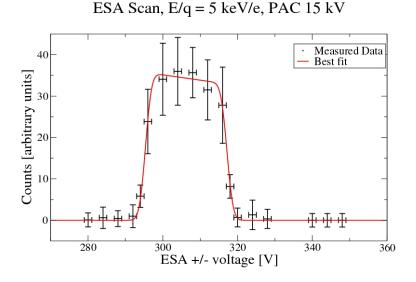
ESA Scan, E/q = 5 keV/e, PAC 15 kV



Figure 5.17: *ESA voltage for E/q = 5 keV/e and 15 kV PAC voltage.*
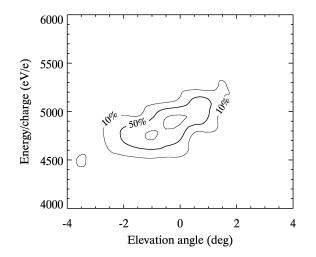


Figure 5.18: *Angular and energy acceptance measurement main channel (geometric factor). Beam energy 5 keV/e, azimuthal angle -6°, PAC voltage 15 kV and CEM voltage 3.2 kV.*
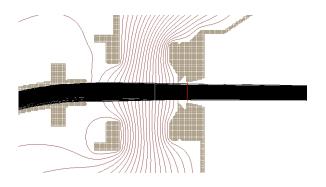
Figure 5.19: *Beam trajectories for $E/q = 15$ $keV/e$ and $V_{PAC} = 15$ $kV$.*



Figure 5.20: *Beam image at CEM entrance position for $E/q = 15$ $keV/e$ and $V_{PAC} = 15$ $kV$.*



Figure 5.21: *ESA scan for suprathermal sector, beam energy 15 keV/e, PAC voltage 15 kV.*
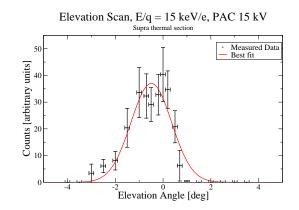


Figure 5.22: *Elevation angle scan for suprathermal sector, beam energy 15 keV/e, PAC voltage 15 kV.*

### 5.3.6 Measurements suprathermal sector WAP

The suprathermal sector of the WAP is used to measure suprathermal particles and pick-up ions [60]. Suprathermal He$^+$ ions are usually in the energy range about 15 keV/e [48]. Hence WAP measurements in this energy range were done. The post-acceleration voltage (PAC) was set to 15 kV which was the highest tested PAC voltage for the used LaserCEM I. For a beam energy of 15 keV/e the post-acceleration voltage of 15 kV is sufficient that all ions should be focused on the carbon foil. For higher PAC voltage the focusing effect is stronger. So all particles should pass as well. The same argument is valid for lower beam energies. See Figures 5.19 and 5.20 for a simulation for $E/q = 15$ keV/e and $V_{PAC} = 15$ kV.
As for the SWS ESA scans, elevation and azimuthal angle scans were performed. In addition the beam spot was mapped, see Subsection 5.3.7.

#### ESA voltage and elevation angle scans

For the suprathermal sector ESA voltage and elevation angle scans were only performed for a beam energy of 15 keV/e and PAC voltage 15 kV. The variation in intensity can be explained with the grids which hold the carbon foil. The beam is partly cut off by the grids. See Figures 5.21 and 5.22 and for the grid structure see Figure 5.12. Looking at the ESA scan the signal is reduced at 940 volts, this can be caused by a supporting grid of the carbon foil. The suprathermal section has a smaller active area than the Solar Wind Sector, see Chapter 3, thus the grid has a relatively higher influence on the total transmission.

#### Azimuthal angle scans

As it was done without post acceleration, an azimuthal response measurement was performed to know the ion optical transmission depending on the azimuthal position. The plot on Figure 5.23 shows that
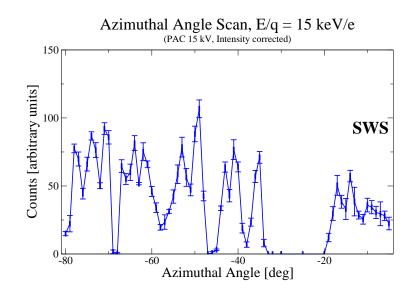
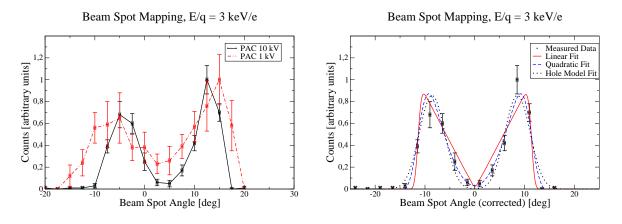Figure 5.23: *Azimuthal angle scan WAP, beam energy 15 keV/e, PAC voltage 15 kV.*



Figure 5.24: *Mapping of beam profile with entire aperture*
*Measured data with fitted lines (see text for explanations)*

the monochromatic and parallel beam of CASYMS resolves all the mechanical structures of the entrance system and of the TOF structure, including the grids that hold the carbon foil. There is a large spoke every 22.5 degree which can be well seen. Additionally the grids are visible, too.

### 5.3.7 Mapping of focused beam

**Measurements with full aperture**

Mapping the beam spot with the entire CEM aperture gave surprising results (see Figure 5.24). In the center, where the signal was expected to be highest, there was a drop in intensity. The reason for this inhomogeneity is the different detection efficiency of the CEM. In the center of the CEM the detection efficiency is very low, possibly due to the hole in the center of the CEM or due to different aging of the CEM surface. With a slit aperture in front of the CEM these effects could be minimized as can be seen in Figure 5.25. For a more profound analysis of the position dependence of the detection efficiency see Section 4.2.
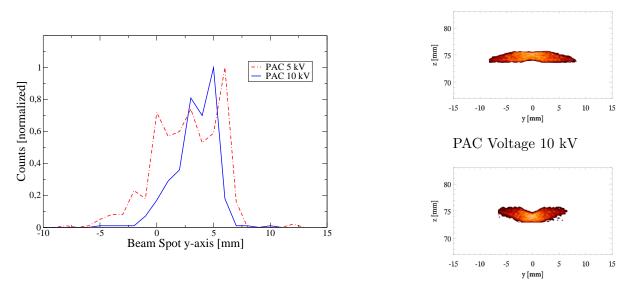
Figure 5.25: *Mapping of beam profile with Slit aperture*
Left: *Azimuthal scan as described in figure 5.10 at two different post acceleration voltages.*
Right Top: *Beam profile at LaserCEM position with 5 kV PAC,* Right bottom: *Beam profile at LaserCEM position with 10 kV PAC*
*(Beam profiles simulated with SIMION)*

## Measurements with slit aperture main channel

With a slit aperture of 1.5 mm it is now possible to map the beam profile. This was done using the procedure described in Figure 5.10. For comparison two beam profiles were plotted in Figure 5.25 which are simulated by SIMION. It can be seen that the width of the profiles are consistent with the measurement performed with two different PAC voltages.

When turning the LaserCEM detector by 1 degree the position of the beam spot is shifted by about 1 mm.

## Measurements with slit aperture suprathermal sector

The beam spot mapping measurements for the suprathermal sector was performed for a beam energy of 15 keV/e and the post acceleration voltage was 15 kV. The center of the measurement was at theta = 18 deg, which corresponds to -42 deg from the SWS center. In Figure 5.26 the plot is shown. For comparison the simulated beam profiles for 0 kV, 5 kV, 10 kV and 15 kV PAC voltage are plotted. The beam profile width does not change much when increasing the PAC voltage, neither does the measured intensity.[8] But one can see that the width of the measured beam spot is always about 10 mm, while the width of the simulated beam spots are always about 20 mm. The explanation for this discrepancy is that the parallel and broad CASYMS beam is cut off on both sides. The width of the aperture, where the ions enter the ESEA, is half of the one of SWS, reducing the active area by a factor of two.

---

[8]The ion trajectories do not show a strong focusing effect for $E/q = 15$ keV/e increasing the PAC voltage.
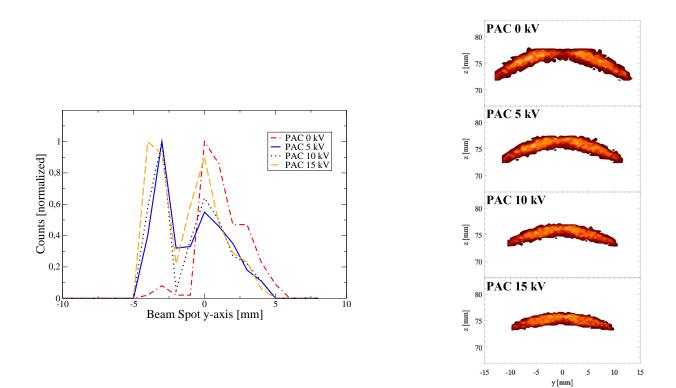
Figure 5.26: *Mapping of beam profile with Slit aperture, Suprathermal section*
Left: *Azimuthal scan as described in figure 5.10 at four different post acceleration voltages.*
Right: *Beam profiles at LaserCEM position for different post acceleration voltages.*
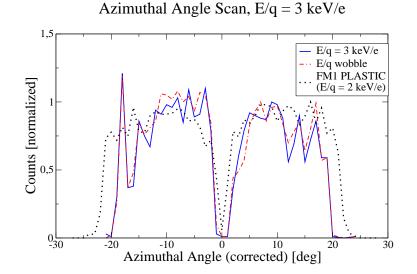*(Beam profiles simulated with SIMION)*

Figure 5.27: *Comparison of Azimuthal scan between a measurement with PAC structure and LaserCEM detector and a measurement with the integrated instrument. Measurements with LaserCEM 10 kV PAC voltage, with integrated instrument 20 kV PAC voltage.*

## 5.4  Comparison with other measurements

The measurements presented in this chapter must be compared to the measurements described in Chapter 3 about the ESEA calibration measurements without post-acceleration and to measurements performed with the integrated instrument. The only difference between the calibration with and without PAC is the reduced transmission due to the additional mechanical structure and the grids used to hold the carbon foil. (But during these measurements no carbon foils were mounted.) The TOF structure is similar for the PAC measurements and for the integrated instruments.

### 5.4.1  Azimuthal Angle Scans

As mentioned above the TOF structure is similar for the integrated instruments and for the PAC measurements, thus the azimuthal scans can be compared with integrated instrument measurements. In Figure 5.27 two azimuthal scans for ESEA with PAC structure and one azimuthal scan for the integrated instrument are shown. The beam energies and the PAC voltages are not identical, but although the distance between peaks is the same.

### 5.4.2  ESA voltage Scans

The Analyzer constants should be the same for all measurements performed with PLASTIC. So the tuned ESA voltage should be the same for measurements with the ESEA without PAC, measurements with PAC and measurement with the integrated instrument. See Figure 5.28 for comparison measurements. For the measurements with E/q = 2, 10 and 15 keV/e two measurements with two different LaserCEM detector positions were plotted. For E/q = 3 keV/e two measurements with two different PAC voltages were plotted instead. When measurements with ESEA only were available they were plotted on the same plots. All data were normalized for comparison. On the plots it can be seen that the maximum ESA voltage is slightly smaller for the measurements with PAC. This can be explained by a small difference in elevation.[9] The FWHM of the measured ESA scans is comparable to the simulated data as well as to the measurements performed with the ESEA without PAC. In all cases the FWHM is about 6 % of the maximum value.

---

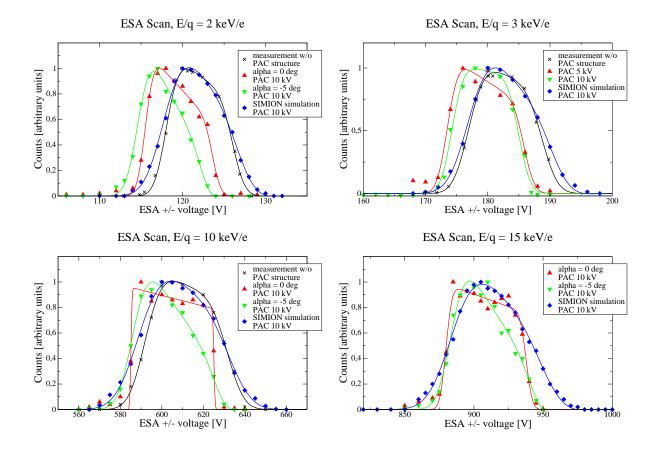[9]A difference in elevation angle of 0.2° causes a difference of 1 % of ESA voltage.

Figure 5.28: *Comparison of ESA voltage scan between simulations with SIMION , measurements with PAC structure and LaserCEM detector and measurements without PAC. For all plots the measurement data were normalized. All data series were fitted with the same fit function as mentioned in figure 5.15.*
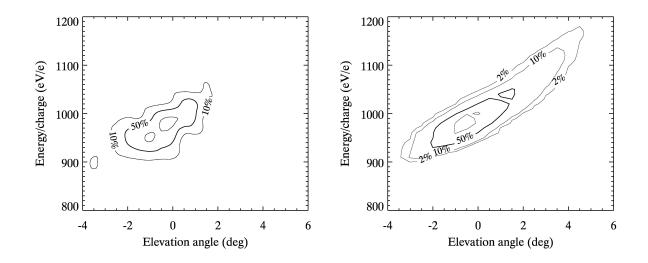
Figure 5.29: *Comparison of the angular and energy acceptance measurement with PAC (*left*) and without (*right*) for FS entrance system/energy analyzer. The plot shows that the total angular and energy acceptance range is the same for both measurements.*

### 5.4.3   Angular and energy acceptance

The low count rates for the LaserCEM I detector only allows a qualitative comparison of the geometric factor measurements with and without post acceleration. But when the total angular and energy acceptance is compared, they show a very good agreement, see Figure 5.29. Even the slight asymmetry is visible, which can be seen in all three models.

## 5.5   Conclusions and Outlook

### 5.5.1   Conclusions and Summary

**Results Summary**

Because absolute signal measurements were not possible with the LaserCEM I, only qualitative result could be obtained. Since the analyzer constant measurements do not depend on the intensity of the transmitted signal, the analyzer constant for the main channel was determined.

|  | FS ESEA with PAC | FS ESEA without PAC |
|---|---|---|
| Analyzer constant $k_{ESA}$ (keV/e /kV) | 8.31(5) | 8.25(2) |
| FWHM of ESA voltage | 5.75 % | 6.3% |

Comparing the results with simulations and ESEA measurements without PAC, they show good agreement.

**Conclusions**

- The ESA voltage scans gave an analyzer constant comparable to the analyzer constant from simulations and ESEA measurements without PAC. Also the FWHM is comparable, 6 % of the applied maximum voltage, according to 6 % energy acceptance of the FS ESEA without PAC.

- The measurements with PAC voltage confirms that the ion optical parameters (analyzer constants, angular and energy acceptance (geometric factor)) do not significantly differ from the measurements without post-acceleration voltage. For particles with high energy per charge ratio ($E/q > 15 keV/e$ it is important that the PAC voltage is as high as possible, meaning at least 20 kV, to ensure that all ions pass through the aperture of the TOF structure. The influence of a possible cut off on the

count rate is small compared to the total number of passing ions. But they can affect the measured distribution function of ions with high $E/q$, and therefore it can distort the measurements. Thus it has to be considered in the data reduction!

- The Azimuthal angle scans showed the intensity differences caused by the spokes and grids of the TOF structure. The measurements are similar to the measurements performed with the Integrated PLASTIC instruments FM1 and FM2. The effect of mechanical blockage is larger than that of the reduced transmission when not all particles pass through the TOF structure apertures.

- Measurements with the open CEM aperture showed a strong spatial detection efficiency variation of the CEM. It further showed that the detection efficiency at the boundaries is higher than in the center of the CEM. This provided an insight into the floatable LaserCEM development and motivated the usage of a slit aperture mounted in front of the CEM to improve spatial resolution measurements.

- The Beam Spot Mapping measurements with the slit aperture showed that the beam spot size at the LaserCEM position agrees well with the SIMION simulations.

- The actual setup using the ESEA, the TOF structure and a floatable detection system like LaserCEM I proved usability for ion optical calibration measurements with post-acceleration.

## 5.5.2   Outlook, further Experiments

If it is necessary, the setup used here, can be used for further study of the ESEA response. However, it cannot replace a complete integrated instrument. For later studies the newer detector LaserCEM II, see Chapter 4, can be used. The problems with low count rate and decreasing detection efficiency have been alleviated with this improved design. Additionally, the handling of the detector and the data accumulation has been simplified.

# Chapter 6

# Calibration of the integrated PLASTIC instrument at the University of Bern

## 6.1 Introduction

The PI-institution (PI: Primary Investigator) of PLASTIC is the University of New Hampshire (UNH). The integrated PLASTIC instruments (Entrance System/Energy Analyzer (ESEA), Time-Of-Flight section (TOF) with detection board and the electronic box (see Chapter 1, Section 1.3)) were completed and first tested in the ion optical calibration facility of UNH. The most thorough ion optical calibrations were performed in CASYMS at the University of Bern (UoB) (see Appendix B.2). Both Flight Models (FM1 and FM2) were calibrated in Bern. For details on the calibration data archive see Appendix E.

In this chapter only aspects of the calibration of the integrated instruments are discussed, namely measurements that are related to the measurements with the ESEA alone, with and without post-acceleration voltage. (See Chapters 3 and 5.)

First, the detection efficiency is briefly discussed. Second, the instrument response dependent on azimuthal angle, elevation angle and ESA voltage settings is presented. In conclusion, measurements with the integrated instruments are compared to the former measurements.

### 6.1.1 Measurement principles

The measurement principles are explained in Chapter 1, Section 1.3. In this chapter the calibration measurements are briefly outlined and interpreted.

For most of the measurements the sweeping of ESA (128 sweeping steps) and deflection plate voltage (32 sweeping steps) was disabled. The ESA and the deflection plate (Duckbills) voltage were set at a certain value for each measurement. A measurement run lasts one minute ($128 \times 32$-sweep steps, 4096 steps totally, 12.8 milliseconds each, short time delay after sweep). For low count rates, several one-minute measurements were taken for the same settings.

#### Voltage sweeping

When sweeping, the ESA and the deflection plates voltage was changed in 128, respectively 32 steps. The deflection plate voltage is directly proportional to the deflection angle according to equation (3.3): $k_{\text{deflection}} = \frac{\phi \cdot E_{\text{kin}}/q}{V_{\text{Defl. Electrode}}}$. The voltage is tuned so that the full range of $\pm 20$ degree can be scanned, each deflection step 1.25 degree.[1] The ESA voltage steps are given as follows:

$$V_{ESA} = \frac{1}{k_{ESA}} D_1 \cdot D_2^{127-n} \tag{6.1}$$

---

[1] To measure also the center of the angular distribution, there is a small overlap at zero degree. It is always positive voltage applied to the Duckbills. At zero degree the other deflection plate is enabled.

with $D_1 = 0.2$ and $D_2 = 1.048954346$. This results in $E/q_{max} = 86.52$ keV/e for the maximum accepted energy per charge and $E/q_{max} = 0.2$ keV/e for the minimum. The ESA and the deflection plate voltage steps are stored in a sweeptable from which the instrument DPU reads out the respective voltage to be set.

## 6.2 Calibration specifications

### 6.2.1 Overview

The following tests were performed in CASYMS:

- Functionality tests after transport

- Detection efficiency and its time evolution

- ESA voltage scans

- Azimuthal angle scans

- Elevation angle scans

- Geometric factor scans (ESA voltage vs elevation angle)

- Sweep tests (ESA and Duckbill voltage sweeping)

- High rate tests

For Flight Model 1 the test period lasted six weeks, for FM2 the test period was only 10 days. Therefore the ion optical calibration data for FM2 is very sparse. As mentioned before I will only report in this chapter on detection efficiency, azimuthal angle response, and geometric factor measurements since these can be compared with ESEA measurements.

### 6.2.2 Experimental setup

The integrated instrument is mounted upsidedown as the the ESEA (see Chapter 3). The turntable in the CASYMS instrument chamber can be turned around the azimuthal axis (alpha angle in CASYMS) and in elevation (beta angle in CASYMS) around an axis through the center of the ESEA (see Figure 6.1). The azimuthal turning was restricted to 90 degrees. Thus for each quadrant (see Figure 6.2) the vacuum had to be broken and the instrument turned. For the elevation angle the restriction was ±22.5 degrees. The horizontal movement ($z$-axis) was restricted as well due to the height of the instrument chamber, but sufficient to change between main and S-channel.

### 6.2.3 Calibration data files

For the measurements presented here three different data file types were used that were extracted from the binary log files produced by the calibration data procession unit (GSE):

**Housekeeping file** `Hk_PLA_FM*-date-time.log`

**Monitor rates file** `Mon_PLA_FM*-date-time.log`

**Pulse height distribution raw file** `PHA_raw_PLA_FM*-date-time.log`

where the * stands for 1 or 2. In Appendix E the calibration data archiving structure and the other log data files are discussed.
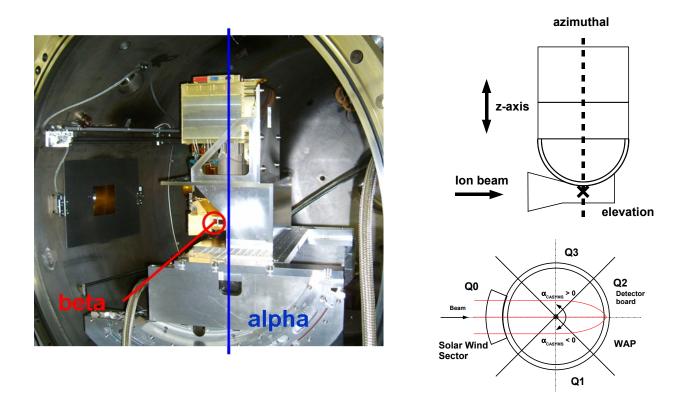
Figure 6.1: *Turning axis in CASYMS for integrated instrument. In CASYMS the azimuthal angle is alpha, the elevation angle is beta. The top view shows the instrument upside down, like the side view. In the text only azimuthal and elevation angle are used, as in Chapters 3 and 5.*

**Housekeeping data**

In the housekeeping file all instrument settings are saved, e.g. post acceleration voltage, MCP voltage. These files are used to obtain the post acceleration voltage to calculate energy, mass and charge of each ion. For the geometric factor measurements (see Section 6.5) the housekeeping values of the ESA and the S-channel electrodes are used. A housekeeping measurement is taken when it is commanded (e.g., the electrode voltages are not recorded during sweeping mode).

**Monitor rates**

All counts are recorded in the monitor rates file for each available monitor value (e.g. start rate, stop rate), each sweeping step (128 ESA voltage steps and 32 deflection voltage steps) on a separate line. The start rate (SF0, SSD side, or SF2, non-SSD side) accumulates all counts during a sweep step that trigger a start signal. The stop rate (STP0 or STO2) then counts all stop trigger signals. The rate SFR0/SFR2 accumulates all events when coincidence happens, defined by the set mode. (E.g., double coincidence when a valid start and stop signal are requested.)

**PHA raw data**

In the pulse height distribution file for each valid time-of-flight measurement the following information is logged:
Date, Time, ESA step (channel), Deflection step (channel), Deflection step (degree), Quadrant, ssd_id (raw), SSD energy (channel), SSD energy (keV), TOF (channel), TOF (ns), Position (channel), Position (degree), Section (raw), Priority (raw)
For the results presented here the ESA step, SSD energy, TOF and Position are used.
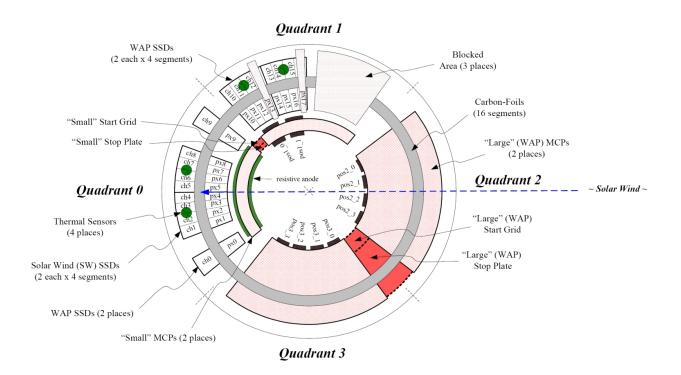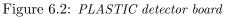
## 6.3 Detection efficiency

### 6.3.1 Detector board

The detectors are below the TOF section. In Quadrant 0 (SWS and suprathermal sectors) and Quadrant 1 solid state detectors (SSD) are used to measure the residual energy. Secondary electrons from the ions incident on the SSD, trigger the stop signal of the time of flight measurement. In Quadrant 2 and 3 only large microchannel plates (MCP) trigger the stop signal of the TOF measurement, see Figure 6.2. For details on the functionality see Chapter 1, Section 1.3.

Figure 6.2: *PLASTIC detector board*
*Quadrant 0 and 1 with SSD to measure time of flight and residual energy, Quadrant 2 and 3 with MCP to measure time of flight.*

### 6.3.2   Time dependant MCP efficiency on PLASTIC/FM1

# Time dependant MCP efficiency on PLASTIC/FM1

Reto Karrer, University of Bern

During measurements of the MCP efficiency it could be observed that the efficiency decreased with time. Here we investigate if the decrease is due to out-gassing or due to particle irradiation.


## Overview
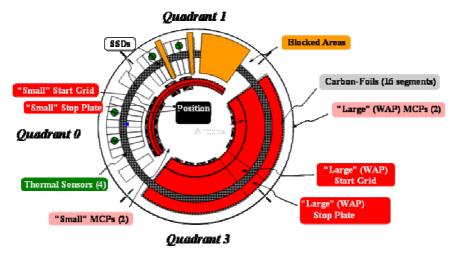


**Figure 1:** *Overview over detectors after TOF section.*

After changing PLASTIC position to another quadrant in CASYMS, the instrument was turned on 24 h after the start of pumping down.


### Test sequence:

| Quadrant: | Time | Measure time |
|---|---|---|
| 2 | 13 Jan. – 16 Jan. 2005 | 14 – 15 Jan. 2005 |
| 1 | 16 Jan. – 19 Jan. 2005 | 17 – 18 Jan. 2005 |
| 3 | 19 Jan. – 23 Jan. 2005 | 20 – 22 Jan. 2005 |

At quadrant 2 it was observed that the MCP efficiency decreased with time. At the beginning the MCP were operated at low bias voltage. Next morning the measured efficiency was much lower than on the previous day.

Additionally, in considering azimuthal scans for one MCP voltage (in which each position was irradiated about one minute) a strong decrease was observed across the azimuth. This is shown in figures 2, 4 and 7. However, MCP efficiency voltage scans were usually measured at position alpha=-8°, resulting in longer irradiation time (about 45 min/scan). Comparing azimuthal scans taken after significant irradiation of position -8°, do not show a preferential decrease in MCP efficiency (see normalized azimuthal scan, figures 3, 5 and 8).

## Quadrant 2



**14 Jan. 1713** MCP: 2809 V

**14 Jan. 2159** MCP: 2824 V

**15 Jan. 1627** MCP: 2930 V
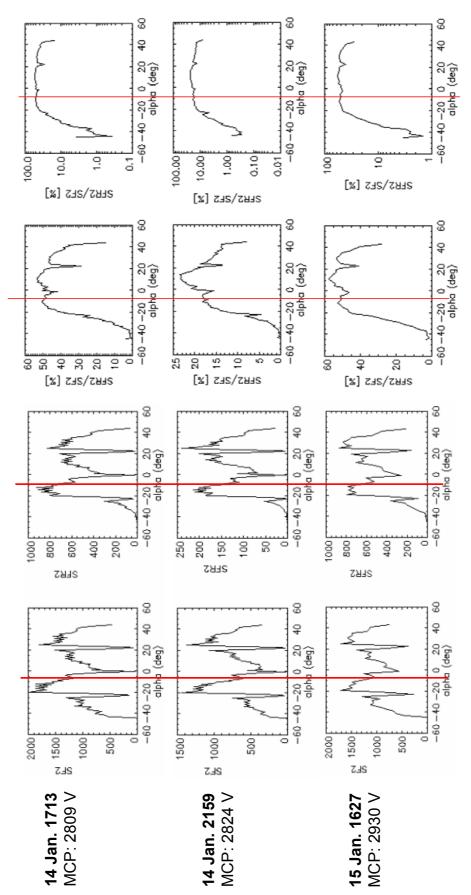
**Figure 2:** *Quadrant 2, He$^+$ beam, E/q=20 keV/e, PAC 15 kV.*
*The red line indicates alpha = -8° position. On January, 15$^{th}$, the MCP voltage was higher than on the previous day. Alpha step $\Delta\alpha$=1 deg for 14$^{th}$ of January, on 15$^{th}$ $\Delta\alpha$=1.5 deg.*
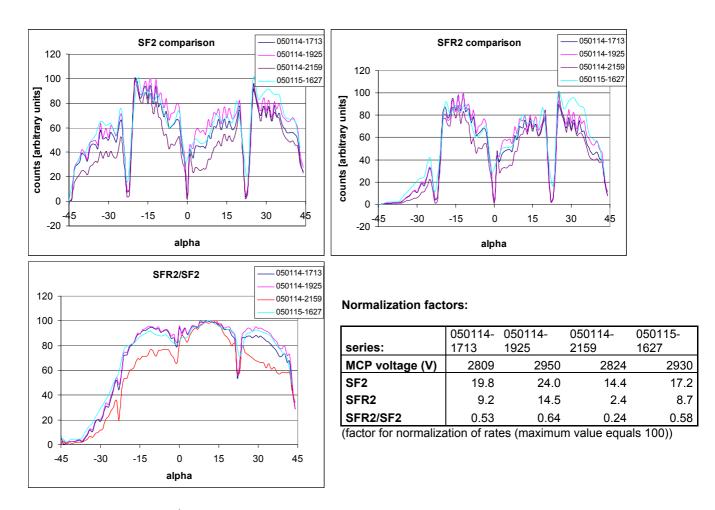
**Normalization factors:**

| series: | 050114-1713 | 050114-1925 | 050114-2159 | 050115-1627 |
|---|---|---|---|---|
| **MCP voltage (V)** | 2809 | 2950 | 2824 | 2930 |
| **SF2** | 19.8 | 24.0 | 14.4 | 17.2 |
| **SFR2** | 9.2 | 14.5 | 2.4 | 8.7 |
| **SFR2/SF2** | 0.53 | 0.64 | 0.24 | 0.58 |

(factor for normalization of rates (maximum value equals 100))

**Figure 3:** *Quadrant 2, He$^+$ beam, E/q=20 keV/e, PAC 15 kV*
*All values normalized to the maximum signal or ratio. Alpha step $\Delta\alpha$=1 deg for 14$^{th}$ of January, on 15$^{th}$ $\Delta\alpha$=1.5 deg.*

Quadrant 2 utilizes an MCP for start electron and stop electron detection.
At quadrant 2 it was observed that the SFR2 rate (the coincidence rate of start and stop signal) decreased in time. The SF2 rate decreased as well but less than the SFR2 rate, resulting in a large decrease of the efficiency (Ratio SFR2/SF2) during irradiation and out-gassing.
The azimuthal signal asymmetry is mostly due to geometrical reasons, does not change with irradiation time.
In Figure 3 it can be noticed that the changes in rate are not higher at position alpha=-8°, suggesting that irradiation time has no influence (or at least no big influence) on MCP efficiency.

## Quadrant 1



**17 Jan. 1930** MCP: 3126 V

**17 Jan. 2141** MCP: 3133 V

**18 Jan. 0732** MCP: 3143 V
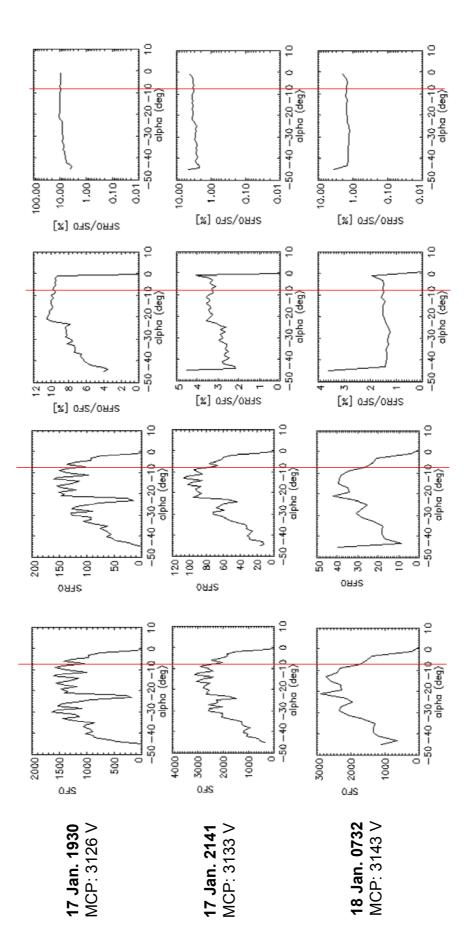
**Figure 4:** *Quadrant 1, SSD side, half of this quadrant is blocked*
*He+, E/q=7 keV/e, PAC 15 kV, alpha scan on 18th January two degree steps. Alpha step Δα=1 deg*
*for 17th of January, on 18th Δα=2 deg.*

**Normalization factors:**

| series: | 050117-1930 | 050117-2141 | 050118-0732 |
|---|---|---|---|
| **MCP voltage (V)** | 3126 | 3133 | 3143 |
| **SF0** | 16.4 | 31.2 | 28.8 |
| **SFR0** | 1.6 | 1.1 | 0.4 |
| **SFR0/SF0** | 0.10 | 0.05 | 0.04 |

(factor for normalization of rates (maximum value equals 100))

**Figure 5:** *Quadrant 1, SSD side, half of this quadrant is blocked*
*He+, E/q=7 keV/e, PAC 15 kV, all values normalized. Alpha step $\Delta\alpha$=1 deg for 17th of January, on 18th $\Delta\alpha$=2 deg.*

Quadrant 1 consists of SSDs and MCPs. The start signal is counted by an MCP, the stop signal is produced by secondary electrons of the SSD. Half of this sector is mechanically blocked.
In this section almost no change of the SF0 rate is visible during out-gassing and irradiation, only the coincidence rate SFR0 showed a large signal decrease. But as noticed on quadrant 2 the drop in MCP efficiency showed no azimuth dependency although position alpha=-8° was mostly irradiated. (see fig. 4)
Here as well the azimuthal asymmetry is due to mechanical structures on the carbon foils or in the TOF section. The large SFR decrease may be due to a low SSD secondary electron efficiency and/or due to a low MCP efficiency on the inner MCP.
During the night between January 17th and 18th an overnight measurement was taken, irradiating detectors and collecting data every 30 minute for 1 minute. This MCP monitoring scan was performed at position alpha=-8°, too. (See Figure 6)
The azimuthal scan the following day showed no further azimuthal dependency of the MCP efficiency.
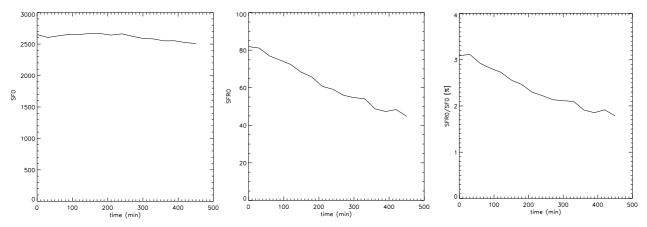


**Figure 6:** *Quadrant 1, SSD side, He+, E/q = 7 keV/e, PAC 15 kV, MCP voltage 3132 V*
*left: SF0 rate during night; middle: SFR0 rate during night; right: Efficiency SFR0/SF0 during night*

# Quadrant 3



**20 Jan. 1855**
MCP: 2897 V

**21 Jan. 0740**
MCP: 2916 V
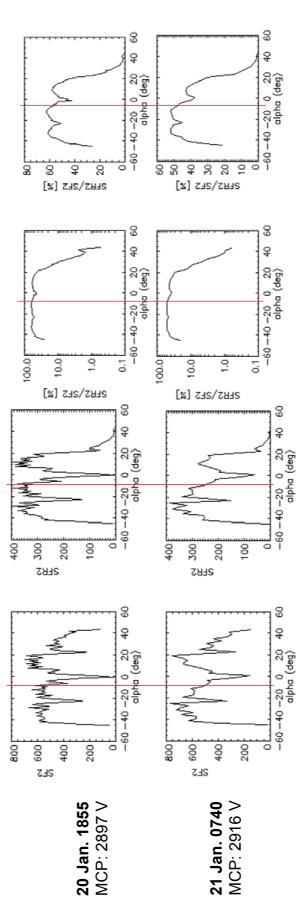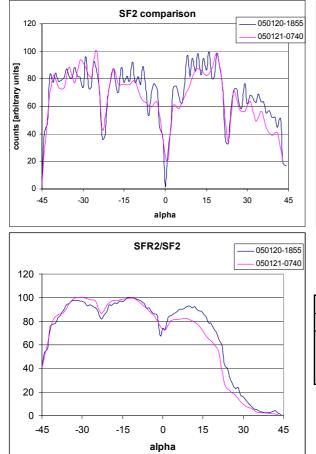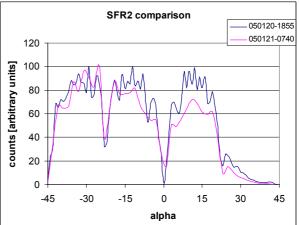
**Figure 7:** *Quadrant 3, non-SSD side*
*He+, E/q = 7 keV/e, PAC 15 kV. Alpha step $\Delta\alpha$=1 deg for $20^{th}$ of January, on $21^{st}$ $\Delta\alpha$=2 deg.*

**Normalization factors:**

| series: | 050120-1855 | 050121-0740 |
|---|---|---|
| **MCP voltage (V)** | 2897 | 2916 |
| **SF2** | 6.9 | 7.7 |
| **SFR2** | 4.0 | 3.9 |
| **SFR2/SF2** | 0.63 | 0.52 |

(factor for normalization of rates (maximum value equals 100))

**Figure 8:** *Quadrant 3, non-SSD side*
*He+, E/q = 7 keV/e, PAC 15 kV, all values normalized.*
*Alpha step $\Delta\alpha$=1 deg for 20<sup>th</sup> of January, on 21<sup>st</sup> $\Delta\alpha$=2 deg.*

As in quadrant 2, in quadrant 3 there is one large MCP as detector for start and stop signal.
During out-gassing and irradiation the start rate SF2 did not decrease much, the coincidence rate SFR2 decreased little as well. As a consequence the efficiency (ratio SFR/SF) decreased little as well.
As on quadrant 1 an overnight measurement was taken during the night between January 20<sup>th</sup> and 21<sup>st</sup>, collecting data every 30 minute for 1 minute. This monitoring scan showed a very small decrease in SF2, about 20% in SFR2 rate and consequently in efficiency SFR2/SF2.
But the azimuthal scans showed a large inhomogeneity on the positive alpha side of the quadrant (see Figure 8). Even that the MCP efficiency measurements were performed at alpha=-8°, the SFR2 rate decreased much around alpha=30° and little at alpha=-8°. (Not due to irradiation but rather due to mechanical blocking.)
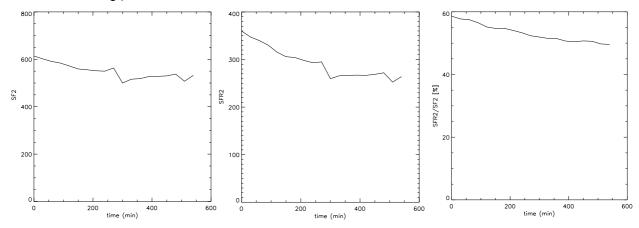


**Figure 9:** *Quadrant 3, non-SSD side, He+, E/q = 7 keV/e, PAC 15 kV, MCP voltage 2916 V*
*left: SF2 rate during night; middle: SFR2 rate during night; right: Efficiency SFR2/SF2 during night*

# Conclusions

Always after venting the MCP efficiency was much higher than after a longer working time. So during the first operation hours the MCP efficiency decreased from more than 50 % to 20% or less.

All MCP measurements were performed at an alpha position of -8°. This part of the carbon foil and the MCP was irradiated mostly. But there is no difference in MCP efficiency as well as in counting rates depending on azimuthal position.

This suggests out-gassing as main reason for decreasing MCP efficiency. The decrease was comparable in quadrant 2 and 3, the non-SSD section, and much stronger in quadrant 1, the SSD-section. In this section the efficiency was lower from beginning of the measurements. The start rate SF was comparable with SFR of quadrants 2 and 3, but on quadrant 1 the coincidence rate SFR was much smaller.

## *Suggestions for further calibration campaigns:*

- o  Detectors should be enabled to increase facility out-gassing.
- o  First day after starting pumps taking an azimuthal scan at nominal MCP voltage with small alpha steps, allowing out-gassing for a longer time.
- o  On first day only MCP efficiency scan for comparison
- o  Overnight MCP monitoring scan, taking a one minute measurement every 30 minutes, MCP on nominal voltage
- o  Assess from MCP monitoring scan if MCP efficiency is stable. If yes, take MCP efficiency scan, if not, take another azimuthal scan, allowing continuing out-gassing.
- o  Fishscans only when MCP efficiency stabilized.

### 6.3.3 Mass-mass/charge matrix

The MCP efficiency measurements for different species and elements allowed to produce a mass versus mass per charge contour plot (e.g. SOHO/CTOF [32] or Ulysses/SWICS [23]). For the following contour plots the data is not yet calibrated. For the plot the PHA_raw-files were used (see Appendix E for explanation), where among others the ESA voltage step, the deflection plate step, the residual energy measured by the SSD (when on Quadrant 0 or 1), and the time of flight is stored for each valid TOF measurement. The mass and the mass/charge is then calculated with the following equations (refer to Equations 1.2 and 1.3):

$$m = 2 \cdot E_{\mathrm{SSD}} \left( \frac{\tau}{d} \right)^2 \tag{6.2}$$

$$m/q = 2 \left( k_{\mathrm{ESA}} \; V_{\mathrm{ESA}} + U_{\mathrm{acc}} \right) \left( \frac{\tau}{d} \right)^2 \tag{6.3}$$

where $E_{\mathrm{SSD}}$ is the residual energy measured with SSD, $\tau$ the time of flight for distance $d$, $V_{\mathrm{ESA}}$ the ESA voltage, and $k_{\mathrm{ESA}}$ the analyzer constant for the energy analyzer. The data for mass and mass/charge is then stored in a 2D histogram and plotted as a contour plot. *Please note that the calculated mass or mass/charge value is not the expected value* since the ions lose energy $U_{\mathrm{CF,loss}}$ when passing through the carbon foils at the bottom of the TOF section and the SSD measurements have a large energy defect ($E_{\mathrm{SSD}} = \alpha_{\mathrm{SSD}}(E, m) \cdot E$. See Chapter 1 for details.

### TOF and energy spectra

Histograms for TOF and SSD energy can be made from the pulse height distribution. The energy loss in the solid state detector can be estimated from the SSD energy histograms. The TOF measurement is not strongly influenced by instrument effects since the energy loss due the carbon foil is very small. In Figures 6.3 and 6.4 TOF and energy histograms for an $Ar^{5+}$ beam are shown. Since the mass/charge ratio for $Ar^{5+}$ and $O^{2+}$ are equal for the same energy/charge ratio, the mass separator in CASYMS cannot discriminate the residual oxygen in the source chamber. The time of flight is equal as well ($E/q = m/q \cdot \frac{v^2}{2}$).

### M-M/Q matrix FM1

During the FM1 calibration campaign the following ions were used:

- Hydrogen, $H^+$

- Helium, $^4He^+$ and $^4He^{2+}$

- Nitrogen, $N^+$ in $Ar^{3+}$ beam

- Oxygen, $O^+$ and $O^{2+}$ in $Ar^{5+}$ beam

- Argon, $^{40}Ar^+$, $Ar^{2+}$, $Ar^{3+}$, $Ar^{4+}$, $Ar^{5+}$ and $Ar^{6+}$

The $N^+$ and $O^{2+}$ were in the argon beam due to similar $m/q$ and $E/q$. The mass separation in the CASYMS facility [21] was not good enough to separate $Ar^{3+}$ ($m/q = 13.333$) from $N^+$ ($m/q = 14$)[2]. The post-acceleration $V_{PAC}$ was between 18.5 and 20 kV. The energy range was between 2 keV/e and 60 keV/e. The time of flight distribution was very broad during calibration (FWHM more than 20 % of peak value). After the Bern calibration period the time of flight electronic was improved, resulting in a smaller TOF distribution (about 10 %). See Figure 6.5 for the mass-mass/charge matrix of FM1.

---

[2]The $O^{2+}$ and the $Ar^{5+}$ can only be distinguished by the residual energy measurement. Both have the same time of flight and $E/q$.
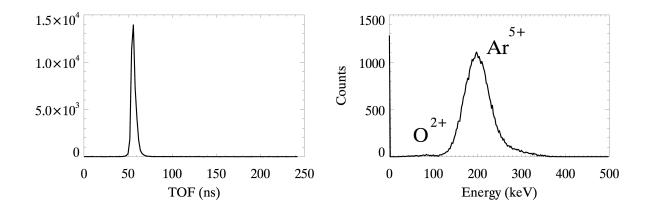
Figure 6.3: *Histograms of TOF (left) and energy measured by SSD (right), FM1. The used beam was an $Ar^{5+}$ beam at 60 keV/e, beam intensity 0.2 kHz/0.1 cm$^2$. The post acceleration was 20 kV. In the energy spectrum the $O^{2+}$ peak is weakly visible. The ion energy of argon after PAC is 400 keV, that of oxygen 160 keV.*
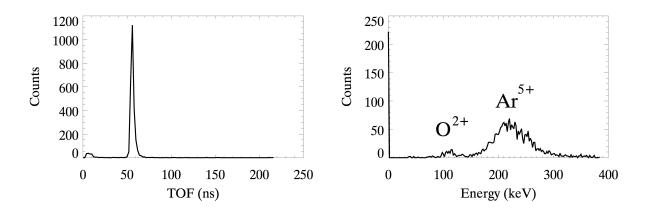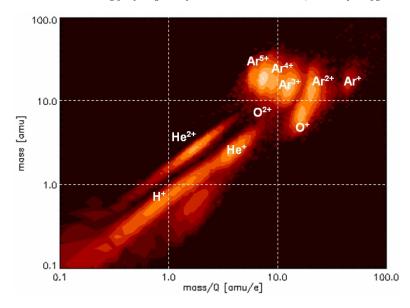


Figure 6.4: *Histograms of TOF (left) and energy measured by SSD (right), FM2. The used beam was an $Ar^{5+}$ beam at 60 keV/e, beam intensity 0.2 kHz/0.1 cm$^2$. The post acceleration was 18 kV. In the energy spectrum the $O^{2+}$ peak is clearly visible. The ion energy of argon after PAC is 390 keV, that of oxygen 156 keV.*



Figure 6.5: *M-M/Q matrix for FM1. Data from MCP efficiency measurements. Intensity is normalized, different beam energy. The data is uncalibrated.*
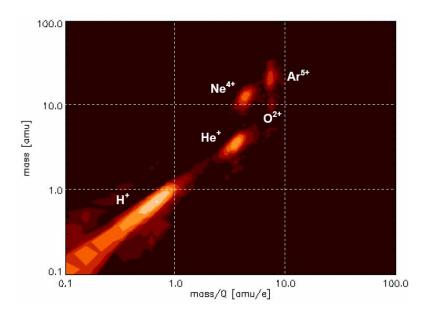
Figure 6.6: *M-M/Q matrix for FM2. Data from MCP efficiency measurements. Intensity is normalized, different beam energy. The data is uncalibrated.*

**M-M/Q matrix FM2**

During the FM2 calibration campaign the following ions were used:

- Hydrogen, $H^+$, $E/q = 60$ keV/e

- Helium, $^4He^+$, $E/q = 2$ keV/e

- Oxygen, $O^{2+}$ in $Ar^{5+}$ beam, $E/q = 60$ keV/e

- Neon, $Ne^{4+}$, $E/q = 60$ keV/e

- Argon, $^{40}Ar^{5+}$, $E/q = 60$ keV/e

The post-acceleration was only 18.5 kV. See Figure 6.6 for the mass-mass/charge matrix of FM2. The time of flight resolution is better than for the FM1 calibration, less than 10 % of the nominal value.
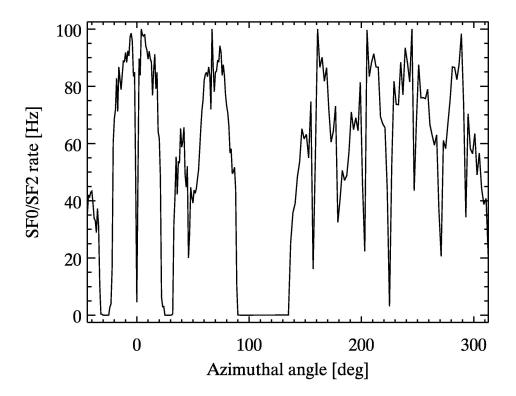
Figure 6.7: *Azimuthal response of integrated FM1. The intensity is normalized to the maximum value of each quadrant. Center of Solar Wind Sector (SWS) is at 0 deg. One half of quadrant 1 is blocked. The start rate for the quadrants with SSD detectors is SF0 (Quadrant 0 and 1), for the quadrants without SSD detectors is SF2 (Quadrant 2 and 3).*

## 6.4   Azimuthal angle response

The detection of ions is strongly dependant on the azimuthal position. The entrance system has blockages that reduce the transmittance of particles at the entrance and at the exit slits. As reported in Section 3.5, these blockage structures can be seen very well. The integrated instrument consists in addition of a TOF section with carbon foils at the bottom that are held by grids. This grid structure has spokes every 22.5 deg. These spokes as well as the grids have an influence on the ion transmission. The position of these features (peaks and dips) depend neither on the applied PAC voltage nor on the beam energy, since it only depends on the center of the focused beam spot, whereas the intensity depends on the size of the beam spot and thus on the PAC voltage and the beam energy. In Chapter 5 these transmission effects are discussed for measurements with the ESEA with post-acceleration. With the integrated instrument these features can be seen, too. Although the grids are thin ($< 1$ mm) the well focused beam is partly cut off by these grids.

Unlike the solar wind with a thermal velocity of more than one percent of the bulk velocity, the ion beam provided in CASYMS is a nearly monochromatic pencil beam, comparable to a delta function, whereas the typical solar wind can be well described with a Gaussian distribution. Therefore it was possible to obtain an ion optical image of the structures of PLASTIC. See Figure 6.7 for an overview of the whole azimuthal range.

### 6.4.1   Main channel

The azimuthal angle range of the main channel is 45 degrees. There is a spoke in the center of the Solar Wind Sector (SWS). The carbon foils are held by a grid. It can clearly be seen that the intensity drops where the well focused ion beam hit the grid of the TOF structure (see Chapter 5 for a similar observation).
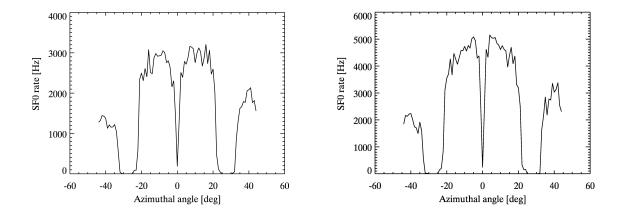
Figure 6.8: *Azimuthal angle scan of integrated FM1 Quadrant 0 main channel.*
*Left: $He^+$, $E/q = 2$ keV/e, $V_{PAC} = 15$ kV, $V_{MCP} = 3060$ V, elevation angle 0 degree.*
*Right: $He^+$, $E/q = 2$ keV/e, $V_{PAC} = 20$ kV, $V_{MCP} = 3060$ V, elevation angle 0 degree.*
*The mechanical structures of the TOF structure can be seen.*

In Figures 6.8 and 6.9 the azimuthal angle scans are shown. The whole quadrant 0 is plotted. Only the range between $-22.5°$ and $+22.5°$ belongs to the SWS. With the small sectors at the sides suprathermal particles will be measured. The active area is much smaller than for the SWS even though the angular acceptance out-of-ecliptic is larger. But the total azimuthal acceptance is half of the azimuthal acceptance of the SWS.

## 6.4.2   S-channel

The S-Channel has a much smaller aperture. To get a decent count rate on the detectors the beam intensity had to be very high. It was important that the angular scan was only restricted to the solar wind sector (SWS) because the detectors would have been saturated if the high rate beam had entered through the small apertures belonging to the suprathermal sector. See Figure 6.10.

## 6.4.3   Wide angle partition

The WAP section consists of the three quadrants 1, 2 and 3 in addition to the two suprathermal sectors on the sides of the SWS (see Figure 6.2). For the two suprathermal sectors of quadrant 0 see Figures 6.8 and 6.9. Half of quadrant 1 is blocked by a mechanical structure of the entrance system and therefore not used. Only the quadrants 0 and 1 have SSD detectors that allow the complete characterization of the incident particles (see Section 1.3). All quadrants of FM1 could be calibrated in CASYMS, whereas only quadrant 0 of FM2 could be tested, due to the short calibration time. But also for quadrants 1, 2 and 3 the calibration time was limited, only a couple days, mainly used for MCP detection efficiency measurements.
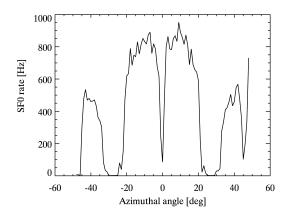
Figure 6.9: *Azimuthal angle scan of integrated FM2 Quadrant 0 main channel.*
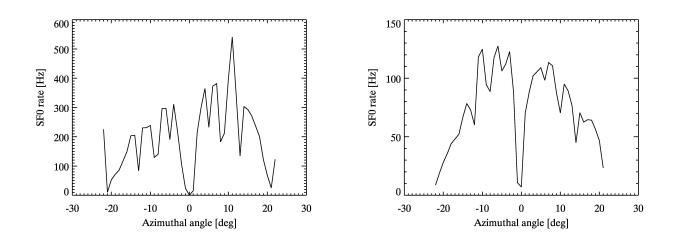*$He^+$, $E/q = 2$ $keV/e$, $V_{PAC} = 15$ $kV$, $V_{MCP} = 3060$ $V$, elevation angle 0 degree.*



Figure 6.10: *Azimuthal angle scan of integrated FM1 and FM2 S-channel:*
Left: *$He^+$, $E/q = 2$ $keV/e$, $V_{PAC} = 20$ $kV$, $V_{MCP} = 3060$ $V$, elevation angle 0 degree*
Right: *$He^+$, $E/q = 2$ $keV/e$, $V_{PAC} = 19$ $kV$, $V_{MCP} = 2800$ $V$, elevation angle 0 degree.*
*The S-channel of FM1 shows a strong asymmetry. This asymmetry was also detected during the calibration of the ESEA, see Section 3.5. It is due to the geometry of the S-channel slits.*
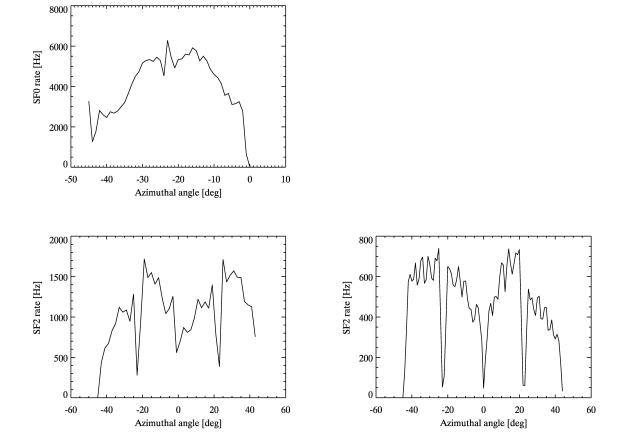
Figure 6.11: *Azimuthal angle scan of integrated FM1 Wide Angle Partition.*
Top: *Quadrant 1, He$^+$, E/q = 2 keV/e, $V_{PAC}$ = 20 kV, $V_{MCP}$ = 3250 V, elevation angle 0 degree.*
Bottom left: *Quadrant 2, He$^+$, E/q = 2 keV/e, $V_{PAC}$ = 15 kV, $V_{MCP}$ = 3060 V, elevation angle 0 degree.*
Bottom right: *Quadrant 3, He$^+$, E/q = 2 keV/e, $V_{PAC}$ = 20 kV, $V_{MCP}$ = 2800 V, elevation angle 0 degree.*
*The mechanical structures of the TOF structure can be seen. For quadrant 2 the PAC voltage could not be brought up to 20 kV because the vacuum pressure in the instrument chamber was not low enough.*

## 6.5    Energy and angular acceptance

For each aperture a geometric factor measurement was performed. The procedure was different than for the ESEA (see Chapter 3). Instead of changing the beam energy, the ESA voltage was changed for each elevation angle. The whole procedure was automatized. The set ESA voltage had to be transformed into energy per charge to get transmission contour plots depending on beam energy and elevation angle. Unlike the ESEA, the transmission is strongly dependent on the azimuthal position. An azimuthal scan was done before launching a geometric factor measurement to choose a good azimuthal angle. For each geometric factor plot it is important to keep the respective azimuthal position in mind. For these measurements, ESA and deflection plate sweeping was disabled so that the counts were accumulated during one minute for each angle and ESA voltage step. At the beginning and at the end of the measurements a beam intensity measurement was performed.

### 6.5.1    Main Channel

For the main channel there are two measurements for each flight model. For each setting the active area (see Table 6.1) and the geometric factor (see Table 6.2) are calculated. Since the detection efficiency of the MCP and the SSD are crucial for both numbers, they depend on the mass, energy and charge of the particles. For FM1 the stop rate STP0 was not used because it was not comparable to the the start and the coincidence rates SF0 and SFR0.

The elevation angle and energy acceptance measurements (Geometric Factor, see Figure 6.12) were automated. The beam energy was set to 2 keV/e and the elevation angle was scanned from -5.5 to +6.0 in steps of 0.5 deg. For each angle step an ESA scan was done, whereby the ESA voltage was increased by about two volts for each step. The ESA voltage scan was not uniformly stepped but rather optimized for best possible range scanning.

| Instrument | Azimuthal angle (deg) | SF0 | SFR0 | RA_TRIG (cm$^2$) |
|---|---|---|---|---|
| FM1 | −8 | 0.37 | 0.5 | 0.6 |
| (`fishscan-050108.txt`[a], He$^+$, $E/q = 2$ keV/e, $V_{PAC} = 20$ kV, $V_{MCP} = 3060$ V) | | | | |
| FM2 | 8 | 0.47 | 0.19 | 0.64 |
| (`fishscan-050620-0636.txt`, He$^+$, $E/q = 2$ keV/e, $V_{PAC} = 18$ kV, $V_{MCP} = 3000$ V) | | | | |
| FM2 | −8 | 0.35 | 0.14 | 0.44 |
| (`fishscan-050622-0915.txt`, He$^+$, $E/q = 2$ keV/e, $V_{PAC} = 18$ kV, $V_{MCP} = 3000$ V) | | | | |

[a]Name of text file with the elevation angles, the respective log files have the name PLA_FM*-date-time.log, one log file for each elevation angle step

Table 6.1: *Active area of MC integrated instruments*

### 6.5.2    S-channel

The S-channel has a much smaller active area than the main channel. Therefore a higher beam rate was needed and a longer accumulation time. For all S-channel measurements compiled in Table 6.3 the integration time was two minutes. The stop rate could not be used for the main channel of FM1, so only the active area and geometric factor of the start rate, coincidence rate and resistive anode trigger rate (`RA_TRIG`) were calculated, see Tables 6.3 and 6.4.

As for the main channel, the geometric factor measurements for the S-channel were automated. The elevation angle was scanned from -0.6 to +0.6 with a step size of 0.1 deg. The electrode voltage is set for each elevation angle step, according to a sweep command table for the voltage settings of the four electrodes SCO-L, SCI-U, ESA-O and ESA-I (see Figure 1.7), using the analyzer constants evaluated in

| Instrument | Azimuthal angle (deg) | SF0 | SFR0 | RA_TRIG |
|---|---|---|---|---|
| | | | (eV/eV cm$^2$ sr) | |
| FM1 | $-8$ | $1.0 \cdot 10^{-3}$ | $1.3 \cdot 10^{-4}$ | $1.5 \cdot 10^{-3}$ |
| (`fishscan-050108.txt`$^a$, He$^+$, $E/q = 2$ keV/e, $V_{PAC} = 20$ kV, $V_{MCP} = 3060$ V) | | | | |
| FM2 | $8$ | $1.8 \cdot 10^{-3}$ | $6.0 \cdot 10^{-4}$ | $4.0 \cdot 10^{-3}$ |
| (`fishscan-050620-0636.txt`, He$^+$, $E/q = 2$ keV/e, $V_{PAC} = 18$ kV, $V_{MCP} = 3000$ V) | | | | |
| FM2 | $-8$ | $1.3 \cdot 10^{-3}$ | $5.0 \cdot 10^{-4}$ | $2.9 \cdot 10^{-3}$ |
| (`fishscan-050622-0915.txt`, He$^+$, $E/q = 2$ keV/e, $V_{PAC} = 18$ kV, $V_{MCP} = 3000$ V) | | | | |

$^a$Name of text file with the elevation angles, the respective log files have the name PLA_FM*-date-time.log, one log file for each elevation angle step

Table 6.2: *Geometric factor of MC integrated instruments*

Chapter 3. The voltage range and step size were optimized for best range coverage. In Figure 6.13 the angular and energy acceptance plots are shown.

| Instrument | Azimuthal angle (deg) | SF0 | SFR0 | RA_TRIG |
|---|---|---|---|---|
| | | | (cm$^2$) | |
| FM1 | $-11$ | $3.0 \cdot 10^{-4}$ | $4.5 \cdot 10^{-5}$ | $4.0 \cdot 10^{-4}$ |
| (`fishscan-041214.txt`$^a$, He$^+$, $E/q = 2$ keV/e, $V_{PAC} = 20$ kV, $V_{MCP} = 3060$ V) | | | | |
| FM2 | $11$ | $5.8 \cdot 10^{-4}$ | $2.4 \cdot 10^{-4}$ | $8.1 \cdot 10^{-4}$ |
| (`fishscan-050620-0636.txt`, He$^+$, $E/q = 2$ keV/e, $V_{PAC} = 18$ kV, $V_{MCP} = 3000$ V) | | | | |

$^a$Name of text file with the elevation angles, the respective log files have the name PLA_FM*-date-time.log, one log file for each elevation angle step

Table 6.3: *Active area of SC integrated instruments*

| Instrument | Azimuthal angle (deg) | SF0 | SFR0 | RA_TRIG |
|---|---|---|---|---|
| | | | (eV/eV cm$^2$ sr) | |
| FM1 | $-11$ | $7.8 \cdot 10^{-8}$ | $1.1 \cdot 10^{-8}$ | $1.7 \cdot 10^{-7}$ |
| (`fishscan-041214.txt`$^a$, He$^+$, $E/q = 2$ keV/e, $V_{PAC} = 20$ kV, $V_{MCP} = 3060$ V) | | | | |
| FM2 | $11$ | $1.3 \cdot 10^{-7}$ | $5.0 \cdot 10^{-8}$ | $4.2 \cdot 10^{-7}$ |
| (`fishscan-050620-0636.txt`, He$^+$, $E/q = 2$ keV/e, $V_{PAC} = 18$ kV, $V_{MCP} = 3000$ V) | | | | |

$^a$Name of text file with the elevation angles, the respective log files have the name PLA_FM*-date-time.log, one log file for each elevation angle step

Table 6.4: *Geometric factor of SC integrated instruments*

### 6.5.3 Wide angle partition

Only the FM1 WAP could be calibrated in Bern as mentioned above. For FM1 a complete geometric factor measurement was only performed for the non-SSD side (Quadrant 2 and 3), see Table 6.5 for a list of the used data files. Since there is no resistive anode on the non-SSD side, only the active area and the geometric factor of two rates, start rate SF2 and coincidence rate SFR2, are calculated, which can be compared to the parameters obtained for main and S-channel. See Tables 6.5 (active area) and 6.6 (geometric factor).
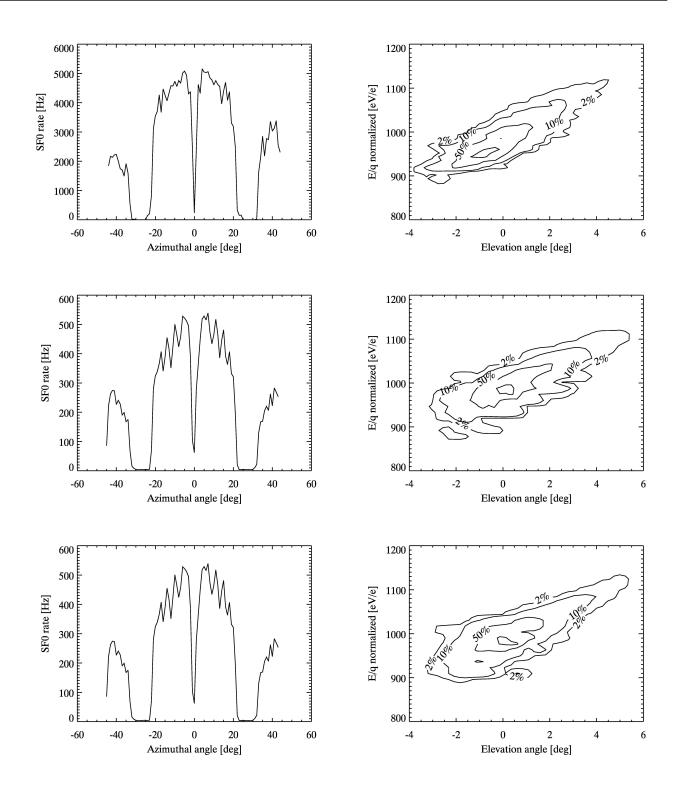
Figure 6.12: *Angular and energy acceptance plot main channel of the integrated instrument:*
*(from top left to bottom right)*
*FM1 azimuthal angle scan, $He^+$, $E/q = 2\ keV/e$, $V_{PAC} = 20\ kV$, $V_{MCP} = 3060\ V$*
*FM1 energy vs elevation angle plot, azimuthal angle $-8°$, same settings*
*FM2 azimuthal angle scan, $He^+$, $E/q = 6\ keV/e$, $V_{PAC} = 18\ kV$, $V_{MCP} = 3000\ V$*
*FM2 energy vs elevation angle plot, azimuthal angle $8°$, $He^+$, $E/q = 2\ keV/e$, $V_{PAC} = 18\ kV$, $V_{MCP} = 3000\ V$*
*FM2 azimuthal angle scan, $He^+$, $E/q = 6\ keV/e$, $V_{PAC} = 18\ kV$, $V_{MCP} = 3000\ V$*
*FM2 energy vs elevation angle plot, azimuthal angle $-8°$, $He^+$, $E/q = 2\ keV/e$, $V_{PAC} = 18\ kV$, $V_{MCP} = 3000\ V$*
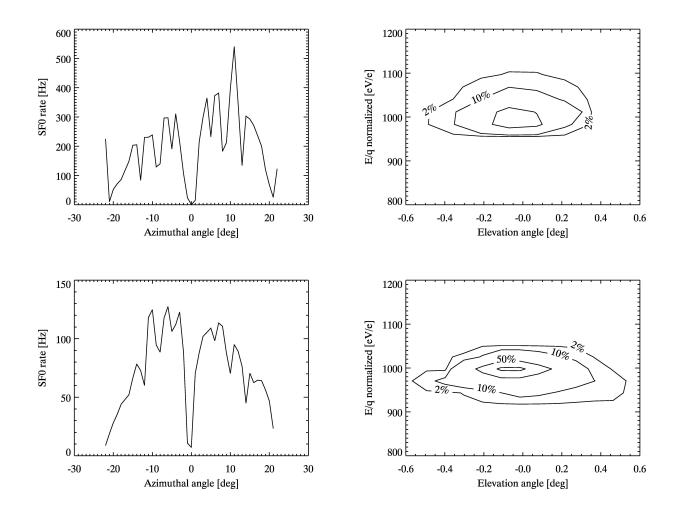
Figure 6.13: *Angular and energy acceptance plot of S-channel of integrated instrument:*
*(from top left to bottom right)*
*FM1 azimuthal angle scan, $He^+$, $E/q = 2\ keV/e$, $V_{PAC} = 20\ kV$, $V_{MCP} = 3060\ V$*
*FM1 energy vs elevation angle plot, azimuthal angle $-11°$, same settings*
*FM2 azimuthal angle scan, $He^+$, $E/q = 2\ keV/e$, $V_{PAC} = 19\ kV$, $V_{MCP} = 2800\ V$*
*FM2 energy vs elevation angle plot, azimuthal angle $11°$, $He^+$, $E/q = 2\ keV/e$, $V_{PAC} = 18\ kV$, $V_{MCP} = 3000\ V$*

The elevation angle and energy acceptance measurements (geometric factor, see Figure 6.14) were automated as for the other channels. The beam energy was set to 2 keV/e and the elevation angle was scanned from -6 to +10 in steps of 1.0 deg. For each angle step an ESA scan was done, whereby the ESA voltage was increased by about two volts for each step. The ESA voltage scan was not uniformly stepped, but rather optimized for best possible range scanning.

| Instrument | Azimuthal angle | SF2 | SFR2 |
|---|---|---|---|
| | (deg) | | (eV/eV cm$^2$ sr) |
| FM1 Quadrant 2 | −8 | 0.13 | 0.05 |
| (`fishscan-050115.txt`[a], He$^+$, $E/q = 2$ keV/e, $V_{PAC} = 20$ kV, $V_{MCP} = 2900$ V) | | | |
| FM1 Quadrant 3 | −8 | 0.22 | 0.10 |
| (`fishscan-050122.txt`, He$^+$, $E/q = 2$ keV/e, $V_{PAC} = 20$ kV, $V_{MCP} = 2900$ V) | | | |

[a]Name of text file with the elevation angles, the respective log files have the name PLA_FM*-date-time.log, one log file for each elevation angle step

Table 6.5: *Active area of WAP integrated instruments*

| Instrument | Azimuthal angle | SF2 | SFR2 |
|---|---|---|---|
| | (deg) | | (cm$^2$) |
| FM1 Quadrant 2 | −8 | $1.0 \cdot 10^{-3}$ | $3.7 \cdot 10^{-4}$ |
| (`fishscan-050115.txt`[a], He$^+$, $E/q = 2$ keV/e, $V_{PAC} = 20$ kV, $V_{MCP} = 2900$ V) | | | |
| FM1 Quadrant 3 | −8 | $1.4 \cdot 10^{-3}$ | $6.9 \cdot 10^{-4}$ |
| (`fishscan-050122.txt`, He$^+$, $E/q = 2$ keV/e, $V_{PAC} = 20$ kV, $V_{MCP} = 2900$ V) | | | |

[a]Name of text file with the elevation angles, the respective log files have the name PLA_FM*-date-time.log, one log file for each elevation angle step

Table 6.6: *Geometric factor of WAP integrated instruments*
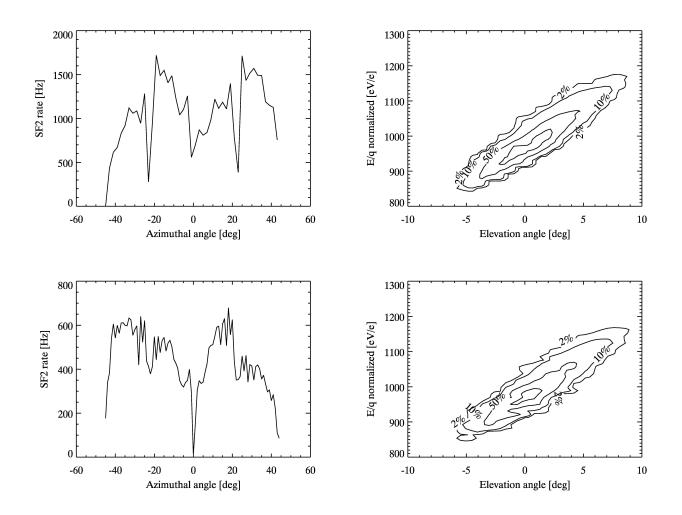
Figure 6.14: *Angular and energy acceptance plot WAP of integrated instrument:*
*(from top left to bottom right)*
*FM1 quadrant 2 azimuthal angle scan, $He^+$, $E/q = 2\ keV/e$, $V_{PAC} = 20\ kV$, $V_{MCP} = 2900\ V$*
*FM1 quadrant 2 energy vs elevation angle plot, azimuthal angle $-8°$, $He^+$, $E/q = 20\ keV/e$, $V_{PAC} = 20\ kV$,*
*$V_{MCP} = 2960\ V$*
*FM1 quadrant 3 azimuthal angle scan, $He^+$, $E/q = 2\ keV/e$, $V_{PAC} = 20\ kV$, $V_{MCP} = 2900\ V$*
*FM1 quadrant 3 energy vs elevation angle plot, azimuthal angle $-8°$, same settings*
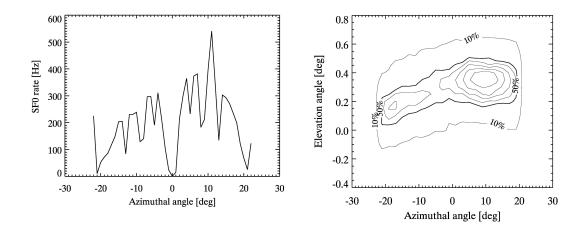
Figure 6.15: *Comparison of S-channel FM1, left side transmission of integrated instrument, right side angular acceptance plot for ESEA, center of the SWS at 60 deg. The transmission on the negative side is significantly smaller than on the positive side, which can be explained by the different transmission of the S-channel aperture.*

## 6.6  Comparison

The ion optical properties of PLASTIC entrance system/energy analyzer (ESEA) were measured extensively at the University of Bern, see Chapter 3. The ion beam facilities in Bern allow a precise characterization of the transmission and deflection abilities of a space instrument such as PLASTIC. In this section the ion optical calibration of the integrated instruments FM1 and FM2 are compared to the ion optical calibration measurements of the ESEA of FM1 and FM2. The two modules are also compared to each other, since the goal of the STEREO mission is to provide two nearly identical instrument suites in space. They are almost identical, see Chapter 3, but the differences between the two instruments made it necessary to use two separate sets of instrument parameters.

Since the absolute transmission factors of the integrated instruments not only depend on the ion optical properties, but also on the detection efficiency of the MCP and the SSD, the parameters are not comparable between ESEA and the integrated instrument. However, the comparison can explain features observed during the calibration campaigns of the integrated instruments.

In the following, azimuthal angle response and energy and angular acceptance (geometric factor) measurements are compared and discussed.

### 6.6.1  Azimuthal angle response

Comparing FM1 and FM2 azimuthal scans, the S-channel measurement for FM1 shows a strong asymmetry between the plus and the minus side of the scan. Comparing it to the S-channel angular acceptance of the ESEA, one can see that the transmission is a factor 1.5 higher on the positive side (see Figure 6.15). For FM2 the azimuthal scan looks symmetric, which agrees with the ESEA measurement, too (see Figure 6.16). The main channel transmission is symmetric, the mechanical parts blocking the beam are clearly visible. On Figure 6.17 the transmission over the complete azimuth is shown for FM1, zero degree corresponds to the center of the solar wind sector (SWS). For FM2 only quadrant 0 was measured. The intensity is normalized for each quadrant. The spokes in the center of each quadrant can clearly be seen as well as the grids holding the carbon foil. Half of quadrant 1 is blocked. All calibration measurements in CASYMS are done with a parallel and monoenergetic beam, imaging all mechanical features of the instrument. In space the solar wind has a thermal velocity that is much higher than that of the CASYMS ion beam. This smoothes the visible transmission differences depending on the azimuthal angle.
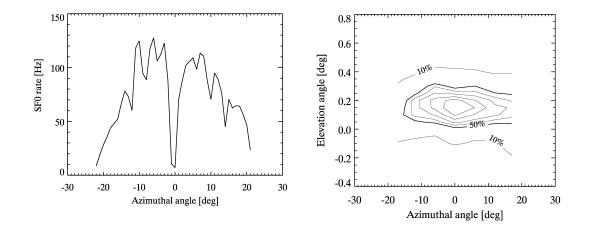
**Figure 6.16:** *Comparison of S-channel FM2, left side transmission of integrated instrument, right side angular acceptance plot for ESEA. Unlike FM1, the S-channel aperture shape is symmetric.*
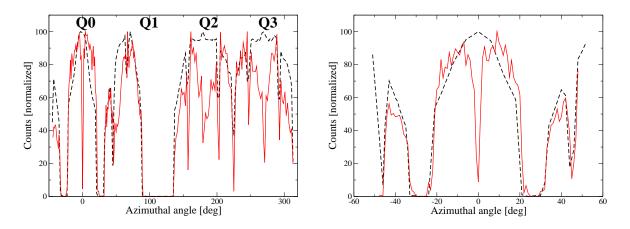


**Figure 6.17:** *Comparison of main channel and WAP transmission depending on the azimuthal angle. (Black dashed line ESEA measurement, red solid line integrated instrument.) Angle zero degree responds to the center of the solar wind sector (SWS). For FM2 there are only quadrant 0 measurements for the integrated instrument. All intensities are normalized to 100 for each quadrant. For the integrated instrument the spoke is clearly visible in the center of each quadrant as well as the grids holding the carbon foil. Half of quadrant 1 is blocked.*
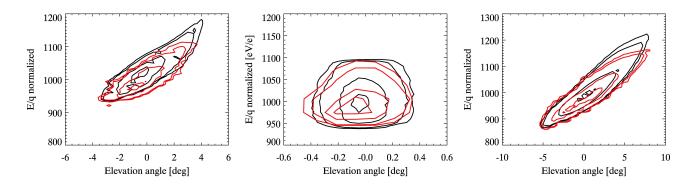
Figure 6.18: *Comparison of angular and energy acceptance of FM1. From left to right main channel, S-channel and WAP. The red contours are those of the integrated instrument measurements.*
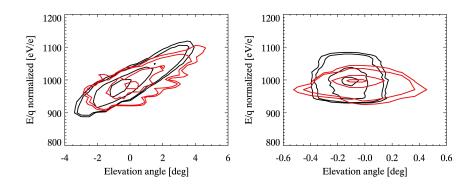


Figure 6.19: *Comparison of angular and energy acceptance of FM2. Main channel and S-channel. The red contours are those of the integrated instrument measurements.*

### 6.6.2    Geometric factor

The comparison of the angular and energy acceptance is suited to check whether the ion optical characteristics of PLASTIC change for the integrated instrument. On Figure 6.18 the transmission is plotted depending on the elevation angle and beam energy for all three apertures of FM1. Main channel and S-channel plots for FM2 are shown on Figure 6.19. There are no WAP measurements for FM2. The transmission contours for the integrated instruments are overplotted in red. The S-channel contour plots for FM1 ESEA are shifted by 0.3 deg, for FM2 ESEA by 0.2 deg. These small offsets are due to the very sensitive angular acceptance of the S-channel. If the turntable in CASYMS, on which the instruments are mounted, is not exactly parallel to the incident ion beam, the maximum angular acceptance angle differs. The accuracy of the elevation angle settings is not better than 0.1 deg. For the two larger apertures this effect does not play an important role, since the angular acceptance width is at least 20 times larger than 0.1 deg.
For main channel and WAP the comparison plots show a very good agreement, while for the S-channel the energy acceptance of the integrated instrument seems to be smaller. But the difference is very small considering that the count rate is very low for the S-channel.

## 6.7    Conclusions and summary

The calibration campaign for the integrated instruments FM1 and FM2 were very restricted. Nevertheless the measurements gave interesting and important knowledge about the ion optical characteristics of the integrated instruments compared to the entrance system/energy analyzer. Since there were major changes in the instruments after the Bern calibration, some of the calibration results gained were no longer valid, e.g., the resolution of the TOF measurement of FM1. Improvements of the electronics give a better TOF resolution than before (before improvement about 20 % of the nominal TOF). This should allow to resolve

the different charge states of iron in the solar wind. Before, the large uncertainty made it impossible to see the different charge states. However, the following conclusions can be drawn:

- There is no big difference in the angular and energy acceptance between ESEA and integrated instruments. (Geometric factor measurements)

- The azimuthal response of the integrated instruments reflect the azimuthal response of the ESEA. Additionally, the mechanical features of the parts below the ESEA could be clearly resolved by the parallel ion beam of CASYMS, reducing the absolute transmission of the instrument.

- The instrument response depends strongly on the settings of the MCP and the SSD. The relation between detection efficiency and energy defects must be incorporated into the data analysis.

- The capabilities of PLASTIC to detect and resolve different charge states and species in the solar wind depend highly on the resolution of the TOF and the SSD energy measurement, as well as on the energy defects of the SSD. Thus, it is important that the post-acceleration voltage is as high as possible.

- It can be expected from calibration results that the measured counts through the main channel and the S-channel are rather small. The relative accumulation time for the ESA and deflection plate voltage steps, which are at the maximum position of the solar wind distribution, is very small. Only about 6 to 8 ESA voltage steps cover the protons in the solar wind.

# Chapter 7

# First in-Flight data from STEREO/PLASTIC

## 7.1 Introduction

On Thursday, 26th of October 2006, at 1:52 a.m. UTC, the Delta II 7925-10L rocket carrying the two STEREO spacecraft, was successfully launched from Cape Canaveral Air Force Station in Florida, see Figure 7.1. The twin spacecraft were separated soon after the launch. After several orbits around the Earth STEREO A (Ahead) left on the 22nd of December the highly eccentric orbit towards its orbit around the Sun. STEREO B (Behind) had one more orbit and with gravitational assist of the Moon it left the Earth's orbit on the 12th of February.

In this short chapter I want to present some preliminary results from in-flight data. It demonstrates that the PLASTIC instrument works fine and delivers scientific measurements. In this concept it is a conclusion to the previous calibration measurements.



Figure 7.1: *Launch of the Delta II rocket carrying the two STEREO spacecraft*
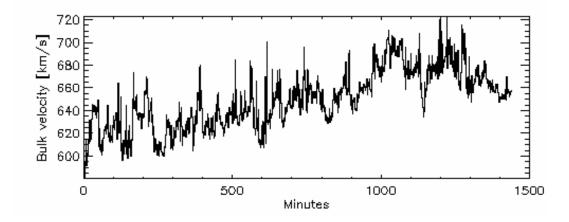
Figure 7.2: *Bulk velocity on the 28th of February, 2007. Measured with the PLASTIC sensor on STEREO A.*

## 7.2 First data from flight

### 7.2.1 Overview

I look at two different data products, the PHA data and the full monitor rate. For each valid time of flight measurement (double coincidence), the $E/q$ step, the deflection angle step, the position, section, quadrant, SSD energy and time of flight is measured and stored, like the PHA data obtained during integrated instrument calibration, see Section 6.2.3. But only a selection is sent to ground in full resolution, 768 events from all quadrants and channels for each complete energy/charge and deflection angle cycle (128 ESA voltage steps and 32 deflection steps), selected according to different priorities (highest priority for heavy solar wind ions). These TOF events are stored in the PHA data file, Apid315. From the PHA all other data products are produced onboard, and then transmitted to ground. Additionally, rates are calculated onboard and sent to ground. For more information on the data products, see [17].
All data studied here are from STEREO A, since STEREO B was still in the Magnetosheath during this work.

### 7.2.2 PHA data

I looked at PHA raw data, the Apid315 file, on the 28th of February. The bulk velocity over the whole day is plotted in Figure 7.2. Histograms of the PHA data accumulated between 8 and 9 a.m. are shown in Figure 7.3. The switch from main to S-channel is visible. From the measured data, ESA step, SSD energy and time of flight, a mass-mass/charge plot can be generated, like in Section 6.3, see Figure 7.4 (conversions used for M-M/Q plot: 2 keV/e per SSD channel and 0.25 ns per TOF channel). One has to keep in mind, that the ion species have different priorities for storage. So the heavy ions are stored with a higher priority than the protons. Therefore, the shown M-M/Q plot does not reflect the solar wind composition. The data has to be corrected for energy defects and offsets. In the classifier data the measured abundances are recorded.
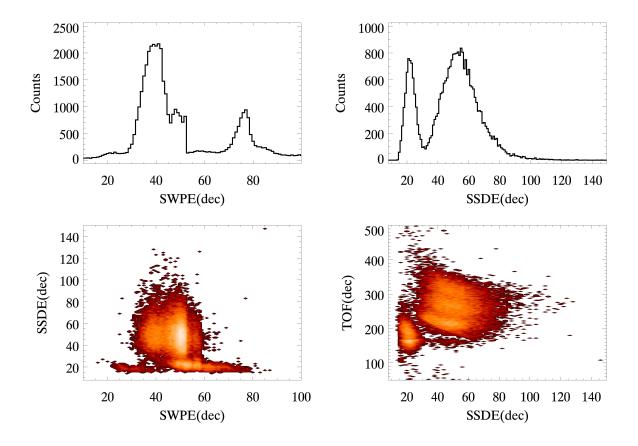
Figure 7.3: *PHA data from STEREO A. Data accumulated between 8 and 9 a.m. on the 28th of February, 2007. The switch from main to S-channel at ESA step 53 is clearly visible on the left plots. The peak at ESA step 77 is from protons and corresponds to a proton velocity of about 640 km/s, the peak a the switch is from alphas and heavy ions like $O^{6+}$.*
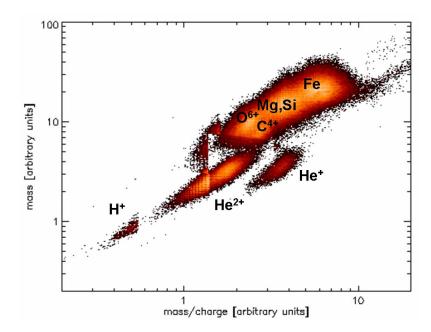


Figure 7.4: *M-M/Q plot 28th of February, 2007. Counts accumulated over a whole day. Measured with PLASTIC sensor on STEREO A. Data is not corrected for energy loss.*
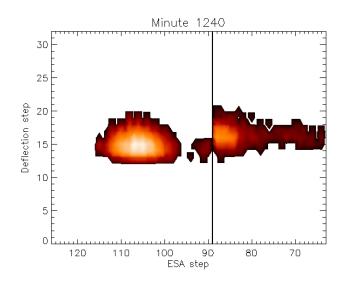
Figure 7.5: *Contour plot of full monitor rate of minute 1240 on the 20th of February, 2007. Deflection step versus ESA step. The switch from main to S-channel is clearly visible at ESA step 89. ESA step 127 corresponds to $E/q = 0.2$ keV/e, ESA step 64 to $E/q = 4$ keV/e. The peak at ESA step 106 is from protons and corresponds to a proton velocity of about 330 km/s, the peak a the switch is from alphas and heavy ions like $O^{6+}$.*

### 7.2.3 Preliminary He/H ratio in slow solar wind

To determine the bulk velocity (proton velocity) of the solar wind, I used the full monitor rates, Apid317, of the 20th of February, 2007 from the STEREO A spacecraft. In this file one rate (e.g., start rate, SF0) is stored in full resolution, for 64 ESA steps. On that day, the RA trigger rate, RA_TRIG, is recorded for ESA steps 64 to 127 for each sweeping cycle. I selected a time period where the bulk velocity was steady. For each cycle the rate for 64 ESA steps and the corresponding 32 deflection steps are available. A contour plot of minute 1240 is shown in Figure 7.5. I applied a 2D Gauss function to the data to obtain the bulk velocity, the thermal velocity and the out-of-ecliptic angle, see Figure 7.6 for the minutes between 6.20 p.m. and 11.20 p.m. UTC.

The $He^{2+}$ velocity was obtained for each minute applying a 1D Gauss function to the velocity distribution, after summation over all deflection steps. Additionally, the counts were corrected for the S-channel switch. From the amplitude of the proton and alpha distributions I calculated a preliminary He/H ratio. The alpha velocity, the He/H ratio versus time and the alpha velocity versus proton velocity are shown in Figure 7.7 for the same time period as above.

#### Summary

Comparing the results with ACE/SWEPAM [44] Level 1 data from the ACE science center web page (`http://www.srl.caltech.edu/ACE/ASC/`), see Figures 7.8 and 7.9, the two instruments show a quite good agreement. ACE orbits around the L1 Lagrangian point, approximately $1.5 \cdot 10^6$ km away from earth. The position of ACE was $x_{GSE} \approx 0.01$ AU and $y_{GSE} \approx 0.001$ AU) on the 20th of February, STEREO A was at $x_{GSE} = 0.02$ AU and $y_{GSE} = -0.01$ AU. The two spacecraft were close, the distances of the two spacecraft from the sun are both about 0.98 AU. Both data sets are preliminary data, PLASTIC data is given per minute, ACE/SWEPAM solar wind values are five minutes averages.

Aellig et al., [1], shows that the alpha/proton ratio varies with the solar cycle. The alpha/proton ratio during solar minimum is lower than 0.02, what would agree with our measurement.

### 7.3 Conclusion and outlook

First preliminary PLASTIC measurements of some solar wind data show promising results. Both space-craft are working fine, hopefully providing us in the next time with data.
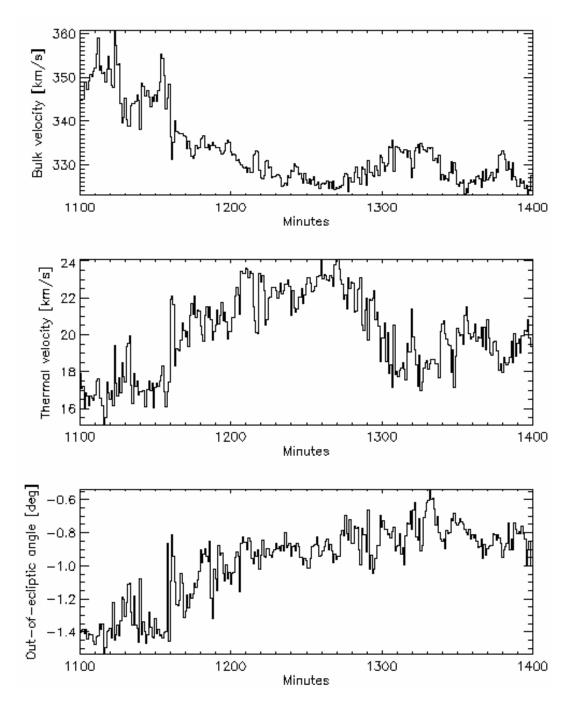
Figure 7.6: *Proton velocity, thermal velocity and out-of-ecliptic angle between 6.20 p.m. and 11.20 p.m. UTC on the 20th of February 2007, STEREO A*
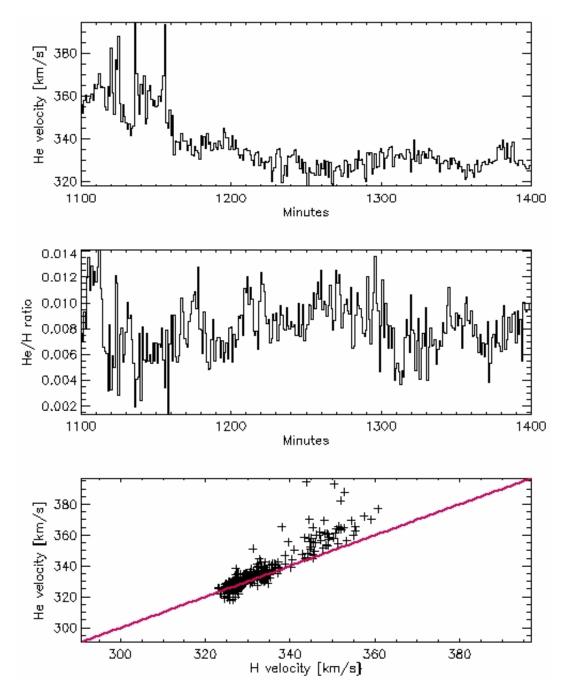
Figure 7.7: *Alpha velocity, He/H ratio versus time and alpha versus proton velocity are shown between 6.20 p.m. and 11.20 p.m. UTC on the 20th of February 2007, STEREO A.*
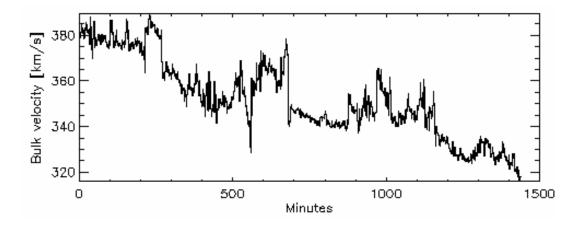
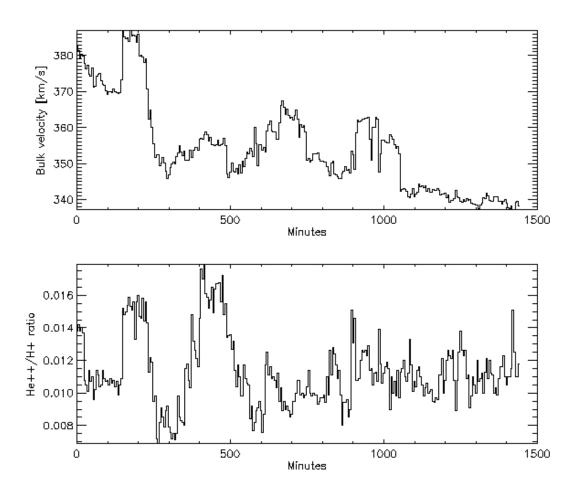Figure 7.8: *Proton velocity measured with PLASTIC on STEREO A, 20th February, 2007.*



Figure 7.9: *Proton velocity and He$^{2+}$/H$^+$ ratio, five minutes averages. ACE/SWEPAM Level 1 data, 20th February, 2007.*

# Chapter 8

# Nickel/iron ratio in the solar wind: Measurements with CELIAS/MTOF on SOHO

## 8.1 Introduction

### 8.1.1 Motivation

The STEREO mission is one of the many missions, which investigate the solar terrestrial relationship. We look forward to the science return phase since so much preparatory calibration work was done to ensure a properly functioning instrument. To be prepared for the STEREO data I evaluated other solar wind composition data provided by the CELIAS/MTOF instrument onboard SOHO, which studies the elemental composition of the solar wind.

In the solar wind the elements with a low first ionization potential (FIP) are enriched relative to their photospheric abundances, see [19]. Nickel as well as iron have a low-FIP compared to oxygen. The iron/oxigen elemental ratio has been studied earlier (see for example [68] or [34]). It was now interesting to study whether nickel also shows an enrichment in the solar wind compared to the elemental abundance in the photosphere. As our study presented in this chapter shows, the nickel/iron elemental ratio is the same for photosphere, solar wind and meteorites, thus it can be concluded that nickel experiences the same enrichment process in the solar corona like other low-FIP elements.

### 8.1.2 SOHO Mission

The Solar and Heliospheric Observatory is a joint space mission of the European Space Agency (ESA) and the National Aeronautics and Space Administration (NASA). The SOHO spacecraft was launched on the 2nd December 1995 from Cape Canaveral Space Center. SOHO was launched to answer the following three fundamental questions:

- What is the structure and dynamics of the solar interior?

- Why does the solar corona exist and how is it heated to the extremely high temperature of about 1'000'000° C?

- Where is the solar wind produced and how is it accelerated?

The last topic is investigated with the CELIAS instruments, which is briefly discussed below. The SOHO mission is up till now one of the most successful missions, providing a broad insight into the structure of the Sun and the inner heliosphere.

SOHO moves around the Sun in step with the Earth, by slowly orbiting around the First Lagrangian Point (L1), where the combined gravity of the Earth and Sun keep SOHO in an orbit locked to the Earth-Sun line. The L1 point is approximately 1.5 million kilometers away from Earth, in the direction of the Sun.

## 8.2    Instrumentation

### 8.2.1    Charge, Element and Isotope Analysis System (CELIAS)

The CELIAS instrument is designed to study the composition of the solar wind and of solar and inter-planetary energetic particles. It consists of three different sensors which are optimized for a particular aspect of the ion composition and a photodiode sensor to study the extreme ultraviolet radiation from the solar disk. The three time of flight (TOF) sensors are CTOF, MTOF and STOF. The MTOF is discussed below. The CTOF (Charge determining TOF) sensor determines the Mass, $M$, ionic charge, $Q$, and speed, $v$, of individual ions from the measurement of their time of flight and energy within a preset $E/Q$ channel. The measurement principle is similar to the measurement principle of PLASTIC, see Chapter 1. The STOF, the Suprathermal Time-of-Flight sensor, is a particle telescope intended to measure ionic charge states of particles with suprathermal energies in the range 20 - 4000 keV/amu from just above the solar wind up to low energy flare particle energies. For more information about CELIAS, see [32].

### 8.2.2    MTOF - Mass Determining Time-of-Flight Sensor

The MTOF sensor, see Figure 8.1, is a high mass resolution system ($M/\Delta M > 100$) which provides solar wind composition data over a wide range of solar wind. MTOF consists of an entrance system, the Wide Angle, Variable Energy/charge (WAVE) passband deflection system and an isochronous time-of-flight system, V-MASS.
Solar wind ions enter the instrument through the WAVE entrance system, which has an energy per charge bandwidth of about half of a decade and a conic field of view of $\pm 25°$ width. The entrance system also suppresses the solar wind proton flux and the solar UV radiation, which would saturate the instrument by start and stop counts. Additionally, it reduces the transmission of scattered ions and neutrals to a minimum. On the other hand, the wide energy bandwidth of WAVE allows, that it transmit almost the full velocity distribution of a given solar wind species. After the WAVE particles can be accelerated or decelerated towards a thin carbon foil (2.1 $\mu$g/cm$^2$) at the entrance of V-MASS. V-MASS is a V-shaped isochronous time of flight spectrometer. The V-shaped and the hyperbola deflection electrodes generate an electrostatic harmonic potential so that the time of flight of an ion between passing through the carbon foil and the stop detector is proportional to the square root of mass per charge $(M/Q^*)^{1/2}$, where $Q^*$ is the charge after the carbon foil. The time of flight does not depend on the ion energy, see [47] and [29]. The time of flight of a single ion is measured between a pulse in a microchannel plate detector (Start MCP) triggered by secondary electrons released at the passage of the ion through the carbon foil as the start signal and the stop pulse, when the ion hits the position sensing ion microchannel plate detector (Ion MCP), see Figure 8.1. For more details see [36] and about the instrument function see Section 8.3.

## 8.3    Instrument function of MTOF

The MTOF instrument function is described in detail in [68]. Here I briefly come to some important features of the instrument function which influence the measurements of nickel and iron abundances. I will outline the influence of the different parts of the sensor.

### 8.3.1    Overview

1. Charge state distribution of species in solar wind

2. WAVE transmission at a given E/q

3. Carbon foil transmission and charge state distribution of species after passing the carbon foil

4. Start efficiency, dependent on secondary electron yield
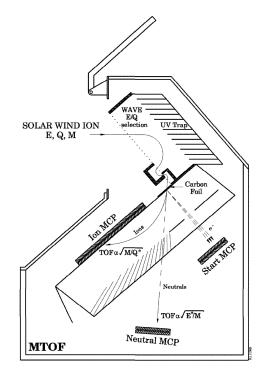
5. Transmission through V-Mass

Figure 8.1: *Schematic view of the MTOF sensor, figure from [34]*

6. Stop efficiency

**Count number of MTOF for species $X$ $n_X$:**

**Charge state distribution and WAVE transmission** Particles after passing WAVE:

$n_{\text{X,WAVE}} = \sum_i n_X \, f_{\text{Q,X}}(q_i) \cdot A_{\text{Act}}(E/q_i)$

**Charge state after carbon foil** Particles with charge state 1+ after passing carbon foil:

$n_{\text{X,CF,1+}} = f_{\text{X,CF}}(1+) \cdot n_{\text{X,WAVE}}$

**Start efficiency** Dependent on energy and species: $\eta_{\text{START,X}} = 1 - \exp(-p_{\text{MCP}} \cdot \gamma_{\text{SEY,X}})$

**Transmission of V-Mass** Not specified further: $\alpha$

**Stop efficiency** $\eta_{\text{STOP}}$

The total counts measured with MTOF (Time of flight events) is given by:

$$
\begin{aligned}
n_{\text{TOF,X}} &= \alpha \cdot n_{\text{X,CF,1+}} \cdot \eta_{\text{STOP}} \cdot \eta_{\text{START,X}} \\
&= \alpha \cdot n_X \sum_i f_{\text{Q,X}}(q_i) A_{\text{Act}}(E/q_i) \cdot f_{\text{X,CF}}(1+) \cdot \eta_{\text{STOP}} \cdot \eta_{\text{START,X}}
\end{aligned}
\tag{8.1}
$$

When measuring elemental abundance and isotopic ratios the absolute species density need not be known. In our case we are only interested in the iron/nickel elemental abundance ratio and the nickel isotope abundances ratio. Considering this Equation 8.1 can be expressed for two species X and Y as follows:

$$
\begin{aligned}
\frac{n_{\text{TOF,X}}}{n_{\text{TOF,Y}}} &= \frac{n_X \sum_i f_{\text{Q,X}}(q_i) A_{\text{Act}}(E_X/q_i) \cdot f_{\text{X,CF}}(1+) \cdot \eta_{\text{STOP}} \cdot \eta_{\text{START,X}}}{n_Y \sum_i f_{\text{Q,Y}}(q_i) A_{\text{Act}}(E_Y/q_i) \cdot f_{\text{Y,CF}}(1+) \cdot \eta_{\text{STOP}} \cdot \eta_{\text{START,Y}}} \\
&= \frac{n_X}{n_Y} \cdot \frac{\sum_i f_{\text{Q,X}}(q_i) A_{\text{Act}}(E_X/q_i) \cdot f_{\text{X,CF}}(1+) \cdot \eta_{\text{START,X}}}{\sum_i f_{\text{Q,Y}}(q_i) A_{\text{Act}}(E_Y/q_i) \cdot f_{\text{Y,CF}}(1+) \cdot \eta_{\text{START,Y}}}
\end{aligned}
\tag{8.2}
$$

The last step assuming that the ion optical properties of V-Mass as well as the stop efficiency of the MCP are similar for species X and Y. For nickel and iron this assumption is valid.
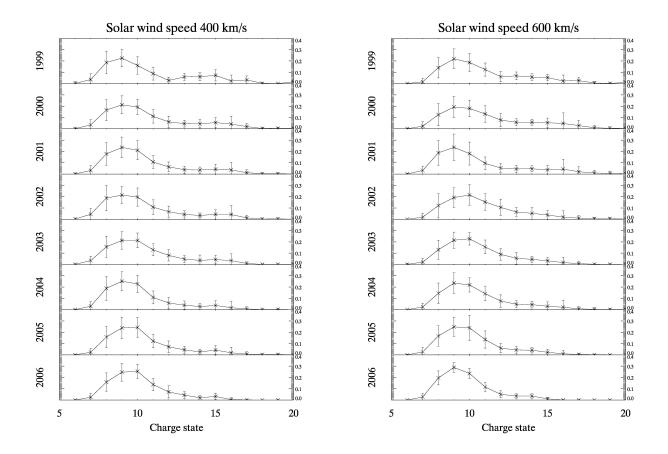
Figure 8.2: *Charge state distribution of iron for solar wind speed 400 km/s and 600 km/s from 1999 to 2006, measured with ACE/SWICS [16]. For details about level 2 data from ACE/SWICS see [55].*

### 8.3.2 Charge state distribution

#### Data evaluation of ACE/SWICS data

ACE/SWICS [22] data from 1999 to 2006 were evaluated. The data was Level 2 data from the public data server of ACE/SWICS (`http://www.srl.caltech.edu/ACE/ASC/level2/lvl2DATA_SWICS-SWIMS.html`). Since the charge state distribution depends on the solar wind speed, only data within a certain velocity range was selected for the evaluation. Three different velocity ranges were chosen ($300 \pm 20$ km/s, $400 \pm 20$ km/s and $600 \pm 30$ km/s). To get a general charge state distribution all data of a velocity interval were collected in one overall distribution for the mentioned 8 years. See Figure 8.2 for the charge state distribution over the last eight years. In Figure 8.3 the average charge state distributions are shown for all three velocity intervals.

#### Charge state distribution for nickel

For nickel charge state measurements were not available over the same period as for iron. Hence we used a simulation of the dynamic equilibrium of charge states established in the coronal expansion of the relevant solar wind velocities, see Figure 8.4. These simulations reproduced approximately the observed iron charge states. See [8] for a review over charge state distributions of heavy ions in the solar wind.

### 8.3.3 WAVE

A drawing of the WAVE entrance system is in Figure 8.5. In [30] the ion optical calibration of the MTOF entrance system WAVE (Wide-Angle Variable Energy/charge) is described. The ion optical transmission
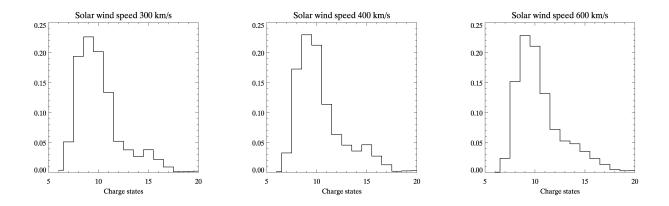
Figure 8.3: *Charge state distribution of iron for solar wind speed 300 km/s, 400 km/s and 600 km/s, measured with ACE. Average charge state distribution from 1999 to 2006. See Figure 8.2.*
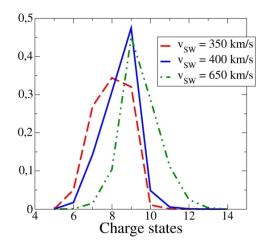


Figure 8.4: *Simulated charge state distribution of nickel for solar wind speed 350 km/s, 400 km/s and 650 km/s.*

was tested with $O^{6+}$ ions in CASYMS ion beam facility (see Chapter B.2). Due to the large energy acceptance range ($\Delta E/E \simeq 5$) the transmission for species with similar energy/charge ratios is not very different. Although I developed a transmission function for the WAVE entrance system, where I used the energy and angular acceptance matrix, which was measured by Hefti, [30]. So the angular and $V_{\text{WAVE}}$ acceptance can be calculated for a given ion energy and charge state, see Figure 8.6.

### 8.3.4 Carbon Foil
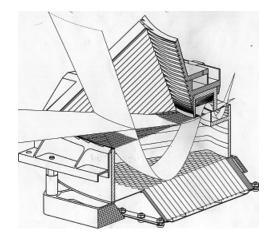
After leaving the WAVE entrance system the solar wind ions can be accelerated or decelerated towards the carbon foil, which is mounted on the entrance of the V-mass. Acceleration or deceleration is chosen to optimize their detection efficiency in V-mass or to prevent them from hitting the hyperbola deflection electrode of V-mass.

**Secondary electron yield in carbon foil**

See internal report in Section 8.5.

**Charge state distribution after carbon foil**

Ions passing carbon foils experience electron electron interactions leading to reduced charge states depending on the residual energy of the ions after the carbon foil. In [25] measurements and simulations
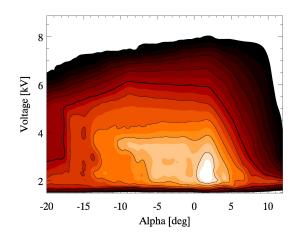
Figure 8.5: *WAVE entrance system. The energy per charge acceptance range is $\Delta E/E \simeq 5$. The angular acceptance is $\pm 25°$ in- and out-of-ecliptic. Figure adapted from [32].*



Figure 8.6: *WAVE azimuthal angle and WAVE voltage acceptance. The matrix gives the transmission for $^{56}Fe^{10+}$ ions with $v = 400$ km/s and $v_{th} = 30$ km/s as a function of in-ecliptic angle and WAVE voltage $V_{WAVE}$. There is no post acceleration voltage $V_f$ applied. Contour lines are at 10 % intervals. Plot adapted from [30].*

are described. See Figure 8.7 for charge state distribution of nickel and iron in solar wind energy range. The charge state distribution of nickel and iron can be calculated for a given particle energy. The part of singly or doubly charged iron ions is higher than for nickel, thus the part of iron ions which pass the V-mass, is higher than the part of nickel ions. This increases the relative transmission of iron compared to nickel.
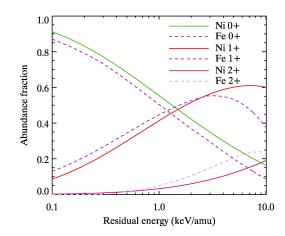


Figure 8.7: *Charge state distribution after carbon foil dependent on residual energy per nucleon. Solid line nickel, dashed line iron. From simulations based on measurements, see [25]*
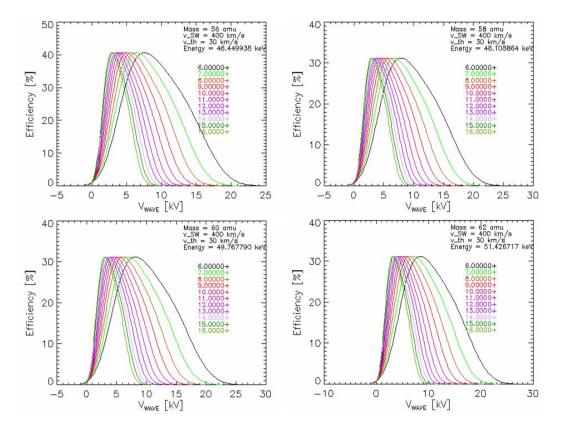
Figure 8.8: *Relative MTOF efficiency for $^{56}Fe$, $^{58}Ni$, $^{60}Ni$ and $^{62}Ni$ as a function of WAVE voltage and charge state, solar wind speed 400 km/s. All efficiency curves for in-ecliptic angle zero and post-acceleration voltage $V_f = 0$ kV.*

### 8.3.5   V-MASS

After the carbon foil the ions enter the V-mass, which is a V-shaped isochronous time of flight spectrometer. The V-shaped and the hyperbola deflection electrode generate an electrostatic harmonic potential so that the time of flight of an ion between the carbon foil and the stop detector is proportional to the square root of mass per charge, $(M/Q^*)^{1/2}$, where $Q^*$ is the ion charge state after the carbon foil, and it does not depend on the ion energy, see [29].
Since I assumed similar transmission for the iron and nickel ions, I do not discuss the V-mass instrument function here. It is discussed thoroughly in [68].

### 8.3.6   MTOF instrument function: Conclusion

Combining all effects discussed above, I get a ratio for two species, see Equation 8.2. This instrument function is a simplification assuming similar transmission through V-MASS and comparable MCP detection efficiency for nickel and iron. In Figure 8.8 the relative efficiency for $^{56}Fe$, $^{58}Ni$, $^{60}Ni$ and $^{62}Ni$ is shown as a function of charge state and WAVE voltage, in-ecliptic angle zero and no post-acceleration voltage. The solar wind speed is 400 km/s. The relative efficiency for a species is obtained combining the charge state distribution with the efficiency. For each WAVE voltage the ratio of the efficiency of nickel and iron can be calculated. Together with the measured ratio of the raw counts of the respective species, it gives the relative abundances of the two species. For the elemental abundances only the two dominant isotopes are taken, corrected by the terrestrial abundance ratio.

## 8.4 Data analysis

### 8.4.1 Data sets

I used MTOF data from January 1996 till January 2006. During this time several WAVE electrodes tunings were used. We chose to study three velocity intervals: 300 km/s, 400 km/s and 600 km/s. The range was $\pm 20$ km/s for 300 and 400 km/s and $\pm 40$ km/s for 600 km/s. The respective data was organized in sets for each WAVE electrode settings. For 400 km/s the data was stored in histograms summed over one day. For 300 km/s and 600 km/s the data was stored in histograms of 5 minute intervals.

For each event the time of flight is stored in the MTOF PHA files, see [67]. From this PHA files histograms were produced, which consists of 1024 bins, one bin 4 ns. As explained in Section 8.2, the time of flight $\tau$ of an ion with mass $M$ is proportional to the square root of mass per charge: $\tau \propto (M/Q^*)^{1/2}$ where $Q^*$ is the charge after the carbon foil.

### 8.4.2 Spectra alignment

I analyzed not each spectrum itself but the sum of all spectra over the ten years since the count rate for nickel is small that they could not be well distinguished from the background signal. Since the time of flight spectra had different offsets during the ten years of data all spectra had to be aligned first. For each WAVE setting the spectra were aligned using different TOF offsets. To find the TOF offset value an asymmetric function was applied to the spectra. The fit function $\mu$ is the sum of a Lorentzian and a Gaussian function with center at the $^{56}$Fe peak:

$$\mu(T) \;=\; (1-f)\frac{H_{\mathrm{Fe}}}{4}\frac{\Gamma_{\mathrm{L,R}}^2}{(T-T_0)^2+\Gamma_{\mathrm{L,R}}^2/4} + fH_{\mathrm{Fe}}\exp\Big(-\frac{(T-T_0)^2}{2\sigma_{\mathrm{L,R}}^2}\Big) \tag{8.3}$$

where $H_{\mathrm{Fe}}$ is the height of the iron peak, $\Gamma_{\mathrm{L,R}}$ the FWHM of the Lorentzian, left or right, $\sigma_{\mathrm{L,R}}$ $\sigma$ of the Gaussian, left or right of the peak position $T_0$, $T$ the time of flight and $f$ the ratio between the Gaussian and the Lorentzian part of the function.

### 8.4.3 Raw counts

A 19 parameter fit function $\mu$ is applied to the aligned spectra to get the raw counts of all resolved iron and nickel isotopes, using the maximum likelihood method. The fit function is expanded from Equation 8.3:

$$\begin{aligned}
\mu(T) \;=\; & \sum_{T_i>T,i=1}^{9} (1-f)\frac{H_i}{4}\Big(\frac{\Gamma_{i,L}^2}{(T-T_i)^2+\frac{\Gamma_{i,L}^2}{4}}\Big) + \sum_{T_i<T,i=1}^{9} (1-f)\frac{H_i}{4}\Big(\frac{\Gamma_{i,R}^2}{(T-T_i)^2+\frac{\Gamma_{i,R}^2}{4}}\Big) \\
+ & \sum_{T_i>T,i=1}^{9} fH_i\exp\Big(-\frac{(T-T_i)^2}{2\sigma_{i,L}^2}\Big) + \sum_{T_i<T,i=1}^{9} fH_i\exp\Big(-\frac{(T-T_i)^2}{2\sigma_{i,R}^2}\Big) \\
+ & \; b_0 + b_1 \cdot T \tag{8.4} \\
T_i \;=\; & \alpha\sqrt{\frac{m_i}{m_0}}T_0 - T_{\mathrm{offset}} \tag{8.5}
\end{aligned}$$

Where $H_i$ is the height of peak $i$, $\Gamma_{\mathrm{L,R}}$ the FWHM of the Lorentzian, left or right, $\sigma_{\mathrm{L,R}}$ $\sigma$ of the Gaussian, left or right of the peak position $T_i$, $T$ the time of flight and $f$ the ratio between the Gaussian and the Lorentzian part of the function. $\alpha$ is an additional fit parameter to account for instrument effects. $m_0$ is the mass of $^{56}$Fe, $m_i$ the mass of the peak i. For this small range of the TOF range a linear background is assumed: $b_0 + b_1 \cdot T$.

All peak shapes were kept similar and the relative proportion of the Lorentzians and Gaussians was kept constant for all nine peaks. To match the asymmetry of the peaks inherent in the isochronous time of flight spectra, two half-Lorentzians and two half-Gaussians with two different widths were applied to describe the peak shapes. One width ($\Gamma_{i,L}$ and $\sigma_{i,L}$) matches the counts on the left-hand side of the peak i, the
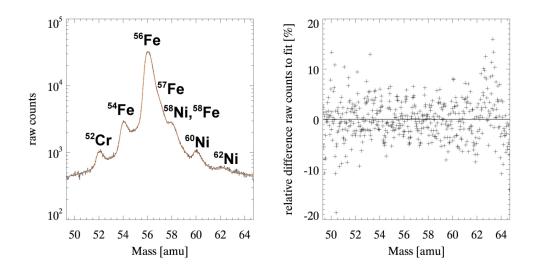
Figure 8.9: Left: *MTOF spectrum from January 1996 until January 2006 for 400 km/s solar wind. $V_f = 0$ kV, $V_{\mathrm{WAVE}} = 12$ kV. The time of flight is converted to mass, the counts are accumulated raw counts during ten years for the given WAVE settings.* Right: *Difference of the measured counts to the value of the 19 parameter fit function divided by the fit function value. One can see that the fit function describes well the measured distribution in the mass range of 54 to 60 amu.*

other ($\Gamma_{i,R}$ and $\sigma_{i,R}$) is to match the right-hand side. See Figure 8.9 for a typical spectrum. The time of flight is already converted to mass, using Equation (8.5). The elemental ratio between nickel and iron can be calculated using the areas of the two dominant isotopes $^{56}$Fe and $^{58}$Ni. Since all peaks have the same shape, the ratio between two areas for the given peaks $i$ and $j$ is:

$$\frac{n(i)}{n(j)} = \frac{H_i}{H_j} \sqrt{\frac{m_i}{m_j}} \tag{8.6}$$

This ratio must be corrected for the different detection efficiencies of the two species $i$ and $j$.

## 8.5	Nickel/Iron with MTOF: Carbon Foil Efficiency Differences

# Nickel/Iron with MTOF: Carbon Foil efficiency differences

Internal report, 30 June 2006

*Reto Karrer*

University of Bern

## Abstract

To measure the elemental abundances with CELIAS/MTOF the time of flight of each particle is measured. The start signal is triggered by secondary electrons from a carbon foil. The secondary electron yield from carbon foils is different for nickel and iron. To get the right Ni/Fe-ratio we have to know, among others, the detection efficiency difference between Ni and Fe. Measurements and simulations showed that the detection efficiency is about 10% higher for iron than for nickel for particles with 1 keV/nuc, with decreasing difference for higher energies.

## 1 Introduction

### 1.1 Motivation

We want to measure the ratio of the different nickel isotopes. To get the right ratio we have to know what the detection efficiency of the different isotopes is, respectively the relative detection efficiency difference. In this short review we gather the information available about secondary electron yield from nickel and iron particles bombarding a Carbon foil.

### 1.2 MTOF

The Mass determining TOF sensor (MTOF) is one of the CELIAS instruments [7]. It consists of a entrance system (WAVE) for E/Q selection, a carbon foil and a isochronous TOF section. See Figure 1. It allows the mass determination of solar wind particles with an accuracy of $M/\Delta M > 100$ for all elements in the solar wind.

## 2 Theory

### 2.1 Electronic Stopping Power

Interactions of particle with a solid may lead to electron emission from the surface of the solid. In a first approximation the yield of the emitted electrons is proportional to the electronic stopping power $S_e = (dE/dx)_e$ of the incident particle in the solid (see [15], [14] and [12] for references): $\gamma = A \cdot S_e / \cos \alpha$ where $A$ is the proportionality constant and $\alpha$ the angle of incidence of the projectile with respect to the surface normal. For our purpose it is now important how the electron yield depends on the mass and charge of the incident ion. It should be noted that for thin targets the electron yield could be smaller than expected from theory. In [18] three different cases of the electronic stopping cross-section are discussed for heavy ions:

1. Electronic stopping of low velocity heavy ions $(v < v_F)$[1]

   Kinetic energy per nucleus less than 25 keV/amu

---

[1] Fermi velocity of target solid with electron density $n$: $v_F = (3\pi^2 n)^{1/3} \cdot \frac{\hbar}{m}$ where $m$ electron mass.
Since $v_F$ of solids is approximately like the Bohr velocity $v_0 = \frac{1}{4\pi\varepsilon_0}\frac{e^2}{\hbar} \simeq 2.2 \cdot 10^6$ m/s, the corresponding energy is about 30 keV/amu.

3. Electronic stopping of high velocity heavy ions ($v > 3v_F$)

   Kinetic energy per nucleus larger than 200 keV/amu

Since $E/nuc \leq 25$ keV/amu in the solar wind only the first case is treated here.

### 2.1.1 Electronic Stopping of Low Velocity Heavy Ions

In [18] this case is shortly discussed, referring to older work (e.g. [10] and [11]). There it is stated that the Electronic Stopping Power $S_e$ is proportional to the projectile velocity $v$ to the power $k_v$ [11]:

$$S_e = \left(\frac{dE}{dx}\right)_e \propto v^{k_v} \propto \left(\frac{E}{m}\right)^{k_E}, \; k_v = 2k_E \qquad (1)$$

$E$ kinetic energy of projectile with mass $m$. In general relation (1) is a good assumption.

In [10] the electronic stopping is calculated in first approximation using a Thomas-Fermi treatment:

$$S_e = \frac{1}{4\pi\varepsilon_0} \xi_\epsilon \cdot 8\pi e^2 a_0 \frac{Z_1 Z_2}{\left(Z_1^{\frac{2}{3}} + Z_2^{\frac{2}{3}}\right)^{\frac{3}{2}}} \frac{v}{v_0} \qquad (2)$$

$Z_1$ nuclear charge of projectile with velocity $v$, $Z_2$ nuclear charge of target, $\xi_\epsilon$ is of the order of 1-2, but may vary with $Z_1$ approximately as $\xi_\epsilon \approx Z_1^{\frac{1}{6}}$. So for $S_e$ it follows:

$$S_e \propto \frac{Z_1^{\frac{7}{6}}}{\left(\left(\frac{Z_1}{Z_2}\right)^{\frac{2}{3}} + 1\right)^{\frac{3}{2}}} \cdot v \qquad (3)$$

So $S_e$ is essentially dependent on the velocity for low velocities. The term (3) $Z_1$ is similar for iron and for nickel ($S_{e,Fe} \propto 6.397 \cdot v$ and $S_{e,Ni} \propto 6.606 \cdot v \Rightarrow \frac{S_{e,Ni}}{S_{e,Fe}} = 1.033$), meaning that in this theory the electron stopping power for nickel and iron is of the same order.

### 2.1.2 Electronic Stopping power according to ERN-Theory

Experiments showed that the theory mentioned above (the so called LSS-theory (Lindhard, Scharff and Schiøtt, [11]) is not accurate enough to completely describe the electronic stopping power. (See



Fig. 1: Left: *Drawing of MTOF*, right: *Spectrum of iron and nickel isotopes.*
Both figures from [8]

2. Electronic stopping of medium velocity heavy ions ($v_F < v < 3v_F$)
   Kinetic energy per nucleus between 25 and 200 keV/amu

Figure 2 and [16]) The influence of screening potentials is weak on the proportionality constant $k_{Z_1}$ in $S_e = k_{Z_1} \cdot v^{k_v}$. Echenique, Nieminen, Ashley and Ritchie present a theory for stopping power considering a density functional calculation of the stopping of slow particles in a free electron gas [4]. See Figure 3.
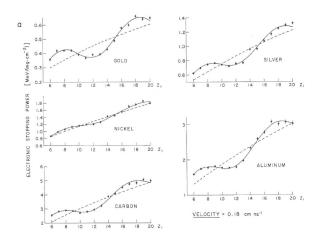


Fig. 2: *Results for the stopping power $S_e$ of all ions with $6 \leq Z_1 \leq 20$ in five materials. The dashed line is the fitted average trend, the solid line is the best fit to the empirical function $S(Z_1) = \alpha Z_1^\beta - \gamma \sin(\Omega Z_1 + \Phi)$, with $\alpha$, $\beta$, $\gamma$ and $\Phi$ as free parameter. $\Omega = 0.59$ for all materials (10.5 in units of $Z_1$). Projectile velocity $v_1 = 1.8 \cdot 10^6$ m/s. Figure from [16].*

They calculate the stopping power using the density-functional method:

$$\frac{1}{v}\frac{dE}{dx} = \frac{3}{k_F r_s} \sum_{l=0}^{\infty} (l+1) \sin^2(\delta_l(E_F) - \delta_{l+1}(E_F)) \tag{4}$$

where $k_F$ Fermi momentum, $r_s$ one-electron-radius, $E_F$ the Fermi energy and $\delta_l$ the phase shift at the Fermi energy for scattering of an electron off a spherical self-consistent potential. This theory shows a strong dependence on the electron configuration in the outermost shell. When the shells are complete the stopping power is smaller than for half-filled shells (e.g. minimum for Mg ($1s^2 2s^2 2p^6 3s^2$, $Z = 12$) and maximum for N ($1s^2 2s^2 2p^3$, $Z = 7$) in Figure 3.). For iron and
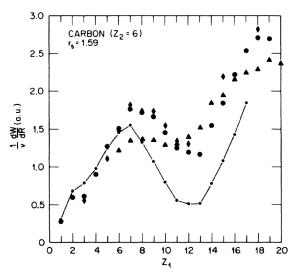


Fig. 3: *Stopping power of carbon $\frac{1}{v}\frac{dE}{dx}$ (here denoted $\frac{1}{v}\frac{dW}{dx}$) as a function of nuclear charge $Z_1$ of the projectile. The carbon density is $\rho \simeq 2$ g/cm$^3$. The solid curve gives the theoretical prediction for the one-electron-radius $r_s \simeq 1.59$. Figure from [4], references for experimental data therein.*

nickel the friction coefficient $\frac{1}{v}\frac{dE}{dx}$ (see eq. (4)) is for carbon foil ($\rho = 2$ g/cm$^3$ and $r_s = 1.59$ a.u., private communication from P.M. Echenique) 1.24 a.u. (Fe) and 0.52 (Ni).

### 2.1.3 Electronic Stopping of Medium Velocity Heavy Ions

For medium velocity heavy ions in an electronic plasma a model based on the ideas of Kreussler, Varelas and Brandt [9] and Brandt and Kitagawa [3] was constructed, called BK theory [18]. In this theory the relative velocity $v_r$ of the projectile to the conduction electrons of the target, $v_e$ is defined as $v_r \equiv <| \mathbf{v_1} - \mathbf{v_e} |>$ with projectile velocity $v_1$. Assuming that the conduction electrons are a free electron gas in the ground state it follows for $v_r \leq v_F$:

$$v_r = \frac{3}{4} v_F \left( 1 + \frac{2v_1^2}{3v_F^2} - \frac{v_1^4}{15v_F^4} \right) \tag{5}$$

3

And then for the ion screening length (i.e. its spatial extent):

$$\Lambda = \frac{2a_0(1-q)^{2/3}}{Z_1^{1/3}\left(1 - \frac{1-q}{7}\right)} \qquad (6)$$

with $a_0 = 5.8 \cdot 10^{-11}$ m Bohr radius, $Z_1$ projectile nuclear charge and $q$ the degree of ionization of the ion $Z_1$. $q$ is given as follows:

$$q = 1 - \exp\left(-\frac{0.92 v_r}{v_0 Z_1^{2/3}}\right) \qquad (7)$$

The fractional effective charge $\zeta = Z_1^*/Z_1$ is:

$$\zeta = q + (1-q)\frac{(v_0/v_F)^2}{2}\log[1 + (2\Lambda v_F/a_0 v_0)^2] \quad (8)$$

Then the final stopping power for medium velocity heavy ions is given by:

$$S_e = S_H (Z_1 \zeta)^2 \qquad (9)$$

with $S_H$ the proton equivalent stopping power. The deduction of the discussed equations can be found in [18].

## 2.2 Secondary electron yield $\gamma$

The secondary electron yield $\gamma$ is the average number of electrons emitted per incident particle. In many models on electronic emission the electron yield is assumed to be proportional to the electronic stopping power $S_e$ (originally formulated by E. Sternglass [15]). For lower projectile energies deviations have been observed [12]. But nevertheless let us assume this proportionality and together with (1):

$$\gamma \propto S_e \propto v^{k_v} \propto \left(\frac{E}{m}\right)^{k_E}$$
$$\gamma = A_{element} \cdot S_e/\cos\alpha, \qquad (10)$$

where $\alpha$ angle of incidence. This relation could be confirmed by F. Allegrini [1], see Figure 8.

## 2.3 Start and Stop efficiency of TOF of MTOF

The start efficiency of the MTOF/TOF is [17]:

$$\eta_{start} = 1 - e^{-p_{electron}\gamma_{forward}} \qquad (11)$$

with $p_{electron}$ the detection efficiency of the start MCP for single electrons and $\gamma_{forward}$ the secondary electron yield in forward direction. $p_{electron}$ depends mostly on the geometrical surface of the MCP.

## 3 Measurements and Simulations

### 3.1 Electronic Stopping Power

With SRIM[2] the electronic stopping power $S_e = \left(\frac{dE}{dx}\right)_e$ can be simulated. In Figure 4 the Z-Oscillation mentioned above (see Figure 3) is clearly visible. In Figure 5 the electronic stopping power was simulated for $Fe^{56}$, $Ni^{58}$ and $Ni^{60}$, energies between 10 and 1000 keV.
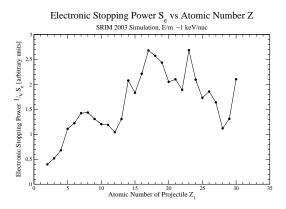


Fig. 4: *Electronic Stopping Power per $v$ $\frac{1}{v}S_e$ versus atomic number of the projectile $Z_1$. The $Z_1$-oscillation can clearly be seen.*

The SRIM simulations show a ratio $S_{e,Ni}/S_{e,Fe}$ of about $(0.6 \pm 0.05)$ for 56 keV. The difference between $Ni^{58}$ and $Ni^{60}$ is about one percent.
The simulation programm SRIM-2003 uses the relation discussed in Section 2.1 as well as experimental data which are implemented into the code. In [5] they remark that for nickel the TRIM/SRIM simulations underestimate the experimental data due to the lack of nickel measurements with carbon targets. The LSS-theory [11] is even lower with their estimation of nickel stopping power. As noted above the LSS-theory states for nickel and iron a similar electronic stopping yield. SRIM simulation

4
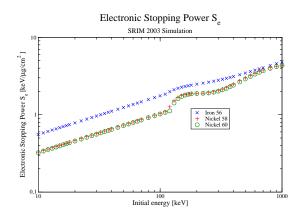
Fig. 5: *Electronic Stopping Power $S_e$ versus initial energy of the projectile. For energies about 1 keV/amu the ratio $S_{e,Ni}/S_{e,Fe}$ is about 0.7. Simulation by SRIM.*

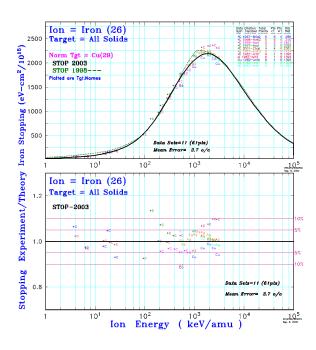gives better results for iron than for nickel (see Figure 6 and 7)



Fig. 6: Top:*Iron stopping power in different targets,*
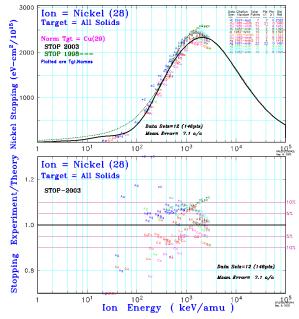Bottom: *Ratio experiments to theoretical data by SRIM*



Fig. 7: Top:*Nickel stopping power in different targets,*
Bottom: *Ratio experiments to theoretical data by SRIM*
*For nickel there are not many experiments. For higher velocities there are some measurements with carbon targets. They are all underestimated by SRIM.*

## 3.2 Secondary electron yields from different particles

F. Allegrini measured the Secondary electron yields for oxygen, argon and iron in MEFISTO [6] using KAFKA [2] and [1] (See Figure 8). He completed measurements done earlier by Rothard et al ([12] and [13]). See Figure 9.

## 3.3 Ratio of Secondary electron yield and Electronic Stopping Power

In Section 2.2 the relationship between the electronic stopping power $S_e$ and the secondary electron yield $\gamma$ was shortly discussed (10). In Figure 9 measured data is shown. These measurements show $\gamma \propto S_e$.

From Figure 9 the constant $A$ in $\gamma = A \cdot S_e$ for nickel is about $A_{Ni} = A_{Fe} \times 0.7$ with an estimated uncertainty of 0.15.

5
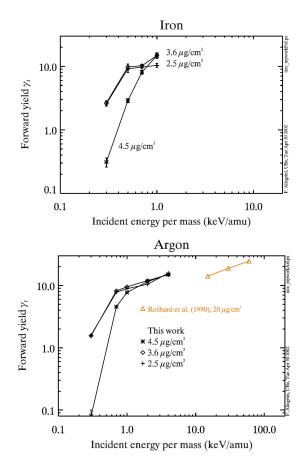
Fig. 8: *Measured forward yields for iron and argon. Figures from [1].*



Fig. 9: *Total Secondary Electron Yield as a function of the electron energy loss. The data are from Rothard et al [12]. Measurements from F. Allegrini [1] are plotted in colors. The electron energy loss was calculated using SRIM. Figure from [1]*

## 4 Calculations and Results

### 4.1 Secondary electron yield ratio for iron and nickel

It is crucial for the interpretation of the MTOF/TOF spectra to know if the start efficiencies $\eta_{start}$ for nickel and iron are comparable.
Assuming $\gamma_{Fe} = A_{Fe} \cdot S_{e,Fe}$ and $\gamma_{Ni} = A_{Ni} \cdot S_{e,Ni}$ the ratio of $\gamma_{Fe}$ and $\gamma_{Ni}$ is interesting:

$$\frac{\gamma_{Ni}}{\gamma_{Fe}} = \frac{A_{Ni}\ S_{e,Ni}}{A_{Fe}\ S_{e,Fe}} \qquad (12)$$

$$= (0.42 \pm 0.1) \qquad (13)$$

So the expected secondary electron yield of nickel is about 0.42 times the secondary electron yield of iron. For iron with 1 keV/amu $\gamma_f \simeq 10$ and so for

nickel $\gamma_{f,Ni} \simeq 4$.
For the start efficiency $\eta_{start}$ (see (11)) it follows ($p_{electron} = 0.5$, less than 0.66 for geometrical reasons, $A_{Fe} = 7.7$ and $A_{Ni} = 0.7 \times A_{Fe}$, $\gamma$ from SRIM and equation (10), here $A$ is already the constant for forward yield $\gamma_{forward}$.). The following results are for particles with 1 keV/amu:

$$
\begin{aligned}
\eta_{start,Fe56} &= (0.99 \pm 0.01) \\
\eta_{start,Ni58} &= (0.88 \pm 0.07) \\
\eta_{start,Ni60} &= (0.88 \pm 0.07) \\
\eta_{start,Ni62} &= (0.88 \pm 0.07)
\end{aligned}
$$

$$(14)$$

In this calculation the SRIM simulation values were used. Considering LSS-theory the start efficiency for nickel would be larger [11]. According to the theory of Echenique et al [4] the difference between nickel and iron can be explained. Because in [1] the

SRIM data were used for measured data ($S_e$ axis in Figure 9, the data has to be treated carefully.

In Figure 10 the Start Efficiency $\eta$ is shown for iron and nickel for energies from 10 keV to 1000 keV. For the calculations the values discussed above were used. The plot shows that with higher energies the difference between iron and nickel decreases.
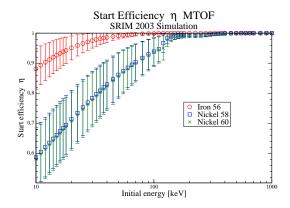


Fig. 10: *Start efficiency as a function of incident energy of the projectile. Start efficiency was calculated with equation (10) and SRIM values. With higher energies the start efficiency of nickel is close to the start efficiency of iron.*

## 5 Conclusion and Summary

The secondary electron emission from the carbon foil at the exit of the WAVE entrance system of MTOF is different for nickel and iron as for other elements. When calculating the nickel/iron elemental abundance ratio the counts for both elements have to corrected to get the right solar wind density.

The dependence on elements of the secondary electron yield and so of the start signal efficiency $\eta_{START}$ is one part of the instrument function of MTOF. Other parts are the ion optical transmission of WAVE, the different charge state distribution of the ions when exiting the carbon foil, different path length and flight angles of the particles and a mass dependent MCP detection efficiency.

The start efficiency for nickel at ambient solar wind speed (440 km/s, 1 keV/nuc) is about 10% lower than for iron. For higher wind speeds the difference becomes smaller. This difference has to be considered when calculating the Ni/Fe elemental abundance ratio.

For nickel there are no measurements of the electronic stopping power $S_e$ for low velocities. The SRIM simulation bases only on theories and measurements for higher projectile energies. The best way to ensure that nickel and iron have comparable start efficiency would be a measurement with KAFKA and/or the MTOF/Flight Spare. The latter would be the most sophisticated and also most certain way.

But in lack of such measurements SRIM is a good tool to approximate the start efficiency. When calculating the real counts from instrument counts SRIM should be used.

## References

[1] Frédéric Allegrini. *The PLASTIC sensor on STEREO: Design of the entrance system/energy analyzer and numerical simulations of solar wind measurements.* Ph.d. thesis, University of Bern, Switzerland, 2002.

[2] Frédéric Allegrini, Robert F. Wimmer-Schweingruber, Peter Wurz, and Peter Bochsler. Determination of low-energy ion-induced electron yield from thin carbon foils. *Nuclear Instruments and Methods in Physics Research B*, 211:487–494, 2003.

[3] Werner Brandt and M. Kitagawa. Effective stopping-power charges of swift ions in condensed matter. *Physical Review B*, 25(9):5631–5637, May 1982.

[4] P.M. Echenique, R.M. Nieminen, J.C. Ashley, and R.H. Ritchie. Nonlinear stopping power of an electron gas for slow ions. *Physical Review A*, 33(2):897–904, February 1986.

[5] V. Harikumar, A.P. Pathak, N. Nath, S. Kumar, S.K. Sharma, S.K. Hui, and D.K. Avasthi. Stopping power of carbon for si, fe, ni and cu ions using the ERDA technique. *Nuclear Instruments and Methods in Physics Research B*, 129:143–146, 1997.

[6] Markus Hohl. *MEFISTO II: Design, setup, characterization and operation of an improved calibration facility for solar plasma instrumentation.* Ph.d. thesis, University of Bern, Switzerland, 2002.

[7] D. Hovestadt, M. Hilchenbach, B. Klecker, F. M. Ipavich, P. Bochsler, H. Balsiger, J. Fischer, J. Geiss, R. Kallenbach, and P. Wurz. CELIAS - charge, element and isotope analysis system for SOHO. *Solar Physics*, 162:441–481, 1995.

[8] F.M. Ipavich, J.A. Paquette, P. Bochsler, S.E. Lasley, and P. Wurz. Solar wind iron isotopic abundances: Results from SOHO/CELIAS/MTOF. *American Institute Physics on* Solar and Galactic Composition, pages 121–126, 2001.

[9] S. Kreussler, C. Varelas, and W. Brandt. Target dependence of effective projectile charge in stopping powers. *Physical Review B*, 23(1):82–84, January 1981.

[10] J. Lindhard and M. Scharff. Energy dissipation by ions in the kev region. *Physical Review*, 124(1):128–130, October 1961.

[11] J. Lindhard, M. Scharff, and H.E. Schiøtt. Range concepts and heavy ion ranges (notes on atomic collisions, ii). *Matematisk-fysiske Meddelelser*, 33(14), 1963.

[12] Hermann Rothard, Kurt Kroneberger, Alexander Clouvas, Erling Veje, Peter Lorenzen, Norman Keller, Jürgen Kemmler, Wolfgang Meckbach, and Karl-Ontjes Groeneveld. Secondary-electron yields from thin foils: A possible probe for the electronic stopping power of heavy ions. *Physical Review A*, 41(5):2521–2535, March 1990.

[13] Hermann Rothard, Jørgen Schou, and Karl-Ontjes Groeneveld. Projectile- and charge-state-dependent electron yields from ion penetration of solids as a probe of preequilibrium stopping power. *Physical Review A*, 45(3):1701–1709, February 1992.

[14] Jørgen Schou. Transport theory for kinetic emission of secondary electrons from solids. *Physical Review B*, 22(5):2141–2174, September 1980.

[15] E. J. Sternglass. Theory of secondary electron emission from high-speed ions. *Physical Review*, 108(1):1–12, October 1957.

[16] D. Ward, H. R. Andrews, I. V. Mitchell, W. N. Lennard, R. B. Walker, and N. Rud. Systematics for the $Z_1$-oscillation in stopping powers of various solid materials. *Canadian Journal of Physics*, 57:645–+, May 1979.

[17] Peter Wurz. Heavy ions in the solar wind: Results from SOHO/CELIAS/MTOF, 2001.

[18] J. F. Ziegler, J. P. Biersack, and U. Littmark. *The Stopping and Range of Ions in Solids*. Pergamon Press, New York, first edition, 1985.

## 8.6 Nickel isotopic composition and nickel/iron ratio in the solar wind: results from SOHO/CELIAS/MTOF

# NICKEL ISOTOPIC COMPOSITION AND NICKEL/IRON RATIO IN THE SOLAR WIND: RESULTS FROM SOHO/CELIAS/MTOF

R. KARRER[1], P. BOCHSLER[1], C. GIAMMANCO[1], F. IPAVICH[2],
J. PAQUETTE[2] and P. WURZ[1]
[1] *Physikalisches Institut, University of Bern, Switzerland*
(`reto.karrer@space.unibe.ch`)
[2] *Department of Physics, University of Maryland, College Park, MD, USA*

**Abstract.** With CELIAS/MTOF on SOHO we derive the nickel isotopic composition for the isotopes with mass 58, 60 and 62 in the solar wind. In addition we measure the elemental abundance ratio of nickel to iron. We use data accumulated during ten years of SOHO operation to get sufficiently high counting statistics and compare periods of different solar wind velocities. We compare our values with the meteoritic ratios, which are believed to be a reliable reference for the solar system and also for the solar outer convective zone, since neither element is volatile and no isotopic fractionation is expected in meteorites. Meteoritic isotopic abundances agree with the terrestrial values and can thus be considered to be a reliable reference for the solar isotopic composition. The measurements show that the solar wind elemental Ni/Fe-ratio and the isotopic composition of solar wind nickel are consistent with the meteoritic values. This supports the concept that low-FIP elements are fed without relative fractionation into the solar wind. Our result also confirms the absence of substantial isotopic fractionation processes for medium and heavy ions acting in the solar wind.

**Keywords:** Sun: solar wind, Sun: elemental composition, Sun: isotopic abundances

## 1. Introduction

The solar wind elemental composition is usually compared to the photosphere and to meteoritic elemental abundances. All three originate from the same source. However, they can differ substantially due to enrichment and fractionation processes. In the solar wind an enrichment of particles with low first ionization potential (low-FIP elements, e.g. calcium, iron, nickel) compared to the photospheric abundances has been observed. If the ratio of iron to nickel agrees in the solar wind with the photosphere and with meteorites, it can be concluded that nickel undergoes the same enrichment processes as iron. Additionally, if the nickel isotopic composition agrees with meteorites, it confirms the absence of substantial isotopic fractionation processes for heavy elements in the solar wind.
We have evaluated ten years worth of SOHO/CELIAS data. We focus on slow solar wind (velocity between 290 and 330 km/s), on intermediate solar wind (370-410 km/s) and on fast solar wind (560-640 km/s) covering the

whole period between 1996-2006 (Fig. 1). The solar wind speed was measured by the Proton Monitor (PM), which is a part of MTOF (Ipavich et al., 1998).
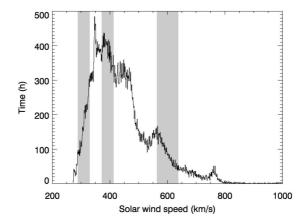


*Figure 1.* Proton Monitor. Distribution of solar wind speeds from January 1996 to January 2006. Investigated solar wind speed ranges are shaded: The speed intervals cover $290 - 330$, $370 - 410$ and $560 - 640$ km/s.

## 2. Instrumentation and data analysis

The Mass Time-of-Flight Spectrometer (MTOF) is part of the Charge, Elements, Isotope Analysis System (CELIAS) onboard the Solar Heliospheric Observatory (SOHO) spacecraft (Hovestadt et al., 1995). The MTOF sensor has an excellent mass resolution for solar wind studies allowing to identify rare elements and isotopes that could not be resolved from more abundant neighboring species (e.g. $^{58}$Ni from $^{56}$Fe) with older instruments.

The MTOF sensor consists of an energy/charge filter (Wide-Angle Variable Energy/Charge (WAVE)) and an isochronous time-of-flight spectrometer in a V-type configuration (V-Mass). Details of the principle of operations of CELIAS/MTOF can be found in Kallenbach et al., 1997.

For each MTOF setting (WAVE electrode voltage $V_{\text{WAVE}}$ and post-acceleration voltage $V_f$ after WAVE) day by day spectra (for 400 km/s) or five minute spectra (for 300 and 600 km/s) were aligned using different TOF offsets. To find the TOF offset value an asymmetric fit function was applied to the spectra. The fit function is the sum of a Lorentzian and a Gaussian function with center at the $^{56}$Fe peak. A 19 parameter fit function was applied to the aligned spectra to get the raw counts of all resolved iron and nickel isotopes, using the maximum likelihood method. To maximize the likelihood

the FORTRAN routine E04KDF of the NAG library was used. The shape of the asymmetric Lorentzian and the asymmetric Gaussian used for the fits are similar for all peaks. The width is proportional to the square root of mass. To fit the background a linear function of the TOF with two free parameters was assumed (see Fig. 2).

To convert raw counts to particle densities a complicated data analysis procedure is necessary, (Wurz, 2001). The WAVE entrance system has different transmission factors depending on the energy/charge of the entering ions. The WAVE electrode voltages were cycled in six steps covering an energy/charge range from helium to nickel. Although iron and nickel have similar kinetic energies, their charge state distributions differs (e.g. $Fe^{8+}$, $Fe^{9+}$ and $Fe^{10+}$ all about 20%, $Ni^{8+}$ about 30% and $Ni^{9+}$ about 50%). For iron we used charge state distributions observed by ACE/SWICS (cf. Gloeckler et al., 1998) in the three investigated velocity intervals to determine the transmission factors through WAVE. Since these data sets do not exist for nickel we used a simulation of the dynamic equilibrium of charge states established in the coronal expansion of the relevant solar wind velocities, which approximately reproduced the observed iron charge states. Additionally, the secondary electron yield from the carbon foil triggering the start signal of the time of flight measurement depends on the mass and the atomic number of the ion (Echenique et al., 1986). Simulations with SRIM (Ziegler, 2004) indicate that the start signal efficiency is 12% lower for nickel than for iron at 1 keV/nuc. For the investigated peaks only the ions exiting the carbon foil with charge state +1 were counted. The fraction of singly ionized iron ions is about 5 % higher than for singly ionized nickel ions at 1 keV/nuc (see Gonin et al., 1995). Evaluating these effects for the three investigated velocity intervals, this results in a 10 to 20 % larger total detection efficiency for the dominant iron isotope $^{56}Fe$ than for the dominant nickel isotope $^{58}Ni$. Additionally, there is a contribution of $^{58}Fe$ to the $^{58}Ni$ peak. The abundance ratio of $^{58}Fe$ and $^{58}Ni$ is approximately 7% on Earth. This is considered in the data analysis.

The differences between the three investigated nickel isotopes are small. The transmission of WAVE is optimized for ambient solar wind ions and it is therefore smaller for fast solar wind iron and nickel. This reduces the accumulated counts and increases the uncertainty of the results for 600 km/s solar wind for nickel and iron, but it is more relevant for nickel due to fewer counts.

We refer to Giammanco et al., 2007 for a detailed discussion of the instrument detection efficiency.
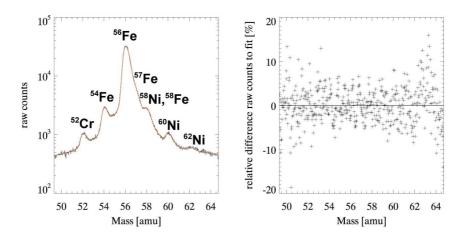
*Figure 2. Left:* MTOF spectrum from January 1996 until January 2006 for 400 km/s solar wind. $V_f = 0$ kV, $V_{WAVE} = 12$ kV. The time of flight is converted to mass, the counts are accumulated raw counts during ten years for the given MTOF settings. The counts at mass 58 come from $^{58}$Fe and $^{58}$Ni. This has to be considered in the data analysis. *Right:* Difference of the measured counts to the value of the 19 parameter fit function divided by the fit function value. One can see that the fit function describes well the measured distribution in the mass range of 54 to 60 amu.

## 3.  Results and discussion

In Tab. I and II the elemental abundances of nickel and iron and the isotopic composition of nickel are listed. The efficiency depends both on the ion energy and on the MTOF instrument settings (WAVE electrode voltages $V_{WAVE}$ and post-acceleration voltage $V_f$). Thus the error bars are composed of varying detection efficiencies within the velocity ranges and for the different instrument settings. Additionally, the detector efficiency changed during the ten years since SOHO launch increasing the estimated uncertainty of the shown results. But since this effect is expected to be similar for iron and nickel, it does not have a large influence on the overall error bars.
 The results are within the error bars in good agreement with the known ratios from photosphere, solar energetic particles (SEP), earth and meteorites. Also the isotope abundance ratios for nickel agree with the known values. Only for the $^{62}$Ni isotope a larger abundance is measured, but still within the large error bars resulting from poor counting statistics.
Our data analysis shows that both nickel and iron experience an enrichment in the solar corona due to the lower FIP compared to the high-FIP elements (e.g., oxygen). This supports the known theories about the FIP and FIT effects named above as it was previously seen for chromium, (Paquette et al., 2001).

Table I. Ni/Fe ratios for different solar wind speeds.

|  | Raw data | Efficiency-corrected data |
|---|---|---|
| Solar wind 310 km/s | 0.043 | $0.051 \pm 0.012$ |
| Solar wind 400 km/s | 0.044 | $0.055 \pm 0.011$ |
| Solar wind 600 km/s | 0.047 | $0.049 \pm 0.011$ |
| Solar wind[a] |  | $0.053 \pm 0.011$ |
| Photosphere[b] |  | $0.060 \pm 0.009$ |
| Coronal SEP[c] |  | $0.048 \pm 0.005$ |
| Meteorites[d] |  | 0.0562 |
| Earth |  | 0.055 |

[a] weighted mean of the measurements above
[b] Asplund et al., 2005
[c] Reames, 1995
[d] Lodders, 2003

Table II. Nickel isotope abundances

|  | $Ni^{58}$ | $Ni^{60}$ | $Ni^{62}$ |
|---|---|---|---|
| Efficiency-corrected data (310 km/s) | $0.66 \pm 0.05$ | $0.26 \pm 0.05$ | $0.08 \pm 0.04$ |
| Efficiency-corrected data (400 km/s) | $0.75 \pm 0.07$ | $0.19 \pm 0.05$ | $0.06 \pm 0.03$ |
| Efficiency-corrected data (600 km/s) | $0.75 \pm 0.07$ | $0.17 \pm 0.05$ | $0.08 \pm 0.04$ |
| Meteorites[a] | 0.6872 | 0.2647 | 0.0367 |
| Earth[b] | 0.68077 | 0.2622 | 0.03635 |

[a] Quitté et al., 2006
[b] Gramlich et al., 1989

## 4. Conclusions

In this work we could show that nickel undergoes similar processes in the solar corona as other low-FIP elements which confirms the FIP effect known from earlier works.

## Acknowledgements

# References

Asplund, M., Grevesse, N., and Sauval, A. J. (2005). In Barnes, III, T. G. and Bash, F. N., editors, *ASP Conf. Ser. 336: Cosmic Abundances as Records of Stellar Evolution and Nucleosynthesis*, pages 25–38.

Echenique, P. M., Nieminen, R. M., Ashley, J. C., and Ritchie, R. H. (1986). *Physical Review A*, 33(2):897–904.

Giammanco, C., Bochsler, P., Ipavich, F., Karrer, R., Paquette, J., and Wurz, P. *this volume*.

Gloeckler, G., Cain, J., Ipavich, F. M., Tums, E. O., Bedini, P., Fisk, L. A., Zurbuchen, T. H., Bochsler, P., Fischer, J., Wimmer-Schweingruber, R. F., Geiss, J., and Kallenbach, R. (1998). *Space Science Reviews*, 86:497–539.

Gonin, M., Kallenbach, R., Bochsler, P., and Bürgi, A. (1995). *Nuclear Instruments and Methods in Physics Research B*, 101:313–320.

Gramlich, J. W., Machlan, L. A., Barnes, I. L., and Paulsen, P. J. (1989). *Journal of Research of the National Institute of Standards and Technology*, 94(6):347–456.

Hovestadt, D., Hilchenbach, M., Bürgi, A., Klecker, B., Laeverenz, P., Scholer, M., Grünwaldt, H., Axford, W. I., Livi, S., Marsch, E., Wilken, B., Winterhoff, H. P., Ipavich, F. M., Bedini, P., Coplan, M. A., Galvin, A. B., Gloeckler, G., Bochsler, P., Balsiger, H., Fischer, J., Geiss, J., Kallenbach, R., Wurz, P., Reiche, K.-U., Gliem, F., Judge, D. L., Ogawa, H. S., Hsieh, K. C., Mobius, E., Lee, M. A., Managadze, G. G., Verigin, M. I., and Neugebauer, M. (1995). *Solar Physics*, 162:441–481.

Ipavich, F. M., Galvin, A. B., Lasley, S. E., Paquette, J. A., Hefti, S., Reiche, K.-U., Coplan, M. A., Gloeckler, G., Bochsler, P., Hovestadt, D., Grünwaldt, H., Hilchenbach, M., Gliem, F., Axford, W. I., Balsiger, H., Bürgi, A., Geiss, J., Hsieh, K. C., Kallenbach, R., Klecker, B., Lee, M. A., Managadze, G. G., Marsch, E., Möbius, E., Neugebauer, M., Scholer, M., Verigin, M. I., Wilken, B., and Wurz, P. (1998). *Journal of Geophysical Research*, 103:17205–17214.

Kallenbach, R., Ipavich, F. M., Bochsler, P., Hefti, S., Hovestadt, D., Grünwaldt, H., Hilchenbach, M., Axford, W. I., Balsiger, H., Bürgi, A., Coplan, M. A., Galvin, A. B., Geiss, J., Gliem, F., Gloeckler, G., Hsieh, K. C., Klecker, B., Lee, M. A., Livi, S., Managadze, G. G., Marsch, E., Möbius, E., Neugebauer, M., Reiche, K.-U., Scholer, M., Verigin, M. I., Wilken, B., and Wurz, P. (1997). *Journal of Geophysical Research*, 102:26895–26904.

Lodders, K. (2003). *Astrophysical Journal*, 591:1220–1247.

Paquette, J. A., Ipavich, F. M., Lasley, S. E., Bochsler, P., and Wurz, P. (2001). In Wimmer-Schweingruber, R. F., editor, *AIP Conf. Proc. 598: Joint SOHO/ACE workshop "Solar and Galactic Composition"*, pages 95–100.

Quitté, G., Meier, M., Latkoczy, C., Halliday, A. N., and Günther, D. (2006). *Earth and Planetary Science Letters*, 242:16–25.

Reames, D. V. (1995). *Advances in Space Research*, 15:41–51.

Wurz, P. (2001). Habilitation thesis, University of Bern, Switzerland.

Ziegler, J. F. (2004). *Nuclear Instruments and Methods in Physics Research B*, 219:1027–1036.

# Chapter 9

# Conclusions

## 9.1 Summary

On the 26th October 2006, the STEREO mission was launched and thus concluded so the main part of this work. The next phase of measurements interpretations and data analysis begins. My attempt here was to summarize the ion optical calibration of the STEREO/PLASTIC instrument, which can now be used in this analysis phase.The ion optical capabilities of PLASTIC should be known to detail degree.

After some basics on solar physics I described the STEREO mission and the functionality of the PLASTIC instrument in Chapter 1. In that chapter I explained the measurement principle to provide motivation for the necessity of obtaining parameters discussed in later chapters.

In the second chapter I presented a first-order simulation of a spherical electrostatic analyzer, which is similar to the electrostatic analyzer of the PLASTIC instrument. The simplified calculations gave an idea of the analyzer constants, which describe the dependence of the energy selection on the applied voltages. Additionally, simulations delivered a rough estimation of the energy and angular acceptance of a spherical ESA. Nevertheless, these simulations cannot replace a careful ion optical simulation as the one presented by Allegrini, [2].

The following four chapters cover the the ion optical calibration of the PLASTIC instrument, starting with the entrance system/energy analyzer without post-acceleration applied, then with a setup using post-acceleration and finally the integrated instruments.

Chapter 3 contains the description of the ion optical calibration of the entrance system/energy analyzer of PLASTIC. Since we have three instrument models, FM1, FM2 and FS, the calibration measurements were time consuming. I attempted to point out the calibration processes and the measured ion optical parameters thoroughly to provide a detail record of instrument response. That chapter may seem very technical but it was intended to help later users of the PLASTIC instruments to understand how the instrument parameter were determined and provide detail information on the collection interface to to TOF section. My emphasis was also to compare the three instruments since it is the first time we have two almost identical instruments at two different positions studying the inner heliosphere.

In the following Chapter 4 I present the novel detection system *LaserCEM* and its functionality. This detector was used in Chapter 5, where I discuss the ion optical calibration of the ESEA with post-acceleration including presentation of the experimental setup, measurement procedure and data acquisition.

Chapter 6 covered a part of the calibration measurements with the integrated instrument, mainly the experiments that are related to the measurements discussed in Chapters 3 and 5.

As a preview, I presented in Chapter 7 some flight data from the STEREO mission. There I show preliminary results from hydrogen and helium in the solar wind as well as first composition data from the heavy ions. That chapter concluded the discussion of the PLASTIC instrument.

To be prepared on the science return phase of the STEREO mission in the next months, I evaluated in Chapter 8 SOHO/CELIAS/MTOF data to study the nickel abundance in the solar wind. The conclusion of that chapter is that nickel undergoes the same enrichment processes in the solar corona as other low-FIP elements.

The Appendix contains additional details, which does not directly belong to the logical sequence of this

work.

## 9.2 Conclusions and outlook

This work consisted of several parts; therefore, I presented conclusions and discussions at the end of each chapter. Since the PLASTIC calibration is discussed in three chapters, I will concentrate in this conclusion on the PLASTIC instrument to give an overall impression of the key findings.

The ESEA calibration measurements give a good specification of the ion optical capabilities of the three models. Since the main and the S-channel use the same detectors the characteristics of the ESEA are crucial for the data reduction. I point out the following conclusions:

- The angular and energy acceptance of the two integrated instruments IFM1 and IFM2 are comparable to the acceptance ranges of the ESEA FM1 and FM2. The geometric factor measurements for the integrated instruments was performed at a low beam energy where the beam is not cut off by the post-acceleration structure, and therefore, it compares well with the ESEA measurements. To ensure also a large transmission for heavy ions, the post-acceleration voltage must be set as high as possible, at least 20 kV in the integrated system.

- The main channel and the WAP of the two instruments do not differ much considering their geometry. Both apertures were very uniform in geometric acceptance.

- The S-channel transmission of both instruments show a large variability depending on azimuthal and elevation angle position due to the difficulty of manufacturing a small, 3D slit. The geometric factor and active area measurements must be corrected for that. I tried to give an average value. Nevertheless, this variability must be considered for rigorous data reduction.

- Comparing the S-channels of FM1 and FM2, FM1 showed a stronger dependence on the azimuthal angle than FM2, whereas the FS showed the highest uniformity due to a refinement of the slit construction process.

- All analyzer and deflection constants were quite similar for all models pointing to uniformity in construction. This should prove advantageous during the flight data reduction process.

- Summarizing the last three bullets, it can be stated that the two integrated models are very similar considering geometry and we command the company Contraves Space AG, Zurich, Switzerland, for producing well-made instruments.

- Regarding the integrated instrumen, the influence of the SSD and MCP detector efficiencies on the particle detection must be considered very carefully.

### 9.2.1 Outlook

With PLASTIC we have an instrument for *in situ* measurements of the solar wind and suprathermal particle, which uses the same detection systems for all species. After the first months of the STEREO mission we can look at a functioning instrument that will hopefully provide the community with reliable data.

# Appendix A

# Derivation of used formulas

## A.1 Geometric factor

### A.1.1 Overview

The name geometric factor implies a instrument parameter describing the geometric acceptance of an instrument. For instruments where the energy and purely geometric acceptance are independent from each other, the geometric factor usually only depend on geometric parameters. For an energy analyzer like PLASTIC, the energy and angular acceptance depend on each other. Thus the energy dependence is included in the geometric factor.

The definition of the geometric factor is different for various sensors. Therefor I present here the derivation of the used geometric factor for PLASTIC which also F. Allegrini used, see [2].

The geometric factor definition goes back on a definition by V. M. Vasyliunas [59]. L. M. Chase [11] introduced the Geometric factor $GF$ as follows:

$$C = GF \cdot j \tag{A.1}$$

with $C$ the count rate (particles/sec), transmitted by the analyzer, and the ambient flux $j$ (particles/cm$^2$ sr sec). And D. T. Young uses the geometric factor [70]:

$$GF = A_e \langle \Delta\alpha \frac{\Delta E}{E} \rangle \int_{\Delta\beta} \cos\beta \mathrm{d}\beta, \tag{A.2}$$

where $A_e$ is approximately the aperture area, $\langle \Delta\alpha(\Delta E/E) \rangle$ the average over the acceptance phase space (like in Figure 3.26) and $\Delta\beta$ the other angle (elevation or azimuthal, according to the instrument coordinate system).

In general the geometric factor is a number to compare different instruments with angular and energy dependent acceptance. To be able to compare the geometric factors, the used equations should always be quoted.

### A.1.2 Derivation of the used geometric factor

To derive the geometric factor used with PLASTIC I start with the differential count rate $\mathrm{d}R$ for an ion optical instrument:

$$\mathrm{d}R(E,\phi,\theta) = j(E,\phi,\theta) \cdot \underbrace{T(E,\phi,\theta) \, \frac{\mathrm{d}E}{E} \, \cos\phi_A \mathrm{d}A\mathrm{d}\Omega}_{\mathrm{d}GF}, \tag{A.3}$$

$j$ : particles flux per energy $E$, azimuthal angle $\phi$ and polar angle $\theta$, $T$ transmission, $\mathrm{d}A$ differential area, $\phi_A$ azimuthal angle between incident particle direction and $\mathrm{d}A$ and $\mathrm{d}\Omega$ is the differential space angle: $\mathrm{d}\Omega = \cos\phi\mathrm{d}\theta\mathrm{d}\phi$, see Figure A.1. Integrated we get the integral count rate over the whole phase space. If

the particle flux is uniform, $j(E, \phi, \theta) = j_0$, then the integral flux for *a given instrument setting* can be written:

$$
\begin{aligned}
R &= \int_E \iint_\Omega j_0 \cdot T(E, \phi, \theta) \; \frac{\mathrm{d}E}{E} \; \cos\phi_A \mathrm{d}A \mathrm{d}\Omega \\
&= j_0 \cdot GF
\end{aligned}
\tag{A.4}
$$

according to Equation A.1. So for the integral geometric factor it follows:

$$
\begin{aligned}
GF &= \int_E \iint_\Omega T(E, \phi, \theta) \; \cos\phi_A \; \mathrm{d}A \; \frac{\mathrm{d}E}{E} \; \mathrm{d}\Omega \tag{A.5} \\
&= \iiiint T(E, \phi, \theta) \; \cos\phi_A \; \mathrm{d}A \; \frac{\mathrm{d}E}{E} \; \cos\phi \mathrm{d}\theta \mathrm{d}\phi \tag{A.6}
\end{aligned}
$$

and now replacing $\mathrm{d}A$ with $\mathrm{d}z \cdot \mathrm{d}l = \mathrm{d}z \cdot r\mathrm{d}\alpha$ with $r$ constant distance instrument center entrance area. And further I replace $\phi_A$ with $\alpha - \phi$, see Figure A.1:

$$
GF = \iiiint\!\!\!\int T(E, \phi, \theta) \; \cos(\alpha - \phi) \frac{\mathrm{d}E}{E} \; r \; \cos\phi \mathrm{d}\theta \mathrm{d}\phi \mathrm{d}\alpha \mathrm{d}z
\tag{A.7}
$$

$r \cos\phi \mathrm{d}\phi = \mathrm{d}y$, since $y = r \cdot \sin\phi$ and $\frac{\mathrm{d}y}{\mathrm{d}\phi} = r \cdot \cos\phi$, see Figure A.1, and in a second step replacing $T(E, \phi, \theta) \cdot \cos(\alpha - \phi)$ with $T^*(E, y, \theta)$:

$$
\begin{aligned}
GF &= \iiiint\!\!\!\int T(E, \phi(y), \theta) \; \cos(\alpha - \sin^{-1}(\frac{y}{r})) \frac{\mathrm{d}E}{E} \; \mathrm{d}\theta \mathrm{d}y \mathrm{d}z \mathrm{d}\alpha \tag{A.8} \\
&= \iiiint\!\!\!\int T^*(E, z, \theta) \; \frac{\mathrm{d}E}{E} \; \mathrm{d}\theta \mathrm{d}z \mathrm{d}y \mathrm{d}\alpha \tag{A.9}
\end{aligned}
$$

Assuming azimuthal uniformity of the transmission, the azimuthal angle $\alpha$ can be integrated separately, $\alpha_{SWS}$, it follows for the geometric factor:

$$
G = \alpha_{SWS} \int \iiint T^*(E, \theta) \mathrm{d}y \mathrm{d}z \; \frac{\mathrm{d}E}{E} \; \mathrm{d}\theta
\tag{A.10}
$$

The measurements were made for discrete values $(\theta_i, E_j)$ so the integrals have to be transformed into sums. And the differential active area $\mathrm{d}A = \mathrm{d}y \mathrm{d}z$ times the transmission $T^*$ gives the active area dependent on $(\theta_i, E_j)$, $(A_{act})_{ij}$. Finally we get as equation for the measured geometric factor $G$:

$$
G = \alpha_{SWS} \sum_i^N \sum_j^M \Delta\theta_i \; \frac{\Delta E_j}{E_j} \; (A_{act})_{ij}
\tag{A.11}
$$
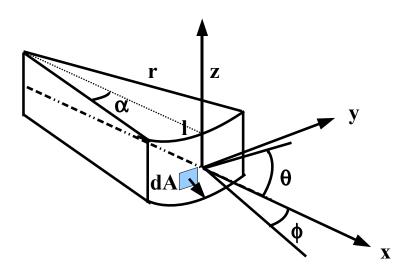
Figure A.1: *The coordinate system and the corresponding angles used in the geometric factor calculation. dA is the differential area, $\phi_A$ the angle between area normal and azimuthal angle $\phi$ of incident particles.*

## A.2  Fit functions for ESEA calibration measurements

### A.2.1  Gaussian

$$f(x) = \frac{K}{\sqrt{2\pi}\sigma} \; \exp\left(-\frac{(x-\mu)^2}{2\sigma^2}\right) \tag{A.12}$$

with the fit parameteres $K$, $\sigma$ and $\mu$. $\sigma^2$ is the variance of the gaussian, $\mu$ the mean value and $K$ is proportional to the height of the distribution.

### A.2.2  Convolution of a Gaussian and a trapezoid

The fit function used for all measurements is a convolution of a gaussian with a trapezoidal function (For details see Appendix C in [2])

$$
f_{\text{GT}}(x) = K\frac{m\sigma}{\sqrt{2\pi}}\left[e^{\dfrac{-\left(\dfrac{1}{b+c}-(x-\mu)\right)^2}{2\sigma^2}} \; e^{\dfrac{-\left(\dfrac{1}{b+c}+(x-\mu)\right)^2}{2\sigma^2}}\right]
$$
$$
+\tfrac{1}{2}K\left(m(x-\mu)+\tfrac{1}{2}(b+c)\right)\left[\text{erf}\left(\frac{\left((x-\mu)+\dfrac{1}{b+c}\right)}{\sqrt{2}\sigma}\right) - \text{erf}\left(\frac{\left((x-\mu)-\dfrac{1}{b+c}\right)}{\sqrt{2}\sigma}\right)\right], \tag{A.13}
$$

with the fit parameters $K$, $\sigma$, $b$, $c$ and $\mu$. $m = \frac{1}{2}(c^2 - b^2)$ is the slope of the trapezoid with $y = b$ at $x = -\frac{1}{b+c}$ and $y = c$ at $x = \frac{1}{b+c}$. $\sigma^2$ is the variance of the gaussian with mean $x_0$. $K$ is proportional to the height of the distribution.

## A.3 Fit functions for LaserCEM measurements

The following fit functions were applied to the data in Section 4.2.1.

1. *Linear Efficiency Model:*
   linear efficiency drop from the sides to the center, $L(x) = \left((a|x| + b)\chi_{[-x_0,x_0]}(x)\right)$, where $a$ and $b$ are parameters of the linear function, $x_0$ is the radial distance from CEM center and $\chi_{[-x_0,-x_0]}$ is 1 for $x \in [-x_0, -x_0]$ and 0 else. (See eq. (A.14))

2. *Quadratic Efficiency Model:*
   quadratic efficiency drop from the sides to the center, $Q(x) = \left((ax^2 + b)\chi_{[-x_0,x_0]}(x)\right)$, where $a$ and $b$ are the parameters of the quadratic function and $\chi_{[-x_0,-x_0]}$ as defined above. (See eq. (A.15))

3. *Hole Efficiency Model:*
   homogeneous efficiency over the whole surface except the center part (1 to 2 mm in diameter). In the center the detection efficiency was considered at least ten times smaller than on the sides, the hole is described with two characteristic functions: $H(x) = \left(\chi_{[-a,-b]}(x) + \chi_{[b,a]}(x)\right)$, where $a$ and $b$ are the radial positions of the hole. (See eq. (A.16))

**Fit functions:** All functions are convolutions of a Gauss function with the corresponding function mentioned above.

$$
\begin{aligned}
f_{lin} &= G * L(z) = \int_{\mathbb{R}} n_0 \exp\left(-\frac{(z-x)^2}{2\sigma^2}\right)\left((a|x| + b)\chi_{[-x_0,x_0]}(x)\right)\mathrm{d}x \\
&= n_0 \Bigg( b\left(\mathrm{erf}(\frac{z-x_0}{\sigma}) - \mathrm{erf}(\frac{z}{\sigma})\right) + az\left(2\mathrm{erf}(\frac{z}{\sigma}) - \mathrm{erf}(\frac{z+x_0}{\sigma}) - \mathrm{erf}(\frac{z-x_0}{\sigma})\right) \\
&\quad + \frac{a\sigma}{\sqrt{2\pi}}\left(2\exp\left(-\frac{z^2}{2\sigma^2}\right) - \exp\left(-\frac{(z+x_0)^2}{2\sigma^2}\right) - \exp\left(-\frac{(z-x_0)^2}{2\sigma^2}\right)\right)\Bigg) \qquad (A.14) \\
f_{quad} &= G * Q(z) = \int_{\mathbb{R}} n_0 \exp\left(-\frac{(z-x)^2}{2\sigma^2}\right)\left((ax^2 + b)\chi_{[-x_0,x_0]}(x)\right)\mathrm{d}x \\
&= n_0 \Bigg( (az^2 + a\sigma^2 + b)\left(\mathrm{erf}(\frac{z+x_0}{\sigma}) - \mathrm{erf}(\frac{z-x_0}{\sigma})\right) \\
&\quad + \frac{a\sigma}{\sqrt{2\pi}}\left(z\left(\exp\left(-\frac{(z+x_0)^2}{2\sigma^2}\right) - \exp\left(-\frac{(z-x_0)^2}{2\sigma^2}\right)\right)\right. \\
&\quad \left.-x_0\left(\exp\left(-\frac{(z-x_0)^2}{2\sigma^2}\right) + \exp\left(-\frac{(z+x_0)^2}{2\sigma^2}\right)\right)\right)\Bigg) \qquad (A.15) \\
f_{hole} &= G * H(z) = \int_{\mathbb{R}} n_0 \exp\left(-\frac{(z-x)^2}{2\sigma^2}\right)\left(\chi_{[-a,-b]}(x) + \chi_{[b,a]}(x)\right)\mathrm{d}x \\
&= n_0 \left(\mathrm{erf}(\frac{-a-z}{\sigma}) - \mathrm{erf}(\frac{-b-z}{\sigma}) + \mathrm{erf}(\frac{b-z}{\sigma}) - \mathrm{erf}(\frac{a-z}{\sigma})\right) \qquad (A.16)
\end{aligned}
$$

# Appendix B

# Calibration facilities

At the university of Bern there are two large ion beam facilities, MEFISTO and CASYMS. Most of the calibrations reported here were performed in CASYMS.

## B.1  CASYMS: CAlibration SYstem for Mass Spectroscopy

The CASYMS ion source is an electron bombardment ion source that provides a broad uniform beam $(12 \times 12 \text{cm}^2)$ with a beam flux up to 2 MHz/cm$^2$ (solar wind flux approximately 0.5 MHz/cm$^2$). Different gas beams can be produced with various charge states (for argon up to 6+).

The facility consists of a source chamber, a drift tube and a large instrument chamber allowing to test complete flight instruments. The instruments can be mounted on a two axes turntable which allows lateral movements, too. All measurements can be automated. See [21] for an overview over the ion source and the ion beam and [56] for a description of the instrument chamber capabilities after automation.

## B.2  MEFISTO: MEsskammer für FlugzeitInStrumente und Time-Of-Flight (Calibration facility for solar wind instrumentation)

The MEFISTO ion source is an electron cyclotron resonance ion source (see [20]) that provides a well focused pencil beam (about 1 cm$^2$) with a beam flux up to 250 GHz/cm$^2$. In addition to highly ionized gas ions (e.g. Ar$^{8+}$), a metal beam can be produced using a furnace to evaporate the metals into the plasma chamber of the ion source.

The MEFISTO facility consists of the ion source and the instrument chamber which is large enough to allow to test the integrated PLASTIC instrument. The ion source and the instrument chamber is described in [43] and [31]. A year ago a new hexapod table was installed in the instrument chamber allowing movements in all three directions. In addition it can be steered by a computer enabling fully automated measurements as in the CASYMS facility.

# Appendix C

# SSL-detector efficiency measurements

## C.1  Introduction

For the calibration of the STEREO/PLASTIC ESEA it was important to know the absolute detection efficiency of the used micro channel plate (MCP) detector.
For the measurements performed in CASYMS calibration facility [21] the MCP calibration was done relative to the channeltron detector used in CASYMS for beam intensity measurements.

## C.2  Instrumentation

### C.2.1  Micro channel plate detector

The used micro channel plate detector (MCP) is a series 3300 MCP/RAE position sensitive detector from Quantar Technology [53]. It consists of a resistive anode position encoder (RAE), five waver type microchannel plate electron multipliers (MCP), and integral anode bias and signal decoupling circuits. A particle incident on MCP results in secondary electron emission which is multiplied down the biased microchannels. The resulting charge pulse is collected as current on anode with four corner read out. The relative level on each of the four corners give the position of the registered particle. Signal processing and spatial position decoding of the four low-level output signals from the sensor is provided by Quantar Technology 2401 Series Position Analyzer [54] in combination with the Option EP preamp, data collection and display system.
The principle of such position sensitive detectors was developed at the Space Science Laboratory of the University of Berkely, see [41]. The SSL detector is not only able to count ions or electrons, it was also used for UV measurements, see [49].

### C.2.2  Channel electron multiplier detector (Channeltron, CEM)

Produced by Dr. Sjuts Optotechnik GmbH [24].

## C.3  Measurements

### C.3.1  General remarks and experimental setup

For some measurements a pinhole mounted on the beam scanner in CASYMS was used to prevent too high fluxes on the SSL detector. For each efficiency measurement a background measurement was taken. The measurements with pinhole and the measurements with full irradiation of the detector had to be normalized to compare. This was done by normalizing the beam intensity measurement to the pinhole size or the full SSL area size, respectively.
All measurements in CASYMS give a relative efficiency to the Channeltron detector used for measuring

the beam intensity in CASYMS. The MCP detector was mounted in beam direction in the center of CASYMS instrumentation chamber (see figure C.1). Three measurement series were performed:

1. January 2004, in CASYMS, Helium and Argon Beam, only beam energies 3 keV/e and higher

2. February 2004, in CASYMS, Argon, Energies between 0.5 keV/e and 20 keV/e

3. July 2005, in CASYMS, Helium, Energies 3 keV/e and below

For the two first measurements a pinhole with diameter 0.8 mm was used, for the latter one a pinhole with diameter 3.6 mm was used. The setup was the same for all measurements.

Figure C.1: Experimental setup for MCP detector efficiency measurements in CASYMS. The MCP detector was mounted in the middle of the chamber. The ion beam can be blocked by the CASYMS beam scanner. To prevent ions passing the beam scanner a plate with a pinhole with diameter 3.6 mm was mounted on the movable beam scanner.
The aluminium foil was used to shield the electric field caused by the high voltage of the MCP detector.

### C.3.2 Measurements with Helium

Helium was used in the first measurements and during July 2005. For each beam energy the SSL count rate was measured for different beam intensities. So the point where detection saturation started could be found as well as the detection efficiency below saturation point. The efficiency was found as the slope of the linear fit of the data points when not saturated.

In table C.1 all measurements are summarized. It shows that the detection efficiency compared to the CEM measurements decreases with lower beam energy.

### C.3.3 Measurements with Argon

Argon was used in the first and second measurements. In the first only to show that the detection efficiency at high energies (above 2 keV/e) is not dependant on ion species.

In February 2004 the detection dependency on the beam energy was measured. The beam intensity measured with the beam scanner channeltron was kept constant at about 1 kHz/0.1 cm$^2$ and the count rate of the SSL detector was measured. Then the relative efficiency against the channeltron count rate was calculated. This measurement is shown in plot C.4.
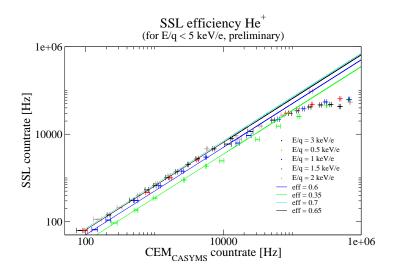
Figure C.2: SSL MCP detector count rate versus Channeltron detector count rate. All rates normalized for a detector area of 12 cm$^2$. Pinhole diameter 3.6 mm.
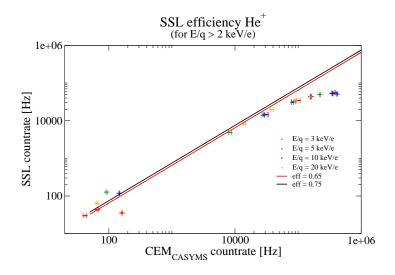


Figure C.3: SSL MCP detector count rate versus Channeltron detector count rate. All Beam scanner rates normalized to detector area (either Pinhole (0.005 cm$^2$) or full detector Area (12 cm$^2$). Pinhole diameter 0.8 mm.

| Beam energy per charge | Detection efficiency | Estimated Error of Eff. |
|---|---|---|
| 0.5 | 0.35 | 0.01 |
| 1.0 | 0.60 | 0.02 |
| 1.5 | 0.63 | 0.02 |
| 2.0 | 0.65 | 0.02 |
| 3.0 | 0.65 | 0.02 |
| 5.0 | 0.65 | 0.02 |
| 10.0 | 0.65 | 0.03 |
| 20.0 | 0.65 | 0.03 |

Table C.1: Detection efficiency for SSL MCP detector, used Ion $^4$He$^+$.
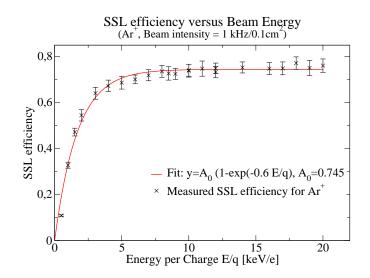
Figure C.4: SSL MCP Detector efficiency versus beam energy. The beam intensity measured with a channeltron detector was kept at 1 kHz/0.1 cm².

## C.4   Summary and Conclusions

The SSL MCP detector efficiency measurements showed:

- The energy dependence follows the empirically found law $\eta_{SSL} = A_0 \cdot (1 - \exp(-0.6E/q))$, $A_0 \simeq 0.75$ and $E/q$ in keV/e [35].

- The maximum efficiency is 0.75 given by the geometry of the micro channel plates. The geometric active area given by the channel apertures is about 0.65. The difference is due to field effects.

- The MCP detector starts to saturate above a count rate of 20000 Hz

- When the beam is too intense, the count rate starts to decrease at count rates higher than 150000 Hz even the beam intensity increases further.

For the calibration measurements of STEREO/PLASTIC the efficiency of the SSL detector was calculated by the following formula:

$$\eta_{SSL}(E/q) = A_0 \cdot (1 - \exp(-0.6E/q)) \tag{C.1}$$

with $A_0 \simeq 0.75$ and $E/q$ in keV/e [35].
For the geometric factor measurements a detection efficiency of 0.67 was used for E/q=5 keV/e and 0.65 for E/q = 3 keV/e. The estimated relative error of the efficiency is 2 %.

# Appendix D

# Calibration data

## D.1 Entrance System/ Energy Analyzer

In this Appendix there are plots from the ESEA calibration of all instruments and channels. The beam energy was always 3 keV. The plots allow to compare the three different instruments.

### D.1.1 Voltage scans
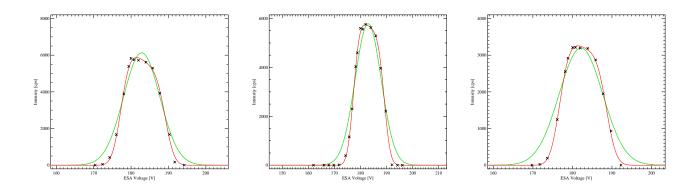


Figure D.1: *ESA voltage scan for Main Channel. E/q=3 keV/e, Ar$^+$, measured intensity by SSL detector versus ESA voltage on each ESA hemisphere.*
*From left to right: FM1, FM2 and FS*
*green line: Gaussian fit; red line: fit using (A.13)*
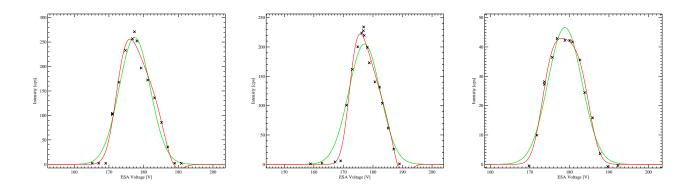


Figure D.2: *ESA voltage scan for S-Channel. E/q=3 keV/e, Ar$^+$*
*From left to right: FM1, FM2 and FS*
*green line: Gaussian fit; red line: fit using (A.13)*
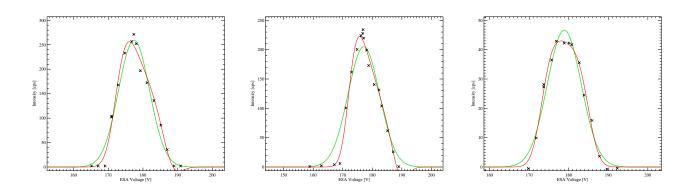
Figure D.3: *SCO-L voltage scan for S-Channel. E/q=3 keV/e, Ar⁺*
*From left to right: FM1, FM2 and FS*
*green line: Gaussian fit; red line: fit using (A.13)*
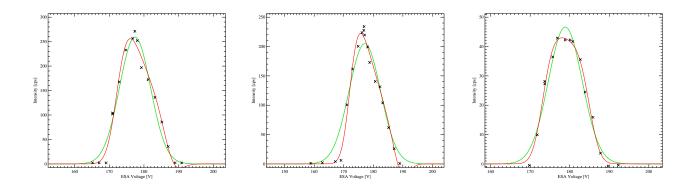


Figure D.4: *SCI-U voltage scan for S-Channel. E/q=3 keV/e, Ar⁺*
*From left to right: FM1, FM2 and FS*
*green line: Gaussian fit; red line: fit using (A.13)*
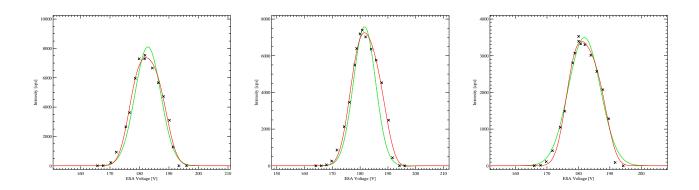


Figure D.5: *ESA voltage scan for WAP. E/q=3 keV/e, Ar⁺*
*From left to right: FM1, FM2 and FS*
*green line: Gaussian fit; red line: fit using (A.13)*

## D.1.2 Elevation angle scans
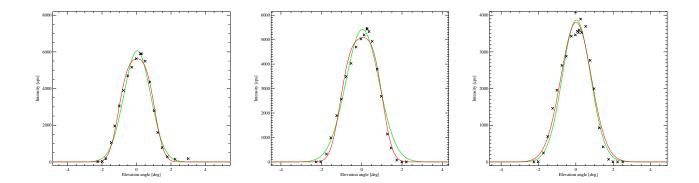


Figure D.6: *Elevation angle scan for Main Channel. E/q=3 keV/e, Ar$^+$*
*From left to right: FM1, FM2 and FS*
*green line: Gaussian fit; red line: fit using (A.13)*
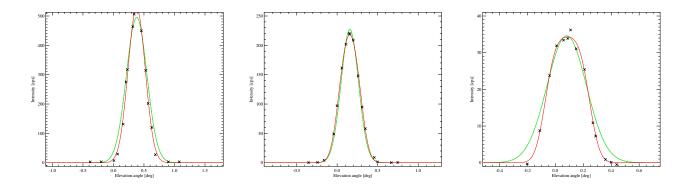


Figure D.7: *Elevation angle scan for S-Channel. E/q=3 keV/e, Ar$^+$*
*From left to right: FM1, FM2 and FS*
*green line: Gaussian fit; red line: fit using (A.13)*
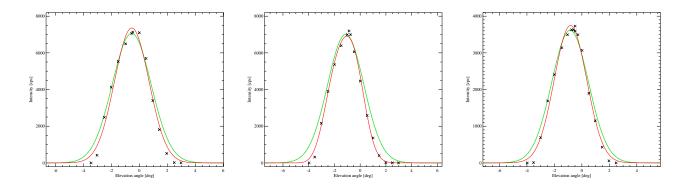
Figure D.8: *Elevation angle scan for WAP. E/q=3 keV/e, Ar$^+$*
*From left to right: FM1, FM2 and FS*
*green line: Gaussian fit; red line: fit using (A.13)*

# Appendix E

# PLASTIC calibration data archiving at University of Bern

## E.1   Introduction

All calibration data acquired at the University of Bern must be organized and made available for later use. In addition, calibration data from measurements of the integrated instruments performed at the University of New Hampshire should be available as well.

To have an easy access the calibration data of all instruments (EQM, FM1, FM2 and FS), a similar structure for each model must be incorporated.

The archive consists of several parts representing the calibration process:

- Ion optical calibration of the Entrance System/Energy Analyzer (ESEA)

- UV suppression test of the ESEA

- MCP efficiency measurements

- SSD efficiency measurements

- Vibration and environmental tests of ESEA

- Partial discharge tests of ESEA

- Ion optical calibration of integrated instruments

## E.2   Overview

In Figure E.1 the structure of the data archive at the University of Bern is shown. All calibration files and reports are stored on the STEREO server at the University of Bern: `/stereo/www/PLASTIC_cal/`. There is a data manual for the calibration data of PLASTIC [39]. The newest version is always available in the same directory: `PLASTIC_data_manual_ver*.pdf`.
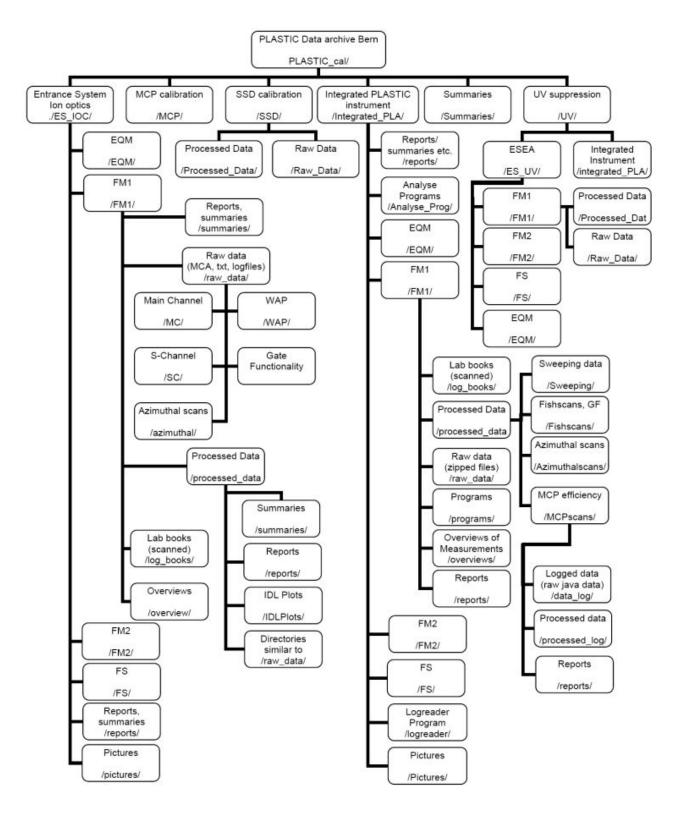
Figure E.1: *Overview over the data archive structure at the University of Bern.*

## E.3 Ion optical calibration of the entrance system/energy analyzer

In this folder, `ES_IOC`, all data files from the calibration of the ESEA are stored in folders for each model, see Chapter 3. Additionally, the measurements with the LaserCEM detector, see Chapter 5, are stored here as well. For each model there are subfolders for raw data and processed data. In addition, there are subfolders for general reports and analyze programs.

### E.3.1 Processed data

In the processed data folder all produced plots are stored. During the calibration, the measured data were written in spreadsheets for later data analysis. The file name of the spreadsheets contains the date and the topic of the measurement.

### E.3.2 Raw data

**Data format**

The SSL-detector (see Appendix C) provides position information for the measured counts. These SSL images were stored in two formats:

**MCA, binary format** When the Quantar software was used to read out the SSL signal, binary MCA files are produced. To read the MCA files, either a dos program, `MCALIST.EXE`, or the IDL program `READ_MCA.PRO` can be used. With mcalist.exe an ascii file with the position information is produced.

**Ascii format** When using the MicroVAX system in CASYMS to read out the SSL signal, the position information is stored in a text file with the suffix `.arr`. All other information (beam intensity, table position, beam energy) is stored in a text file with the suffix `.par`. The parameters to be stored can be selected in the user program to control the measurements. The used PASCAL programs are in the folder `programs`. These two text files are combined in a new text file with suffix `.prr`, the first lines are the parameter information from the `.par` file, followed by the counts per pixel, each line one pixel.
To read these `.prr` files, there are several IDL programs available, also in the folder `programs`.

**Calibration measurements**

All SSL images are stored in subfolders for each model. For the measurements that were automated (e.g., geometric factor measuremenst), a text file explains the measurement (e.g., table positions, number of energy steps). For the measurements logged in spreadsheets, only the MCA files are in the subfolders, whose name contains the calibration topic (e.g., Energyscan/E3keV).

## E.4 Ion optical calibration of the integrated instruments at University of Bern

The calibration data obtained during the measurements with the integrated instruments at the University of Bern, see Chapter 6, are stored in the folder `integrated_PLA`. The data of each model is stored in separate subdirectories. Each model directory contains a folder for processed data, raw data, programs, lab books, see Figure E.1. In the top directory there are also the folder containing analyze programs and the program to process raw data, *logreader*. For each model there is a spreadsheet containing the calibration program.

### E.4.1 Processed data

In this folder there are presentations and spreadsheets with first data analysis.

### E.4.2    Raw data

All raw data files are zipped to save space. They are stored in subfolders for each day. The data format is in binary format. With the program *logreader* provided by UNH, they can be converted into ascii files. Instruction to process these files are in the data manual. There are several IDL programs to look at the processed text files. These programs are stored in the folder `/integrated_PLA/Analyse_Prog/`. Each program contains either a header explaining the program, or there is a `read_me` file in the directory.

## E.5    Summary

In this appendix I briefly described the data archive of the PLASTIC calibration data. More details can be found in the mentioned data manual [39]. It is important that the archive is continuously maintained.

# Bibliography

[1] M. R. Aellig, A. J. Lazarus, and J. T. Steinberg. The solar wind helium abundance: Variation with wind speed and the solar cycle. *Geophysical Research Letters*, 28:2767–2770, 2001.

[2] F. Allegrini. *The* PLASTIC *sensor on* STEREO*: Design of the entrance system/energy analyzer and numerical simulations of solar wind measurements.* Ph.D. thesis, University of Bern, Switzerland, 2002.

[3] F. Allegrini, R. F. Wimmer-Schweingruber, P. Wurz, and P. Bochsler. Determination of low-energy ion-induced electron yield from thin carbon foils. *Nuclear Instruments and Methods in Physics Research B*, 211:487–494, 2003.

[4] M. Asplund, N. Grevesse, and A. J. Sauval. The Solar Chemical Composition. In T. G. Barnes, III and F. N. Bash, editors, *ASP Conf. Ser. 336: Cosmic Abundances as Records of Stellar Evolution and Nucleosynthesis*, pages 25–38, 2005.

[5] L. Biermann. Kometenschweife und solare Korpuskularstrahlung. *Zeitschrift für Astrophysik*, 29:274–286, 1951.

[6] L. M. Blush, F. Allegrini, P. Bochsler, H. Daoudi, A. Galvin, R. Karrer, L. Kistler, B. Klecker, E. Möbius, A. Opitz, M. Popecki, B. Thompson, R. F. Wimmer-Schweingruber, and P. Wurz. Development and calibration of major components for the STEREO/PLASTIC (plasma and suprathermal ion composition) instrument. *Advances in Space Research*, 36:1544–1556, 2005.

[7] L.M. Blush, F. Allegrini, P. Bochsler, A. Galvin, M. Hohl, R. Karrer, L. Kistler, B. Klecker, E. Möbius, M. Popecki, T. Thompson, X. Wang, R. F. Wimmer-Schweingruber, and P. Wurz. Tests and Calibrations of the PLASTIC Entrance System: Design Verification for Flight Models on the STEREO Spacecraft. *Proceedings of the 30th EPS conference on Controlled Fusion and Plasma Physics, St. Petersburg, Russian Federation, Europhys. Conf. Abstr. 27A*, pages P–2.2.11, 2003.

[8] P. Bochsler. Abundances and charge states of particles in the solar wind. *Reviews of Geophysics*, 38:247–266, 2000.

[9] C. W. Carlson, D. W. Curtis, P. Paschmann, and W. Michael. An Instrument for rapidly measuring Plasma Distribution Function with high Resolution. *Advances in Space Science*, 2(7):67–70, 1983.

[10] S. Chapman and J. Bartels. *Geomagnetism.* Oxford University Press, Oxford, UK, 1940.

[11] L. M. Chase. The geometrical factor of large aperture hemispherical electrostatic analyzers. *Review of Scientific Instruments*, 44(8):998–1002, August 1973.

[12] J. Chen. *Coronal Mass Ejections: Causes and Consequences A theoretical View*, pages 65–81. In Crooker et al. [13], 1997.

[13] N. Crooker, J. A. Joselyn, and J. Feynman, editors. *Coronal Mass Ejections.* Geophysical Monograph 99, American Geophysical Union, Washington, DC,USA, 1997.

[14] David A. Dahl. SIMION for the personal computer in reflection. *International Journal of Mass Spectrometry*, 200:3–25, April 2000.

[15] Hagar Daoudi. *STEREO PLASTIC simulation*. Ph.D. thesis, University of Bern, Switzerland, 2007.

[16] ACE/SWICS Level 2 data. http://www.srl.caltech.edu/ace/asc/level2/lvl2data_swics-swims.html.

[17] L. Ellis and L. Kistler. *PLASTIC Level 1 Data Document, Version C.* University of New Hampshire, USA, 2007.

[18] L. A. Fisk. Journey into the Unknown Beyond. *Science*, 309:2016–2017, September 2005.

[19] J. Geiss. Processes affecting abundances in the solar wind. *Space Science Reviews*, 33:201–217, 1982.

[20] Richard Geller. *Electron cyclotron resonance ion sources and ECR plasmas.* Institute of Physics Publishing, Bristol and Philadelphia, 1996.

[21] A.G. Ghielmetti, H. Balsiger, R. Baenninger, P. Eberhardt, J. Geiss, and D.T. Young. Calibration System for satellite and rocket-borne ion mass spectrometers in the energy range from 5 eV/charge to 100 keV/charge. *Review of Scientific Instruments*, 54(4):425–436, April 1983.

[22] G. Gloeckler, J. Cain, F. M. Ipavich, E. O. Tums, P. Bedini, L. A. Fisk, T. H. Zurbuchen, P. Bochsler, J. Fischer, R. F. Wimmer-Schweingruber, J. Geiss, and R. Kallenbach. Investigation of the composition of solar and interstellar matter using solar wind and pickup ion measurements with SWICS and SWIMS on the ACE spacecraft. *Space Science Reviews*, 86:497–539, 1998.

[23] G. Gloeckler, J. Geiss, H. Balsiger, P. Bedini, J. C. Cain, J. Fisher, L. A. Fisk, A. B. Galvin, F. Gliem, and D. C. Hamilton. The Solar Wind Ion Composition Spectrometer. *Astronomy and Astrophysics Supplement Series*, 92:267–289, 1992.

[24] Dr. Sjuts Optotechnik GmbH. http://www.sjuts.com.

[25] Marc Gonin. *Ein semiempirisches Modell des Ladungsaustausches von niederenergetischen Ionen beim Durchgang durch dünne Folien, zur Eichung von isochronen Flugzeit-Massenpektrometern.* Ph.D. thesis, University of Bern, Switzerland, 1995.

[26] J. T. Gosling. *Coronal Mass Ejections: An Overview*, pages 9–16. In Crooker et al. [13], 1997.

[27] J. T. Gosling, J. R. Asbridge, S. J. Bame, and W. C. Feldman. Effects of a long entrance aperture upon the azimuthal response of sperical section electrostatic analyzer. *Review of Scientific Instruments*, 49(9):1260–1268, September 1978.

[28] N. Grevesse and A. J. Sauval. Standard Solar Composition. In C. Fröhlich, M. C. E. Huber, S. K. Solanki, and R. von Steiger, editors, *Solar Composition and Its Evolution – From Core to Corona*, pages 161–+, 1998.

[29] D. C. Hamilton, G. Gloeckler, F. M. Ipavich, R. A. Lundgren, and R. B. Sheldon. New high-resolution electrostatic ion mass analyzer using time of flight. *Review of Scientific Instruments*, 61:3104–3106, October 1990.

[30] Simon Hefti. *Solar Wind Freeze-in Temperatur and Fluxes Measured with SOHO/CELIAS/CTOF and Calibration of the CELIAS Sensors.* Ph.D. thesis, University of Bern, Switzerland, 1993.

[31] Markus Hohl. *MEFISTO II: Design, setup, characterization and operation of an improved calibration facility for solar plasma instrumentation.* Ph.D. thesis, University of Bern, Switzerland, 2002.

[32] D. Hovestadt, M. Hilchenbach, A. Bürgi, B. Klecker, P. Laeverenz, M. Scholer, H. Grünwaldt, W. I. Axford, S. Livi, E. Marsch, B. Wilken, H. P. Winterhoff, F. M. Ipavich, P. Bedini, M. A. Coplan, A. B. Galvin, G. Gloeckler, P. Bochsler, H. Balsiger, J. Fischer, J. Geiss, R. Kallenbach, P. Wurz, K.-U. Reiche, F. Gliem, D. L. Judge, H. S. Ogawa, K. C. Hsieh, E. Mobius, M. A. Lee, G. G. Managadze, M. I. Verigin, and M. Neugebauer. CELIAS - Charge, Element and Isotope Analysis System for SOHO. *Solar Physics*, 162:441–481, 1995.

[33] A. J. Hundhausen. *The solar wind*, pages 91–128. In Kivelson and Russell [40], 1995.

[34] F.M. Ipavich, J.A. Paquette, P. Bochsler, S.E. Lasley, and P. Wurz. Solar Wind Iron Isotopic Abundances: Results from SOHO/CELIAS/MTOF. *American Institute Physics on* Solar and Galactic Composition, CP-598:121–126, 2001.

[35] Sarah Jans. Ionization of energetic neutral atoms for application in space instrumentation. Master thesis, University of Bern, Switzerland, 1999.

[36] R. Kallenbach, F. M. Ipavich, P. Bochsler, S. Hefti, D. Hovestadt, H. Grünwaldt, M. Hilchenbach, W. I. Axford, H. Balsiger, A. Bürgi, M. A. Coplan, A. B. Galvin, J. Geiss, F. Gliem, G. Gloeckler, K. C. Hsieh, B. Klecker, M. A. Lee, S. Livi, G. G. Managadze, E. Marsch, E. Möbius, M. Neugebauer, K.-U. Reiche, M. Scholer, M. I. Verigin, B. Wilken, and P. Wurz. Isotopic composition of solar wind neon measured by CELIAS/MTOF on board SOHO. *Journal of Geophysical Research*, 102:26895–26904, 1997.

[37] R. Karrer. Time dependant MCP efficiency on PLASTIC FM1. Technical report, University of Bern, February 2005.

[38] R. Karrer. Nickel/iron with MTOF: Carbon foil efficiency differences. Technical report, University of Bern, October 2006.

[39] R. Karrer. *Data archive for PLASTIC calibration data University of Bern, User Manual*. University of Bern, Switzerland, 2007.

[40] M. G. Kivelson and C. T. Russell, editors. *Introduction to Space Physics*. Cambridge University Press, Cambridge, UK, 1995.

[41] M. Lampton and C. W. Carlson. Low-distortion resistive anodes for two-dimensional position-sensitive MCP systems. *Review of Scientific Instruments*, 50(9):1093–1097, September 1979.

[42] K. Lodders. Solar System Abundances and Condensation Temperatures of the Elements. *Astrophysical Journal*, 591:1220–1247, July 2003.

[43] Adrian Marti, Reto Schletti, Peter Wurz, and Peter Bochsler. New calibration facility for solar wind plasma instrumentation. *Review of Scientific Instruments*, 72(2):1354–1360, February 2001.

[44] D. J. McComas, S. J. Bame, P. Barker, W. C. Feldman, J. L. Phillips, P. Riley, and J. W. Griffee. Solar Wind Electron Proton Alpha Monitor (SWEPAM) for the Advanced Composition Explorer. *Space Science Reviews*, 86:563–612, 1998.

[45] R. A. Mewaldt, G. M. Mason, G. Gloeckler, E. R. Christian, C. M. S. Cohen, A. C. Cummings, A. J. Davis, J. R. Dwyer, R. E. Gold, S. M. Krimigis, R. A. Leske, J. E. Mazur, E. C. Stone, T. T. von Rosenvinge, M. E. Wiedenbeck, and T. H. Zurbuchen. Long-Term Fluences of Energetic Particles in the Heliosphere. In R. F. Wimmer-Schweingruber, editor, *AIP Conf. Proc. 598: Joint SOHO/ACE workshop "Solar and Galactic Composition"*, pages 165–170, 2001.

[46] J.-P. Meyer. The baseline composition of solar energetic particles. *Astrophysical Journal Supplement Series*, 57:151–171, January 1985.

[47] E. Möbius, P. Bochsler, A. G. Ghielmetti, and D. C. Hamilton. High mass resolution isochronous time-of-flight spectrograph for three-dimensional space plasma measurements. *Review of Scientific Instruments*, 61:3609–3612, 1990.

[48] E. Möbius, D. Hovestadt, B. Klecker, M. Scholer, and G. Gloeckler. Direct observation of He$^+$ pick-up ions of interstellar origin in the solar wind. *Nature*, 318:426–429, 1985.

[49] Andrea Opitz. *STEREO PLASTIC calibration, simulation and data analysis.* Ph.d. thesis, University of Bern, Switzerland, 2007.

[50] F. R. Paolini and G. C. Theodoridis. Charged particle transmission through spherical plate electrostatic analyzers. *Review of Scientific Instruments*, 38(5):579–588, May 1967.

[51] E. N. Parker. Dynamics of the Interplanetary Gas and Magnetic Fields. *The Astrophysical Journal*, 128:664–676, 1958.

[52] E. N. Parker. *Interplanetary dynamical processes.* New York, Interscience Publishers, 1963., 1963.

[53] Quantar Technology Inc., 3004 Mission Street, Santa Cruz, CA 95060. *3300 series open-face MCP/RAE sensors, installation and maintenance manual*, August 1991.

[54] Quantar Technology Incorporated, 3004 Mission Street, Santa Cruz, CA 95060. *3300/2400 series, system installation and operation manual*, November 1991.

[55] J. Raines, S. T. Lepri, T. H. Zurbuchen, G. Gloeckler, and L. A. Fisk. Heavy Ions in the Solar Wind: A New Dataset from ACE. In *ESA SP-592: Solar Wind 11/SOHO 16, Connecting Sun and Heliosphere*, 2005.

[56] M. Steinacher, F. Jost, and U. Schwab. A modern and fully automated calibration system for space ion mass spectrometers. *Review of Scientific Instruments*, 66:4180–4187, 1995.

[57] Michael Stix. *The Sun, An Introduction.* Springer-Verlag, Berlin and Heidelberg, second edition, 2004.

[58] G. C. Theodoridis and F. R. Paolini. Charged particle transmission through cylindrical plate electrostatic analyzers. *Review of Scientific Instruments*, 39(3):326–330, March 1968.

[59] V. M. Vasyliunas. Deep Space Plasma Measurements. In R. H. Lovberg and H. R. Griem, editors, *Plasma Physics, Part B: Volume 9.*, pages 49–88, 1970.

[60] V. M. Vasyliunas and G. L. Siscoe. On the flux and the energy spectrum of interstellar ions in the solar system. *"Journal of Geophysical Research"*, 81:1247–1252, 1976.

[61] R. von Steiger, J. Geiss, G. Gloeckler, and A. B. Galvin. Kinetic properties of heavy ions in the solar wind from SWICS/ULYSSES. *Space Science Review*, 72:71–76, 1995.

[62] Martin Wieser. *Detection of Energetic Neutral Atoms and its Application to Heliospheric Science.* Ph.D. thesis, University of Bern, Switzerland, 2005.

[63] Robert F. Wimmer-Schweingruber. *Oxygene, Helium and Hydrogen in the Solar Wind: SWICS/ULYSSES Results.* Ph.D. thesis, University of Bern, Switzerland, 1994.

[64] H. Wollnik, T. Matsuo, and H. Matsuda. The electrostatic potential in a toroidal condenser. *Nuclear Instruments and Methods*, 102:13–17, 1972.

[65] Hermann Wollnik. Electrostatic prisms. In Albert Septier, editor, *Focusing of charged particles*, volume II, pages 163–202. Academic Press, Inc., Orlando, Florida, USA, 1967.

[66] Hermann Wollnik. Mass seperators. *Nuclear Instruments and Methods in Physics Research A*, 258:289–296, 1987.

[67] P. Wurz, M. Aellig, and S. Hefti. *The Dataphase Manual for the Charge, Element, and Isotope Analysis System (CELIAS) on the Solar and Heliospheric Observatory (SOHO) Mission, Version 1.3.* University of Bern, Switzerland, May 1997.

[68] Peter Wurz. *Heavy ions in the solar wind: Results from* SOHO/CELIAS/MTOF. Habilitation thesis, University of Bern, Switzerland, 2001.

[69] Peter Wurz and Reto Schletti. Optical signal coupling in microchannel plate detectors with a sub-nanosecond performance. *Review of Scientific Instruments*, 72(8):3225–3229, August 2001.

[70] D. T. Young, S. J. Bame, M. F. Thomsen, and R. H. Martin. $2\pi$-radian field-of-view toroidal electrostatic analyzer. *Review of Scientific Instruments*, 59(5):743–751, May 1988.

[71] D. T. Young, J. A. Marshall, and J. L. Burch. A $360^o$ field-of-view toroidal ion composition analyzer using time-of-flight. In Jr. J.H. Waite, J.L. Burch, and R.L. Moore, editors, *Solar System Plasma Physics*, volume 54, pages 171–176. AGU Geophysical Monograph Series, USA, 1989.

# List of Figures

# List of Tables

# List of Acronyms

| | | |
|---|---|---|
| ACE | : | Advanced Composition Explorer |
| AU | : | Astronomical Unit |
| CASYMS | : | CAlibration SYstem for Mass Spectrometers |
| CELIAS | : | Charge, ELement, and Isotope Analysis System on SOHO |
| CEM | : | Channel Electron Multiplier |
| CLUSTER | : | ESA cornerstone mission to explore the interaction between the Sun and the Earth's magnetosphere |
| CME | : | Coronal Mass Ejection |
| DB | : | DuckBill |
| EQM | : | Engineering Qualification Model |
| ESA | : | ElectroStatic Analyzer |
| ESEA | : | Entrance System / Energy Analyzer |
| FM | : | Flight Model |
| FOV | : | Field-Of-View |
| FS | : | Flight Spare |
| FWHM | : | Full Width at Half Maximum |
| HV | : | High Voltage |
| HWHM | : | Half Width at Half Maximum |
| ICME | : | Interplanetary CME |
| IFM | : | Integrated Flight Model |
| IDL | : | Interactive Data Language (software for programming and plotting) |
| IDPU | : | Instrument Data Processing Unit |
| IMPACT | : | *In-situ* Measurements of Particles and CME Transients |
| LP | : | Laboratory Prototype |
| $M_\odot$ | : | Solar mass |
| MC | : | Main Channel of PLASTIC |
| MCP | : | MicroChannel Plate |
| MEFISTO | : | MEsskammer für FlugzeitInStrumente und Time-Of-flight |
| MPE | : | Max Planck Institute for Extraterrestrial Physics, Germany |
| MTOF | : | Mass TOF sensor. Part of the CELIAS package |
| PLASTIC | : | PLasma And SupraThermal Ion Composition investigation on STEREO |
| $R_\odot$ | : | Solar Radius |
| SC | : | S-Channel of PLASTIC ESEA |
| SECCHI | : | Sun-Earth Connection Coronal and Heliospheric Investigation |
| SEE | : | Secondary Electron Emission |
| SIMION | : | Ion optics simulation program designed to study and analyze ion optics in both two and three dimensional modes or views |
| SOHO | : | SOlar and Heliospheric Observatory |
| SRIM | : | The Stopping and Range of Ions in Matter (Software) |

| SSD | : | Solid State Detector |
| SSL | : | Surface Science Laboratories. An SSL detector is a position |
| | | sensitive detector |
| STEREO | : | Solar-TErrestrial RElations Observatory |
| SWAVES | : | STEREO/WAVES |
| SWICS | : | Solar Wind Ion Composition Spectrometer on ACE and Ulysses |
| SWS | : | Solar Wind Sector |
| TOF | : | Time-Of-Flight ($\tau$) |
| UBe | : | University of Bern, Switzerland |
| Ulysses | : | Mission to explore the region of space above the poles of the Sun |
| UNH | : | University of New Hampshire, Durham, New Hampshire, USA |
| UV | : | Ultra-Violet |
| V-MASS | : | V-shaped isochronous time of flight spectrometer, part of MTOF |
| WAP | : | Wide Angle Partition |
| WAVE | : | Wide Angle, Variable Energy/charge, entrance system of MTOF |

Abbreviations used for the ESEA electrodes:

| SAD | : | S-channel Aperture Diaphragm |
| SA-L | : | S-channel Aperture Lower duckbill electrode |
| SA-U | : | S-channel Aperture Upper duckbill electrode |
| MA-L | : | Main channel Aperture Lower duckbill electrode |
| MA-U | : | Main channel Aperture Upper duckbill electrode |
| SCI-U | : | S-Channel Inner Upper electrode |
| SCO-L | : | S-Channel Outer Lower electrode |
| SCI-L | : | S-Channel Inner Lower electrode |
| SCO-U | : | S-Channel Outer Upper electrode |
| MG-L | : | Main channel Gate Lower electrode |
| MG-U | : | Main channel Gate Upper electrode |
| MC | : | Main Channel electrode |
| ESA-TC | : | ElectroStatic Analyzer Top-Cap electrode |
| ESA-I | : | ElectroStatic Analyzer Inner electrode |
| ESA-O | : | ElectroStatic Analyzer Outer electrode |
| WA-L | : | Wide Angle partition Lower electrode |
| WA-U | : | Wide Angle partition Upper electrode |

# Acknowledgements

- All my friends for the many good moments and discussions during the last years

- A very special thank goes to my wife Carola Karrer-Glanz for her support, her love and her understanding when I sometimes came home later than expected

- And last but not least I would like to thank my parents for their long-standing and continuous support. I am very grateful that I could pursue my studies with your help.

# Curriculum Vitae

**Personal Data**

| | |
|---|---|
| Name | Reto Karrer |
| Date of birth | June 2, 1974 |
| Place of birth | Uster, Switzerland |

**Education**

| | |
|---|---|
| 1981 - 1987 | Primary school in Russikon, Switzerland |
| 1986 - 1993 | Studies at the Kantonsschule Zürcher Oberland, Wetzikon, Switzerland |
| 1993 | Federal Maturity with emphasis in ancient languages (Typus A) |
| 1994 - 2001 | Studies at the University of Zürich in physics, mathematics and philosophy |
| 1997 - 1998 | Exchange student at the University of Bergen, Norway |
| 2001 | Diploma in experimental physics at the physics institute, University of Zürich, in the surface science group of Prof. Dr. J. Osterwalder: "Bau einer Elektronenkanone für zeitaufgelöste Beugung mit langsamen Elektronen (LEED)" |
| 2003 - 2007 | PhD thesis in physics at the *Physikalisches Institut*, Dept. of Space Research and Planetary Sciences: "Ion optical calibration of the PLASTIC sensor on STEREO" Supervisor: Prof. Dr. P. Bochsler Referee: Prof. Dr. E. Möbius |

**Professional Training**

| | |
|---|---|
| 1999 - 2000 | Physics teacher at the Kantonsschule Zürcher Oberland in Wetzikon, Switzerland |
| 2001 - 2003 | Physics teacher at the Kantonsschule Küsnacht, Switzerland |
| Since 2003 | Teaching assistant in the physics laboratory for medical, biology and physics students |